

**Characterization of a Fracture-Controlled Enhanced Geothermal System (EGS) in the Trans-Mexican-Volcanic-Belt (TMVB)**

**Predictive Mechanical Model for Fracture Stimulation in an Enhanced Geothermal System Context (EGS)**

Lepillier, B.P.

**DOI**

[10.4233/uuid:8c8e04ec-b697-4ebd-ae4-46a01434021c](https://doi.org/10.4233/uuid:8c8e04ec-b697-4ebd-ae4-46a01434021c)

**Publication date**

2020

**Document Version**

Final published version

**Citation (APA)**

Lepillier, B. P. (2020). *Characterization of a Fracture-Controlled Enhanced Geothermal System (EGS) in the Trans-Mexican-Volcanic-Belt (TMVB): Predictive Mechanical Model for Fracture Stimulation in an Enhanced Geothermal System Context (EGS)*. [Dissertation (TU Delft), Delft University of Technology]. <https://doi.org/10.4233/uuid:8c8e04ec-b697-4ebd-ae4-46a01434021c>

**Important note**

To cite this publication, please use the final published version (if applicable). Please check the document version above.

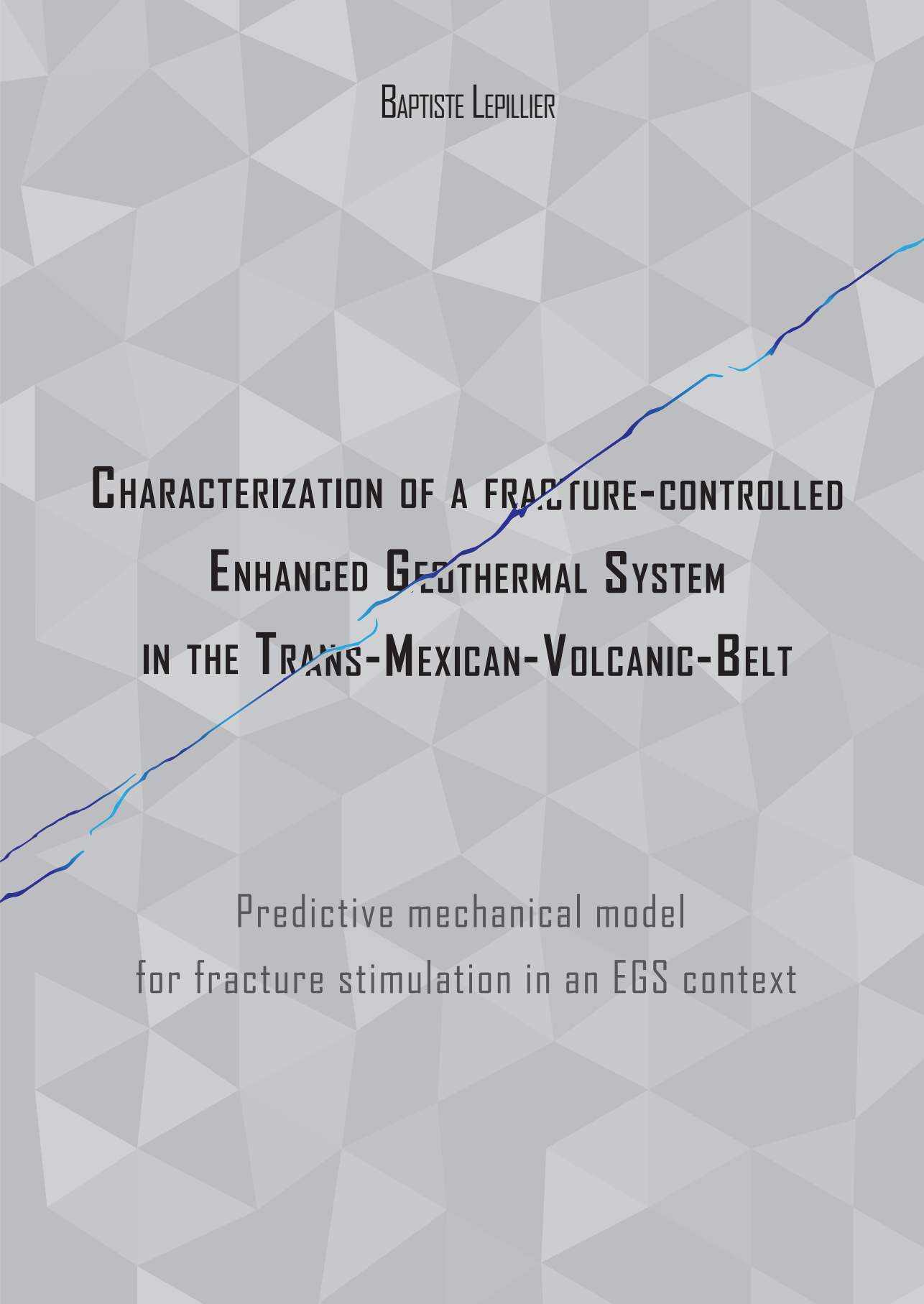
**Copyright**

Other than for strictly personal use, it is not permitted to download, forward or distribute the text or part of it, without the consent of the author(s) and/or copyright holder(s), unless the work is under an open content license such as Creative Commons.

**Takedown policy**

Please contact us and provide details if you believe this document breaches copyrights. We will remove access to the work immediately and investigate your claim.

BAPTISTE LEPILLIER



**CHARACTERIZATION OF A FRACTURE-CONTROLLED  
ENHANCED GEOTHERMAL SYSTEM  
IN THE TRANS-MEXICAN-VOLCANIC-BELT**

Predictive mechanical model  
for fracture stimulation in an EGS context





**CHARACTERIZATION OF A FRACTURE-CONTROLLED  
ENHANCED GEOTHERMAL SYSTEM (EGS) IN THE  
TRANS-MEXICAN-VOLCANIC-BELT (TMVB)**

PREDICTIVE MECHANICAL MODEL FOR FRACTURE  
STIMULATION IN AN ENHANCED GEOTHERMAL SYSTEM  
CONTEXT (EGS)



# **CHARACTERIZATION OF A FRACTURE-CONTROLLED ENHANCED GEOTHERMAL SYSTEM (EGS) IN THE TRANS-MEXICAN-VOLCANIC-BELT (TMVB)**

**PREDICTIVE MECHANICAL MODEL FOR FRACTURE  
STIMULATION IN AN ENHANCED GEOTHERMAL SYSTEM  
CONTEXT (EGS)**

## **Dissertation**

for the purpose of obtaining the degree of doctor  
at Delft University of Technology  
by the authority of the Rector Magnificus Prof.dr.ir. T.H.J.J. van der Hagen  
Chair of the board of Doctorates.  
This thesis will be defended publicly on  
Tuesday 29 September 2020 at 18:00 o'clock

by

**Baptiste Patrick LEPILLIER**

Master of Science in Geology,  
Institut Polytechnique LaSalle Beauvais, France  
Born in Harfleur, France

This Dissertation has been approved by the promotors

Promotor: Prof. dr. D.F. Bruhn

Promotor: Prof. dr. G. Bertotti

Composition of the doctoral committee:

Rector Magnificus,  
Prof. dr. D. Bruhn,  
Prof. dr. G. Bertotti,

Chairperson  
Promotor | Delft University of Technology  
Promotor | Delft University of Technology

*Independant members:*

Dr. M. Brehme,  
Prof. dr. R. Horne,  
Prof. dr. D. Liotta,  
Prof. dr. J.D.A.M. van Wees,  
Prof. dr. ir. P.L.J. Zitha,

Delft University of Technology  
Stanford University  
University of Bari Aldo Moro  
TNO, Utrecht University  
Delft University of Technology

*Reserve member:*

Prof. dr. W.R. Rossen,

Delft University of Technology

This research received funding from the European Union's Horizon 2020 research and innovation programme, DESTRESS Grant agreement number 691728; GEMex Grant agreement No. 727550; and The Mexican Energy Sustainability Fund CONACYT-SENER, project 2015-04-268074



*Keywords:* Geothermal reservoir, Enhanced Geothermal System, Natural fractures, Discrete fracture network, thermo-hydro-mechanical modelling, hydraulic fracture modelling, phase-field, Finite Element Method

*Printed by:* ProefschriftMaken

*Front & Back:* BatL

Copyright © 2020 by B. Lepillier

ISBN 978-94-6384-168-9

An electronic version of this dissertation is available at  
<http://repository.tudelft.nl/>.

*All models are wrong,  
but some are useful*

KY quoting George Box



# CONTENTS

<b>Summary</b>	<b>xi</b>
<b>Samenvatting</b>	<b>xiii</b>
<b>1 Introduction</b>	<b>1</b>
1.1 Enhanced Geothermal Systems . . . . .	2
1.1.1 Geothermal History . . . . .	2
1.1.2 EGS Potential & Principle . . . . .	2
1.2 Hydraulic fracturing, The knowledge gap . . . . .	3
1.3 The GEMex Project . . . . .	4
1.4 Geological Context . . . . .	5
1.4.1 Regional geology. . . . .	5
1.4.2 Local geology . . . . .	5
1.4.3 Structural context . . . . .	7
1.5 Thesis Outline . . . . .	11
<b>2 Characterization of Natural Fractures</b>	<b>13</b>
2.1 Introduction . . . . .	14
2.2 Background, Existing methods . . . . .	16
2.2.1 Existing methods for the scanline survey. . . . .	16
2.2.2 Existing scripts for scanline or fracture data processing . . . . .	16
2.2.3 Existing methods for DFN computation . . . . .	17
2.3 Method: Workflow description . . . . .	17
2.3.1 Using SkaPy . . . . .	18
2.3.2 Method: DFN creation using Multiple point statistics . . . . .	20
2.4 Results: Case study of Acoculco geothermal site in Mexico . . . . .	22
2.4.1 Geological context . . . . .	22
2.4.2 Case Study: Applying the scanline survey . . . . .	25
2.4.3 Case Study: Running SkaPy . . . . .	26
2.4.4 Case Study: Creating the Training Images (TIs) and running MPS . . . . .	27
2.4.5 Case Study: created DFNs . . . . .	27
2.5 Discussion & Way Forward . . . . .	27
2.6 Conclusion . . . . .	29
<b>3 Characterization of Acoculco Reservoir Rock Properties</b>	<b>41</b>
3.1 Introduction . . . . .	42
3.2 Rock Physics Laboratory Experiments . . . . .	43
3.2.1 XRF-XRD. . . . .	43
3.2.2 Porosity & Permeability . . . . .	44
3.2.3 Unconfined Compressive Strength Test . . . . .	46



3.2.4	Unconfined Tensile Strength (Brazilian disc) Test . . . . .	48
3.2.5	Chevron Bend Test . . . . .	50
3.2.6	Hydraulic fracturing test using the Hoek cell . . . . .	51
3.3	Discussion of the results . . . . .	53
3.4	Conclusion . . . . .	55
<b>4</b>	<b>Thermo-Hydro-pseudo-Mechanical flow model, in fractured reservoir</b>	<b>57</b>
4.1	Introduction . . . . .	58
4.1.1	Background . . . . .	58
4.1.2	Study context . . . . .	58
4.1.3	Innovation . . . . .	59
4.2	Methods: Simulation model implementation . . . . .	60
4.2.1	General implementation . . . . .	60
4.2.2	Governing Equations . . . . .	60
4.2.3	Model Scenarios . . . . .	61
4.3	Application: field example . . . . .	61
4.3.1	Input data, and domain delimitation . . . . .	61
4.3.2	Stress field . . . . .	63
4.3.3	Problem definition and simulation implementation . . . . .	63
4.4	Results . . . . .	63
4.4.1	Aperture dependency to the stress field . . . . .	63
4.4.2	Production scenarios . . . . .	64
4.4.3	Heat transfer . . . . .	66
4.5	Discussion . . . . .	66
4.6	Conclusion . . . . .	70
4.7	List of abbreviations . . . . .	71
<b>5</b>	<b>Hydraulic Fracture stimulation model, with 3D planar fracture</b>	<b>73</b>
5.1	Introduction . . . . .	74
5.1.1	Problem definition . . . . .	74
5.2	Input data . . . . .	76
5.2.1	Inputs for Well-bore design . . . . .	76
5.2.2	Inputs for the sensitivity analysis . . . . .	78
5.2.3	Inputs for the EAC1 HF stimulation analysis . . . . .	78
5.3	Results of the sensitivity analysis . . . . .	80
5.3.1	Sensitivity analysis using perfos from 800 to 1900 mMD . . . . .	81
5.3.2	Sensitivity analysis using perfos from 800 to 900 mMD . . . . .	82
5.3.3	Sensitivity analysis using perfos from 1800 to 1900 mMD . . . . .	83
5.3.4	Sensitivity analysis Conclusions . . . . .	84
5.4	EAC1 HF predictive stimulation, laboratory data model . . . . .	86
5.4.1	Stimulating the well, with an open-hole, from 800 to 1900m MD. . . . .	86
5.4.2	Stimulating the well, with a cased-hole, perforated from 1500 to 1600m MD . . . . .	86
5.4.3	Stimulating the Skarn, with a cased hole, perforated from 1700 to 1800m MD . . . . .	88

5.4.4	Stimulating the Granodiorite, with a cased hole, perforated from 1800 to 1900m MD . . . . .	88
5.5	EAC1 HF predictive stimulation, Hoek-Brown GSI model . . . . .	89
5.5.1	Stimulating the open-hole well, from 800 to 1900m MD . . . . .	91
5.5.2	Stimulating the Marble, cased hole perforated from 1500 to 1600m MD. . . . .	91
5.5.3	Stimulating the Skarn, with a cased hole, perforated from 1700 to 1800m MD. . . . .	92
5.5.4	Stimulating the Granodiorite, with a cased hole, perforated from 1800 to 1900m MD. . . . .	92
5.6	Conclusion . . . . .	93
5.7	Abbreviations & Symbols . . . . .	95
<b>6</b>	<b>Hydraulic Fracture stimulation model, in 2D fractured reservoir</b>	<b>97</b>
6.1	Introduction . . . . .	98
6.2	Variational Phase-field Model. . . . .	100
6.2.1	Variational approach to fracture . . . . .	100
6.2.2	Governing Equations. . . . .	101
6.2.3	Phase-field Approximation. . . . .	102
6.2.4	Numerical Implementation . . . . .	103
6.3	Applications . . . . .	105
6.3.1	Sensitivity Analyzes . . . . .	105
6.3.2	The Acoculco Geothermal Reservoir . . . . .	106
6.4	Results . . . . .	108
6.4.1	Sensitivity Analysis. . . . .	108
6.4.2	Stimulation of the Acoculco Geothermal Reservoir . . . . .	111
6.5	Discussion . . . . .	116
6.6	Conclusion . . . . .	118
6.7	Acknowledgments . . . . .	119
<b>7</b>	<b>Results, A fully integrated EGS evaluation workflow</b>	<b>121</b>
7.1	Introduction . . . . .	122
7.1.1	Background . . . . .	122
7.1.2	Study context . . . . .	122
7.1.3	Innovation . . . . .	123
7.2	Method & Results . . . . .	123
7.2.1	From Scanline to DFN . . . . .	123
7.2.2	Hydraulic fracture modeling with the variational phase-field (V-pf) . . . . .	124
7.2.3	Thermal & fluid flow model . . . . .	126
7.3	Discussion . . . . .	127
7.4	Conclusion . . . . .	128
<b>8</b>	<b>Conclusion</b>	<b>129</b>
<b>A</b>	<b>Appendix</b>	<b>133</b>
<b>B</b>	<b>Abbreviations</b>	<b>139</b>

<b>C Bibliography</b>	<b>143</b>
<b>References</b>	<b>145</b>
<b>Curriculum Vitæ</b>	<b>169</b>
<b>List of Publications</b>	<b>171</b>
C.1 Publications. . . . .	171
C.2 Conferences. . . . .	172

# SUMMARY

In 2020, as the world Energy demand keeps on rising (International Energy Agency (IEA), 2019), and with the global climate warming a reality (The Organisation for Economic Co-operation and Development (OECD), 2020), reducing our societal impact on Earth is of utmost importance. Energy and Climate have always been intrinsically related. Therefore, solving the Energy-Climate problem is a challenge where not one but several solutions should come together. Part of this global solution is the potential of geothermal resources. Geothermal energy is a renewable energy resource which has large potential to reduce the dependency on fossil fuels.

Within the several uses of geothermal resources, a promising technique is titled Enhanced Geothermal Systems. More than renewable, this method has the potential to be sustainable. EGS consists of an originally low permeability reservoir rock that is artificially enhanced. The enhancement can be achieved by different stimulation techniques, such as mechanical, chemical, thermal or a combination of all.

This thesis focuses on the mechanical EGS stimulation, where opening of existing fractures and creation of new ones is achieved by injecting a pressurized fluid in the reservoir rock formation. Such a process results in propagating a hydraulic fracture. The complexity of the EGS technique stands in predicting the hydraulic fracture propagation phenomena.

EGS research and development is part of the GEMex goals. The GEMex project is a collaboration between Mexican institutions and the European Commission, dedicated to the development of non-conventional geothermal techniques. The Acoculco geothermal field, located in Puebla, is foreseen as a potential EGS. Because this field has been explored with two geothermal wells, and because an analogue exhumed system is available nearby, in the Las Minas area, this system constitutes a great research site for developing knowledge on EGS.

In this thesis, I propose an integrated workflow for evaluating the EGS potential of a reservoir rock formation. The workflow starts with **Chapter 2**, introducing a novel method used to predict the fracture network in the subsurface, by computing Discrete Fracture Networks (DFN) from outcrop data. More specifically, a compilation of scanline survey datasets is acquired at the field. This dataset is analyzed using the newly written Python<sup>TM</sup> script SkaPy. SkaPy helps compiling Training Images which can then be extrapolated into the field scale using the Multiple Points Statistic method.

In **Chapter 3**, I describe the rock physics laboratory work realized to characterize the rock properties. These measurements span from mineral analyses to original hydraulic fracture experimental setup. All these measurements are applied to rock samples collected in Acoculco and Las Minas analogue outcrops. The characterization is used to predict the behavior of the potential reservoir rocks during the hydraulic fracture propagation process.

Continuing on fracture characterization, **Chapter 4** presents a model built to evaluate

the extent to which fractures in the subsurface can influence the reservoir thermal and fluid flow. As the Acoculco geothermal field enhancement could be achieved in different reservoir formations, the model handles a multi-reservoir analysis. And because the fracture distribution within a reservoir formation is not homogeneous, the model compares multi-production scenarios.

Moving on the prediction of the hydraulic fracture propagation, **Chapter 5** approaches the question by modeling a hydraulic fracturing process using a perfectly planar 3 dimensional (3D) fracture. In this chapter I analyze the influence of different parameters involved in a hydraulic fracturing process to identify the most influencing ones. Then, using the Acoculco specific geothermal case study, I calculate the relation between the total injected volume and the hydraulic fracture dimensions.

Because the propagating hydraulic fracture can be influenced by reservoir heterogeneities, such as natural pre-existing fractures, **Chapter 6** introduces a novel approach. Here, I propose to build on the classical hydraulic fracture method, by adding the reservoir heterogeneities related to pre-existing natural fractures. The model uses the variational phase-field, a smeared representation of the damage, thus the hydraulic fracturing process and its propagation over time are represented using a smooth transition function instead of a sharp interface implemented. Discretization uses a non-conforming mesh, which enables complex geometries. Hence, I can solve the hydraulic fracture propagation process accounting for its interaction with pre-existing natural fractures. The model is applied to the three potential reservoirs studied at the Acoculco geothermal field.

In **Chapter 7**, I apply the entire workflow to the Marble reservoir formation of the Acoculco Geothermal system. This chapter offers a review of the workflow and tests its application to a real case, by observing the modeled enhancement of the Marble formation. Finally, in **Chapter 8** I discuss the extent to which this workflow could be used in deploying EGS over the world.

# SAMENVATTING

In 2020, waar de wereldwijde energievraag blijft toenemen en de globale klimaatopwarming een realiteit is, is het van het hoogste belang om onze maatschappelijke impact op onze aarde te reduceren. Energie en klimaat zijn altijd intrinsiek met elkaar verbonden geweest. Daarom is het oplossen van het energie/klimaat probleem een uitdaging waar verschillende oplossingen samen zouden moeten komen. Een onderdeel van deze globale oplossing is het potentieel van geothermie. Geothermie is een hernieuwbare energiebron die een hoge potentie heeft om de afhankelijkheid van fossiele brandstoffen te reduceren.

Van de verschillende types geothermie is de techniek genaamd ‘Enhanced Geothermal System’ (EGS) veelbelovend. Naast dat het een hernieuwbare bron is, heeft deze methode ook de potentie om duurzaam te zijn. Een EGS bestaat uit een reservoir gesteente met een van nature lage permeabiliteit die artificieel is gestimuleerd. Deze stimulatie kan worden bereikt met verschillende technieken zoals mechanische, chemische of thermische stimulatie of een combinatie hiervan.

Deze scriptie focust op mechanische EGS stimulatie, waarbij het openen van bestaande scheuren (‘fracks’) en het creëren van nieuwe wordt bereikt met behulp van het injecteren van vloeistof in het reservoirgesteente onder hoge druk. Dit proces zorgt voor het propageren van een hydraulische scheur. De moeilijkheid van deze EGS techniek zit hem in het voorspellen van de verspreidings fenomenen van deze hydraulische scheur.

Het onderzoek naar en ontwikkeling van EGS is onderdeel van de GEMex doelstellingen. Het GEMex project is een samenwerking tussen Mexicaanse instituten en de Europese Commissie gericht op het ontwikkelen van onconventionele geothermie technieken. Het Acoculco geothermale veld wat zich in Puebla bevindt, wordt gezien als een potentieel EGS. Omdat dit veld met twee geothermale putten is verkend en er een analog systeem is ontsloten in het nabijgelegen Las Minas gebied, vormt het een uitstekende onderzoeksplek om kennis over EGS te ontwikkelen.

In deze scriptie stel ik een geïntegreerde aanpak voor om de potentie van EGS in een reservoirgesteente te evalueren. De aanpak start met **Chapter 2**, waarin een vernieuwende methode wordt geïntroduceerd om de scheuren te karakteriseren aan de hand van het berekenen van “Discrete Fracture Networks” (DFN) van ontsloten gesteente. Specifieker gezegd wordt er een compilatie van scanlijn datasets verkregen van het veld. Deze dataset wordt vervolgens geanalyseerd met het nieuw geschreven Python script SkaPy. SkaPy helpt bij het compileren van Training Afbeeldingen die daarna kunnen worden geëxtrapoleerd tot op het niveau van het veld door gebruik te maken van de “Multiple Points Statistic” methode.

In **Chapter 3**, beschrijf ik het fysische gesteente laboratoriumwerk dat is uitgevoerd om de gesteente-eigenschappen te karakteriseren. Deze metingen variëren van mineraal analyses tot de originele experimentele opstelling voor hydraulische scheuren. Al deze metingen zijn toegepast op gesteentemonsters verzameld in Acoculco en de Las

Minas analoge ontsluitingen in Mexico. De karakterisatie wordt gebruikt om te voorspellen hoe de potentiële reservoirgesteentes zich gedragen gedurende het proces van hydraulische scheur verspreiding.

**Chapter 4** gaat verder over het karakteriseren van scheuren en presenteert een model om te evalueren in hoeverre ondergrondse scheuren de thermische- en vloeistofstromen in het reservoir beïnvloeden. Aangezien het Acoculco geothermie veld kan worden geproduceerd vanuit verschillende reservoirs, kan het model werken met een multi-reservoir analyse. Daarnaast kan het model verschillende productie scenario's vergelijken omdat de distributie van scheuren binnen een reservoirgesteente niet homogeen is.

**Chapter 5** gaat verder over het voorspellen van hydraulische scheur verspreiding aan de hand van het modelleren van het hydraulische scheur proces in een perfect vlakke driedimensionale scheur. In dit hoofdstuk analyseer ik de verschillende parameters die invloed hebben op het hydraulische scheur proces om de parameters te identificeren die de meeste invloed hebben. Daarna bereken ik aan de hand van de specifieke Acoculco casus de relatie tussen het totaal geïnjecteerde volume en de dimensies van de hydraulische scheuren.

Omdat de verspreidende hydraulische scheur beïnvloed kan worden door heterogene zones in het reservoir, zoals al bestaande natuurlijke scheuren, wordt in **Chapter 6** een vernieuwende aanpak geïntroduceerd. Hierin stel ik voor om voort te bouwen op de klassieke hydraulische scheur methode door het toevoegen van deze heterogene zones gerelateerd aan reeds bestaande scheuren. Het model gebruikt een "variational phase-field", oftewel een uitgesmeerde representatie van de schade, en het hydraulische scheur proces en de verspreiding hiervan wordt dus gerepresenteerd aan de hand van een soepele overgangs functie in plaats van een abrupte overgang. Discretisatie maakt gebruik van een niet-conform netwerk waardoor er met complexe geometrieën gewerkt kan worden. Hierdoor kan ik het hydraulische scheur proces modelleren, rekening houdend met al bestaande natuurlijke scheuren. Het model is vervolgens toegepast op drie potentiële reservoirs in het Acoculco geothermie veld.

In **Chapter 7** pas ik de gehele aanpak toe op de Marble reservoir formatie van het Acoculco Geothermie systeem. Dit hoofdstuk geeft een overzicht van de aanpak en test de toepasbaarheid op een werkelijk veld door te kijken naar de gemodelleerde verbetering van de Marble formatie.

Tenslotte bediscussieer ik in **Chapter 8** de mate waarin deze aanpak kan worden toegepast bij het inzetten van EGS over de hele wereld.

# 1

## INTRODUCTION



## 1.1. ENHANCED GEOTHERMAL SYSTEMS

### 1.1.1. GEOTHERMAL HISTORY

Geothermal energy has been discovered before beginning of recorded history. It started in pre-historical times by using hot springs for primary human needs as for cooking, washing and therapeutic purposes (Stober and Bucher, 2016). Later, during the Middle-Ages, a first geothermal heating system has been installed in France. First heat-related electricity was generated in 1904, using steam produced by a geyser in Larderello, Italy. In 1913, the first commercial power plant using a turbine was developed in Larderello, generating 250 kilowatts of electricity (Lund, 2005). The next major achievements occurred after the World War II in 1958, when New Zealand developed their first commercial production of electricity obtained from steam-operated turbines. Since then, hydrothermal sources have been commonly developed, as at The Geysers in California; the hot water systems at Wairakei in New Zealand; Cerro Prieto in Mexico; Reykjavik in Iceland; Indonesia and Philippines, leading to an installed world electrical capacity of nearly 10000 MWe, and, more than 100000 MWt at the beginning of the 21<sup>st</sup> Century (Tester et al., 2006).

### 1.1.2. EGS POTENTIAL & PRINCIPLE

Enhanced Geothermal Systems (EGS) is a promising method to turn geothermal renewable energy into an efficient power source. Traditionally, the idea of producing electricity using a geothermal source is associated with the idea of finding an existing hydrothermal system (e.g. Olasolo et al., 2016). The limitations of this concept are that it is only applicable to places where these geothermal sources can be found, and their exploitation is limited to the reservoir capacity.

The concept of the EGS consists of extracting the thermal energy stored in a low permeability rock by enhancing its permeability, and thereby releasing the trapped water present in the reservoir formation. Once released, the water circulates through the hot rock and is pumped out to the surface where it can be used for space heating or be converted into electricity using a turbine (e.g. Gallup, 2009). At the end of the process, the water is injected back into the reservoir. For that reason the EGS approach is foreseen as a potentially sustainable electric power source.

Enhancing the reservoir permeability is achieved by stimulating the rock formation. The stimulation can be mechanical, chemical, thermal or a combination of all aforementioned. The most sensitive part of the EGS creation is the process of hydraulic fracturing used when mechanically enhancing the reservoir permeability (Tester et al., 2006). During a hydraulic fracture stimulation process, a pressurized fluid is pumped into the reservoir, until reaching the formation breakdown pressure, where fractures are created or re-opened. Predicting the hydraulic fracturing process is a difficult exercise because it depends on multiple variables, which evolve over time. One of the most influencing variables is the reservoir heterogeneity, which is also one of the most difficult to predict. However, accurately predicting the hydraulic fracture propagation process is essential to evaluate the potential of an EGS project. The hydraulic fracture process can also become a matter of safety as hydraulic fracturing can in some cases be related to induced seismicity risks (Kwiatk et al., 2019; Schmittbuhl et al., 2014; McClure and Horne, 2011;

Majer et al., 2007).

## 1.2. HYDRAULIC FRACTURING, THE KNOWLEDGE GAP

Reservoir permeability enhancement was first developed in oil and gas reservoirs (e.g. Economides and Nolte, 1989) while nowadays the principles of hydraulic fracture mechanics are applied to a broad range of subsurface problems, such as nuclear waste disposal (Zoback et al., 2003), carbon-capture & storage (Fu et al., 2017), and geothermal systems (Legarth and Saadat, 2005; McClure and Horne, 2014; Fox et al., 2013). When considering a wellbore, a drilling fluid (water or mud) is pumped into the rock formation inducing stresses at the wellbore walls. The fluid injection is maintained until the induced stresses are large enough to cause a fracture to open and propagate (Jaeger et al., 2007).

For a wellbore to sustain, the pressure has to be kept in what is commonly called the mud-window. This mud-window corresponds to the pressure equilibrium where the fluid injected pressure is higher than the formation pore pressure so that the injected fluid does not flow back or the well collapses, but lower than the minimum principal stress so that it does not hydraulically fracture the formation. In other words, increasing the drilling-fluid pressure until it becomes higher than the minimum principal stress will hydraulically fracture the formation Zoback (2007).

The main factors controlling hydraulic fracture mechanisms are (Economides and Nolte, 1989):

1. the rock stress and strain state, from lithostatic pressure to tectonic forces;
2. the reservoir pore pressure and temperature conditions;
3. the stress changes due to wellbore implementation and fluid injection.
4. the rock mechanical properties (such as Young's modulus, Poisson ratio and angle of internal friction);
5. the reservoir geometry and structure: orientation of layers, faults and fractures;

Hydraulic fracture mechanisms can be divided into three major types (McClure and Horne, 2014):

1. the first one is the *pure opening mode (POM)* stimulation, which refers to the tensile fracture *mode-I* creation.
2. the second type is the *pure shear stimulation (PSS)* or "hydro-shearing", and corresponds to a slip along pre-existing fractures, refers to shear fracture *mode-II*.
3. the third one is the *mixed-mechanism stimulation (MMS)*, is a compromise between the two first concepts: it admits that the bottom hole fluid pressure injected induces the shearing and opening of natural fractures.

As the fracture mode-I corresponds to a pure opening tensile fracture, it closes again once the fluid pressure is dropped. Thus, a shear fracture mode-II or mixed-mechanism fracture mode-III is more efficient to permanently enhance the reservoir permeability (Zoback, 2007). All rock reservoir formations contain pre-existing natural fractures, or more generally flaws and weak planes, such as joints, veins, faults or sedimentary bedding surfaces, thereby the most realistic approach of the hydraulic fracture process is represented by the mixed-mechanism stimulation. The pressurized fluid and inherent

hydraulic fracture reach a pre-existing natural fracture which re-opens due to the pressure along the weak interfaces. The pressurized fluid then concentrates at the fracture tips triggering the opening of secondary fractures, resulting into a wing-crack fracture shape. This wing-fracture model (Jung, 2013), was initially proposed as “kinked-crack” (Cotterell and Rice, 1980; Lehner and Kachanov, 1996). The wing-crack model is derived into sub-concepts as among others the “splay fracture” from McClure and Horne (2014) or the “hybrid fracture” from Zoback (2007).

To a larger extent, hydraulic fracture models need to account for the interaction of a stimulated hydraulic fracture with pre-existing natural fractures. Natural fractures, when cemented during mineralization processes might respond as barriers, when others are weaker and thereby prone to slippage. Hence, in some cases natural fractures can stop (arrest) hydraulic fracture propagation; in some other natural fractures can be re-activated during the stimulation (branching); or natural fractures can be crossed by the hydraulic fracture (Warpinski and Teufel, 1987; Jeffrey et al., 1994, 2009; Renshaw and Pollard, 1995; Weng, 2014; McClure et al., 2015; Dehghan et al., 2015).

To date, most Hydraulic Fracture (HF) simulators (such as for example ResFrac<sup>®</sup>, GOHFER<sup>®</sup>, FRACMOD<sup>®</sup>, or MFrac<sup>®</sup>) assume a single planar mode-I fracture opening over time. The dimensions of the hydraulic fracture (such as its length, height and aperture) change as the fluid injection process is simulated. The injected fluid is implemented following the laws of Linear Elastic Fracture Mechanics (LEFM) (Griffith, 1921) to the domain, and the criterion for fracture propagation is given by the energy-release rate such as the fracture propagates if the stress intensity factor at the tip matches the rock toughness (Adachi et al., 2007). The hydraulic fracture geometry evolves with time following trajectories that are determined by the rock properties (elastic moduli, toughness, leak-off coefficient), fluid viscosity, and injection rate. This amounts to simulating a three dimensions (3D) bi-wing planar fracture as found in common industrial simulators implementing the known fracture models from Perkins, Kern and Nordgren (PKN), Geertsma and de Klerk (GDK) and 3D models (Perkins and Kern, 1961; Geertsma and De Klerk, 1969; Nordgren, 1972).

These models give good estimates of the expected fracture dimensions, but still lead to unrealistic fracture models as the reservoir heterogeneities are not considered. Understanding the interaction between HF and natural fractures helps predicting the HF propagation pathway, which is essential for well positioning, especially when developing a geothermal doublet system. The foundation of modeling hydraulic fracture interaction with natural fractures has been established, among others, by Warpinski and Teufel (1987); Jeffrey et al. (1994, 2009); Renshaw and Pollard (1995); Weng (2014). The objective now is to develop these predictive capabilities for hydraulic fracture propagation, handling interaction with complex natural fractures (arresting, branching, or crossing).

### 1.3. THE GEMEX PROJECT

The GEMex project is a collaboration between Mexican institutions and the European Commission for the development of non conventional geothermal systems. Two non-conventional systems are studied: one is the Enhanced Geothermal System technology, which is studied on the Acozulco geothermal system site, located in Puebla. The geothermal system has been explored by *Comisión Federal de Electricidad* (CFE), who

drilled two wells in 1995 and 2008. Both wells found temperatures around 300 °C but hardly any fluids. The second non-conventional system studied by GEMex is the Super-Hot Geothermal System technology, analyzed on the site of Los Humeros. Los Humeros geothermal system is currently exploited. Both sites would require site investigation for geological and geophysical characterization. The GEMex project intends to combine Mexican and European knowledge on conventional and non-conventional geothermal energy to accelerate the learning curve for geothermal development.

## 1.4. GEOLOGICAL CONTEXT

### 1.4.1. REGIONAL GEOLOGY

Acoculco is located in the Trans-Mexican volcanic belt (TMVB), about 100 km North-East of Mexico City. The TMVB is a mountain range resulting from the subduction of the Avalon, Rivera, Orozco and Cocos plates beneath the North American plate (Ferrari et al., 2012; Manea et al., 2013; Keppie, 2004; Padilla, 2013) (fig. 1.1). The TMVB is composed of a thick series of Pliocene to Quaternary volcanic deposits forming a high volcanic plateau. This plateau overlies a fold and thrust belt resulting from the Sierra Madre Oriental, a Laramide deformation of the Jurassic to Cretaceous deposition of the carbonate sequence (Carrasco Núñez et al., 2017; Norini et al., 2015; López-Hernández et al., 2009; Campos-Enriquez and Garduño-Monroy, 1987).

Geophysical studies (known as MARS for Mapping of the Rivera Subduction Zone, MASE for Middle America Subduction Experiment and VEOX for Veracruz-Oaxaca seismic-line) carried out from 2006 to 2010 (Ferrari et al., 2012) indicate that lithospheric mantle can be very thin or even absent. Hence, the TMVB is divided into two parts: i) East of 101°W, the TMVB is built on a Precambrian to Paleozoic with a 50 – 55 km thick crust; ii) West of 101°W, the TMVB is underlain by Jurassic to Cenozoic marine and continental arcs with a 35 – 40 km thick crust.

Mexico geology can be described using the Terranes classification, summarized by Keppie (2004) (fig. 1.2). This classification gives approximately 12 Terranes describing the different geological regions composing Mexico: Baja California, Western Mexican Basin & Range (or Pacific Coastal lowlands), Sierra Madre Occidental, Eastern Mexican Basin & Range, Mexican Mesa (or Mesa Central), Sierra Madre Oriental (SMO), Gulf Coastal Plain, Trans-Mexican-Volcanic-Belt, Sierra Madre Del Sur, Chiapas Massif, Southern Highlands (or Maya Mountains) and Yucatan Peninsula. Acoculco geothermal field is located on the SMO and the TMVB Terranes. SMO is made of folded Mesozoic Shales & Limestones that have been thrust and folded during Laramide orogenesis. In the SMO terrane, the Early Cretaceous Limestones are referred to as the Tamaulipas. The TMVB consists of late Miocene to Holocene, Andesitic to Dacitic volcanic rocks and active volcanoes that extend across Mexico from East to West coasts.

### 1.4.2. LOCAL GEOLOGY

Two geothermal exploration wells, EAC1 & EAC2, were drilled in Acoculco, about 500 m apart, in 1995 and 2008. The geological log derived from EAC1 could be simplified as in (fig. 1.3).

A simplified geological cross-section of Acoculco area is given in Figure 1.4. The sec-

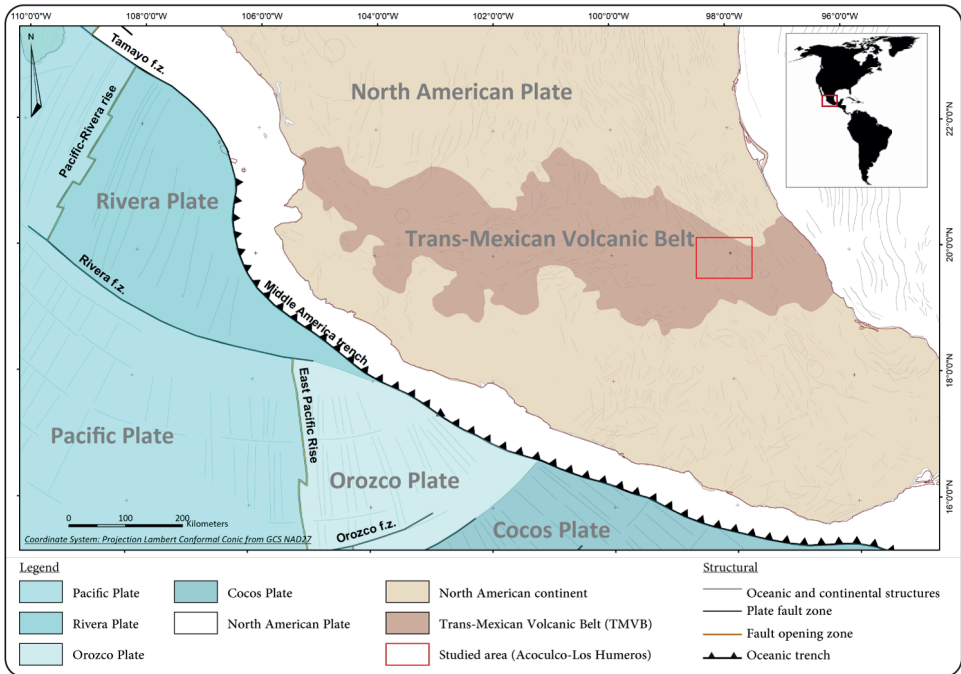


Figure 1.1 – Simplified tectonic map of Mexico, indicating Acoculco site location, modified from Padilla (2013).

tion is a model based on gravity, magnetic and well data (Canet et al., 2015b; Viggiano-Guerra et al., 2011; Lorenzo Pulido et al., 2010; López-Hernández et al., 2009). The carbonate section consists of dolomitic Limestones, Limestones metamorphised into Marbles or metasomatised into Skarns due to the intrusion of a granodioritic pluton.

**L**as Minas is a village located down in a valley, about 120 km East of Acoculco. Las Minas valley is considered here as an excellent analogue of the Acoculco geothermal system. As seen on the geological map (fig. 1.5), Acoculco and Las Minas are made of rocks that were deposited in the same geological environment. The exposed rock sequence in the Las Minas analogue is comparable to the log of Acoculco well-bores, from the recent volcanic cover, overlaying the carbonate sequence made of the Early Cretaceous Limestones called the Tamaulipas formation, all the way to the granodioritic pluton, which is exposed deep in the valley, where the river Rio Las Minas runs. Hundreds of meters away from the river bed, two outcrops, named Boquillas and Eldorado, expose Skarns (Olvera-garcía et al., 2020); higher on the flanks of the valley, two Marble outcrops are found: Pueblo Nuevo and Tatatila. Further away is first an outcrop made of marbled dolomitic Limestones called Rinconada, and much further, beyond the influence of the intrusion, San Antonio Tenextepec is made of unaltered dolomitic limestones. These outcrops represent a proximal to distal context for the granodioritic intrusion into the carbonates. Figure 1.6 is a simplified representation of the geological context.

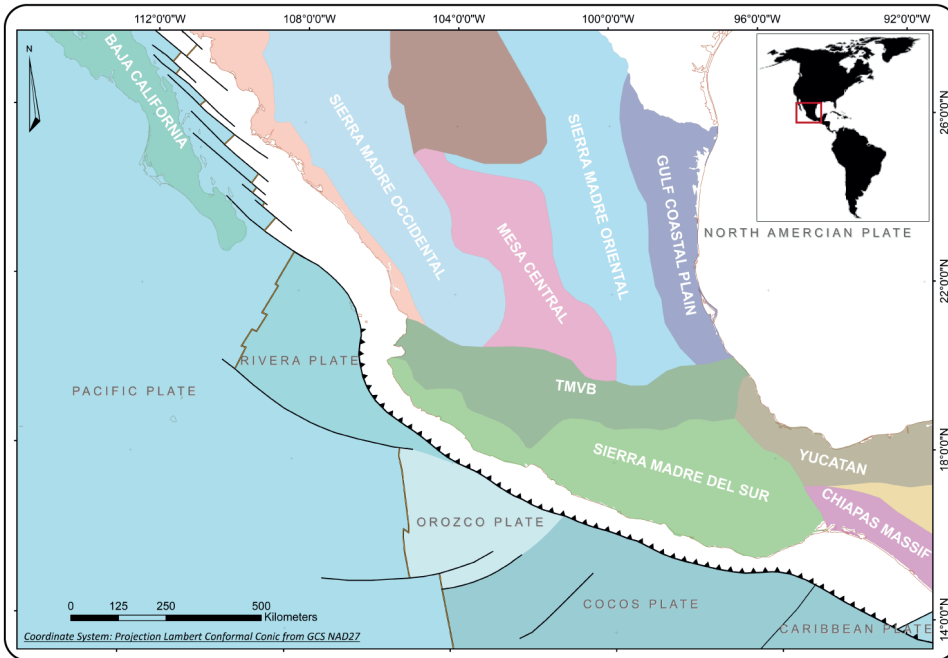


Figure 1.2 – Mexican main geological terranes (modified from Keppie (2004); Padilla (2013))

### 1.4.3. STRUCTURAL CONTEXT

Four major structural trends are identified in the region from Acozulco to Las Minas. The Acozulco Caldera is located at the intersection of two regional fault systems, one trending NE and the other NW (López-Hernández et al., 2009). The main structures in the region are inherited from: i) the Laramide Orogeny, Late Cretaceous with a NE-SW compression, inducing NW-SE thrusts and folds affecting the lithological sequence from the metamorphic basement up to the Mesozoic sedimentary rocks; ii) the Eocene-Pliocene extensional and transtensional phases that produced N-S to NE striking faults (Carrasco Núñez et al., 2017; Norini et al., 2015). A micro-structural study identified two major structural directions: i) the first direction is from N140 to N170; ii) these structures are cut by a second trend oriented from N40 to N70; this confirms the regional trends and identifies the direction N40 as a maximum regional stress (Campos-Enriquez and Garduño-Monroy, 1987).

In the Los Humeros Volcanic Complex (a few tens of kilometers westwards from Las Minas), the main structures driving the ascending hot fluids have been identified as the NNW-SSE east-dipping faults (Jentsch et al., 2020; Norini et al., 2015), which is confirmed by the producing geothermal wells that are located either along the main NNW-SSE active faults or near the N-S striking fault splays Carrasco Núñez et al. (2017).

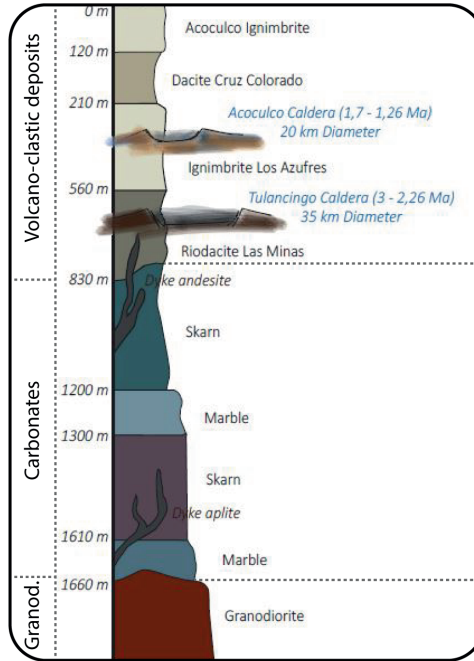


Figure 1.3 – Schematic geological log from EAC1 (modified from Viggiano-Guerra et al. (2011); López-Hernández et al. (2009)).

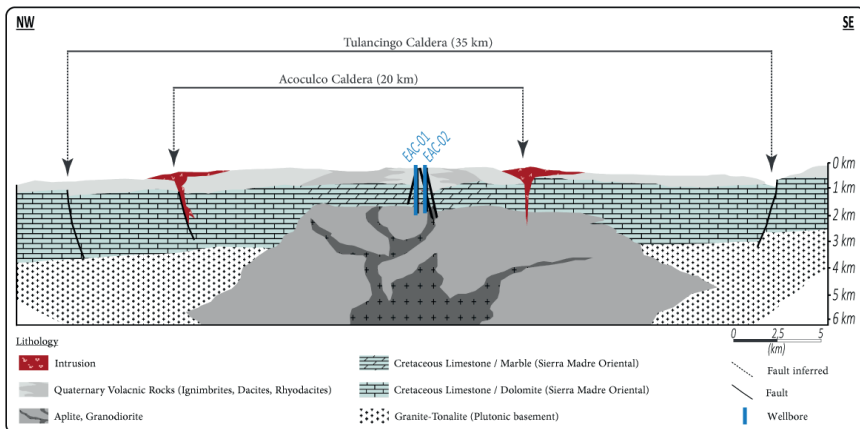


Figure 1.4 – Schematic geological section of the Tulancingo-Acoculco caldera Complex, modified from López-Hernández et al. (2009).

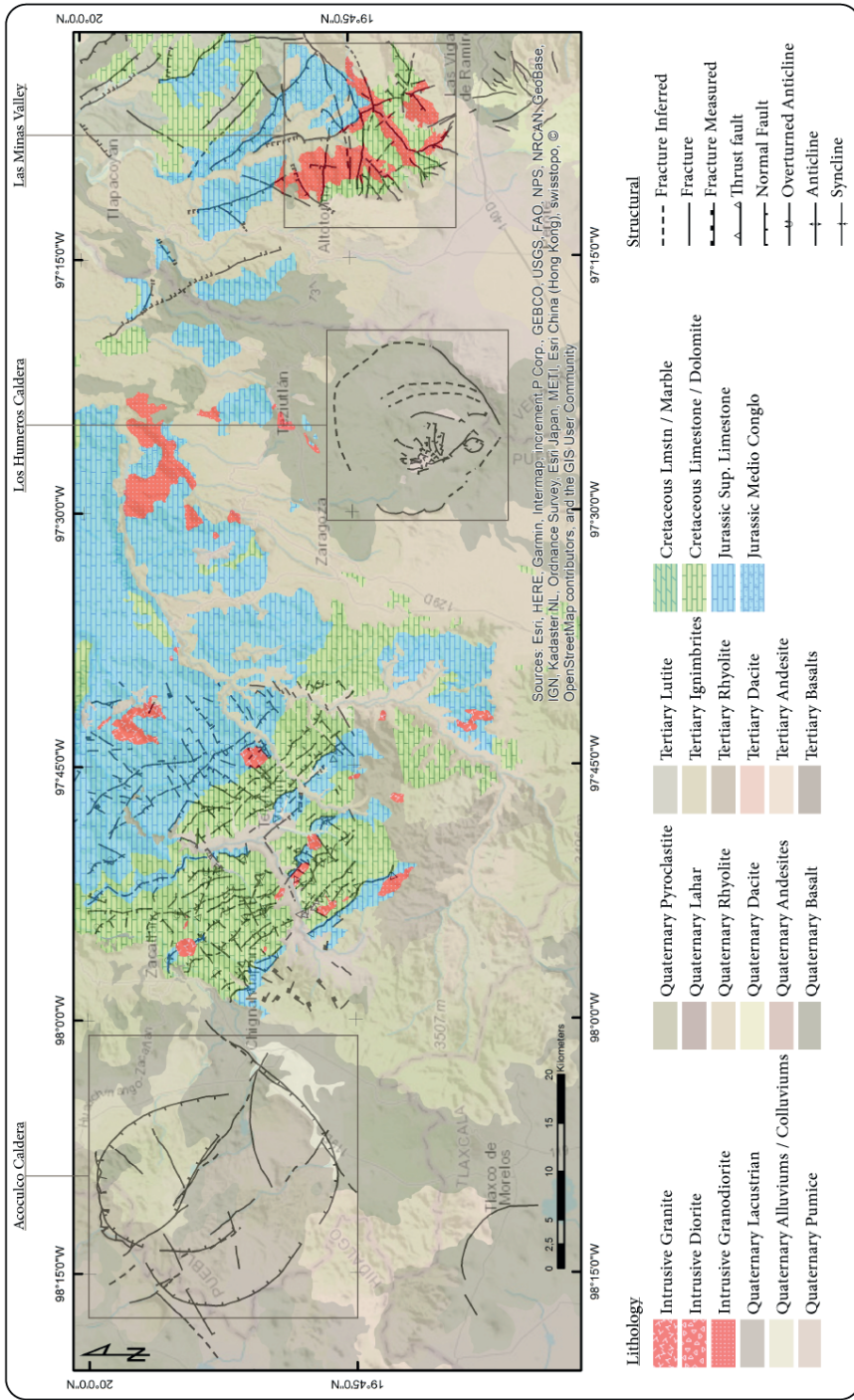


Figure 1.5 – Geological map of Aocolco – Los Humeros – Las Minas area, modified from (Servicio Geológico Mexicano, 1997, 2002) maps.



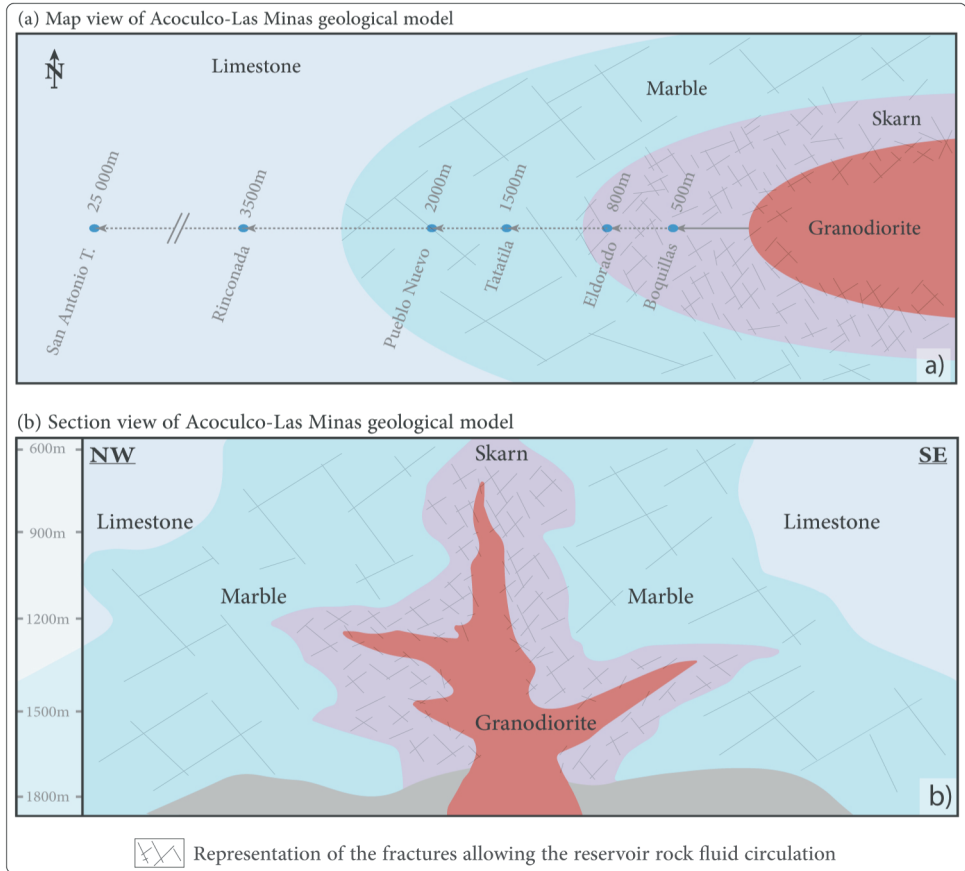


Figure 1.6 – Acoculco-Las Minas conceptual model: (a) Map view, (b) Section view.

## 1.5. THESIS OUTLINE

The objective of this thesis is to propose a predictive mechanical model for an Enhanced Geothermal System. Hence, the thesis outline follows the integrated workflow developed which helps assessing for an EGS feasibility (fig. 1.7). The workflow starts in the field by reporting structural measurements and collecting samples. From the measurements, we compute representative Discrete Fracture Network (DFN) models of the reservoirs. From the samples, we measure the rock mechanical properties in the laboratory. Using the computed DFNs together with the reservoir rock properties we model: the hydraulic fracturing processes and the fluid and thermal transport in the fractured reservoir.

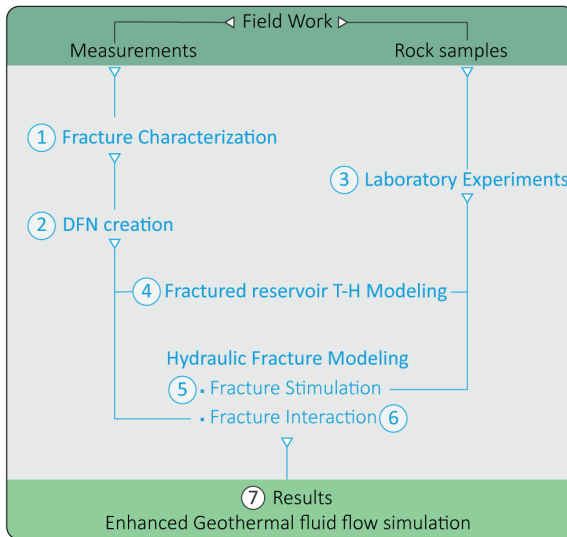


Figure 1.7 – Workflow for developing an Enhanced Geothermal System predictive model. Starting in the field with fracture measurements and rock sampling: Step 1) Fracture characterization; Step 2) DFN computation; Step 3) Rock laboratory testing; Step 4) Fractured Reservoir Thermo-Hydro modeling; step 5) Hydraulic Fracture Modeling: for fracture stimulation and step 6) for fracture interaction; 7) Results: Enhanced Geothermal System fluid and thermal flow modeling through fractured media

**Chapter 2**, published in *Journal of Structural Geology*, introduces a novel method used to compute the DFNs. The problem we address here is on the feasibility to predict the fractures and the fracture network of an area when no large scale information is available, as for example from seismic data or aerial images (Unmanned Aerial Vehicle - UAV, or drone). To solve this question we propose a method which uses the scanline survey together with the Multiple Point Statistics (MPS) method to generate geologically meaningful DFNs.

Then **Chapter 3**, which was partly integrated into the *GEMex deliverables*, describes the rock physics laboratory experiments realized to characterize the rock properties quantitatively, in the aim of predicting the hydraulic fracture propagation process. The chapter covers from rock samples identification using mineral and chemical compositions all the way to an experimental hydraulic fracture test.

Building on the two previous chapters, **Chapter 4**, published in the journal of *Geothermal Energy*, presents a model to evaluate the extent to which fractures in the subsurface can influence the reservoir flow characteristics. For this purpose, we developed a thermo-hydro-pseudo mechanical model simulating a geothermal well doublet production through a fractured reservoir. Complex fracture networks are discretized; the fracture apertures are corrected to the stress state at depth. The mass and heat transfer are simulated through the fracture-controlled reservoir, over a 100 years. As the Acoculco geothermal field could be stimulated in different reservoir formations, the model handles a multi-reservoir analysis. Because, the fracture distribution within a reservoir formation is not homogeneous, the model compares multi-production scenarios. As a result, we introduce a model for fracture flow permeability and stress dependency simulation applied to multi-reservoirs, multi-production scenarios analysis. One of the conclusions drawn in this chapter is the confirmation of a need to enhanced the Acoculco reservoir permeability.

The first way to model hydraulic fracturing is presented in **Chapter 5**, which is part of the *GEMex deliverables*. In this chapter, the questions we want to answer are: i) which one of the different parameters involved in a stimulation process is the most influencing? ii) and considering the Acoculco case study, to what extent does the total injected volume influence the hydraulic fracture dimensions? To answer these questions we use a planar 3-Dimensional (3D) fracture model implemented in MFrac<sup>®</sup> Hydraulic Fracturing Software from Baker Hughes.

**Chapter 6**, submitted to *Journal of Geophysical Research*, introduces the second method: a novel approach to model hydraulic fracturing in heterogeneous domains. As an EGS feasibility goes far beyond predicting a 3D planar fracture dimensions, but also relies upon predicting accurately the hydraulic fracture propagation pathway, it is essential to take into account the reservoir heterogeneities and especially the natural or pre-existing fractures. This novel approach uses the variational phase-field (V-pf) and is implemented in OpenGeoSys FEM software (Kolditz et al., 2012). The model is applied to the three potential reservoirs of the Acoculco geothermal field.

As a result, **Chapter 7**, published in *Stanford University Proceedings 45<sup>th</sup> Workshop on Geothermal Reservoir Engineering*, applies the whole workflow to the Marble reservoir formation of Acoculco geothermal system. The chapter reviews the following questions: i) How to predict a field scale fracture model from outcrop measurements? ii) How to predict a hydraulic fracture stimulation in a highly fractured reservoir? And iii) how to quantify the effect of NF and stimulated fractures in a geothermal reservoir system?

Finally, **Chapter 8** discusses the overall workflow developed in this thesis to evaluate an EGS field potential. In addition to that we venture to discuss the limits of the Enhanced Geothermal System method and its potential developments as a safe and reliable energy resource.

The workflow presented in this thesis offers a physically sound prediction of the reservoir flow characteristics as well as an accurate mechanical model of the fracture propagation and the pressure distribution for well borehole stimulation. Because the workflow is based on easily accessible data and thanks to its simplicity, this approach could be applied in most EGS case studies.

# 2

## CHARACTERIZATION OF NATURAL FRACTURES

*Understanding fractures and fracture networks is essential for the investigation and use of subsurface reservoirs. The aim is to predict the fractures and the fracture network when there is no direct access to subsurface images available. This article presents a universal workflow to numerically compute a discrete fracture network by combining the 1D scanline survey method, processed with the newly written SkaPy script, together with the multiple point statistic method (MPS). This workflow is applied to a potential geothermal site in Mexico called Acoculco. We use Las Minas outcrops and quarries as surface analogues for the Acoculco reservoir, as Las Minas and Acoculco are both formed by the influence of a plutonic intrusion into the Jurassic-Cretaceous carbonate sequence of the Sierra Madre Oriental in the Trans-Mexican volcanic belt (TMVB). The intrusion is associated with contact metamorphism and metasomatic phenomena, providing the basis for the mining activities at Las Minas. The results obtained using this workflow demonstrate the feasibility of the approach, which presents a solution combining the efficiency of data processing and an interpretation-driven approach to build realistic discrete fracture networks. This workflow can be used in the process of estimating the permeability of a fracture controlled reservoir, with using only scanline surveys data as input. This is essential in the process of evaluating the feasibility to develop an enhanced geothermal system.*

## 2.1. INTRODUCTION

The use of the subsurface and the exploitation of subsurface resources require prior knowledge of fluid flow through fracture networks, particularly in low permeability rocks. For nuclear waste disposal, for the enhancement of hydrocarbon recovery from a field, or the development of an enhanced geothermal system (EGS), it is fundamental to constrain the fractures and the fracture network. The question we address here is how to predict the fractures and the fracture network of an area when there is no large scale information available, for example from seismic data or aerial images (Unmanned Aerial Vehicle - UAV, or drone). To overcome this potential problem, we developed a workflow to numerically compute a discrete fracture network based on the combination of the scanline survey method performed at single outcrops, processed with the newly written SkaPy script, together with the Multiple Point Statistic method (MPS) (e.g. Liu et al., 2002; Chugunova et al., 2017) proposed by (Bruna et al., 2019). This workflow is then applied to the case study of the Aocolco EGS test site in Mexico.

The development of EGS requires stimulation treatments of the reservoir to enable or increase the flow rate of the geothermal fluid for the extraction of heat from high temperature and initially low permeability rocks, (e.g. Gallup, 2009). In EGS, the production and injection wells are hydraulically connected by increasing the rock permeability (Tester et al., 2006), which for a fractured tight reservoir corresponds to stimulating the pre-existing natural fractures and using them as fluid pathways and heat exchangers.

Reservoir permeability is measured at two scales: the matrix rock permeability, referring to the natural pore space of the rock; and the reservoir bulk permeability, which includes faults and fractures and the pore network of the rock.

In nature, fractures are organized as networks, from microscopic to regional scale (e.g. Gillespie et al., 1993; Zhang et al., 2016). These networks generally present a regular arrangement (i.e. orthogonal networks, conjugated network; Healy et al. (2015)) which may vary in terms of orientation, size, density and topology (Bruna et al., 2019) at various scale (from meter scale to reservoir scale). Fracture network geometries vary spatially due to local variation of the stress field and over time. Hence, it is difficult to predict the geometry of these networks. Understanding fracture network starts with the characterization of the fracture geometry. The International Society for Rock Mechanics (ISRM) proposes a method for this fracture characterization (ISRM, 1978). The key elements used to describe fractures are:

- the orientation (strike and dip);
- the length (also called fracture “trace”, or “extent”);
- the connectivity (also called “abutment” or “node” as for example in term of modeling (Peacock et al., 2016));
- the aperture (“mechanical aperture” when measured at the outcrop);
- the filling (cement or clay filling the fracture void);
- and finally, the shape, commonly described with a joint roughness coefficient (JRC) (Barton and Choubey, 1977; Tse and Cruden, 1979; Li and Zhang, 2015).

Because the reservoir is not accessible, these fracture networks cannot be measured directly. Therefore, reservoir properties can best be studied at suitable analogue outcrops (Barbier et al., 2012). Analogues are rock sections, made of comparable composition and geometry, cropping out at the surface. Therefore, outcrop analogues can be

used to measure the fracture geometries. As explained in Li et al. (2018), an analogue can always have its own local variations from the subsurface reservoir. For this reason, the surface analogue is used as the base case, which can evolve as new information becomes available, to better represent reservoir geometries.

When working on large-scale outcrops, a common method is to use aerial images of wide, well-exposed surfaces, where fracture networks can be explicitly characterized. Unfortunately, there is no suitable outcrop available to be imaged near Acoculco. For that reason, we used another method, based on simple and systematic measurements. The scanline survey method is a common approach to obtain the statistics required to predict the fracture geometry of the network at the scale of a geothermal field. The method consists of reporting, measuring and describing all fractures visible at the surface of the rock and intersecting with the measuring tape (ISRM, 1978; Lavenu et al., 2014). The dataset, created from the scanline survey, can then be used for computing a global discrete fracture network (DFN).

A Discrete Fracture Network (DFN) model is a mathematical representation of fracture distribution in space and fracture characteristics. As explained in Lei et al. (2017), the DFN concept is broad, since the geometry of the DFN depends on the need for which it is created, or on the way the fracture characteristics are obtained. For example, a DFN can be generated by digitizing fractures on large scale imagery or it can also be obtained from samples at a laboratory scale. In the context of this article, we compute the DFNs numerically from scanline datasets. We use the scanline datasets as input to extrapolate to a much larger geographical domain. We assume that the fracture parameters measured at the outcrop are representative of the geometry of the network in its near neighborhood. The extrapolation far from this point is unknown and has been taken into consideration by means of gradual transitions from one sampling area to the other. Common approaches as used in standard software tools would achieve this using a stochastic method, which honors the scanline input data and returns statistically accurate results. In this workflow, we extrapolate the scanline surveys with the multiple point statistics (MPS) method, which in addition to being statistically accurate preserves the geological patterns and therefore preserves the geometry of the fractures.

This article presents a new workflow using the specially developed Python<sup>TM1</sup> based SkaPy script, which computes statistics on multiple scanline surveys, classifies the fractures, and represents them in a geo-referenced system. This representation is further analyzed to provide the input for the calculation of the DFN by the MPS method proposed by Bruna et al. (2018, 2019). In this article, Bruna et al. (2019) analyses applicability of the MPS method to reproduce a known fracture network (i.e. manually interpreted from an outcrop), preserving the geometrical characteristics of the fractures. This workflow combines the efficiency of data processing and an interpretation-driven approach. The script is freely available on GitHub<sup>TM</sup>.

We apply the present workflow to the Acoculco geothermal field, within the framework of the GEMex project (e.g. Jolie et al., 2018), where two exploratory wells reached high temperatures (300 °C) at reasonable depth (2 km). Unfortunately, the wells did not access any productive geothermal layers. For this reason, Acoculco could eventually be developed as an EGS. Thus, the objective of this paper is to provide a characterization of

---

<sup>1</sup>Python Software Foundation (2019)

the existing fracture network prior to stimulation.

## 2.2. BACKGROUND, EXISTING METHODS

### 2.2.1. EXISTING METHODS FOR THE SCANLINE SURVEY

The linear scanline survey method has been widely described (ISRM, 1978; Lavenue et al., 2014; Watkins et al., 2015). The principle of this method is based on laying a measuring tape along the outcrop and reporting every fracture crossing this tape, describing the fracture characteristics such as strike, dip, length, connectivity, aperture, filling and shape. Even though the method is known for potentially biasing the fracture representativity (Terzaghi, 1965), it is still broadly used. Several studies have discussed the fracture length and the fracture representativity in the scanline survey (Priest and Hudson, 1981). As more recently explained in Zeeb et al. (2013), “[the] probability of a fracture [to intersect] with [the] scanline is proportional to [its] length. Therefore, short fractures are underrepresented” (p.13). This under-representation impacts the statistical distribution of the fracture lengths. The measured fracture lengths are also controlled by the outcrop dimensions. Nonetheless, the method remains a good tool thanks to its simplicity and reliability to give exhaustive characterization of the fractures. Some variations of this linear scanline survey exist as for example the circular window surveys proposed by Mauldon (1998); Mauldon et al. (2001) and a mixed method of transect linear scanlines and circular windows Watkins et al. (2015).

### 2.2.2. EXISTING SCRIPTS FOR SCANLINE OR FRACTURE DATA PROCESSING

Markovaara-Koivisto and Laine (2012) published a MATLAB<sup>®</sup> <sup>2</sup> script for scanline data processing. The script automates the dataset computation: it classifies the fractures into sets, provides statistics on the fractures, and builds a 2D or 3D visualization of the scanline. The advantage of their MATLAB<sup>®</sup> script is that it handles the shape of the fractures, comparable to the joint roughness coefficient (JRC), named “undulation” of the discontinuities. FraNEP is a script developed in Visual Basic<sup>™</sup>, written by Zeeb et al. (2013). The FraNEP script automatically analyses the statistical properties of 2D fracture networks by applying the linear and circular scanlines methods. The script includes length and orientation corrections in the calculations and also analyses fractures as a network, calculating their spacing, intensity and length distributions. The script includes the fractures classification into sets and computes rose diagrams of the fractures. More recently, Healy et al. (2017) published a MATLAB<sup>®</sup> script under the name FracPaQ. This script is intended to be a “software-based toolbox” to quantify fracture patterns in 2D. Similarly to FraNEP, the FracPaQ toolbox is mainly implemented to process photography or interpreted imagery of fracture networks and to analyze the statistical distributions of the fracture properties. Among other results, the code estimates the bulk permeability of the system studied. The strength of FracPaQ is that it can process a wide range of spatial scales.

None of these approaches combine a multiple scanline datasets analysis, classification of the fractures, and geographic representation. To transfer this information into a DFN, we needed to develop our own method. SkaPy is designed to fill this gap.

<sup>2</sup>The MathWorks Inc. (2019)

One advantage of scripting is to automate a workflow, which increases efficiency and reduces personal bias. This means, scripting also contributes to decreasing the risk of error. Another advantage is the possibility to analyze the statistical distributions of the fractures. Even more important is the possibility to run these statistics on multiple scanline surveys together. However, to compute any statistics on the fractures, it is fundamental to first separate the fractures into sets.

SkaPy has been written in the continuation of the Markovaara-Koivisto and Laine (2012) script, which processes scanline datasets. SkaPy is a flexible tool that handles surveys with constant or varying orientations. This allows surveys along curved outcrop surfaces. To compute the statistical analysis on fracture characteristics, SkaPy analyses not only one scanline dataset but processes multiple datasets. Therefore, it becomes easy to constrain the fracture characteristics over multiple outcrops. Then, as in the Markovaara-Koivisto and Laine (2012) script, SkaPy generates statistical plots, such as histograms, box-plots and stereonet. Because visualization is also important, SkaPy plots the scanline(s) in a geo-referenced system. A geo-referenced representation of the discretized fractures is the first step towards extrapolation to a DFN.

### 2.2.3. EXISTING METHODS FOR DFN COMPUTATION

Many tools already exist and are still being developed to improve DFN generation. Commonly used programs and algorithms for this purpose include the Move<sup>TM3</sup> software from Midland Valley, and FracMAN<sup>TM4</sup> from Golder Associates, which was implemented in Petrel<sup>TM5</sup> (Schlumberger). FracMAN<sup>TM</sup> is very effective at assessing the influence of fractures on bulk permeability (Chesnaux et al., 2009). The two most common methods to express the role of fractures on the reservoir flow are: i) conversion of the DFN into an equivalent porous medium (Dershowitz et al., 2004); ii) or more generally, to upscale the DFN into a continuum of fluid flow model representative of the fractured reservoir (Surrette, 2006). For creating DFNs, most of the methods, such as FracMAN<sup>TM</sup> or Move<sup>TM</sup>, use similar approaches based on statistics to populate a simulation domain. The results of these models are statistically correct but often do not represent the geology correctly. The multiple point statistic approach is an emerging method that, in addition to being statistically accurate, identifies the fracture network patterns and preserves them throughout the extrapolation.

## 2.3. METHOD: WORKFLOW DESCRIPTION

The workflow developed in this article can be summarized into four steps (fig. 2.1): 1) the data collection using the linear scanline survey. The data, from one or several surveys, is gathered in one table-like file format (such as “.csv”); 2) the file is loaded in the Python<sup>TM</sup> script SkaPy which processes the dataset; 3) using the output from SkaPy, the users manually create, so called Training Images (TIs), an extrapolation of the fractures and their distribution to the outcrop scale and a probabilistic map; 4) The MPS method computes the DFN.

<sup>3</sup>Midland Valley (2019)

<sup>4</sup>Golder Associates (2019)

<sup>5</sup>Schlumberger Limited (2019)



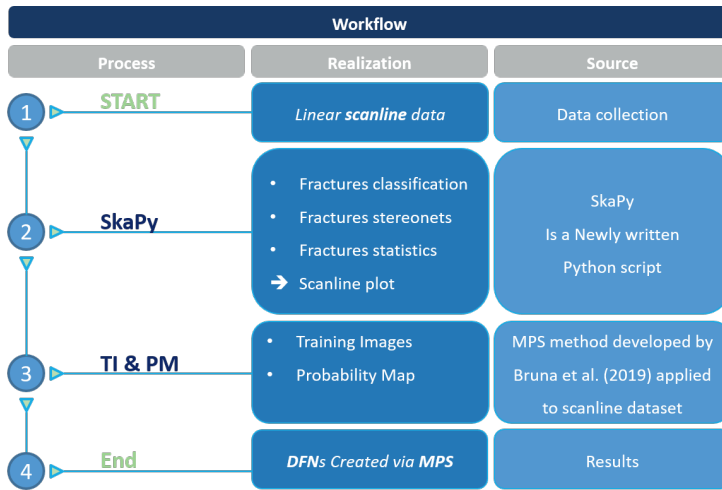


Figure 2.1 – Workflow chart, from scanline to DFN

### 2.3.1. USING SKAPY

SkaPy is made of two scripts. The first one classifies, analyses and plots the scanline; the second one assigns the geo-referenced coordinates. To run properly, SkaPy uses common Python™ open-source libraries such as Numpy, Matplotlib, Pandas and mplstereonet. The input file is loaded and converted into a Pandas DataFrame, which is a Python™ library implemented to manipulate numerical tables. For the analysis of the scanlines, the input data must contain at least the following information: the name of the outcrop; the name of the survey; the lithology; the position along the scanline survey; the orientation of the survey and the slope of the outcrop; the type of discontinuity (stylolite, fracture, fault, dyke); the structural measurements (strike, dip); the “*a priori*” fracture family, even though this is re-calculated during the script compilation; and the quantity “Q” that this fracture type has been observed in the interval; the aperture of the fracture (and when possible the filling material) and the length of the fracture trace. To be able to plot the scanline in a georeferenced system, the geographic coordinates of the starting point of the scanline survey are necessary (fig. 2.2).

The first SkaPy script is split in seven parts. In SkaPy part–1, the script plots the statistical distribution and histogram of the length and aperture measurements for the whole dataset. This gives a global overview of the data to identify eventual correlations between the two parameters, the fracture trace length and the fracture aperture. In SkaPy part–2, the users need to define the values to be used for the classification of the fractures into sets. The script returns a stereoplot with all the structural measurements, and then one stereoplot per set defined. Proceeding on from this classification, the script computes box-plots, showing the distributions of the fracture heights and fracture apertures per set. The box-plot format emphasizes which values are representative of the core of the distribution as opposed to the ones behaving as outliers. i) In SkaPy part–3, a first batch of plots is generated, gathering the data per outcrop. ii) In SkaPy part–4

Index	m_in	m_out	Dir.	Surf_Dir	Surf_Dip	Type	Str.	F_Az	F_Dip	F_Quadrant	F_F	Q
0	0	1	N	160	54	fracture	N	160	82	E	F5	1
1	0	1	N	160	54	fracture	N	150	89	E	F5	1
2	0	1	N	160	54	fracture	N	150	80	W	F5	1
3	0	1	N	160	54	fracture	N	70	85	S	F1	5
4	0	1	N	160	54	fracture	N	28	60	E	F3	2
5	0	1	N	160	54	fracture	N	93	30	N	F6	8
6	1	2	N	160	67	fracture	N	172	85	W	F5	4
174	2.95	5.5	N	20	90	fracture	N	140	10	W	F2	3
175	2.95	5.5	N	20	90	fracture	N	142	50	SW	F2	2
176	2.95	5.5	N	20	90	fracture	N	95	60	N	F4	4
177	2.95	5.5	N	20	90	fracture	N	280	15	N	F6	1
599	157	158	N	170	70	fracture	N	216	55	NW	F3	2
600	157	158	N	170	70	fracture	N	48	63	SW	F1	1
601	158	159	N	170	70	fracture	N	208	88	NW	F3	7
602	159	160	N	107	70	fracture	N	190	59	W	F3	7
603	160	161	N	112	70	fracture	N	25	34	SW	F3	15
604	160	161	N	112	70	fault	N	180	64	W	F5	1
605	161	162	N	112	70	fault	N	347	46	E	F5	1
606	161	162	N	112	70	fracture	N	39	35	SW	F3	15

Figure 2.2 – Example of a Scanline input dataset; Description of the headers: 1) Index: single index to reference all rows of the dataset; 2) m in, m out: these stands for “meter in and out” as to describe the interval treated in this row; 3) Dir, Surf Dir, Surf Dip : Survey orientation ('Dir' = Direction of the outcrop relative to the North 'N') and slope of the outcrop; 4) Type: stands for the type of structural feature; 5) Str, F Az, F Dip, F Quadrant: ('Str' = Structural measurement direction relative to the North 'N') are used to fill information relative to the structural feature, such as strike, dip, quadrant towards which it dips; 6) F F: is the “*a priori*” structural set; and 7) Q: stands for the number of these features, when a same feature is being repeated within the same interval.

a second batch of plots is generated, gathering the data per lithology. In SkaPy part–5, the script builds and plots the scanlines. Figure 2.3 shows the method used to script the construction of the scanline. For clarity, the fields “m in” and “m out” of the table are here referred to as “stations”. The offsets calculated between these stations would be called the “intervals”. In a first loop, SkaPy builds the trace of the scanline survey: it calculates the length of an interval by determining the positions of the stations, and compiles these intervals following the orientation given in “Surf Dir”. Then, in a second loop, SkaPy calculates the quantity of fractures Q belonging to each of the fracture sets within this interval. The algorithm then splits the intervals into (Q + 1) sections in order to equally distribute the fractures, and to assign a specific position to each of the fractures. X and Y coordinates are calculated from the origin station of the scanline.

In SkaPy part–6, the script is used for the extrapolation of the scanlines into training images (TIs). In this part, instead of using the fracture length and strike values as in SkaPy part–5, the script plots the average strike value representative for each set, and extends the lengths of the fractures such that they fill the entire plot. The objective of this step is to offer guidance to the users for the following step of the workflow, which consists of creating the training images (TIs). In SkaPy part–7, the script computes the stereonet and rose diagrams for each outcrop. The second script, SkaPy–UTM, assigns the UTM coordinates to the scanline, including all the fractures, by modifying the origin of the reference system.

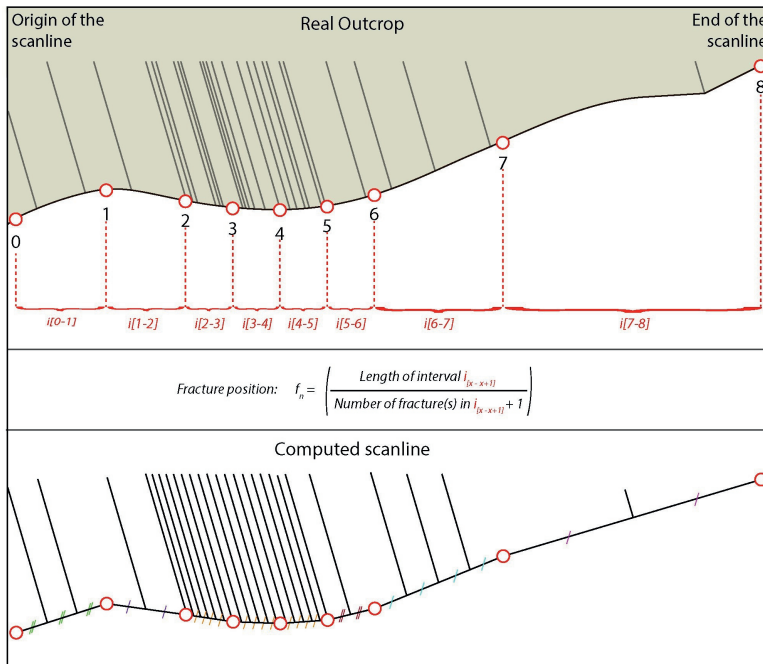


Figure 2.3 – Illustration of the method used to build the scanline in SkaPy: Upper part: shows the simplified fractures (as grey straight lines) in the real outcrop (brown background). Red and white dots with numbering from 0 to 8 represent the stations. These stations delimit intervals (here marked in red); Middle part: gives the expression used to calculate fracture positioning from the dataset to computed scanline; Lower part: shows the computed scanline. Small colored oblique lineaments in between the fractures describe equal spacing

### 2.3.2. METHOD: DFN CREATION USING MULTIPLE POINT STATISTICS

Multiple point statistics (MPS) is used to extrapolate geological patterns to larger scales. Classical geostatistical methods use variograms; the MPS method uses the training images (TIs) as input data for the simulation. The concept is based on analyzing the pixel content of the TI to identify the spatial patterns to be reproduced into a larger domain (Tahmasebi, 2018). The TI is considered as a grid of pixels which contains geological patterns. For that reason, the TI needs to include the possible range and shape of the geological entities to be modeled (Bruna et al., 2019). In this study, we used the Direct sampling (MPS) code as presented in Straubhaar et al. (2011).

#### CREATION OF THE TRAINING IMAGE

The TIs of the fracture network, created from the scanline generated by SkaPy (Figure 2.4), are then extrapolated into a larger model, creating the DFN. Scanline surveys provide datasets of very localized data, usually from tens to hundreds of meters. In comparison, the DFN is often used to represent fracture geometries over a much larger area, such as kilometer scale reservoirs. Building the TIs is the opportunity for the users to adjust this scaling issue: not every fracture reported in the scanline is represented in the DFN. Users can decide which fractures matter and need to be represented at a larger scale.

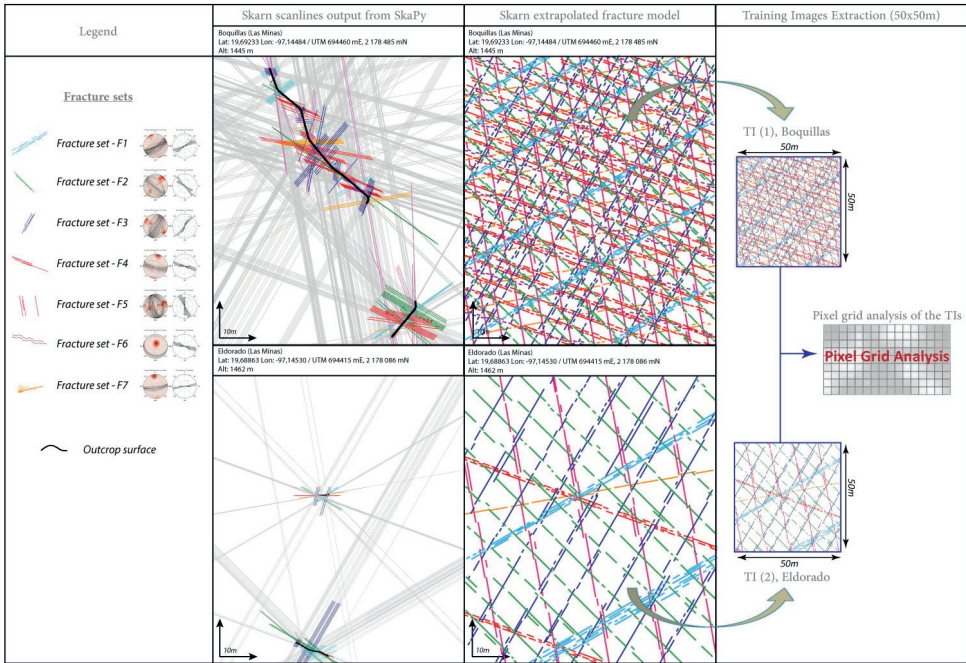


Figure 2.4 – From SkaPy output to Training Images creation

The method used to populate the TIs from the scanlines is: i) the scanline is used as firm value; ii) the guidelines, created in SkaPy part–6, are displayed in the background (section 2.3.1); iii) the users manually digitize the fractures following the guidelines; for the fracture lengths, use the values of the distribution from the quantiles calculated in SkaPy part–4, excluding the outliers. Because the TIs are created from the scanlines output from SkaPy, the geo-references are derived from the scanline coordinates.

**TRAINING IMAGES AND PROBABILITY MAP**

The TI is the only input for fracture geometries in the MPS method. For this reason, all ranges of dimensions, orientations of the fracture patterns need to be represented in the TI. The TI is saved as an image format, so that it can be analyzed as a grid where every pixel has a color value coding the structural entity. A reference table is given in Table 2.1 as an example. The algorithm of the MPS analyses the value of every pixel and pixel associations to identify the pattern composing the TI.

The MPS then builds one DFN based on two TIs and a probability map (fig. 2.5). The probability map is a representation of the destination domain where to populate the extrapolated fracture networks. This map defines the areas where each TI should be used to populate the DFN in the simulated domain. The probability map could represent geological entities, such as faults or fluvial channels or different lithologies. In this study, however, we linearly interpolate between the two TIs for simplicity.

Table 2.1 – Fracture sets, colors and orientations

Fracture set	Pixel code	Pixel color	Average strike	Average Dip
Fracture set F1	161	Cyan	N 60°	70°
Fracture set F2	140	Green	N 135°	60°
Fracture set F3	69	Navy	N 30°	68°
Fracture set F4	123	Red	N 130°	73°
Fracture set F5	127	Magenta	N 170°	56°
Fracture set F6	90	Violet	N 105°	20°
Fracture set F7	173	Orange	N 80°	74°
No fracture	255	White	NA	NA

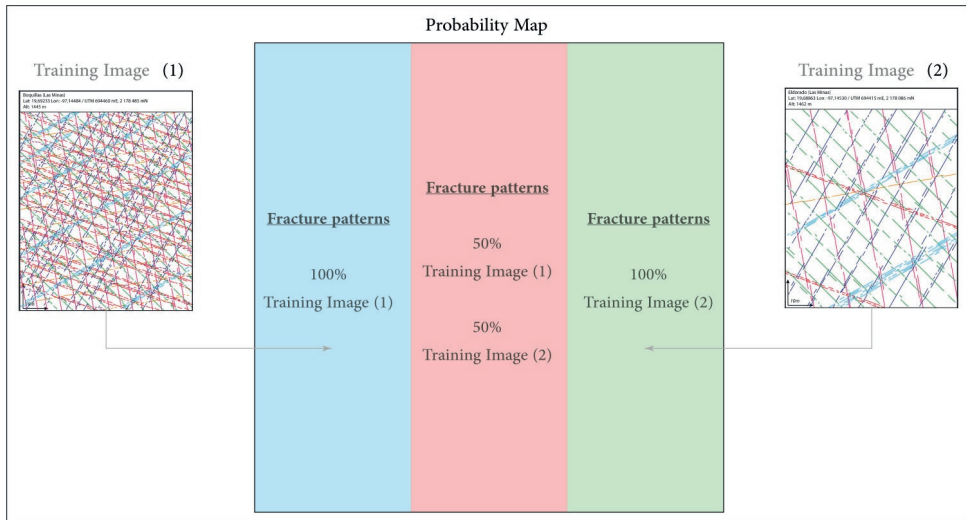


Figure 2.5 – Training images and Probabilistic map, as used in this study. Here Training Image (1) corresponds to the TI of Boquillas outcrop, and Training Image (2) corresponds to the TI of Eldorado outcrop, for the Skarn lithology

## 2.4. RESULTS: CASE STUDY OF ACOULCO GEOTHERMAL SITE IN MEXICO

### 2.4.1. GEOLOGICAL CONTEXT

#### ACOULCO WITHIN THE REGIONAL GEOLOGICAL CONTEXT

The method we developed creates discrete fracture networks (DFNs), where the main input are scanline datasets measured at outcrops near the Acoculco test site.

When reporting a scanline in the field, measurements are done objectively. Later, when processing the data, the users want to set these measurements in context. This is why it is essential to know the regional structural context to classify the scanline dataset.

Acoculco is located in the Trans-Mexican volcanic belt (TMVB), about 100 km North-



East of Mexico City. The TMVB is a mountain range resulting from the subduction of the Avalon, Rivera, Orozco and Cocos plates beneath the North American plate (Ferrari et al., 2012; Manea et al., 2013) (fig. 2.6). The TMVB is composed of a thick series of Pliocene to Quaternary volcanic deposits forming a high volcanic plateau. This plateau overlies a fold and thrust belt resulting from the Sierra Madre Oriental, a Laramide deformation of the Jurassic to Cretaceous deposition of the carbonate sequence (Carrasco Núñez et al., 2017; Norini et al., 2015; López-Hernández et al., 2009; Campos-Enriquez and Garduño-Monroy, 1987).

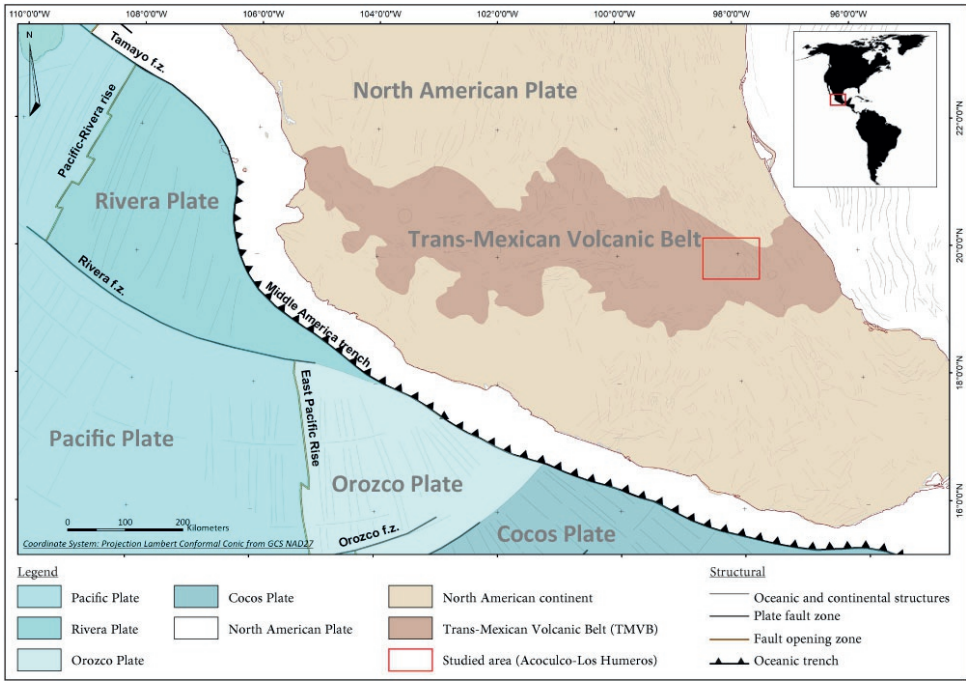


Figure 2.6 – Simplified tectonic map of Mexico, indicating Acoculco site location, modified from Padilla (2013).

Two geothermal exploration wells, EAC1 & EAC2, were drilled in Acoculco, about 500 m apart, in 1995 and 2008. Since the wells are really close to each other and even though the well-markers position suggest a fault could cause an offset between the two wells, their lithological sequence is very similar and can be summarized, as described by (Viggiano-Guerra et al., 2011; López-Hernández et al., 2009), in Table 2.2 :

Figure 2.7 is a representation of the geological section in Acoculco adapted from the model of López-Hernández et al. (2009), based on gravity, magnetic and well data, which has been further developed by Lorenzo Pulido et al. (2010) and Canet et al. (2015b). The carbonate section consists of dolomitic Limestones, Limestones metamorphised into Marbles or metasomatised into Skarns due to the intrusion of a granodioritic pluton.

Table 2.2 – Lithology from EAC 1 and EAC 2 well-markers (Abbreviations: Measured Depth (MD) and Total Depth (TD))

Lithology	EAC 1 well-marker depth	EAC 2 well-marker depth
Volcano-clastic deposits	0 to 830m MD	0 to 340m MD
Carbonates section	830 to 1650m MD	340 to 1580m MD
Granodiorite – Granite	1650 to 2000m MD (TD)	1580 to 1900m MD (TD)

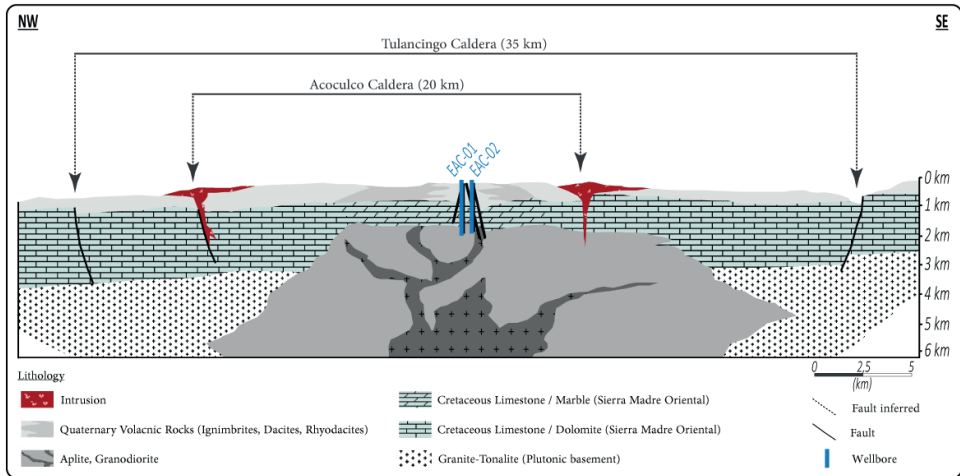


Figure 2.7 – Schematic geological section of the Tulancingo-Acoaculco caldera Complex, modified from López-Hernández et al. (2009).

### LAS MINAS ANALOGUE

Las Minas is a village located down in a valley, about 120 km East of Acoaculco. Las Minas valley is considered here as an excellent analogue of the Acoaculco geothermal system. As seen on the geological map (fig. 2.8), Acoaculco and Las Minas are made of rocks that were deposited in the same geological environment. The exposed rock sequence in the Las Minas analogue is comparable to the log of Acoaculco well-bores, from the recent volcanic cover, overlaying the carbonate sequence made of the Early Cretaceous Limestones called the Tamaulipas Formation, all the way to the granodioritic pluton, which is exposed deep in the valley, where the river Rio Las Minas runs. Hundreds of meters away from the river bed, two outcrops, named Boquillas and Eldorado, expose Skarns; higher on the flanks of the valley, two marble outcrops are found: Pueblo Nuevo and Tatatila. Further away is first one outcrop made of marblized dolomitic Limestones called Rinconada, and much further, beyond the influence of the intrusion, San Antonio Tenextepc is made of unaltered dolomitic Limestones. These outcrops represent a proximal to distal context for the granodioritic intrusion into the carbonates. Figure 2.9 is a simplified representation of the geological context.

### STRUCTURAL CONTEXT

Four major structural trends are identified in the region from Aocolco to Las Minas. The Aocolco Caldera is located at the intersection of two regional fault systems, one trending NE and the other NW (López-Hernández et al., 2009). The main structures in the region are inherited from: i) the Laramide Orogeny, Late Cretaceous with a NE - SW compression, inducing NW - SE thrusts and folds affecting the lithological sequence from the metamorphic basement up to the Mesozoic sedimentary rocks; ii) the Eocene-Pliocene extensional and transtensional phases that produced N - S to NE striking faults (Carrasco Núñez et al., 2017; Norini et al., 2015). A micro-structural study identified two major structural directions: i) the first direction is from N140 to N170; ii) these structures are cut by a second trend oriented from N40 to N70; this confirms the regional trends and identifies the direction N40 as a maximum regional stress (Campos-Enriquez and Garduño-Monroy, 1987).

In the Los Humeros Volcanic Complex (a ten of kilometers westwards from Las Minas), the main structures driving the ascending hot fluids have been identified as the NNW - SSE east-dipping faults (Norini et al., 2015). Additionally, Carrasco Núñez et al. (2017) report that producing geothermal wells are located along the main NNW - SSE active faults or near the N-S striking fault splays NW - SE and NE - SW-trending regional faults systems appear to have been permeable fluid flow pathways (López-Hernández et al., 2009).

#### 2.4.2. CASE STUDY: APPLYING THE SCANLINE SURVEY

In the Aocolco field, we want to predict the distribution of the fractures in the reservoir formation which corresponds to the carbonate sequence. As described in Section 2.4.1, the carbonate sequence includes three lithologies: the Limestones, Marbles and Skarns. For that reason, the linear scanline survey method was recorded in two outcrops for each of these rock types, for a total of six outcrops (table 2.3).

Table 2.3 – Outcrop names, locations and lithologies

Outcrop	lithology	latitude [ <i>dec.deg</i> ]	longitude [ <i>dec.deg</i> ]
Boquillas	Skarn	19.692277	-97.144793
Eldorado	Skarn	19.688609	-97.145828
Pueblo Nuevo	Marble	19.708514	-97.158178
Tatatila	Marble	19.696589	-97.136941
Rinconada	Limestone	19.668151	-97.16112
San Antonio Tenex-tepec	Limestone	19.496045	-97.291252

The trace of the scanline survey follows the direction of the outcrop walls. As explained in Section 2.3.1, each interval is delimited by two stations in between which the wall follows a constant direction (fig. 2.10). Within these intervals, fractures are counted individually or per group of fractures having the same strike and dip values; the number of fractures is then reported in column “Q” of the dataset (fig. 2.2). The value reported for the aperture is the average value of the aperture measured for a fracture, or a set of fracture. The length and height of the fractures are measured along the outcrop. Because



of that, if a fracture trace is longer than the outcrop, its measurement is limited to the length of the trace visible within the outcrop.

The fracture trace length measurements closely depend on the morphology of the outcrop. The height and slope of the outcrop walls change from the start to the end of the survey. For that reason, we applied a correction on our fracture trace length measurement, by converting it into a vertical height and a horizontal length, based on the slope of the outcrop, using a simple trigonometric rule. The measurements are well constrained up to 5 m ( $\pm 1 \times 10^{-3}$  m), fairly well constrained up to 10 m and eventually less over 20 m ( $\pm 5$  m), depending on the regularity of the outcrop morphology and its accessibility for the measurements. Figure 2.11 shows a sample of the Las Minas outcrops.

### 2.4.3. CASE STUDY: RUNNING SKAPY

The dataset, containing the scanlines from the six outcrops, is composed of about 600 rows. The total length of scanlines is 257 m, which includes 2090 fractures (table 2.4).

Table 2.4 – Scanline surveys realized and frequency of measured fractures

Outcrop	lithology	Scl-length	Nbr.Fractures	Frequency (frac/meter)
Boquillas	Skarn	29 m	351	12.10
Eldorado	Skarn	10 m	104	10.40
Pueblo Nuevo	Marble	15 m	50	3.33
Tatatila	Marble	30 m	63	2.10
Rinconada	Limestone	11 m	224	20.36
San Antonio T.	Limestone	162 m	1298	8.01
<b>Average</b>		257 m	<b>2090</b>	<b>8.13</b>

According to this dataset, most of the fractures in the Skarn outcrops, Boquillas and Eldorado are tight to closed (in this study, fracture aperture classification results from qualitative and quantitative description. As indication, open fracture refers to aperture  $> 0.1$ cm, partly open: aperture of the fracture varies from 0.05 to 0.1cm, tight to partly open: aperture of the fracture varies but is always  $< 0.05$ cm, closed: the fracture never has any aperture aperture). In the marble outcrops, the quantity of fractures is much lower, but most of them are open to widely open. Regarding the limestone outcrops, Rinconada is located on a regional fault and San Antonio Tenextepec is on a thrust fault. Both of them are highly fractured. As the scanline in San Antonio Tenextepec is the longest, a higher range of variability within the dataset is expected.

When running SkaPy, the first figure shows the distribution of fracture heights and fracture apertures for the whole dataset. In this case there is no direct correlation between the size of the fracture and the width of the aperture (fig. 2.12).

In SkaPy, part 2, we first classified the fractures in 4 sets, based on the regional structures described in the literature presented in section 2.4.1. These 4 sets are: N50, N100, N135, N170. Since there is a large amount of fractures, we decided to apply a more detailed classification, adding 3 more sets, based on the dip angle of the fractures (fig. 2.13).

As the objective is to characterize the fractures, we want to calculate the representative values, per lithology, of the fractures height and aperture. In Figure 2.14, the left

column shows the box-plots and distributions of fracture heights and apertures measured in the outcrops, and the right column shows the box-plots and distributions recalculated for all the examples of a given rock type. Then, SkaPy builds the scanlines, and SkaPy-UTM plots them in the UTM system (fig. 2.15).

#### 2.4.4. CASE STUDY: CREATING THE TRAINING IMAGES (TIs) AND RUNNING MPS

Following the workflow chart (fig. 2.1), the next step is the creation of the TIs. Figure 2.4 shows the method used to create the TI of the Boquillas outcrop, one of the two Skarn outcrops. In this example, the scanline survey is made of two orthogonal sections separated by 20 m: the main one is about 25 m and the second one 6 m long. We used the output from SkaPy part-6, where the extended fractures serve for guidance. This tool emphasizes the fracture patterns. In this case, the scanline shows that the blue and red sets, representing sets F3 and F4 respectively, are organized as clusters of fractures, while the sets yellow F7 and green F2, are much more equally distributed. This extrapolation works as the process of up-scaling: the scanline is a very high resolution dataset (decimetric), extrapolated to a DFN of a much larger scale, as in this case  $(600 \times 600)\text{m}^2$ . Therefore, not all fractures can be populated, and the TI serves as a transition tool representative of the scanline survey at a large scale.

Following this method, Figures 2.16 to 2.18 shows the TIs obtained for the three lithologies: the Skarns, the Marbles and the Limestones. These training images, together with a probabilistic map, as presented in Figure 2.5, are used as inputs for the computation of the DFNs, using the multiple point statistics method.

In this case study, the objective is to obtain a DFN model representing the transition of the fracture distributions, from one outcrop to the second, within the same rock type. For this reason, we used a linear extrapolation from one TI to the other. Therefore, the probability map consists of a domain of  $(600 \times 600)\text{m}^2$ , divided into three equivalent sub-domains of  $(200 \times 600)\text{m}^2$ . The first sub-domain is populated using one TI, the second with the other TI and the third, in the middle is populated with the calculated interpolation.

#### 2.4.5. CASE STUDY: CREATED DFNs

The fracture patterns are very well preserved during the MPS extrapolation (fig. 2.19). For example, the Marble rock type stays, after extrapolation, consistent to its sparse and homogeneous fracture distribution, while the extrapolation of the fracture distribution for the Limestones well represents the influence of regional faults, which causes the higher fracture frequency. Another element to control the fracture patterns extrapolation is the fracture lengths. The 3 created DFNs show longer fractures on their right side, corresponding to the influence of the second TIs of these three lithologies.

## 2.5. DISCUSSION & WAY FORWARD

In the process of generating DFNs, several issues affect the quality of the resulting model. When DFN is created following the method described here, one has to be aware that the error or biases induced by the scanline survey itself, as for example the

fracture trace length or fracture representativity, are not overcome. Scanline data collection also present a limitation regarding fracture relationships, as in this study, we do not report information regarding fracture abutments. A first clear solution, would be to complete the scanline dataset with interpretation of virtual outcrop images from drone imagery as developed by NORCE Research with Lime™ software (Buckley et al., 2019). This would mitigate the issue of fractures representativity and provide data on fractures relationships. Eventually, this could be coupled with the Facets plugin developed by Dewez et al. (2016) and implemented in the CloudCompare™ platform<sup>6</sup>. This Facets plug-in is an algorithm that detects automatically the orientations of the outcrop surfaces. Assuming these surfaces are the result of erosion working along weaknesses of the rock, the algorithm could be used to estimate the most frequent fracture directions over an outcrop.

Another solution would be to integrate the circular scanlines surveys at regular intervals along the linear one, as proposed by Watkins et al. (2015), to obtain a more complete dataset and reduce these biases, providing data on fracture chronologies and topology relationships.

Another limitation is the accessibility of the reservoir itself. In this study we used Las Minas as analogue system of the Acoculco geothermal field. This gives us a good prediction of the fracture network at the surface. By essence, there might be differences regarding past and present tectonic stresses between Acoculco subsurface reservoir and its surface analogue of Las Minas. To get a more accurate model, it would be possible to correct Las Minas fracture models by calibrating to the Acoculco well core samples. In addition, the present day local stress field in Acoculco at depth may differ from the one at the surface of Las Minas. This may be compensated by measuring the current stress field down-hole, and applying a correction on the fracture aperture and orientation. More generally, using well log data, such as Formation Imagery (FMI), would significantly refine the prediction of the fracture distribution in the subsurface.

Regarding the approach itself, three elements related to SkaPy have to be considered: Markovaara-Koivisto and Laine (2012) in their MATLAB® script, include an automatic classification of the fractures into sets. SkaPy does not automatize this part; we ask the users to define their own sets. We prefer to leave this classification to the users rather than to statistics. This could be debated as it makes room for personal bias. The choice of leaving this is based on the assumption that the users know which fracture sets to expect, and reinforces the will to keep control on the geological meaning of this processing. The users can control the quality of their classification by checking the plotted stereonets (fig. 2.11). Nevertheless, the automated classification tool could be implemented for guidance.

In the SkaPy scripts, as described in this manuscript, fracture geometry is not taken into account. We see two possible ways to improve this limitation: the first would be to integrate the fracture abutments; and the second is the classification of fracture shapes proposed by ISRM (1978).

A starting point to define the fracture abutment could be made by defining a chronology of the fractures determining the 'priority' on fracture intersections.

Regarding the fracture typology, the populating of the TIs, could follow a similar clas-

<sup>6</sup>CloudCompare (2019)

sification, as initiated by Markovaara-Koivisto and Laine (2012) describing the fracture tortuosity.

In SkaPy part-5, at the scanline construction, the script induces a small error of fracture positioning, which is described in the Figure 2.3. As explained in (2.3.1), the scanline is built using “stations” and “intervals”. In these intervals, fractures from the same set are distributed at equal distances over the interval. As a consequence of that method, a single fracture will be placed in the middle of the interval instead of its exact position in reality. This error is kept small by the choice of interval length. The larger the interval, the bigger the error.

This workflow has been developed to analyze the feasibility of establishing an enhanced geothermal system in the Acoculco field. For that reason, we need to predict the fractures and the fracture network structuring the reservoir formations. The aim is to be able to calculate the role of the fractures for the fluid flow circulation. The DFN provides the basis for simulating the fluid circulation using a doublet of two wells, one injector and one producer, connected by fractures. Preliminary results are presented in Figure 2.20 and the full study is available in Lepillier et al. (2019).

## 2.6. CONCLUSION

In the context of developing an enhanced geothermal system (EGS), it is fundamental to evaluate the fracture system present in the subsurface. Very often no detailed information for such an evaluation is available. In the study presented here, we propose a workflow to predict the fractures and the fracture network from outcrops. The four steps from data collection in suitable analogue systems at the surface to generating a Discrete Fracture Network provide results that go well beyond a statistical representation of the fracture networks observed at the surface. By preserving the real fracture distribution as well as measured fracture characteristics such as apertures, derived lengths and orientations, the DFNs computed this way can be used to predict reservoir properties, such as bulk permeability and provide the basis for reservoir enhancement procedures for a potential EGS development. While the method cannot replace information retrieved from direct access to the subsurface by down-hole images and measurements, it does provide, to our knowledge, the currently most realistic extrapolation of a surface fracture model from outcrop to field scale.

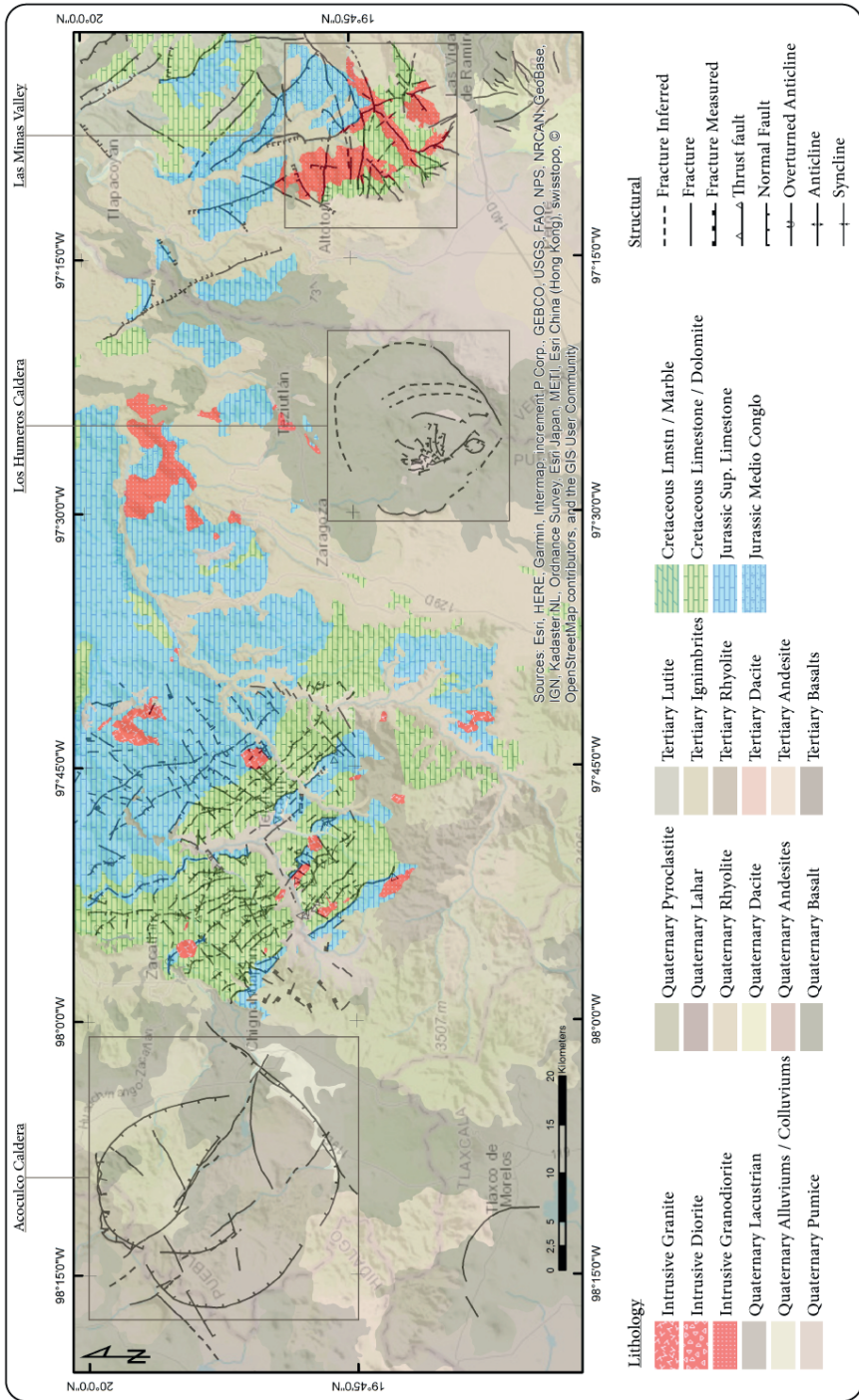


Figure 2.8 – Geological map of Acozulco – Los Humeros – Las Minas area, modified from (Servicio Geológico Mexicano, 1997, 2002) maps.

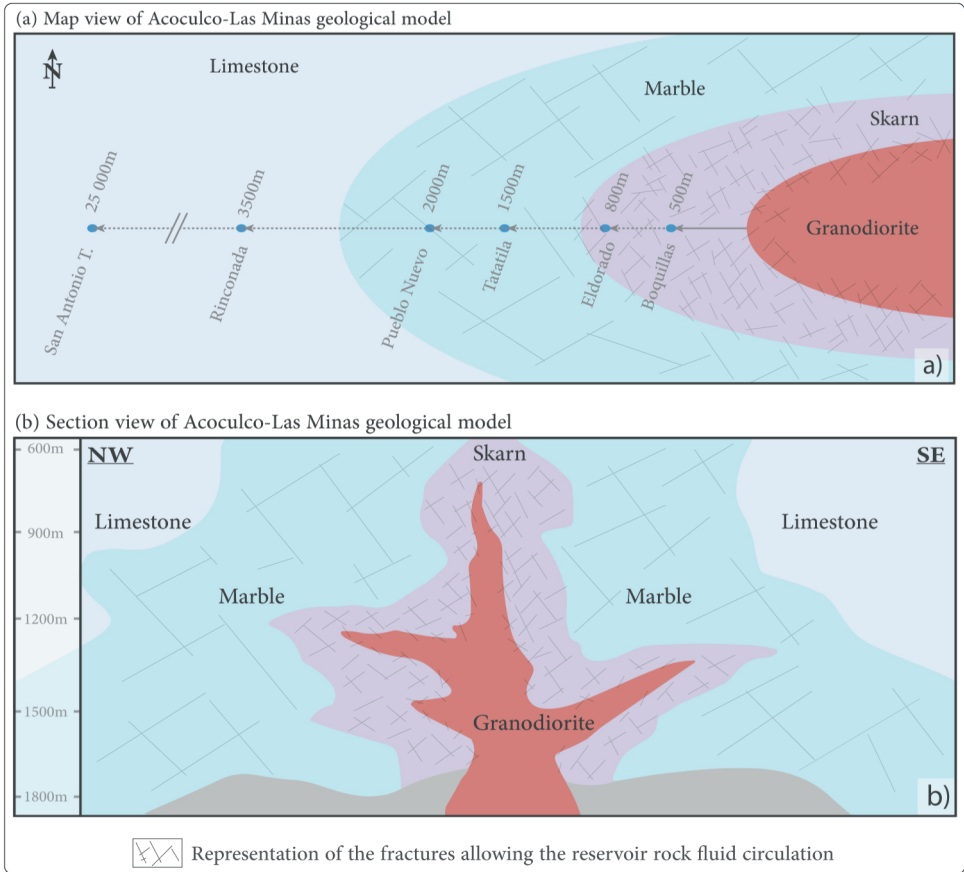


Figure 2.9 – Acoculco-Las Minas conceptual model: (a) Map view, (b) Section view.

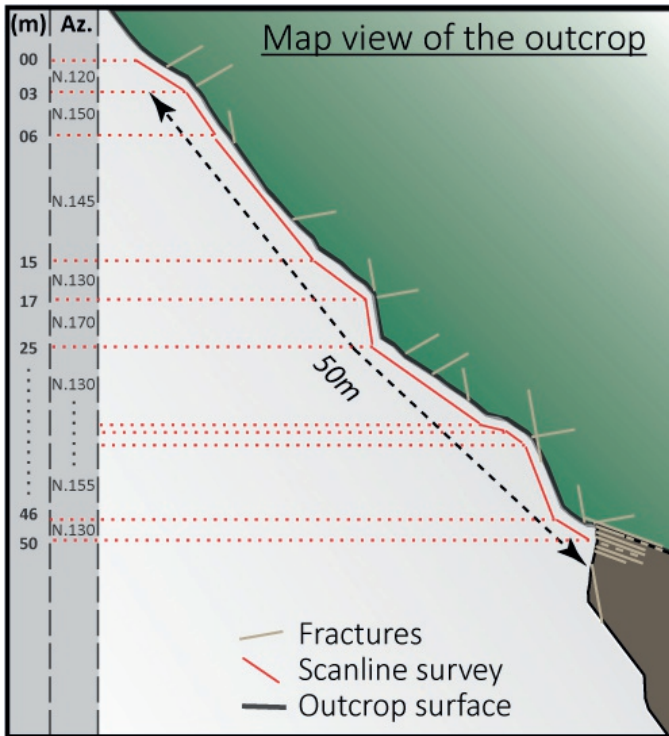


Figure 2.10 – Illustration describing the scanline survey method in a map view.

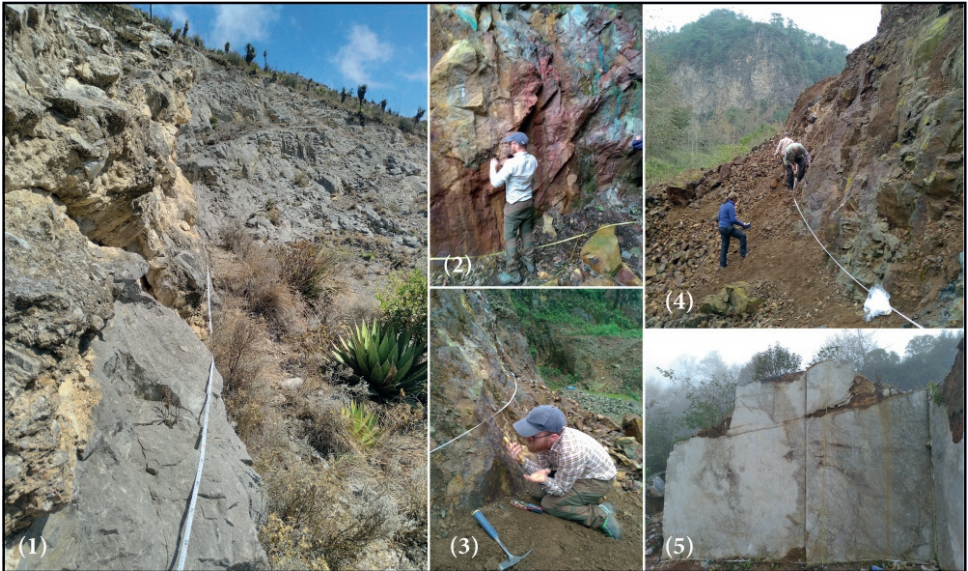


Figure 2.11 – Illustration of scanlines at the outcrops: (1) at San Antonio Tenextepe outcrop, Limestone; (2) at Eldorado outcrop, Skarn; (3,4) at Boquillas outcrop, Skarn; (5) at Pueblo Nuevo outcrop, Marble.



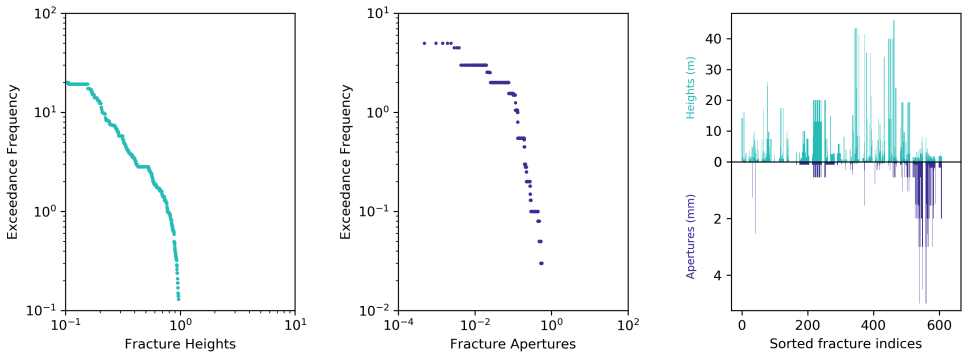


Figure 2.12 – SkaPy output part–1: The dataset at glance, from left to right: exceedance frequency of the fracture heights, then exceedance frequency of the fracture apertures and finally plotting fracture apertures against fracture heights; fractures are in this last plot sorted by using fracture numerical index from the database. As the database consists of a succession of scanline surveys, fractures are plotted in the following order: (from start to end of surveys) Boquillas, Eldorado, Pueblo Nuevo, Tatatila, Rinconada, San Antonio Tenextepec

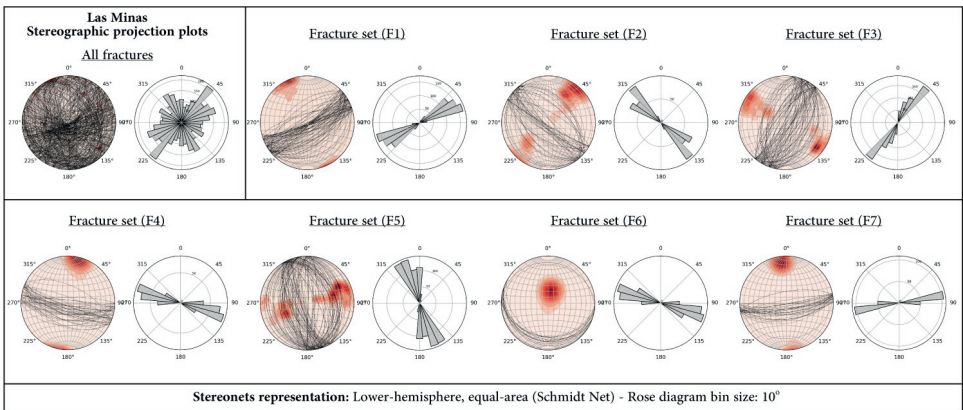


Figure 2.13 – SkaPy output part–2: Las Minas stereonet plots and rose diagrams - On the left, before classification into sets; On the right, fractures are separated into sets.



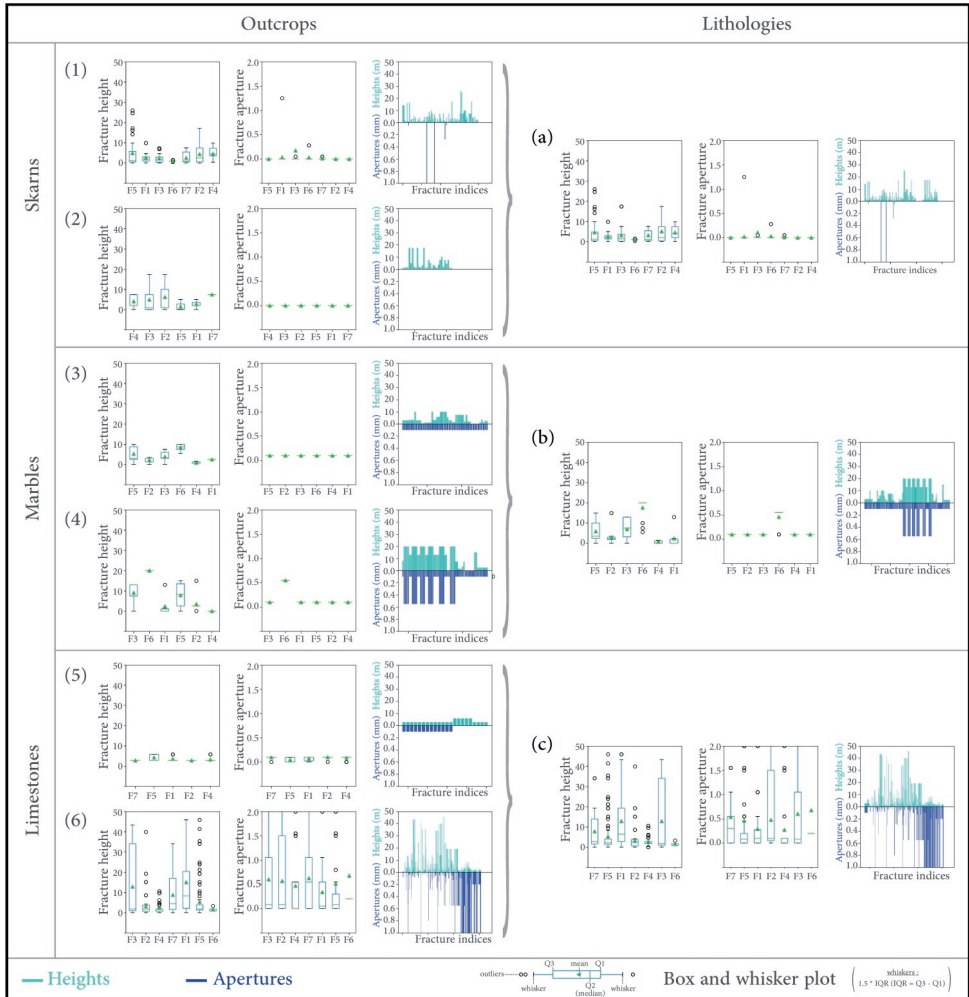


Figure 2.14 – SkApy output part–3,4: Tri-plots showing the fracture heights box-plots, apertures box-plots and distributions, per outcrops and finally, per lithologies: (1) Outcrop: Boquillas, (2) Outcrop: Eldorado, (3) Outcrop: Pueblo Nuevo, (4) Outcrop: Tatatila, (5) Outcrop: Rinconada, (6) Outcrop: San Antonio Tenex-tepec, (a) lithology: Skarns, (b) lithology: Marbles, (c) lithology: Limestones.

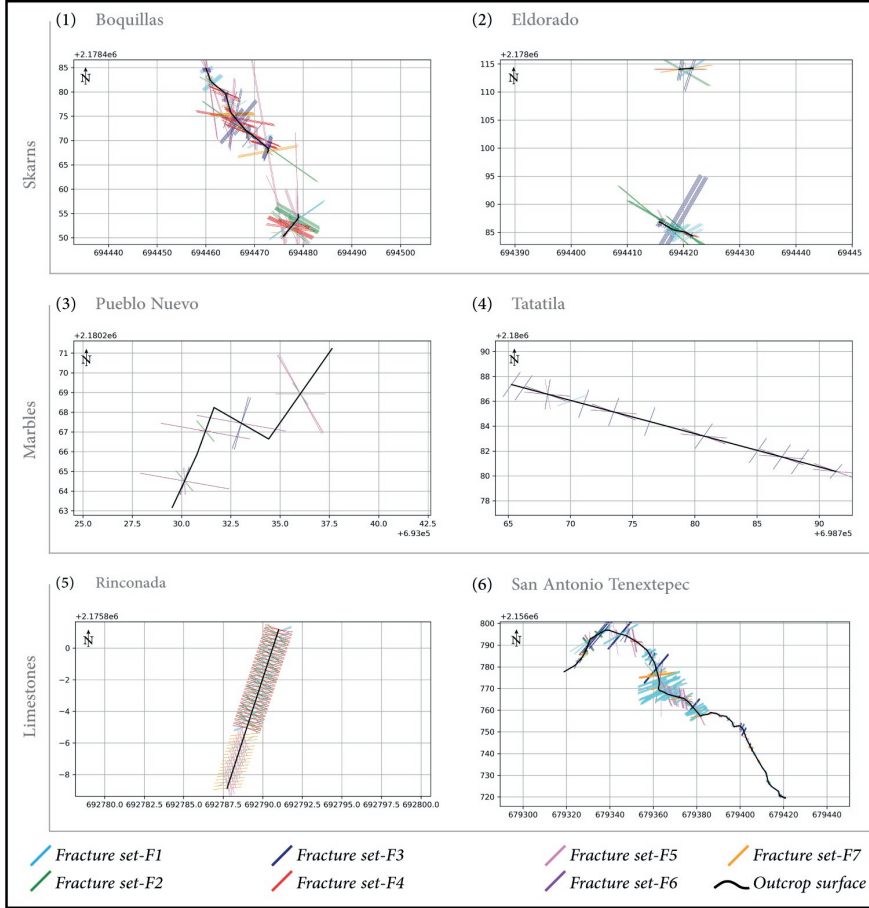


Figure 2.15 – SkaPy output part–5: Scanlines in Las Minas: (1) Skarn: Boquillas, (2) Skarn: Eldorado, (3) Marble: Pueblo Nuevo, (4) Marble: Tatatila, (5) Limestone: Rinconada, (6) Limestone: San Antonio Tenextepec. The black line represents the trace of the scanline, thus an approximation of the outcrop morphology. Along this line, fractures are plotted as vectors. The vector color depends on the fracture set and its length depends on the fracture height. These scanlines are all plotted in the same grid UTM Q14.

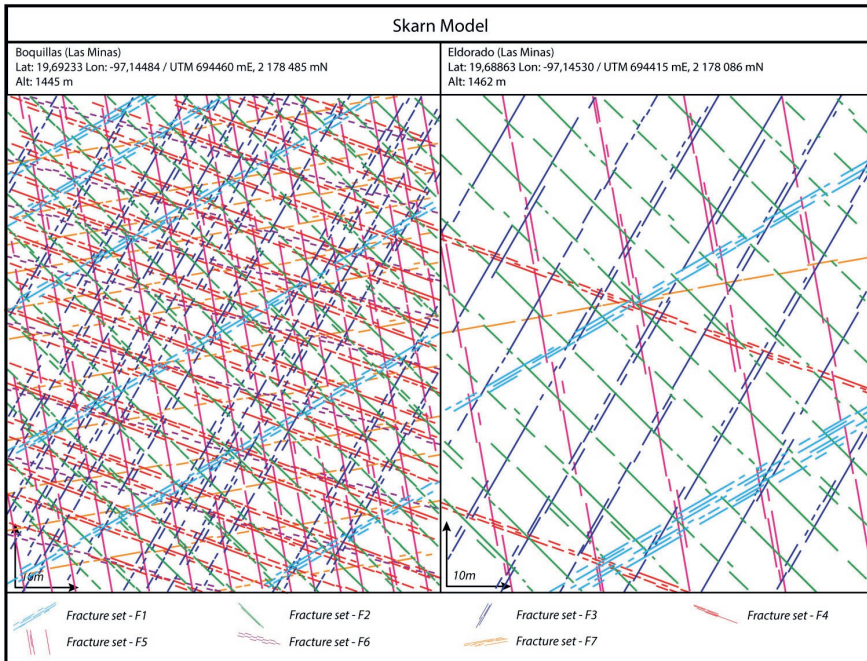


Figure 2.16 – Results of the manually populated TIs for the Skarn.

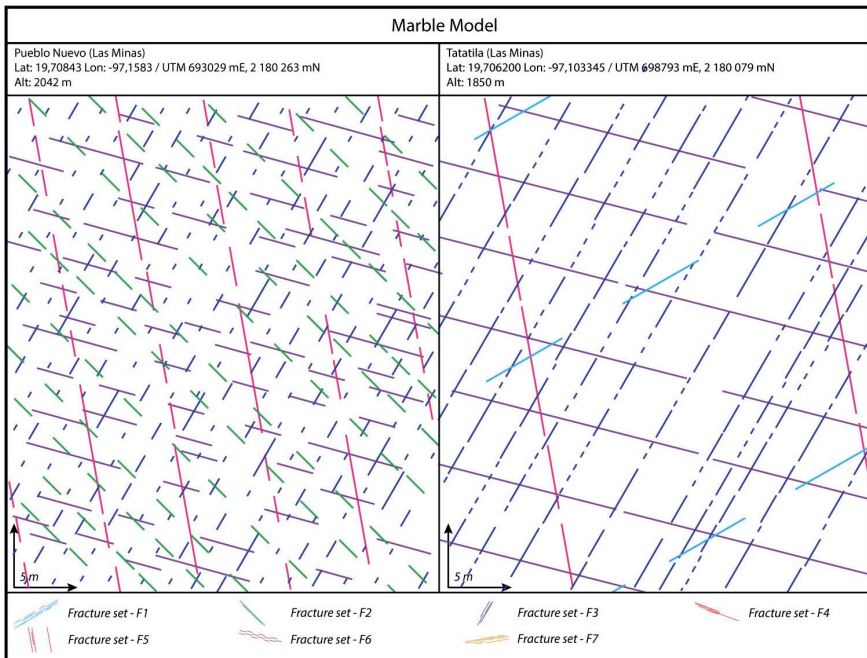


Figure 2.17 – Results of the manually populated TIs for the Marble.

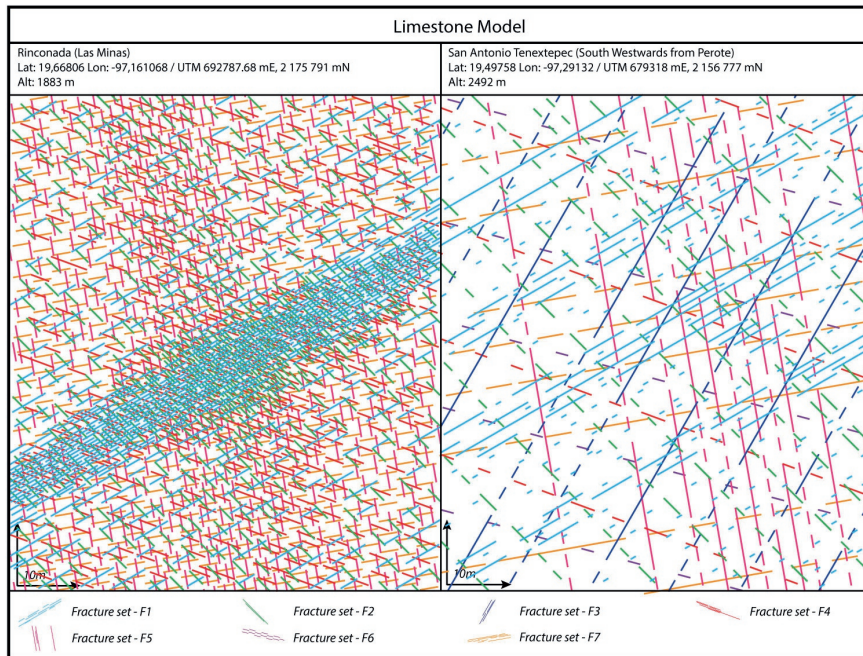


Figure 2.18 – Results of the manually populated TIs for the Limestones.



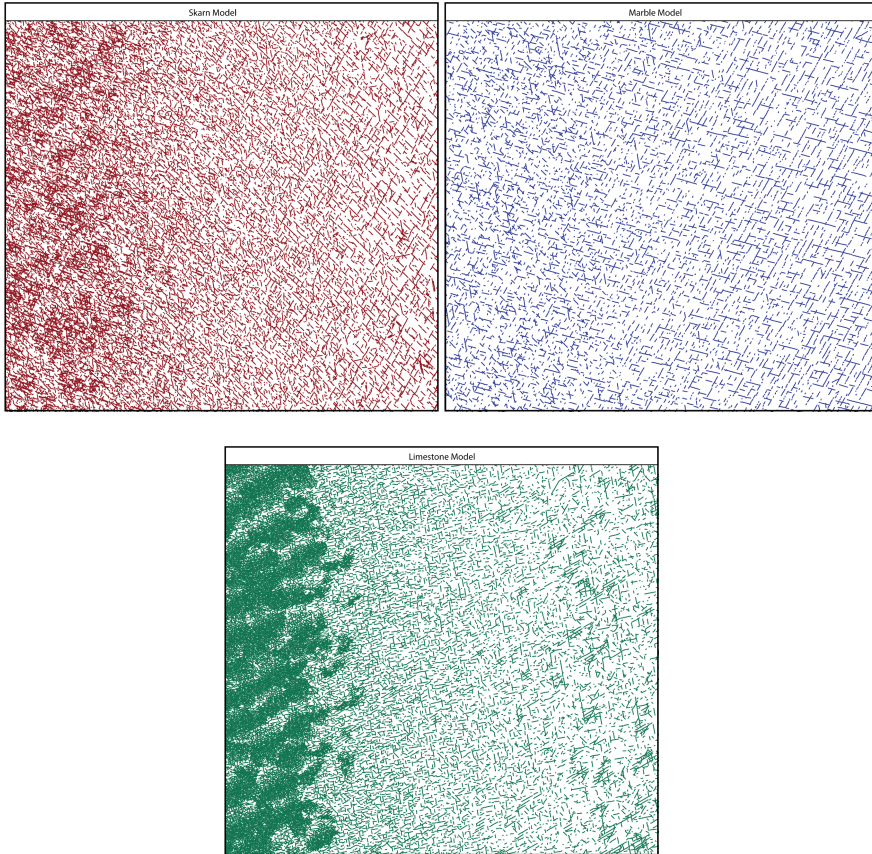


Figure 2.19 – Results of computed DFNs using the MPS method, from left to right: for the Skarns, Marbles, Limestones.

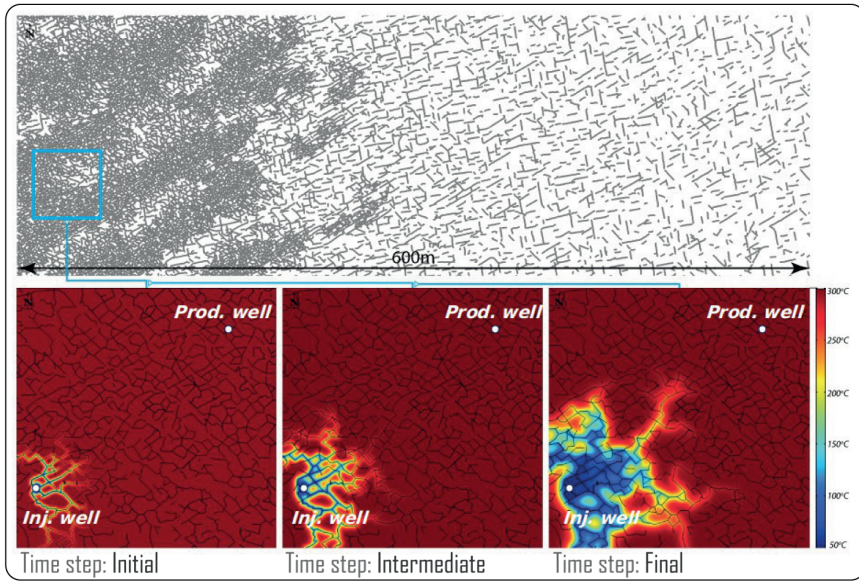


Figure 2.20 – Preliminary result of a fracture controlled fluid flow simulation of a doublet of wells pumping via the DFN created in using this workflow. The upper part of the figure shows the entire created DFN for the Limestones; The lower part of the figure shows, 3 different stages in chronological order from left to right, of the fluid flow from injection well into the fracture network.



# 3

## CHARACTERIZATION OF ACOCULCO RESERVOIR ROCK PROPERTIES

*Here we gather the results from the different tests realized in the rock physics laboratory to characterize Acoculco rocks properties. Experiments have been realized on samples collected in Las Minas or other analogue outcrops representative of the Acoculco Geothermal system. The main objective is to characterize the material rock properties for the potential reservoir lithologies of Acoculco geothermal site. Therefore, we need to quantify the permeability, porosity and the mechanical properties of the following lithologies: Limestones, Marbles, Skarns and Granodiorite.*



### 3.1. INTRODUCTION

To evaluate the Acoculco field as potential EGS development site, we need to quantify the reservoir rock properties. The first step is to identify the different lithologies. To do so, we analyze the chemical composition and mineral content of each material (1, XRF-XRD). Then, we need to confirm by measuring, the low permeability of the tested lithologies in the two exploratory wells EAC1 and EAC2. Therefore, we measure the porosity and permeability of the samples (2, porosity and permeability). Considering the modeling of hydraulic fracturing, mechanical rock properties are essential: especially we need to measure the material elastic properties, such as the rock stiffness parameters given by Young's modulus  $E$  and Poisson's ratio  $\nu$  (3, Unconfined Compressive Strength tests). Fracture initiation and propagation is mainly controlled by the Griffith energy release rate criterion  $G_c$ , itself derived from the fracture toughness  $K_{IC}$  (4, Unconfined Tensile Strength and Chevron Bend tests). A last test is presented: a set-up reproducing hydraulic fracturing condition using the Hoek cell apparatus. This test is a trial for hydraulic fracture behavior prediction (5, Hydraulic fracturing using the Hoek cell apparatus).

Las Minas is a an exhumed geothermal system, considered a good analogue where a comparable system as Acoculco is cropping out at surface. A conceptual model of the Acoculco-Las Minas geological system is represented in section 1.4.2. Most of the samples were collected in the following outcrops: "GDPA", Granodiorite (Las Minas river bed), "BOQ", Boquillas Skarns (assumed as Endo-skarn); "ELD", Eldorado Skarn (assumed as Exo-skarn); "PNO & MAPA", Pueblo Nuevo and "TAT" Tatatila Marbles; and "RIN", Rinconada to "SAT", San Antonio Tenextepec Limestones. A few more samples from the recent volcano-clastic lithological unit were also sampled and analyzed. Figure A.1, Figure A.2 and Figure A.3 gives the list of the collected samples with their name, lithology and location.

Here after is the experimental program:

1. the results of XRF-XRD analyses,
2. the porosity and permeability measurements,
3. the Unconfined Compressive Strength tests,
4. the Unconfined Tensile Strength (Brazilian discs test) and Chevron Bend tests,
5. the hydraulic fracture test using the Hoek cell.

## 3.2. ROCK PHYSICS LABORATORY EXPERIMENTS

### 3.2.1. XRF-XRD

Chemical and mineral compositions of the samples were measured with X-ray Fluorescence (XRF) and X-ray Diffraction (XRD). The XRF spectrometer analyses the chemical composition of the rock material, and the XRD helps determining the mineral composition. The measurements and analyses have been done at the Department of Materials Science and Engineering of the Delft University of Technology. Figure 3.1 shows the interpreted results combining X-ray diffraction and X-ray fluorescence.

Code name	Location Name	Rock type	XRD	Chemical formula
A	Rinconada	Marble	Calcite	Ca(CO <sub>3</sub> )
			Quartz	SiO <sub>2</sub>
B	Tatatila	Marble	Calcite	Ca(CO <sub>3</sub> )
			Quartz	SiO <sub>2</sub>
C	Tatatila	Marble	Calcite	Ca(CO <sub>3</sub> )
			Quartz	SiO <sub>2</sub>
D	Las Minas	Skarn	Quartz, low	SiO <sub>2</sub>
			Albite, calcian	Na <sub>0.84</sub> Ca <sub>0.16</sub> Al <sub>1.16</sub> Si <sub>2.84</sub> O <sub>8</sub>
			Magnesio-hornblende, ferroan	Ca <sub>2</sub> (Mg,Fe+2)4Al(Si <sub>7</sub> Al)O <sub>22</sub> (OH,F) <sub>2</sub>
			Calcite	CaCO <sub>3</sub>
E	Rinconada	Limestone/Dolomite	Calcite	Ca(CO <sub>3</sub> )
			Quartz	SiO <sub>2</sub>
F	San Antonio Tenex-tepec	limestone	Calcite	Ca(CO <sub>3</sub> )
			Quartz	SiO <sub>2</sub>
G	Acoculco Quarry	Rhyolite	Sanidine, potassian, disordered	(Na,K)(Si <sub>3</sub> Al)O <sub>8</sub>
			Quartz, low	SiO <sub>2</sub>
H	Tatatila	Marble	Dolomite	CaMg(CO <sub>3</sub> ) <sub>2</sub>
I	Eldorado	Exo-Skarn	Quartz, low	SiO <sub>2</sub>
			Pyrite	FeS <sub>2</sub>
			Grossular(Garnet)	Ca <sub>3</sub> (Al <sub>0.9</sub> Fe <sub>0.03</sub> ) <sub>2</sub> Si <sub>2.05</sub> (O <sub>0.79</sub> F <sub>0.1</sub> (H <sub>2</sub> O) <sub>0.11</sub> ) <sub>12</sub>
			Magnetite	Fe+2Fe <sub>2</sub> +3O <sub>4</sub>
J	Pueblo Nuevo	Marble	Calcite	Ca(CO <sub>3</sub> )
			Dolomite	CaMg(CO <sub>3</sub> ) <sub>2</sub>
			Quartz	SiO <sub>2</sub>
K	Boquillas	Endo-skarn	Magnetite	Fe <sub>3</sub> O <sub>4</sub>
			Magnesio-hornblende, ferroan	Ca <sub>2</sub> (Mg,Fe+2)4Al(Si <sub>7</sub> Al)O <sub>22</sub> (OH,F) <sub>2</sub>

Figure 3.1 – Table of interpreted results combining X-ray Diffraction (XRD) and X-ray Fluorescence (XRF) analyses

### 3.2.2. POROSITY & PERMEABILITY

Porosity measurements have been done using the *Ultracycrometer 1000* Version 2.12 (Quantachrome Corporation). Every sample was measured 20 times. Each rock type was tested on 3 to 5 specimens, depending on available material. Results are consistent even if one could think that the porosity is globally slightly over-estimated by the apparatus.

Note on the results: Boquillas samples porosity is significantly over-estimated. The error is due to the principle of the method, which assumes a perfect volume of sample with straight cuts. Boquillas is a granular rock, made of, for instance, pyrite minerals. These Pyrites are altered and easily washed away while coring. Because of that, Boquillas cores are not perfect flat surfaces but rough and irregular. This surface roughness creates an apparent pore space, biasing the pore sample volume calculation.

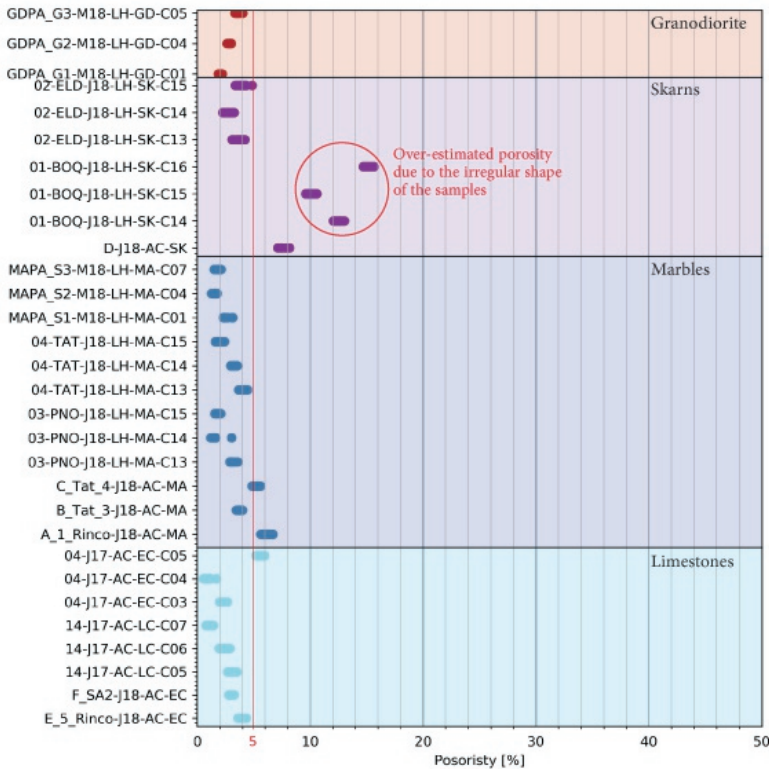


Figure 3.2 – Porosity plot.

Permeability measurements were performed at German Research Centre for Geosciences (GFZ) at conditions corresponding to room temperature on oven-dry sample cores using the steady state gas flow method described by Tanikawa and Shimamoto (2009). The cores had a diameter of 30 mm and variable lengths between 15–30 mm. At least five pore pressure levels,  $P_{up}$ , ranging from 0.5 to 3.5 MPa were applied to the upstream-side of the samples, at a constant isotropic confining pressure of 8.0 MPa, with Ar as both

confining and pore pressure medium. The corresponding gas flow rates through the samples were measured with one of four different commercial flow-meters (MKS Instruments) that can measure flow rates in the range of 10, 100, 1000, and 10'000 cm<sup>3</sup>min<sup>-1</sup>, respectively. As the gas is released from the sample to atmospheric pressure, we assume a constant pore pressure at the downstream side,  $P_{down}$ , of 0.1 MPa. The apparent gas permeability was calculated after Scheidegger (1974) as:  $k_{gas} = \frac{\eta L Q 2 P_{down}}{A(P_{up}^2 - P_{down}^2)}$ ; where  $\eta$  is

the viscosity of the pore fluid at given pressure and temperature,  $L$  is the sample length,  $Q$  is the flow rate and  $A$  is the cross-sectional area of the sample. The water permeability was derived from the gas permeabilities that were Klinkenberg-corrected for the gas slip flow effect at the gas-mineral interface (Klinkenberg, 1941):  $k_{gas} = k_w \left(1 + \frac{2b}{P_{up} + P_{down}}\right)$ ; where  $k_w$  is the (intrinsic) water permeability and  $b$  is the Klinkenberg factor. In the low pressure range gas permeabilities were significantly enhanced due to 'slip flow'. Thus, gas permeabilities measured at differential pore pressures lower than 0.75 MPa were predominantly ignored for the conversion and water permeabilities were obtained from linear plots of gas permeabilities vs. the inverse of at least four different mean pore pressures. The measurement accuracy was better than 1.5 %.

Table 3.1 gives the results of these measurements. Note, for guidance to the reader, it is commonly agreed that a permeability of 1 Darcy would represent a fair reservoir. 1 Darcy =  $1 \times 10^{-12}$  m<sup>2</sup>. Then everything higher would be considered as having a very good permeability (range from  $1 \times 10^{-7}$  to  $1 \times 10^{-10}$  m<sup>2</sup>), such as gravel sand or highly fractured rock formations; and below  $1 \times 10^{-17}$  is considered as nearly non-permeable. According to these orders of permeability ranges, the following results are all showing extremely poor permeabilities.

Lithology	$\phi$	$k$ m <sup>2</sup>
Limestone Late Cretaceous	0.02	$1 \times 10^{-20}$
Limestone Early Cretaceous	0.03	$1 \times 10^{-20}$
<b>Limestone</b>	<b>0.03</b>	<b><math>1 \times 10^{-20}</math></b>
Marble from Pueblo Nuevo	0.02	$6.5 \times 10^{-19}$
Marble from Tatatila	0.03	$1.2 \times 10^{-18}$
<b>Marble</b>	<b>0.03</b>	<b><math>9.5 \times 10^{-19}</math></b>
Exo-skarn from Eldorado	0.03	$1.5 \times 10^{-19}$
Endo-skarn from Boquillas	0.12	$5.2 \times 10^{-16}$
<b>Skarn</b>	<b>0.08</b>	<b><math>2.6 \times 10^{-16}</math></b>
Granodiorite	0.3	$1.25 \times 10^{-18}$

Table 3.1 – This table summarizes the results of the porosity ( $\phi$ ) and permeability ( $k$ ) measured in the laboratory for the concerned lithologies: limestones, marbles, skarns and granodiorite.

### 3.2.3. UNCONFINED COMPRESSIVE STRENGTH TEST

Unconfined Compressive Strength (UCS) tests were run in the Geoscience & Engineering Laboratory of the Civil Engineering and Geosciences department of Delft University of Technology. The apparatus is a uni-axial stress/strain device, with a capacity of 500 kN. Axial displacement is recorded using two vertical sensors, axial LVDTs. Radial displacement is recorded using a radial chain with LVDT sensor around the sample. Measurements and calculations are realized following the “Standard method of test for elastic moduli of rock core specimens in uniaxial compression”, by American Society for Testing and Materials, ASTM Designation D 3148-72.

The current results are based on 20 experiments, with 2 to 3 cores per outcrop, giving a good control for Granodiorite, Skarn, Marble and Limestone characterization: each core has been cut to the dimensions of: length: 75mm ; diameter: 30mm. Plots of the experiments are given in Figure 3.3 and resulting values are given in Figure 3.4.

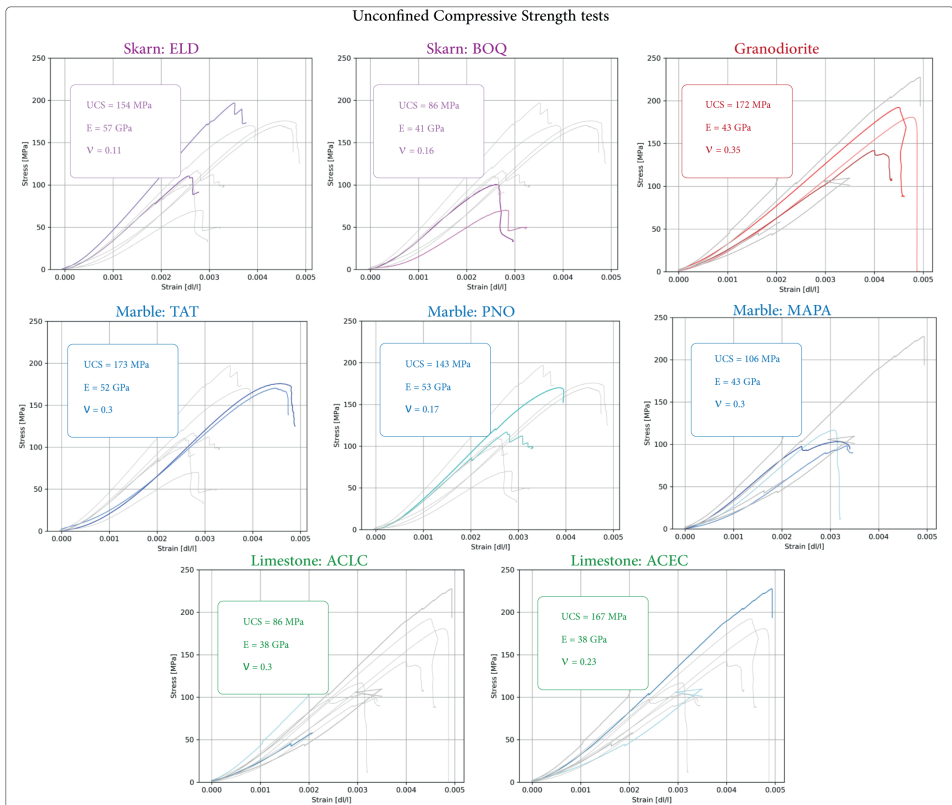


Figure 3.3 – UCS test plots and results (average values of the tests is given with: *UCS* standing for Ultimate Compressive Strength, *E* for Young's modulus, and *v* for Poisson's ratio).

BOQ	$\sigma_c$ (Mpa)	$E$ (GPa)	$\nu$	ELD	$\sigma_c$ (Mpa)	$E$ (GPa)	$\nu$	PNO	$\sigma_c$ (Mpa)	$E$ (GPa)	$\nu$	TAT	$\sigma_c$ (Mpa)	$E$ (GPa)	$\nu$
BOQ-01	100,59	48,00	0,18	ELD-01	110,57	49,32	0,08	PNO-01	170,06	55,13	0,21	TAT-01	170,36	49,03	0,26
BOQ-02	70,3	34,20	0,14	ELD-02	196,93	64,62	0,13	PNO-02	116,9	50,32	0,13	TAT-02	175,77	54,19	0,32
<b>Avg</b>	<b>85,45</b>	<b>41,10</b>	<b>0,16</b>		<b>153,75</b>	<b>56,97</b>	<b>0,11</b>		<b>143,48</b>	<b>52,73</b>	<b>0,17</b>		<b>173,07</b>	<b>51,61</b>	<b>0,29</b>
B4ACEC	$\sigma_c$ (Mpa)	$E$ (GPa)	$\nu$	14ACLC	$\sigma_c$ (Mpa)	$E$ (GPa)	$\nu$	MAPA	$\sigma_c$ (Mpa)	$E$ (GPa)	$\nu$	GDPA	$\sigma_c$ (Mpa)	$E$ (GPa)	$\nu$
B4ACEC-013	109,65	26,14	0,10	14ACLC-015	113,13	46,62	0,42	MAPA-011	98,22	36,29	0,23	GDPA-011	180,67	43,61	0,44
B4ACEC-014	227,68	49,67	0,35	14ACLC-016	58,13	29,03	0,20	MAPA-012	116,88	46,02	0,37	GDPA-012	192,32	46,71	0,38
								MAPA-013	103,31	46,02	0,32	GDPA-013	141,83	38,06	0,24
<b>Avg</b>	<b>168,67</b>	<b>37,91</b>	<b>0,23</b>		<b>85,63</b>	<b>37,83</b>	<b>0,31</b>		<b>106,14</b>	<b>42,78</b>	<b>0,31</b>		<b>171,61</b>	<b>42,79</b>	<b>0,35</b>

Figure 3.4 – UCS tests and results per outcrop (*UCS* standing for Ultimate Compressive Strength, *E* for Young's modulus, and *ν* for Poisson's ratio).

### 3.2.4. UNCONFINED TENSILE STRENGTH (BRAZILIAN DISC) TEST

Tensile Strength is measured with the Unconfined Tensile Strength, or also called Brazilian disc (BD), test. BD tests were run in the Geoscience & Engineering Laboratory of the Civil Engineering and Geosciences department of Delft University of Technology. The apparatus is a uni-axial stress/strain device, with a capacity 50 kN. The BD test used for determining indirect tensile strength has been realized in accordance with "Standard Test Method for Splitting Tensile Strength of Intact Rock Core Specimens", by American Society for Testing and Materials, ASTM Designation D 3967-08.

The current analysis is based on 80 experiments, with 10 cores per outcrop: granodiorite, skarn, marble and limestones. Each core has been cut to the dimensions of: length (thickness): 15mm ; diameter: 30mm.

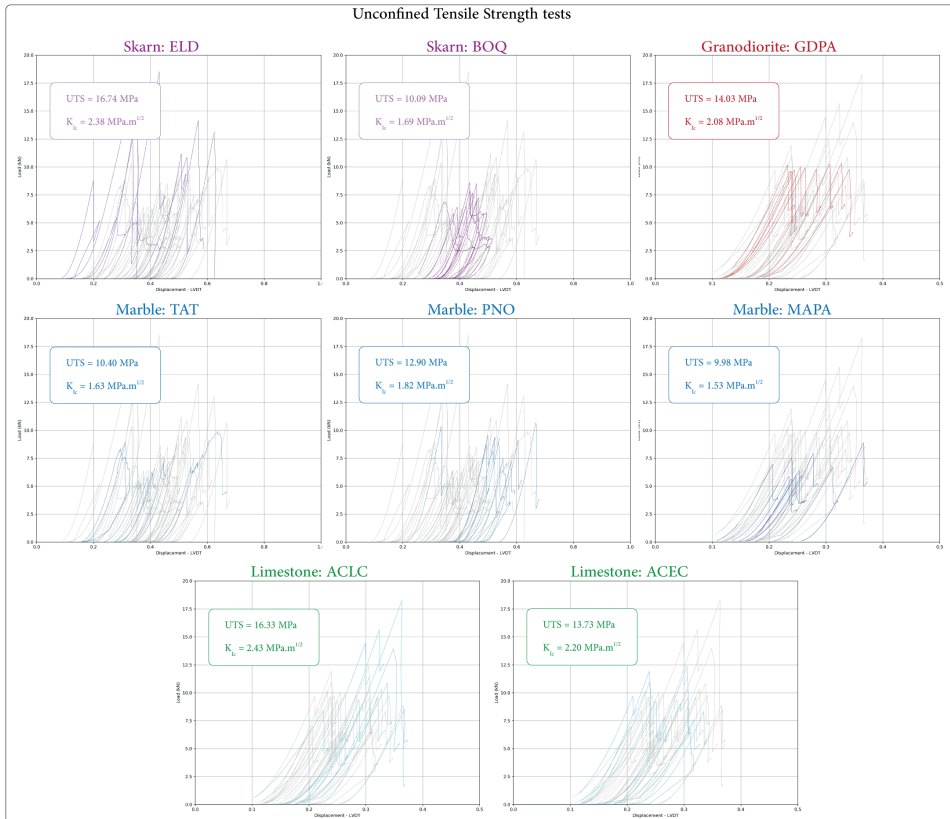


Figure 3.5 – Brazilian disc UTS test plots and results per outcrop ( $UTS$  standing for Ultimate Tensile Strength,  $K_{IC}$  for the fracture toughness).

Fracture toughness ( $K_{IC}$ ) is calculated following the method proposed by Guo et al. (1993). The results for both the tensile strength and the calculated fracture toughness are given in Figure 3.6.

BOQ	Tensile			Tensile			Tensile			Tensile	
	Strength (Mpa)	K1c (BOQ)	ELD	Strength (Mpa)	K1c (ELD)	PNO	Strength (Mpa)	K1c (PNO)	TAT	Strength (Mpa)	K1c (TAT)
BOQ-04	9.79	1.66	ELD-03	18.72	2.03	PNO-04	13.3	2.24	TAT-03	14.54	1.80
BOQ-05	11.25	1.96	ELD-04	20.14	2.95	PNO-05	13.19	1.79	TAT-04	10.35	1.63
BOQ-06	9.68	1.64	ELD-05	14.42	2.41	PNO-06	11.04	1.85	TAT-05	10.86	1.57
BOQ-07	11.72	2.04	ELD-06	14.84	1.91	PNO-07	10.58	1.76	TAT-06	7.82	1.33
BOQ-08	8.49	1.41	ELD-07	19.87	2.63	PNO-08	13.38	1.93	TAT-07	12.64	2.02
BOQ-09	8.47	1.48	ELD-08	12.44	2.13	PNO-09	9.3	1.51	TAT-08	11.36	1.95
BOQ-10	9.31	1.17	ELD-09	23.51	2.05	PNO-10	14.21	2.00	TAT-09	8.55	1.36
BOQ-11	11.1	1.90	ELD-10	20.97	2.33	PNO-11	13.19	1.68	TAT-10	9.46	1.56
BOQ-12	10.12	1.76	ELD-11	27.08	4.10	PNO-12	16.29	1.56	TAT-11	10.08	1.66
BOQ-13	10.96	1.86	ELD-12	7.31	1.22	PNO-13	14.47	1.85	TAT-12	8.41	1.40
<b>Avg</b>	<b>10.09</b>	<b>1.69</b>		<b>16.74</b>	<b>2.38</b>		<b>12.90</b>	<b>1.82</b>		<b>10.41</b>	<b>1.63</b>
04ACEC	Tensile			Tensile			Tensile			Tensile	
	Strength (Mpa)	K1c (04ACEC)	14ACLC	Strength (Mpa)	K1c (14ACLC)	MAPA	Strength (Mpa)	K1c (MAPA)	GDPA	Strength (Mpa)	K1c (GDPA)
04ACEC-003	14.62	2.51	14ACLC-005	12.93	2.25	MAPA-001	8.75	1.27	GDPA-001	13.62	1.90
04ACEC-004	13.3	2.15	14ACLC-006	11.9	1.75	MAPA-002	9.1	1.58	GDPA-002	14.24	1.93
04ACEC-005	11.19	1.96	14ACLC-007	19.33	3.04	MAPA-003	8.88	1.36	GDPA-003	13.57	2.14
04ACEC-006	10.21	1.71	14ACLC-008	11.57	1.69	MAPA-004	12.5	1.80	GDPA-004	14.83	2.07
04ACEC-007	17.54	2.49	14ACLC-009	15.15	2.19	MAPA-005	10.17	1.72	GDPA-005	13.35	2.14
04ACEC-008	NA	NA	14ACLC-010	22.43	3.69	MAPA-006	12.42	1.76	GDPA-006	14.2	2.13
04ACEC-009	12.79	2.13	14ACLC-011	25.86	3.07	MAPA-007	8.4	1.42	GDPA-007	14.63	2.26
04ACEC-010	11.8	1.84	14ACLC-012	13.71	1.86	MAPA-008	10.81	1.76	GDPA-008	14.19	2.40
04ACEC-011	16.6	2.47	14ACLC-013	20.55	3.09	MAPA-009	8.48	1.24	GDPA-009	14.21	1.72
04ACEC-012	15.48	2.53	14ACLC-014	9.86	1.69	MAPA-010	10.24	1.42	GDPA-010	13.5	2.06
<b>Avg</b>	<b>13.73</b>	<b>2.20</b>		<b>15.62</b>	<b>2.43</b>		<b>9.98</b>	<b>1.53</b>		<b>14.03</b>	<b>2.08</b>

Figure 3.6 – Tensile strength and Fracture Toughness values measured and calculated from Unconfined Tensile Strength tests



### 3.2.5. CHEVRON BEND TEST

Chevron Bend tests were run in the Geoscience & Engineering Laboratory of the Civil Engineering and Geosciences department of Delft University of Technology. The apparatus is a uni-axial stress/strain device, with a capacity 50 kN. The Chevron Bend test is used to measure the fracture toughness ( $K_{IC}$ ). The method employed has been realized in accordance with the "Suggested methods for determining the fracture toughness of rock", by International Society for Rock Mechanics, ISRM 1988. The procedure consists of two steps (called *Levels*):

1. Direct loading to failure to measure ( $K_{IC}$ ) at Level I;
2. Cyclic loading to calculate the correction to assign on ( $K_{IC}$ ) at Level I and obtain ( $K_{IC}^c$ ) at Level II

The current analysis is based on 12 experiments, with 6 cores per outcrop: Granodiorite and Marble. Each core has been cut to the dimensions of: length: 200mm; diameter: 50mm. Results of the tests are given in Figure 3.7

MAPA	$K_{Ic}$ (MAPA)	$K_{Ic}$ (MAPA) · $K_{Ic}^c$ (MAPA)		GDPA	$K_{Ic}$ (GDPA)	$K_{Ic}$ (GDPA) · $K_{Ic}^c$ (GDPA)	
	-BraDisc-	Chevron- Level I	-Chevron- Level II		-BraDisc-	Chevron- Level I	-Chevron- Level II
MAPA-001	1,26	1,41		GDPA-001	1,91	2,23	
MAPA-002	1,58		1,61	GDPA-002	1,94		2,36
MAPA-003	1,36		2,46	GDPA-003	2,13		2,78
MAPA-004	1,80		1,73	GDPA-004	2,07		
MAPA-005	1,72		1,60	GDPA-005	2,12		2,08
MAPA-006	1,76			GDPA-006	2,13		
MAPA-007	1,42			GDPA-007	2,24		
MAPA-008	1,76			GDPA-008	2,40		
MAPA-009	1,24			GDPA-009	1,79		
MAPA-010	1,42			GDPA-010	2,07		
AVG	1,53	1,41	1,85		2,08	2,23	2,41

Figure 3.7 – Fracture Toughness values measured from Chevron Bend Tests

### 3.2.6. HYDRAULIC FRACTURING TEST USING THE HOEK CELL

This hydraulic Fracturing (HF) test is not yet described in any official procedure. The intention of this test is to observe the hydraulic fracture behavior under the injection of a pressurized fluid. The set-up still lack sensors to thoroughly control the entire process. The test already tells the stimulated fracture shape (which can be observed with a micro-CT scan), and the fluid pressure at which the sample under confining pressure starts failing. The HF tests were run in the Geoscience & Engineering Laboratory of the Civil Engineering and Geosciences department of Delft University of Technology. As this test is experimental, there is no referenced certified documentation describing the protocol.

The setup used is described in Figure 3.8. The method consists of increasing the fluid pressure from a fluid pump, and wait for sensors to record any change in sample geometry (axial displacement), or in the fluid flow circulation. The apparatus is a uni-axial stress/strain device, with a capacity 500 kN, used together with the Hoek Cell apparatus, which allows to apply the confining pressure around the tested sample. Axial displacement is recorded using two vertical sensors, axial LVDTs. As the sample is placed in the Hoek cell, radial displacement cannot be recorded. Each core has been cut to the dimensions of: length: 60mm ; diameter: 30mm. The sample is pre-drilled in its bottom edge. the drilled hole dimensions are: diameter: 3.2mm, depth: 4mm. Pre-drilling the sample helps avoiding fluid leakage along hoek cell sleeves by concentrating the injected fluid in the notch. A piston and o-rings connect the flow line to the sample notched-edge. A pressure gauge is placed along the flow line between the fluid pump and the piston.

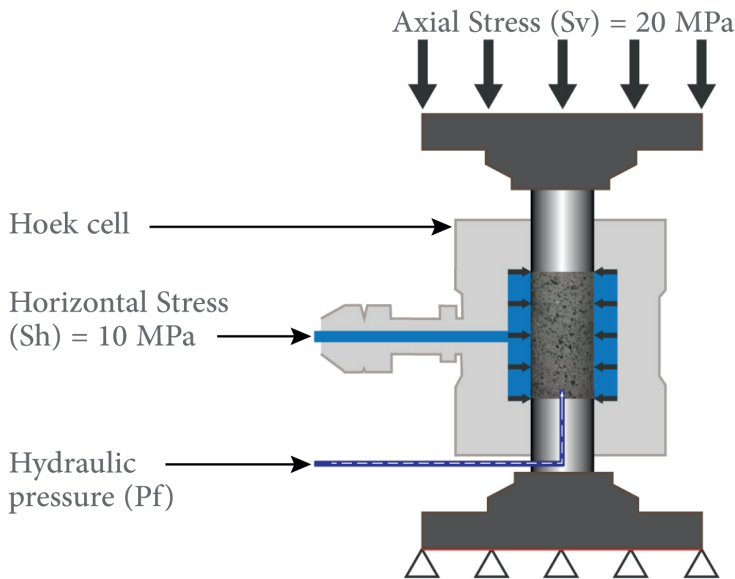


Figure 3.8 – Experimental set-up for the Hydraulic fracturing using the Hoek cell

Qualitative and quantitative results of this experiment are given in Figure 3.9.

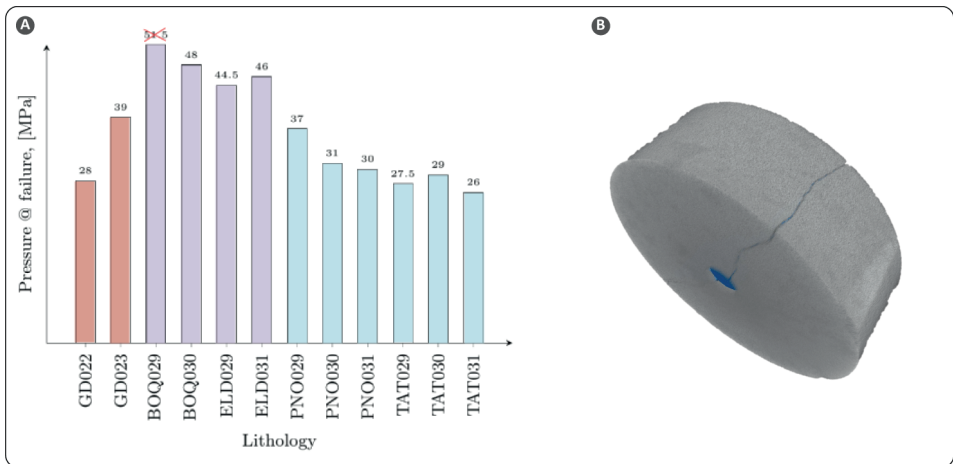


Figure 3.9 – Hoek cell hydraulic fracturing experiment results: A) fluid pressure reached at sample failure; B)  $\mu$ -CT-Scan image of a hydraulically fractured marble sample (image analyzed with Avizo<sup>TM</sup> software)

### 3.3. DISCUSSION OF THE RESULTS

Experimental works are used to characterize the rock properties quantitatively, in the aim of populating numerical models, which are used to predict the hydraulic fracture propagation and thermal-fluid flow reservoir properties.

The chemical and mineral analyses confirm the lithological descriptions by identifying the mineral components composing the samples. The analyses results confirmed the expected rock compositions. The main information obtained concerns the Skarns, as we distinguish endo- versus exo-skarns. The chemical composition confirms this distinction, as the endo-skarn is essentially composed of iron oxides, where the exo-skarn also contains silicates, inherited from the carbonates.

Porosity and permeability measurements show extremely low values as expected from the well tests. What is more surprising here is that the Limestones are showing the lowest permeability, is somewhat counter-intuitive, because limestones are usually expected to have fair reservoir properties. One possible explanation is that the pores of these limestones are filled with recrystallized material due to alteration or weathering.

UCS tests show a high heterogeneity from one lithology to the other but also within the same lithological units (i.e. ELD or ACEC). These strength differences reflect heterogeneities in the rock matrix and lithological units (such as differences between ELD and BOQ), which is important to consider when populating numerical models and when interpreting the results.

UTS and especially the values for fracture toughness are really important for hydraulic fracture modeling. In Figure 3.10, we look at the matching of the fracture toughness determined with UTS or Chevron bend test approach. The Chevron bend test approach is known for being more accurate but is also much more expensive (especially in term of material volume required for the experiment). The results from both experiments are fairly matching, even though a slight offset appears. Therefore, we decided to calibrate the UTS measurements to best-fit the Chevron bend test values for the numerical model inputs. All results and the fracture toughness correction factor are given in Figure 3.11.

The limitation of the measurements performed here is that they were done at an ambient temperature and pressure (with the exception of the HF test). It would be interesting to investigate the influence of confining pressure and temperature on the mechanical properties. Liverpool University for instance, specialized in Volcanology and rock mechanics, has equipment combining UCS, UTS with furnaces able to reach until 500 °C.

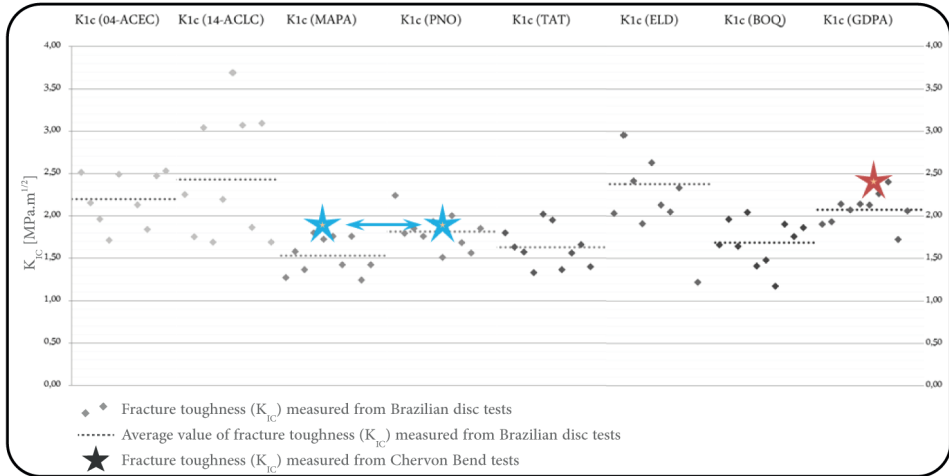


Figure 3.10 – ( $K_{IC}$ ) plots: Grey diamonds represents  $K_{IC}$  values derived from UTS tests; Grey dashed-line show the average value per rock sample; Blue and red stars show  $K_{IC}$  values measured with the Chevron Bend tests for Pueblo Nuevo Marbles and Granodiorites respectively

Formation	$\phi$ [-]	K [1/m <sup>2</sup> ]	E [GPa]	$\nu$ [-]	UCS [MPa]	UTS [MPa]	HF [MPa]	K1c_BrazD [MPa.m <sup>1/2</sup> ]	K1c_Chvr [MPa.m <sup>1/2</sup> ]	K1c_Normalized [MPa.m <sup>1/2</sup> ]	Gc [J/m <sup>2</sup> ]
Lm (LC)	0.02	1.00E-20	37.825	0.31	85.63	16.329		2.432		2.76	201.44
Lm (EC)	0.03	1.00E-20	37.905	0.225	168.67	13.73		2.198		2.49	164.19
<b>Limestone (AVG)</b>	<b>0.03</b>	<b>0.00</b>	<b>37.87</b>	<b>0.27</b>	<b>127.15</b>	<b>15.03</b>		<b>2.32</b>		<b>2.63</b>	<b>182.33</b>
Marble (PNO)	0.02	6.48E-19	46.756	0.252	121.074	11.435	32.666	1.675	1.85	1.90	77.30
Marble (Tat)	0.03	1.25E-18	51.61	0.29	173.065	10.407	27.5	1.628		1.85	66.16
<b>Marble (AVG)</b>	<b>0.03</b>	<b>9.49E-19</b>	<b>49.18</b>	<b>0.27</b>	<b>147.07</b>	<b>10.92</b>	<b>30.08</b>	<b>1.65</b>	<b>1.85</b>	<b>1.87</b>	<b>71.44</b>
Skarn (Eld)	0.03	1.51E-19	56.97	0.105	153.75	16.74	45.5	2.376		2.70	127.66
Skarn (Boq)	0.12	5.23E-16	41.10	0.16	85.45	10.089	47.50	1.69		1.92	89.31
<b>Skarn (AVG)</b>	<b>0.08</b>	<b>2.62E-16</b>	<b>49.04</b>	<b>0.13</b>	<b>119.60</b>	<b>13.41</b>	<b>46.50</b>	<b>2.03</b>		<b>2.31</b>	<b>108.48</b>
Granodiorite	0.03	1.25E-18	42.7933	0.3533	171.606	14.034	33.5	2.075	2.406	2.36	129.61

*(K1c\_Normalized = [K1c\_brazD \* 1.135])*

Figure 3.11 – Laboratory experiment results summarizing measured mechanical properties for the Limestones, Marbles, Skarns and Granodiorites

### 3.4. CONCLUSION

Enhanced Geothermal Systems stimulation prediction is strongly related to the rock mechanical properties. This set of laboratory analyses gives a detailed characterization of the rock formations evaluated for the Acoculco EGS project. The experiments covers from the micro-meters with XRF & XRD measurements, to the core sample size scale. The conclusions of these measurements are: currently, none of the tested formations present sufficient permeability to allow natural fluid circulation. To evaluate the Acoculco EGS stimulation feasibility, we compare the mechanical properties of each considered formations: the limestones, the marbles, the skarns and the granodiorite. The first conclusion is that the marble has the lowest fracture toughness and is therefore the easiest formation to stimulate. As seen on UCS and UTS experiments, marbles show more consistent results than limestones or skarns, and are thereby more reliable when building predictive models. According to this experimental work only, the EGS would be easier to stimulate in the marble formation at the Acoculco geothermal site.



# 4

## THERMO-HYDRO-PSEUDO-MECHANICAL FLOW MODEL, IN FRACTURED RESERVOIR

*The use and exploitation of subsurface resources require prior knowledge of fluid flow through fracture networks. For nuclear waste disposal, for the enhancement of hydrocarbon recovery from a field, or the development of an enhanced geothermal system (EGS), it is fundamental to constrain the fractures and the fracture network. This chapter presents a model for fracture flow permeability and stress dependency simulation applied to multi-reservoirs, multi-production scenarios analysis. This study is part of the GEMex project, an international collaboration of two consortia, one from Europe and one from Mexico. The research is based on exploration, characterization and assessment of two geothermal systems located in the Trans-Mexican volcanic belt, Los Humeros and Acoculco. In Acoculco, two wells reached very high temperatures, but did not find any fluids. For that reason, the Acoculco Caldera is foreseen as an EGS development site, hoping to connect existing wells to a productive zone. This implies that the fluid flow through the geothermal reservoir would be mainly fracture-dominated. This study investigates the dependency of fracture permeability, constrained by fracture lengths and apertures, with stress field conditions. Simulations are computed in 2D, using COMSOL Multiphysics® Finite Elements Method Software, populated with mechanical data obtained in the rock physics laboratory and with dense discrete fracture networks generated from 1D scanline surveys measured in Las Minas analogue outcrops for Acoculco reservoir. The method offers a prediction for multiple scenarios of the reservoir flow characteristics which could be a major improvement in the development of the EGS technology.*



## 4.1. INTRODUCTION

### 4.1.1. BACKGROUND

The understanding of fractures is crucial for several subsurface activities such as Oil and Gas, nuclear waste disposal, Enhanced Geothermal System or CO<sub>2</sub> sequestration (Fox et al., 2015). In the case of fluid flow circulation, fractures can act either as flow boundaries or fluid pathways.

The first general question here is to evaluate to what extent fractures in subsurface can be characterized. Two main methods are commonly used to predict the impact of the fractures: one method is using a Discrete Fracture Model (DFM) and the second method is using a continuum described as the Representative Volume Element (RVE) (Geiger and Matthäi, 2012; Surrrette, 2006). In the first case, using DFM, all fractures are explicitly described as boundary elements. Therefore, a DFM model simulates the geometry of real fractures and is a closer representation of reality (Li et al., 2013). Computationally, handling a DFM drastically increases the number of elements and the complexity in the mesh. Because of that, the calculation takes longer to converge to a solution (Garipov et al., 2016; Zhang et al., 2007). In the second case, using RVE consists of modeling the bulk impact of the fractures on the reservoir properties. These properties are averaged to represent the matrix and the fractures together in a continuum model (Flemisch et al., 2018; Singhal and Gupta, 2010; Surrrette, 2006; Dershowitz et al., 2004). Because working with DFM is computationally very expensive, it is more common to use the RVE approaches to model fluid flow through fractured media. However, working with DFM allows a higher level of details, such as separating fractures properties based on the structural fracture sets. Additionally, a DFM allows the coupling of the mechanical properties and stress field to the flow properties of the fracture network. The characterization of the fractures is therefore of utmost importance to the results.

### 4.1.2. STUDY CONTEXT

In this study a combination of a field study fracture characterization in Acoculco, with porosity, permeability, rock strength laboratory tests, stress field and coupled Thermal-Hydraulic (TH) modeling is carried out. A streamlined integration of a DFM generated from field data, mechanical rock properties of field samples measured in the rock physics laboratory, stress field data and simulation of a geothermal field production has not been presented before to the best of our knowledge.

This study is in the context of analyzing the feasibility of developing an Enhanced Geothermal System (EGS) in the Acoculco geothermal field, which is being studied within the GEMex project. Acoculco is located in the Trans-Mexican volcanic belt (TMVB), about 100 km northeast of Mexico City. Two exploration wells were drilled, EAC1 & EAC2, at about 500 m apart, in 1995 and 2008, respectively. Their lithological sequence is similar and can be summarized, as described by (Viggiano-Guerra et al., 2011; López-Hernández et al., 2009), in table 4.1 :

The carbonate section regroups from dolomitic Limestones, to carbonates metamorphosed into marbles or metasomatized into Skarns due to the intrusion of a granodioritic pluton. Acoculco lithological reservoir section is composed of Limestones, marbles and Skarns. The main assumption here is that these reservoirs are not permeable because the

Lithology	EAC1 well-marker depth	EAC2 well-marker depth
Volcano-clastic deposits	0 to 830m MD	0 to 340m MD
Carbonates section	830 to 1650m MD	340 to 1580m MD
Granodiorite – Granite	1650 to 2000m MD (TD)	1580 to 1900m MD (TD)

Table 4.1 – Lithology from EAC 1 and EAC 2 well-markers (Abbreviations: Measured Depth (MD) and Total Depth (TD))

fractures are not connected enough to allow a meaningful production of fluid through the fractures. The problem is then to quantify the role of the fractures for these three formations. This implies an understanding of the fracture properties in term of mechanics and their impact regarding the fluid circulation (i.e. determining whether fractures behave as fluid barriers or fluid pathways). How are fractures spatially distributed in the formation? How are these fractures connected? To what extent does the stress field deform the aperture of the fracture (DAF), and therefore, how much does it influence the fracture permeability?

#### 4.1.3. INNOVATION

To answer this question, we propose a numerical method to calculate the fluid flow and heat exchange in a fracture controlled reservoir. The models are built using real data from the field. The Discrete Fracture Models (DFMs) are obtained from scanline surveys measured in the field on Las Minas analogue outcrops, and processed using the SkaPy script and then extrapolated using the multiple point statistic method as presented in Bruna et al. (2019). The rock properties have been measured in the rock physics laboratory on rocks sampled on the analogue outcrops of Las Minas. The numerical model runs two studies: i) a static analysis measuring the influence of the stress field on the fracture aperture; ii) a transient analysis which couples fluid flow in porous media and thermal exchange through the discrete fracture models (DFMs). Because Acoculco reservoir is composed of Limestone, Marble and Skarn, a comparison is made between these three formations. Therefore, we created three models representing the three formations. Each formation is populated with its own mechanical properties and its own DFM.

The main innovations of this study are to cover a geothermal doublet reservoir scale of  $600 \times 600\text{m}$ , with a very dense fracture system, with an amount of tens of thousands of fractures (exact amount is given in Table 4.2), and material properties with very low rock matrix permeability (model populated with a matrix permeability of  $1 \times 10^{-17} \text{m}^2$ ). The second innovation concerns the method implemented to be able to use these real field data. We solve this problem by looking at 2D (xy) models, then we solve the mechanical part in a steady state study. Then, we calculate the fluid flow and thermal exchange using the Deformed Aperture Fracture (DAF) from the steady state study. Finally, a field development perspective is applied by simulating production over 100 years. For that purpose, the model is implemented in multiple reservoir geometries and multiple wells positioning. This method helps to evaluate which formation, and more precisely, which part of each formation, is best suited for the development of an EGS. For each of the three analyzed reservoirs, four development scenarios are considered. Acoculco case study is

given to illustrate our results.

This multi-scenario model is simulated using the COMSOL Multiphysics software for Finite Elements Method (FEM) analysis. All data are freely available on: [https://github.com/BatLep/Sim\\_THM\\_Multi\\_Res-Sc.git](https://github.com/BatLep/Sim_THM_Multi_Res-Sc.git).

## 4.2. METHODS: SIMULATION MODEL IMPLEMENTATION

### 4.2.1. GENERAL IMPLEMENTATION

Assuming a 2D horizontal domain  $\mathbf{D}$ , composed of the rock matrix defining a first sub-domain  $\Omega$ , and several fractures that all together constitute a second sub-domain  $\Gamma$ , such as  $\mathbf{D} = \{\Omega + \Gamma\}$ . The solid mechanics for 2D plane stress and plane strain, the sub-surface fluid flow in porous media and the heat transfer are solved by using the Finite Elements Method (FEM), implemented in the COMSOL Multiphysics<sup>®</sup> software. The simulation computes two studies: the first one is steady state and solves the solid mechanics; the second one is transient and solves the fluid flow and thermal exchange. The time-dependent solver used the implicit Backward Differentiation Formula (BDF), and especially the Backward Euler, where the fraction of the initial step is set at 0.001. The rock matrix sub-domain  $\Omega$ , and the linear elements for fractures in 2D model sub-domain  $\Gamma$  are discretized into triangular elements following a conform mesh which honors the geometrical characteristics of the fracture system as defined by Flemisch et al. (2018). The fractures are modeled as “single layers material” (zero thickness) to which specific material properties are applied, independently of the rock matrix  $\Omega$  material properties. Boundary conditions are applied to the outer boundaries of the domain  $\mathbf{D}$  such that no displacement is allowed, but thermal transfer and fluid flow is free along these edges. Injection and production of fluid from the well bores are idealized as points and placed on a fracture for calculation simplicity.

### 4.2.2. GOVERNING EQUATIONS

#### STUDY 1: SOLID MECHANICS, STEADY STATE

For the solid mechanics analysis, the physical descriptions are based on the laws for the balance of forces and the constitutive relations that relate the stresses to strains (Jaeger et al., 2007; Zoback, 2007; Fossen, 2013). In this study, a relation between the fluid flow and the stress field is induced by using the fracture aperture. The effect of fracture slippage and shearing and consequently its influence of fracture permeability is not considered in this study. The stress field acts as a load on the fracture aperture. The Deformed aperture of the Fracture (DAF) follows the linear elasticity behavior of a spring as described with the constitutive relation of the Hooke's law as:

$$f_s = -K(u - u_0) \quad (4.1)$$

where  $f_s$  is a force/unit area,  $u$  is the displacement deforming the spring, and  $K$  is the stiffness matrix.  $u_0$  is an optional offset, which describes the stress-free state of the spring. As in the case of analyzing the fracture elasticity, the stiffness is a function of the fracture material properties and the fracture width (aperture)  $d_f$ . The stiffness in the

normal direction is computed based on a state of plane strain, so that:

$$k_n = \frac{E(1 - \nu)}{d_f(1 + \nu)(1 - \nu)} \quad (4.2)$$

where  $k_n$  is the normal stiffness (or spring constant),  $E$  the Young's modulus and  $\nu$  the Poisson's ratio. The assumption of plane strain conditions is relevant when the material of the elastic layer (in this case the fracture material), is softer than its surroundings (in this case the rock matrix).

The regional stress field is then assigned by creating a second reference system defined by the principal stress vector system. Using the solid mechanics physics analysis, initial stresses and strains are assigned to the whole domain  $D$  as the far field stress  $S$ , with:

$$S = \begin{bmatrix} S_{Hmax} & 0 & 0 \\ 0 & S_{hmin} & 0 \\ 0 & 0 & S_v \end{bmatrix} \quad (4.3)$$

where  $S_{Hmax}$  is the maximum horizontal stress,  $S_{hmin}$  is the minimum horizontal stress,  $S_v$  is the vertical stress and  $S$  the stress tensor.

#### STUDY 2: COUPLED SUBSURFACE FLOW AND THERMAL EXCHANGE, TRANSIENT

The second study is a transient analysis simulating over 100 years. The heat transfer is coupled to the subsurface fluid flow. In fluid flow, heat transfer, and mass transfer, the simulations are solved based on the laws for conservation of momentum, mass, and energy. The mass transfer is governed by Darcy's law, and heat transfer is governed by Fourier's law of heat conduction. As the fluid flow in the reservoir is mainly controlled by the fractures, a distinction can be made between the fracture permeability  $k_f$  and the inter-granular rock matrix permeability  $k_m$ . The fracture permeability is calculated using the Cubic law (Snow, 1969; Zhang et al., 2007; Singhal and Gupta, 2010), as:

$$k_f = \frac{d_f^2}{12} \quad (4.4)$$

where  $k_f$  is the fracture permeability and  $d_f$  is the aperture of the fracture.

### 4.2.3. MODEL SCENARIOS

The model is built with a core frame that can be populated with different properties based on conditionals. Hence, this model handles multi-analyses of multiple formations with multiple well positioning scenarios.

## 4.3. APPLICATION: FIELD EXAMPLE

### 4.3.1. INPUT DATA, AND DOMAIN DELIMITATION

#### $\Omega$ , MATRIX MATERIAL PROPERTIES

Determination of the material properties were measured in the Geoscience and Engineering Laboratory of the Civil Engineering and Geosciences department of Delft University of Technology. All tests have been run on sample taken from the analogue outcrops of Las Minas. All the method for rock measurements is presented in Chapter 3. All parameters used as input in the model are given in table 4.3.

### Γ, THE DFMS

The fractures are implemented in the model using existing DFMs. The fractures were measured in the field using the linear scanline reporting method on several outcrops. The trace of the scanline survey follows the direction of the outcrop walls, offering to capture different angles, hence a better prediction of the fracture distribution. The scanline surveys are then processed using the SkaPy<sup>1</sup> Python<sup>TM2</sup> script, together with the multiple point statistic method (Bruna et al., 2019), to extrapolate the fracture distributions into a larger spatial domain. As mentioned in 4.1.2, the reservoir formation of Acoculco geothermal site is composed of limestone, marble and skarn. Hence, each of these formations has its own DFM. These DFMs are separated in fractures sets based on their strike and dip values, related to the regional structural trends described in literature (Campos-Enriquez and Garduño-Monroy, 1987; López-Hernández et al., 2009; Carrasco Núñez et al., 2017; Norini et al., 2015). For each of the three formations treated here, we calculated the statistical distributions of the fracture apertures from our field measurements. As a result, we obtain for each formation, and for each fracture set, one specific aperture value. All these DFMs represent a 2D horizontal plane covering  $600 \times 600$  m. These DFMs represents the spectrum of fracture distributions in between the two outcrops measured with the scanline surveys for each rock type. Therefore, the domain of  $(600 \times 600)\text{m}^2$  is divided into three equivalent sub-domains of  $(200 \times 600)\text{m}^2$ . The first sub-domain is populated using scanline survey dataset, the second with the other dataset and the third, in the middle is populated with the calculated interpolation. This explains why west and east parts of the domain present different fracture distributions.

More detail is given in table 4.2 regarding the quantity of fractures per set and the value given for their aperture.

Fracture Set	Limestone		Marble		Skarn	
	<i>Amount</i>	<i>Ap. [cm]</i>	<i>Amount</i>	<i>Ap. [cm]</i>	<i>Amount</i>	<i>Ap. [cm]</i>
Set 1	12970	0.55	36	0.1	353	0.01
Set 2	4762	1.55	862	0.1	8073	0.01
Set 3	466	2	4882	0.01	3555	0.01
Set 4	2995	1.5	-	-	3181	0.01
Set 5	3921	2	482	0.1	3431	0.01
Set 6	139	0.68	3008	1	24	0.14
Set 7	4447	1.55	-	-	366	0.05
Total	29700	-	9270	-	18983	-

Table 4.2 – Fracture numbers, and initial apertures (Ap.) per Fracture sets and per formation

These values of aperture corresponds to the fracture aperture at the surface, measured at the outcrop. To correct the aperture of the fractures at the reservoir depth, we apply stress dependency to the fracture aperture. This correction first requires an esti-

<sup>1</sup><https://github.com/BatLep/SkaPy.git>

<sup>2</sup>Python Software Foundation (2019)

mation of the mechanical properties of these fractures. The aperture  $d_f$  is a function of the spring constant  $k_n$ , itself a function of the Young's modulus  $E$  and the Poisson's ratio  $\nu$ . According to Jeanne et al. (2017); Rutqvist et al. (1998), the following can be safely used:

$$\begin{aligned} E_{fracture} &= 0.1E_{matrix} \\ \nu_{fracture} &= 0.4\nu_{matrix} \end{aligned} \quad (4.5)$$

### 4.3.2. STRESS FIELD

The stress field conditions are constrained using the World Stress Map (Heidbach et al., 2016), with two data points, at stations (19,79;-98,47) and (19,97;-98,63) from "drilling induced fractures", about 40 km away from the wells. Both stations indicate a normal fault stress regime, and giving an average maximum horizontal stress  $S_{Hmax}$  of azimuth N55°. Vertical stress is estimated to be hydrostatic according to  $S_v = \rho gz$ . Being in a normal stress regime,  $S_v > S_{Hmax} > S_{hmin}$ .

### 4.3.3. PROBLEM DEFINITION AND SIMULATION IMPLEMENTATION

In this study we analyze three potential reservoirs, here named the Limestone, the Marble and the Skarn formations. Each of these formation is modeled using a rock matrix domain  $\Omega$  populated using its own mechanical parameters. For each of these formations, a specific DFM is implemented and discretized. As these DFMs are varying spatially, we want to analyze their influence on production performances. Therefore, we simulate four scenarios of well doublets located at different parts of the domain  $\mathbf{D}$ . The model implementation is summarized in Figure 4.1.

## 4.4. RESULTS

### 4.4.1. APERTURE DEPENDENCY TO THE STRESS FIELD

When assigning the stress field to the material we expect to see the fracture width (aperture) decreasing depending on the orientation of the fracture compare to the direction of the stress field. Figure 4.2 gives the orientation of the seven fracture sets considered in this study. In the Acoculco area, as mentioned in section 4.3, the stress field is oriented N55°. Therefore, the fracture sets F2 and F5 are expected to be the most affected by a decrease in aperture, while the fracture sets F1 and F7 should experience less deformation.

In Figure 4.3 we compare the fracture sets deformation (from initial aperture measured at the outcrop, corresponding to 100%) with using two different stress field orientations: in the first case, we are using the Acoculco N55°; in the second case, we are using an East-West direction (N90°). The use of this East-West stress field is only meant to emphasize the aperture dependency to stress and observe the influence of stress field direction on the calculated DAF. The plots represent, for each formation, the percentage of aperture deformation. The results confirm the above mentioned expectation: in all the formations, when assigning a N55° stress field, the fracture sets F2 and F5 are the most deformed and F1 and F7 the least. Similarly, when using the N90° stress field orientation, the sets F3, F5 are the most deformed and F1, F6, F7 the least.

Description	Parameter	Value	
Domain	Thickness of the model (pseudo-3D)	10 m	
	Reservoir depth	-2000 m	
	Pressure initial	20 MPa	
	Flow rate - Per 10m Thickness	0.1 m <sup>3</sup> /s	
	Temperature initial	300 °C	
	Temperature at injection	50 °C	
	Vertical stress, $S_v$	50 MPa	
Material	Maximum horizontal stress, $S_{Hmax}$	40 MPa	
	Minimum horizontal stress, $S_{Hmin}$	30 MPa	
	Matrix permeability	$1 \times 10^{-17}$ m <sup>2</sup>	
	Matrix porosity	0.1	
	Matrix density	2700 kg/m <sup>3</sup>	
	Fracture porosity	0.5	
	Fracture density	Matrix density	
	Fracture heat capacity	828 J kg <sup>-1</sup> K <sup>-1</sup>	
	Fracture heat conductivity	3 W m <sup>-1</sup> K <sup>-1</sup>	
	Matrix heat capacity	828 J kg <sup>-1</sup> K <sup>-1</sup>	
	Matrix heat conductivity	3 W m <sup>-1</sup> K <sup>-1</sup>	
	Poisson ratio, $nu_{limestone}$	0.26	
	Poisson ratio, $nu_{marble}$	0.27	
	Poisson ratio, $nu_{skarn}$	0.13	
	Young's modulus, $E_{limestone}$	$38 \times 10^9$ GPa	
	Young's modulus, $E_{marble}$	$49 \times 10^9$ GPa	
	Young's modulus, $E_{skarn}$	$49 \times 10^9$ GPa	
	Bulk Modulus matrix	$E_{matrix} \times (3(1 - 2nu))$	
	Fluid	Fluid Compressibility	$2 \times 10^9$ Pa
		Density of fluid	1000 kg/m <sup>3</sup>
Dynamic Viscosity of Water @ 20degC		$1.00 \times 10^{-3}$ Pa s <sup>-1</sup>	
Dynamic Viscosity of Water @ 300degC		$8.58 \times 10^{-5}$ Pa s <sup>-1</sup>	

Table 4.3 – Input parameters for simulation

#### 4.4.2. PRODUCTION SCENARIOS

In this part the field production performance based on spatial well positioning is analyzed. Due to the fact that DFMs are not homogeneous (fig. 4.1) the positioning of the wells can have a significant impact on the production. For instance, the fracture density is much higher on the western part of the DFMs, especially for the Limestone and Marble formations. Because of that, one would expect a higher fracture connectivity, and therefore a higher bulk permeability. Here the performance is evaluated as the estimated fluid flow between the two wells, injection and production. As the in-flow and out-flow at the wells, are constrained by the boundary conditions of the model, we look at the lowest  $\Delta P$  as a representation of the best flow. As a consequence, the scenario 1 would be expected to have the best performance. Because the scenario 4 implies a fluid cir-

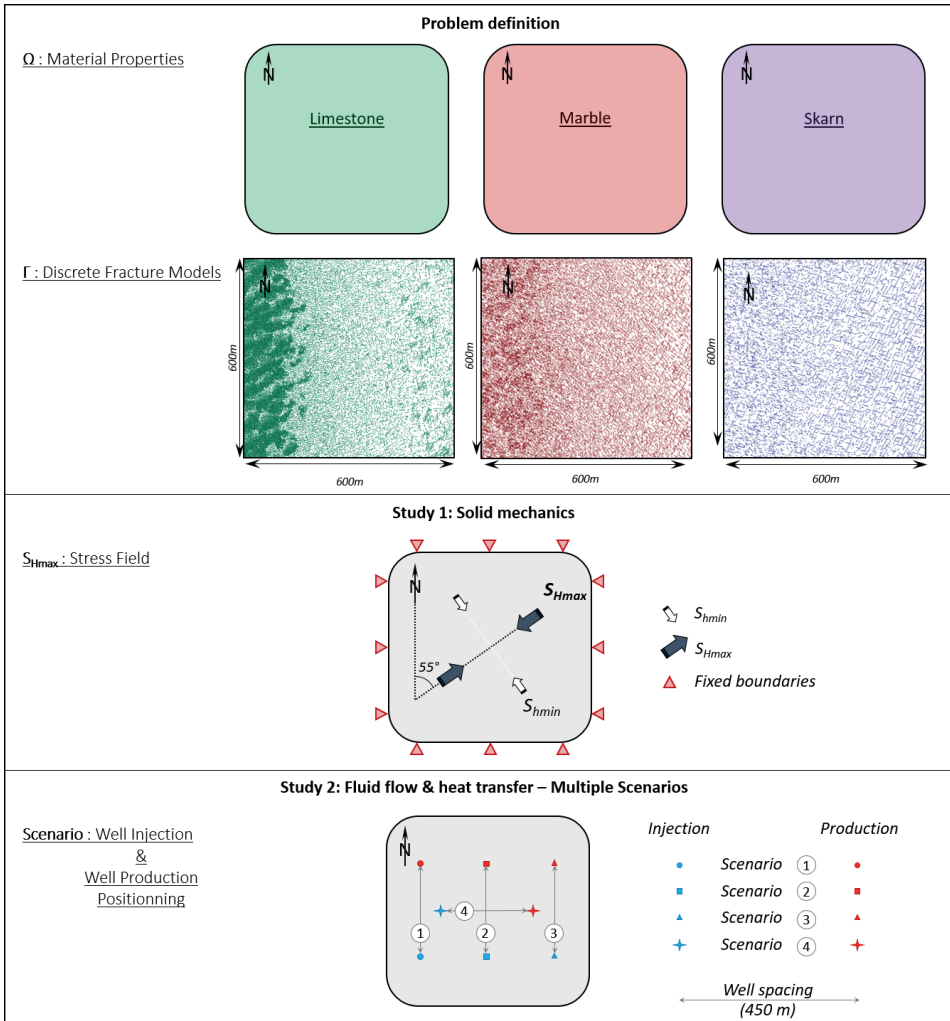


Figure 4.1 – Model implementation (from top to bottom):  $\Omega$ , the material properties;  $\Gamma$ , the DFMs; assignment of the stress field; well production scenarios

culatation across the fracture density variation, we would expect a medium performance compare to the others. The first result to observe on Figure 4.4 is that the well positioning scenario 4 results in a medium performance compared to the other three scenarios. The second information is that the scenario 1 in the Limestone formation gives a good performance, as expected. However, this in not the case in the Marble formation even though the fracture density is higher in the western part. Referring back to the Marble DFM (fig. 4.1); even though the fracture density is lower on the eastern part, the fracture length is higher and therefore the degree to which these fractures are connected is much higher. This explains why the scenario 3, in both the Marble and the Skarn, has the best



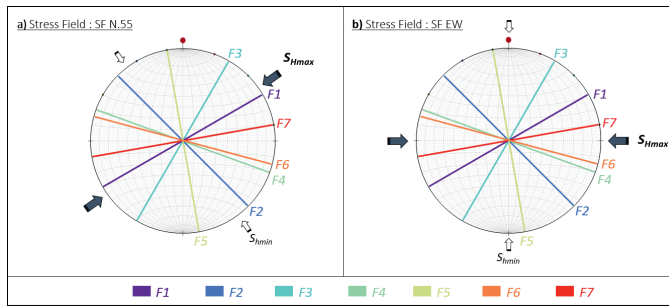


Figure 4.2 – Stress field orientation and fracture sets: a) stress field where  $S_{Hmax}$  is N55°; b) stress field where  $S_{Hmax}$  is N90°

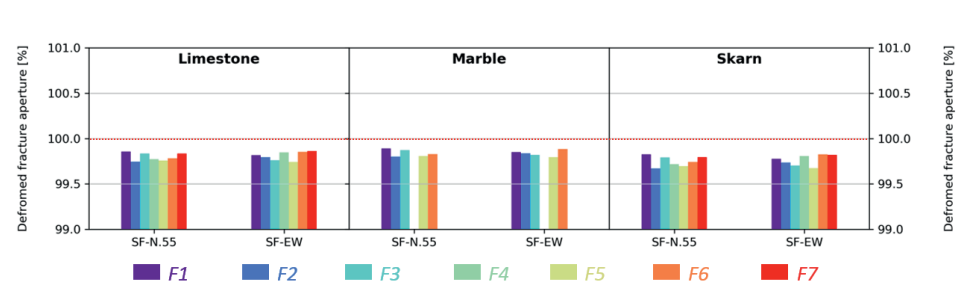


Figure 4.3 – Fracture aperture deformation, for each fracture sets, in: a) the Limestone formation; b) the Marble formation; c) the Skarn formation (The vertical scale shows the deformation as a percentage. Fractures sets F4 and F7 are not present in the marble formation).

performance in terms of required  $\Delta P$ .

#### 4.4.3. HEAT TRANSFER

Looking at the heat transfer (fig. 4.5), a few observations can be made: i) despite the high fracture density and the permeability trends created by the fractures, the thermal front is circular, hence homogeneous. This can be explained by the poor continuity and connectivity of the fractures. ii) However, even though the fractures ( $\Gamma$ ) are not creating a continuous fluid pathway, they are always showing lower temperatures than the matrix ( $\Omega$ ). This confirms that the fluid flow propagates quicker in the fractures, and hence corroborates higher permeability in the fractures. iii) Considering the implemented conditions of pumping flow rate and the resulting bulk permeability of the reservoir: for this example of the Limestone, the injected fluid, pure water at 50 °C, needs a hundred meters to reach the initial reservoir temperature of 300 °C.

## 4.5. DISCUSSION

In this study, we relate the fluid flow and the stress field by calculating the deformation on the fracture aperture. The Deformed aperture of the Fracture (DAF) follows

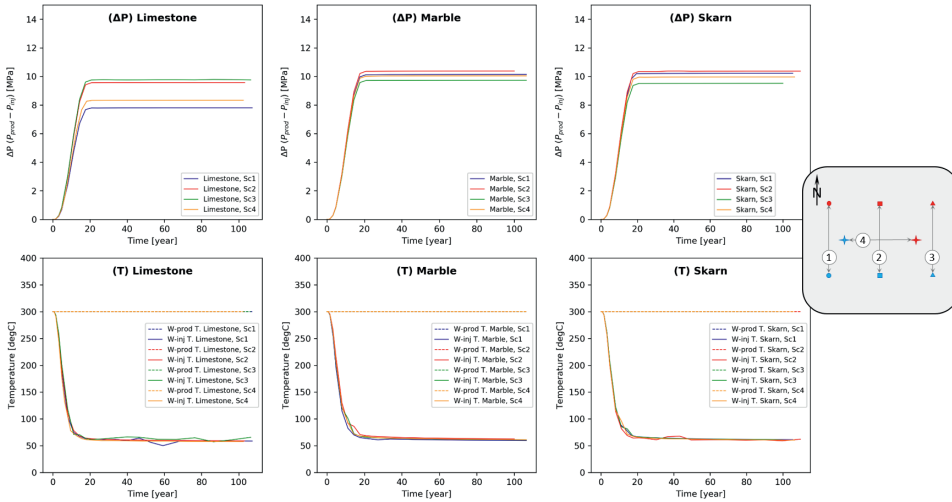


Figure 4.4 – Pressure ( $\Delta P = W_{prod} - W_{inj}$ ) and temperature profiles probed near injection and production wells, for different injection scenarios (Sc1-Sc4), using Acoaculco local stress field (N.55).

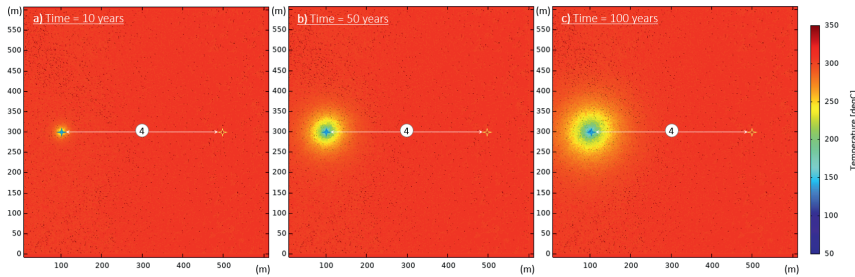


Figure 4.5 – Map view model of heat transfer over time in the Limestone formation, with well scenario 4; a) time=10 years; b) time=50 years; c) time=100 years

the linear elasticity behavior of a spring as described with the Hooke's law. Therefore, the DAF is directly related to the spring constant  $k_n$ , itself depending on the mechanical material properties, such as Young's modulus  $E$  and the Poisson's ration  $\nu$ . Figure 4.6 shows the strong relation between  $k_n$  and the DAF. Hence, the direct relation between the elastic material properties ( $E, \nu$ ) and the deformation. In this case, we see a threshold where  $k_n = 1 \times 10^{12} \text{ Pam}^{-1}$ . When  $k_n < 1 \times 10^{12} \text{ Pam}^{-1}$ , the deformation happens. If  $k_n > 1 \times 10^{12} \text{ Pam}^{-1}$ , almost no deformation (i.e. closure) occurs.

The geothermal site studied here is foreseen as a potential EGS. For that reason, the permeability is very low even when including the fractures. As a consequence, we do not see any thermal breakthrough at the production well. Increasing the flow rate would show a thermal breakthrough. However, we assume that having a pressure difference

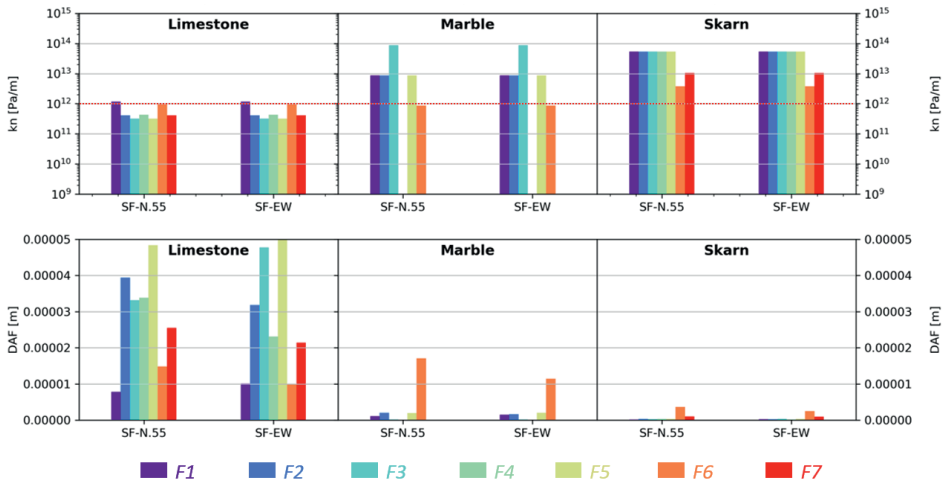


Figure 4.6 – The spring constant, and how mechanical properties influence fracture deformation (DAF) under stresses

( $\Delta P$ ) higher than 10 MPa would be unrealistically too high as it would eventually induce some hydraulic fracturing. Unfortunately the mechanics of hydraulic fracturing is not implemented here. For that reason, we maintain the  $\Delta P$  below or around 10 MPa.

Increasing the fracture trace length would improve the fracture network connectivity, and the fracture aperture would necessarily increase the global permeability (fig. 4.7). In further works, we would investigate the hydraulic fracture stimulation prediction.

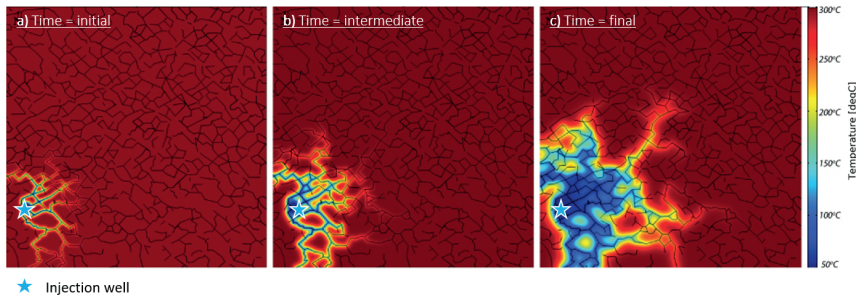


Figure 4.7 – Example of simulation with connected fractures and high fracture aperture

Thanks to that we can implement an extra dimension to this analysis by looking at fracture connectivity and fluid flow performance, before and after well stimulation.

Another characteristic which influences the model results is the thermal conductivity of the material. The matrix and the fracture material is not always made of the same mineral composition. Therefore, the thermal conductivity in the fracture could be much

higher than in the rock matrix (fig. 4.8).

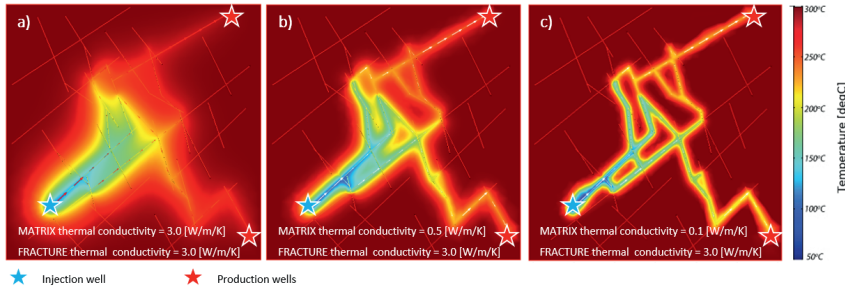


Figure 4.8 – Thermal conductivity contrasts, in a test model.

From the current results, without stimulation, the scenario 1 has the best performance in the Limestone formation, while for the Marble and the Skarn formations, the scenario 4 would be best.

Finally, Table 4.4 and Table 4.5 give the computation information per reservoir and scenario, such as number of meshed elements, degrees of freedom, and computation memory or computation time.

Reservoir	Scenario	Nbr of mesh elements	DoF	Internal DoF
Limestone	Scenario 1	220228	550602	366544
Limestone	Scenario 2	220340	550882	366662
Limestone	Scenario 3	220124	550342	366336
Limestone	Scenario 4	220368	550952	366760
Marble	Scenario 1	122028	305102	171888
Marble	Scenario 2	121870	304707	171678
Marble	Scenario 3	122014	305067	171872
Marble	Scenario 4	121996	305022	171850
Skarn	Scenario 1	184708	461802	278404
Skarn	Scenario 2	184790	462007	278498
Skarn	Scenario 3	184714	461817	278408
Skarn	Scenario 4	184674	461717	278338

Table 4.4 – Number of elements in Mesh and Degrees of freedom (*DoF*)

The computation time so far is relatively short. The next step to be fully challenging the RVE approach would be to perform the same simulations on 3D models. The fracture prediction would be even more accurate and would certainly influence the fluid flow circulation.

Reservoir	Scenario	Physical mem. [GB]	Virtual mem. [GB]	Computing time [s]
Limestone	Sc. 1	5.55	10.54	1394
Limestone	Sc. 2	5.51	10.51	1401
Limestone	Sc. 3	5.35	10.41	1349
Limestone	Sc. 4	5.58	10.61	1661
Marble	Sc. 1	3.13	8.14	519
Marble	Sc. 2	3.14	8.17	522
Marble	Sc. 3	3.11	8.14	525
Marble	Sc. 4	3.08	8.14	527
Skarn	Sc. 1	4.12	9.14	378
Skarn	Sc. 2	4.1	9.17	367
Skarn	Sc. 3	4.1	9.12	368
Skarn	Sc. 4	4.06	9.15	370

Table 4.5 – Computational physical and virtual memories (mem.) and computation time

## 4.6. CONCLUSION

When developing subsurface activities such as Oil and Gas, nuclear waste disposal, CO<sub>2</sub> sequestration or, as in this case, Enhanced Geothermal System, it is fundamental to quantify the role of the fracture system present in the subsurface. Very often, fractures are up-scaled to represent the matrix and the fractures together in a continuum model. In this article, we present a stress dependent fracture aperture model, hence a stress field dependent fluid flow and heat transfer model, using field data to populate the material properties and the fracture networks. These discrete fracture models (DFMs) are composed with tens of thousands of fractures. The DFMs are separated into fracture sets, related to the regional structural context. Each fracture set is characterized with its own aperture value from field measurements, corrected to depth stress conditions. Thanks to these simulations, we can identify the threshold, on the mechanical properties of the fractures, below which deformation takes place. The purpose of this multiple scenarios analysis is to evaluate the risks of the project. Combining multiple formations and multiple well positioning scenarios gives a thorough evaluation of the reservoir performance. This is fundamental in the context of field production risks analysis. Based on our results, the safer scenario for this project would be developed according to the scenario 4, which simulates a well doublet across the different fracture distribution patterns instead of targeting one zone in particular. This is even more important in the case of developing the Marble and the Skarn formations. This method provides, to our knowledge, a more realistic model of the existing and expected fracture network at depth. This would certainly be a major improvement in the development of the EGS technology.

## 4.7. LIST OF ABBREVIATIONS

Table 4.6 – List of abbreviations

Abbreviations	Descriptions
EGS	Enhanced Geothermal System
FEM	Finite Elements Method
DFM	Discrete Fracture Model
RVE	Representative Volume Element
TH	Thermo-hydraulic (modeling)
GEMex	Geothermal Mexico ( <a href="http://www.gemex-h2020.eu/">http://www.gemex-h2020.eu/</a> )
TMVB	Trans-Mexican Volcanic Belt
MD	Meter drilled
TD	Total Depth
DAF	Deformed Aperture of the Fracture
D	Whole simulated Domain
$\Omega$	Matrix domain
$\Gamma$	Fractures domain
$f_s$	force/unit area
$u$	displacement
$K$	stiffness matrix
$d_f$	fracture aperture
$k_n$	spring constant, stiffness in the normal direction
$E$	Young's modulus
$\nu$	Poisson's ratio
$S$	Far field stress tensor
$S_V$	Vertical Stress
$S_{Hmax}$	Maximum Horizontal Stress
$S_{hmin}$	Minimum Horizontal Stress
$k_f$	fracture permeability
$k_m$	matrix permeability
UCS	Unconfined Compressive Strength
LVDT	Linear Variable Differential Transformer
L	sample length for rock physics laboratory tests
A	the cross-sectional area of the sample
Q	flow rate for rock physics laboratory tests
$\mu$	fluid viscosity



# 5

## HYDRAULIC FRACTURE STIMULATION MODEL, WITH 3D PLANAR FRACTURE

*This chapter presents a Hydraulic Fracture (HF) stimulation model applied to the Aocolco well EAC1, using a planar 3-Dimensional HF geometry model. The mathematical model is really oriented towards operational applications. Hence, the model assumes idealized homogeneous geological conditions but can integrate a large number of input variables to describe the stimulation conditions, such as fluid properties or well architecture and more. In this study we propose to analyze the HF possible geometries when stimulating the Aocolco well EAC1. Because the geological context is still subject to significant uncertainties, and because the well architecture could still be modified, we analyze several stimulation scenarios. We compare the influence of different geological variables, such as stress state or mechanical properties, and we vary the stimulation zone depths to compare the efficiency in terms of HF geometry. Finally, assuming one favorable scenario, we compare the influence of Natural Fractures (NF) when simulating with rock mechanical properties measured in the laboratory, and with using the corrected values from the Geological Strength Index (GSI). The simulations are implemented in the MFrac<sup>®</sup> Hydraulic Fracturing Software from Baker Hughes. This work contributes to the GEMex project.*

---

Parts of this chapter are published with the GEMex Deliverables: Lepillier, B. and Hofmann, H.: Task 7.2: Stimulation design, in Hofmann, H., Peters, L. (2020): Concepts for the development and utilization of EGS, Deliverable D7.2, WP7, GEMex H2020 project, European Commission, <http://www.gemex-h2020.eu>, (2020).



## 5.1. INTRODUCTION

### 5.1.1. PROBLEM DEFINITION

Modeling the hydraulic fracture (HF) stimulation process is still a challenging exercise as it combines a complex mathematical problem to be solved over time, with potentially complex geometries and ranges from very small to very large scales. A common approach for solving the HF calculation is to simplify the HF as a planar object that opens over time: the geometry of the HF (such as its length, height and aperture) changes as the fluid is injected in the reservoir formation. Therefore the simulation assumes a single mode-I fracture, and is derived from common models, as the fracture models from Perkins, Kern and Nordgren (PKN), and Geertsma and de Klerk (GDK) (Perkins and Kern, 1961; Geertsma and De Klerk, 1969; Nordgren, 1972). In this study we model the HF using the 3D model where the HF is function of the fluid injection pressure. The geological domain responds to the laws of Linear Elastic Fracture Mechanics (LEFM) (Griffith, 1921), and the criterion for fracture propagation is given by the energy-release rate (i.e., the fracture propagates if the stress intensity factor at the tip matches the rock toughness) (Adachi et al., 2007). This HF propagation model is coupled with the fluid flow in the fracture, the leak-off from fracture faces to the formation, the fluid viscosity and the injection rates (Detournay and Cheng, 1993; Detournay, 2016).

The questions we want to answer here are: *i*) which of the involved parameters in a stimulation process is the most influencing? *ii*) and how the total injected volume would influence the HF dimensions in the Acoculco specific case study?

In this study, the simulations are implemented using the commercial hydraulic fracturing simulator MFrac<sup>®</sup>. Our simulations were realised with the following software settings:

- Fracture Geometry used: is 3-Dimensional;
- Fracture flow-back: off;
- Fracture simulate to closure: off;
- Fracture fluid gradient: included;
- Fracture propagation parameters: positive growth only;
- Fracture initiation interval: Min. Stress Interval;
- Fracture friction model: off;
- Fracture wall roughness: off;
- Fracture tip effects: off.

The Acoculco geothermal reservoir and the two exploratory wells are still subject to significant uncertainties. Therefore, the main objective of this work is to estimate the range of variability of the HF dimensions, related to injected volume and pressure flow rates.

As the fluid leak-off refers to the fluid infiltrating in the rock matrix from fracture faces (but does not refer to the fluid losses while drilling), and because the rock formations in Acoculco have been measured as not permeable, the leak-off is not considered in the simulations. As matter of simplicity, we are not considering any proppant in the problem and therefore assume the injected fluid properties as pure water (fig. 5.1).

In a first part of this chapter (section 5.2), we present the data used as inputs for the well-bore architecture, the stress regime, and the rock properties. Then, in section 5.3,

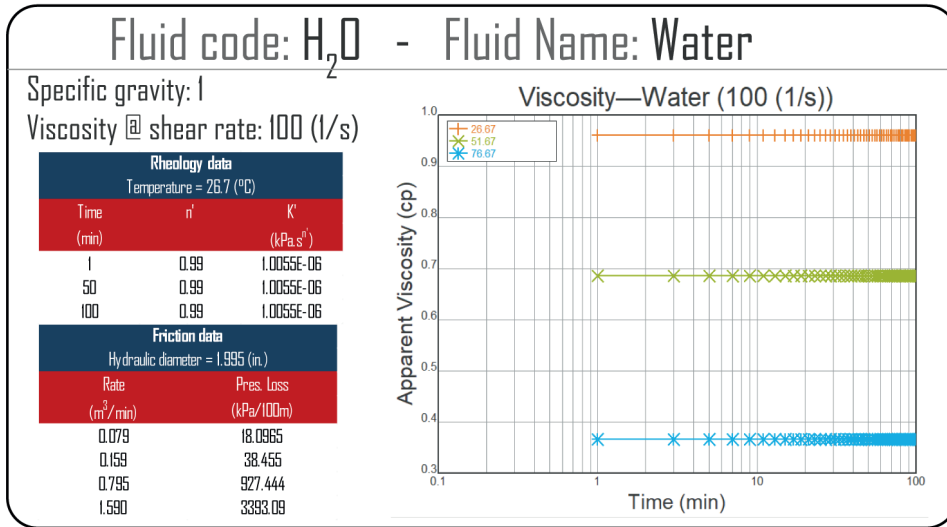


Figure 5.1 – Fluid properties inputs for Water in MFrac

5

we propose a sensitivity analysis evaluating the influence of different variables involved in a stimulation process: *i*) for *in-situ* parameters, such as the fracture toughness or stress field, and especially  $\nabla S_{hmin}$ ; *ii*) for induced parameters, such as the injection flow rate (here called 'slurry rate',  $SR$ ), and the total injected volume ( $V_{tot}$ ). *iii*) the stimulation depth intervals, as: *a*) interval 800 to 1900 m; *b*) interval 800 to 900 m; and *c*) interval 1800 to 1900 m. Once the influence of each involved parameters is better constrained, we present the predictive models for HF stimulation treatment in well EAC1. In section 5.4, we simulate different amounts of total injected volume, such as 500 m<sup>3</sup>, 1000 m<sup>3</sup>, 2500 m<sup>3</sup>, using the rock physical properties measured on the samples in the laboratory. In section 5.5, we repeat the same simulations using corrected rock physics properties following (Hoek et al., 2002; Marinos and Hoek, 2018) Geological Strength Index correction, which accounts for the Natural Fractures (NF) present in the formation. In both parts, we calculate 4 different stimulation scenarios:

- open-hole well from 800 to 1900m MD, as it is today;
- cased hole with perforations: 1500 to 1600 m MD (Marble rock properties);
- cased hole with perforations: 1700 to 1800 m MD (Skarn rock properties);
- cased hole with perforations: 1800 to 1900 m MD (Granodiorite rock properties).

## 5.2. INPUT DATA

### 5.2.1. INPUTS FOR WELL-BORE DESIGN

Well design architecture, such as casing sizes and depths are taken from Kruszewski (2019). In MFrac, the depth for Bottom Hole Treatment Pressure (BHTP) must be defined. In this study, the BHTP is calculated at the depth of the stimulated interval where  $\nabla S_{hmin}$  is the lowest.

MD (m)	Length sec. (m)	Casing			Tubing		
		OD (in.)	Wt (Kg/m)	ID (in.)	OD (in.)	Wt (Kg/m)	ID (in.)
10	10	14	54.5	13.4	–	–	–
200	190	9.625	47	9	–	–	–
800	600	7	54.5	6.456	–	–	–
1900	1100	5.875	20	5.2	–	–	–

Table 5.1 – Well design input data following MFrac description

5

The stress state and pressure inputs in MFrac are defined, for the minimum horizontal stress gradient ( $\nabla S_{hmin}$ ) in the tab “Data, rock properties, Stress Gradient”, and for the Pore pressure ( $P_p$ ) in “Data, Fluid Loss, Reservoir Pressure Gradient”. Stresses are derived from the calculated values given by Kruszewski (2019) in fig. 5.2, with the minimum horizontal stress gradient as:  $\nabla S_{hmin} = 0.56\nabla S_v \rightarrow \nabla S_{hmin} = 16 \text{ MPam}^{-1}$ :

- $S_{hmin}$  calculated in the Marble @ 1550 m MD is about 25 MPa.
- $S_{hmin}$  calculated in the Skarn @ 1750 m MD is about 28 MPa.
- $S_{hmin}$  calculated in the Granodiorite @ 1850 m MD is about 30 MPa.

Stresses plotted in fig. 5.2, are the pore pressure ( $P_p$ ), the minimum horizontal stress ( $S_{hmin}$ ) and the vertical stress ( $S_v$ ). The stress regime is assumed to be Normal Fault regime, with:

$$S_v > S_{Hmax} > S_{hmin} \quad (5.1)$$

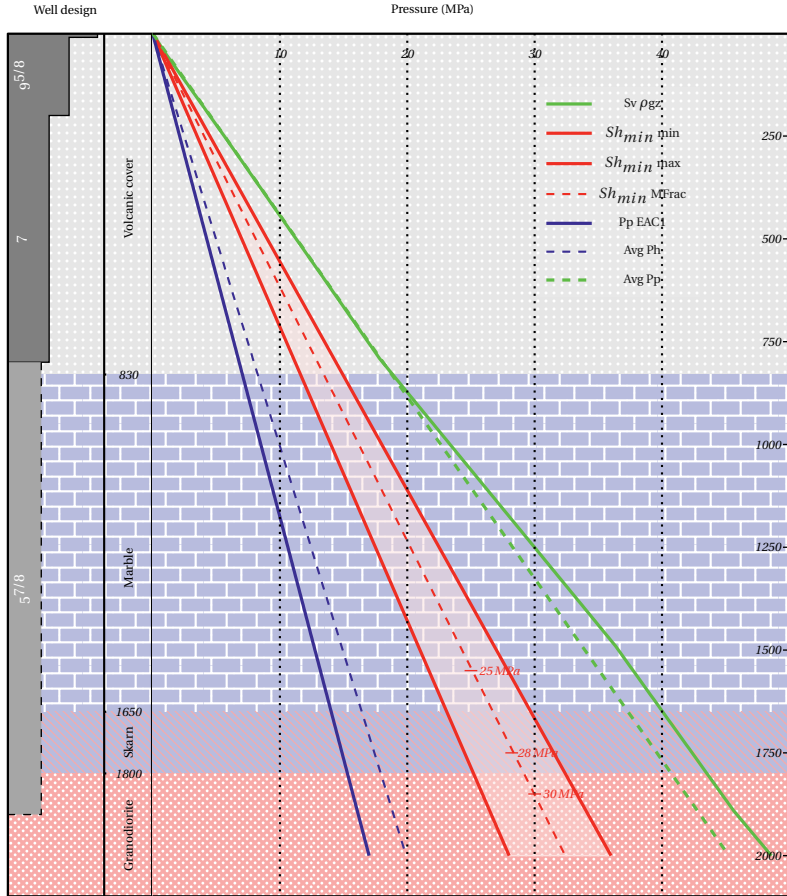


Figure 5.2 – EAC1 input data in MFrac: well design, lithology and pressure gradients with:  $S_v$  (green continuous line) calculated from  $\rho g z$ ;  $Avg P_p$  (green dashed line) calculated from world average pore pressure:  $23 \text{ MPa km}^{-1}$ ;  $P_p$  EAC1 (blue continuous line) pore pressure measured in the well, EAC1  $\nabla P_p = 8.7 \text{ MPa km}^{-1}$ ;  $Avg P_h$  (blue dashed line) calculated from world average hydrostatic pressure:  $10 \text{ MPa km}^{-1}$ .  $S_{hmin}$  (red lines: continuous are the *extremums*, dashed is the average) calculated from the gradient:  $\nabla S_{hmin} = 16 \text{ MPa km}^{-1}$

### 5.2.2. INPUTS FOR THE SENSITIVITY ANALYSIS

This part consists of testing the influence of several parameters on the HF model. To better quantify these influences, we need to simplify the problem, ensuring that only the tested variable is expressing a change in the solution. Therefore, the well design is kept identical along the whole sensitivity study, and the lithology is defined as one single homogeneous formation from surface to bottom (table 5.2). Similarly, we keep the hydraulic conditions identical (table 5.3). We therefore consider these as base-case conditions, from where we vary parameters one by one.

Zone (lithology)	TVD Bot. ( <i>m</i> )	$\nabla$ Stress ( <i>Pa/m</i> )	Stress ( <i>Pa</i> )	<i>E</i> ( <i>Pa</i> )	$\nu$	$K_{Ic}$ ( <i>MPa.m<sup>1/2</sup></i> )
SensAn	1900	13075	2.48e+07	4.9.00e+10	0.27	2

Table 5.2 – Rock properties input data following MFrac description, for the Sensitivity Analysis; - As the well is vertical with no deviation, True Vertical Depth (TVD) and Measured Depth (MD) are identical

5

Zone (lithology)	TVD Bot. ( <i>m</i> )	$\nabla P_{res}$ ( <i>Pa/m</i> )	$P_{res}$ ( <i>Pa</i> )	$c_t$ ( <i>1/kPa</i> )	<i>k</i> ( <i>mD</i> )	$\Phi$ (–)	$\mu_{Res}$ ( <i>cp</i> )	$\mu_{filt}$ ( <i>cp</i> )
SensAn	1900	8500	1.60e+07	1.02e+05	0.001	0.03	0.1	0.5

Table 5.3 – Well Fluid Loss input data following MFrac description, for the Sensitivity Analysis; - As the well is vertical with no deviation, True Vertical Depth (TVD) and Measured Depth (MD) are identical

### 5.2.3. INPUTS FOR THE EAC1 HF STIMULATION ANALYSIS

Acocolco geological and pressure inputs are implemented in respect to the geological context described in Section 1.4.2, and the rock physics laboratory experiments presented in Chapter 3. Acocolco model inputs are given in Table 5.4 and Table 5.5

Zone (lithology)	TVD Bot. ( <i>m</i> )	$\nabla$ Stress ( <i>Pa/m</i> )	Stress ( <i>Pa</i> )	<i>E</i> ( <i>Pa</i> )	$\nu$	$K_{Ic}$ ( <i>MPa.m<sup>1/2</sup></i> )
Volcanic cover	830	16000	1.33e+07	3.00e+10	0.3	1.648
Marble	1650	16000	2.64e+07	4.90e+10	0.27	1.87
Skarn	1800	16000	2.88e+07	4.90e+10	0.13	2.31
Granodiorite	1900	16000	3.04e+07	4.28e+10	0.35	2.36

Table 5.4 – Rock properties input data following MFrac description, for EAC1 well-bore; - As the well is vertical with no deviation, True Vertical Depth (TVD) and Measured Depth (MD) are identical

Zone (lithology)	TVD Bot. ( <i>m</i> )	$\nabla P_{res}$ ( <i>Pa/m</i> )	$P_{res}$ ( <i>Pa</i> )	$c_t$ ( <i>1/kPa</i> )	$k$ ( <i>mD</i> )	$\Phi$ (-)	$\mu_{Res}$ ( <i>cp</i> )	$\mu_{filt}$ ( <i>cp</i> )
Volcanic cover	830	7.22e+06	1.45e+05	0.001	0.05	0.1	0.5	
Marble	1650	14.3e+07	1.02e+05	0.001	0.04	0.1	0.5	
Skarn	1800	8700	15.7e+07	1.02e+05	0.001	0.04	0.1	0.5
Granodiorite	1900	8700	16.5e+07	1.02e+05	0.001	0.02	0.1	0.5

Table 5.5 – Well Fluid Loss input data following MFract description, for EAC1 well-bore; - As the well is vertical with no deviation, True Vertical Depth (TVD) and Measured Depth (MD) are identical

### 5.3. RESULTS OF THE SENSITIVITY ANALYSIS

From the defined base case scenario presented in Section 5.2, Table 5.6 presents the tested variables and values to which we tested them. This sensitivity analysis is applied for 3 different scenarios testing the influence of the stimulated depth interval: 1) stimulation from 800 to 1900 m (table 5.7); 2) stimulation from 800 to 900 m (table 5.8); 3) stimulation from 1800 to 1900 m (table 5.9).

Variable	<i>value-1</i>	<i>value-2</i>	<i>value-3</i>	<i>value-4</i>	Unit
Slurry rate	1	4	6	10	$m^3/min$
Fracture toughness ( $K_{IC}$ )	1	1.5	2	2.5	$MPa.m^{1/2}$
Min. horizontal stress ( $S_{hmin}$ )	10000	13075	16000	20000	$Pa/m$
Total injected volume	100	300	450	600	$m^3$

Table 5.6 – Sensitivity analysis: table summarizing the tested variables and values

5.3.1. SENSITIVITY ANALYSIS USING PERFOS FROM 800 TO 1900 MMD

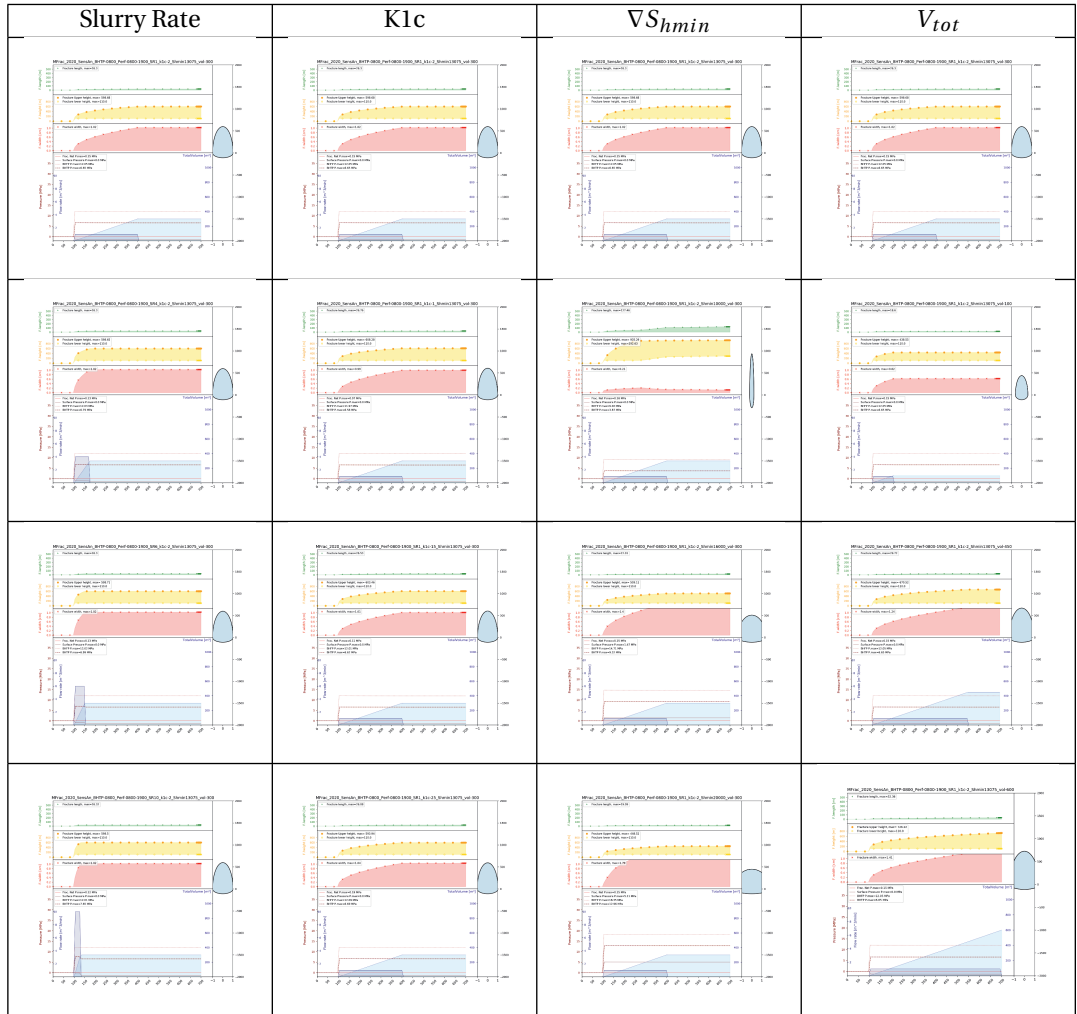


Table 5.7 – Sensitivity analysis: Perfos @ Depth 800 to 1900 m MD



5.3.2. SENSITIVITY ANALYSIS USING PERFOS FROM 800 TO 900 MMD

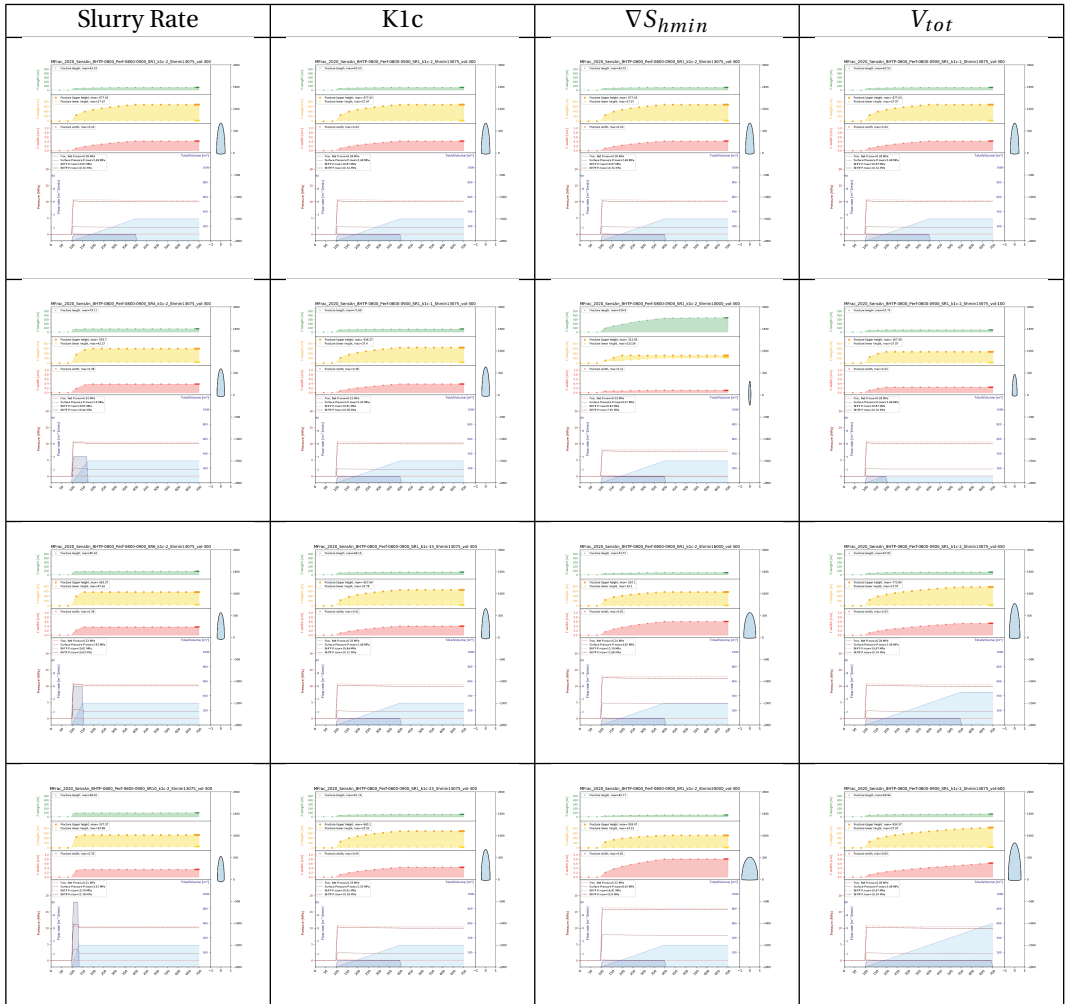


Table 5.8 – Sensitivity analysis: Perfos @ Depth 800 to 900 m MD

5.3.3. SENSITIVITY ANALYSIS USING PERFOS FROM 1800 TO 1900 MMD

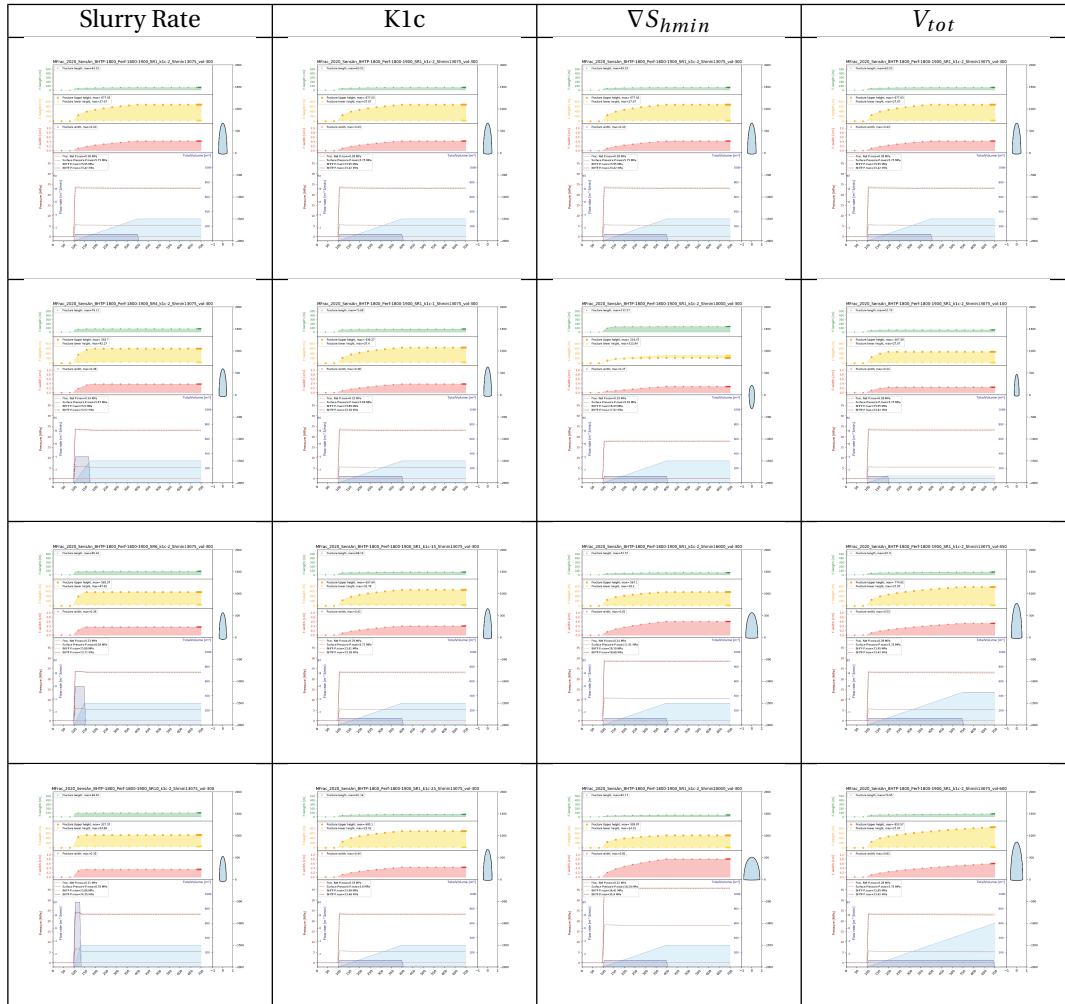


Table 5.9 – Sensitivity analysis: Perfos @ Depth 1800 to 1900 m MD

### 5.3.4. SENSITIVITY ANALYSIS CONCLUSIONS

Results are summarized in Figure 5.3 (and a higher resolution is given in appendix Figure A.4). Based on these quantitative results the following conclusions can be drawn:

- the  $SR$  significantly influences the fracture geometry dimensions but does not severely impact the induced pressures. Increasing the  $SR$  mainly increases the lateral propagation of the fracture, which indirectly, reduces its vertical propagation. A higher  $SR$  helps propagating the fracture horizontally.
- the  $K_{Ic}$  of the stimulated formation influences the fracture geometry dimensions but does not really impact the induced pressures but the fracture internal pressure. When  $K_{Ic}$  increases, the fracture internal pressure needs to be higher to propagate the fracture. The consequence is that the dimensions of the created fracture are smaller.
- the  $\nabla S_{hmin}$  variation strongly influences the fracture dimensions, especially the fracture length. As horizontal stress increases, the fracture propagates preferentially up-wards more than side-wards. Mainly, the  $\nabla S_{hmin}$  variation impacts the borehole pressure.
- the  $V_{tot}$  when increasing, increases significantly the fracture dimensions. But, as the slurry rate stays constant, then the pressure (as surface pressure, internal fracture pressure, BHFP, BHTP) does not change at all.

5

	Perfos 800-1900			Perfos 800-900			Perfos 1800-1900				Perfos 800-1900			Perfos 800-900			Perfos 1800-1900				Perfos 800-1900			Perfos 800-900			Perfos 1800-1900		
	L	H	w	L	H	w	L	H	w		L	H	w	L	H	w	L	H	w		L	H	w	L	H	w	L	H	w
$K_{Ic}=2$	26.3	63.53	63.53	26.3	63.53	63.53	26.3	63.53	63.53	$K_{Ic}=2$	26.3	63.53	63.53	26.3	63.53	63.53	26.3	63.53	63.53	$K_{Ic}=2$	26.3	63.53	63.53	26.3	63.53	63.53	26.3	63.53	63.53
$K_{Ic}=3$	708.68	704.1	704.1	708.68	704.1	704.1	708.68	704.1	704.1	$K_{Ic}=3$	708.68	704.1	704.1	708.68	704.1	704.1	708.68	704.1	704.1	$K_{Ic}=3$	708.68	704.1	704.1	708.68	704.1	704.1	708.68	704.1	704.1
$\nabla S_{hmin}$	1.02	0.43	0.43	1.02	0.43	0.43	1.02	0.43	0.43	$\nabla S_{hmin}$	1.02	0.43	0.43	1.02	0.43	0.43	1.02	0.43	0.43	$\nabla S_{hmin}$	1.02	0.43	0.43	1.02	0.43	0.43	1.02	0.43	0.43
$V_{tot}$	0	0	0	0	0	0	0	0	0	$V_{tot}$	0	0	0	0	0	0	0	0	0	$V_{tot}$	0	0	0	0	0	0	0	0	0
$P_{surf}$	0	2.49	5.75	0	2.49	5.75	0	2.49	5.75	$P_{surf}$	0	2.49	5.75	0	2.49	5.75	0	2.49	5.75	$P_{surf}$	0	2.49	5.75	0	2.49	5.75	0	2.49	5.75
$P_{inf}$	12.05	10.87	23.95	12.05	10.87	23.95	12.05	10.87	23.95	$P_{inf}$	12.05	10.87	23.95	12.05	10.87	23.95	12.05	10.87	23.95	$P_{inf}$	12.05	10.87	23.95	12.05	10.87	23.95	12.05	10.87	23.95
BHFP	6.65	10.34	23.42	6.65	10.34	23.42	6.65	10.34	23.42	BHFP	6.65	10.34	23.42	6.65	10.34	23.42	6.65	10.34	23.42	BHFP	6.65	10.34	23.42	6.65	10.34	23.42	6.65	10.34	23.42
BHTP	26.3	79.11	79.11	26.76	73.68	73.68	26.76	73.68	73.68	BHTP	127.46	339.8	132.57	127.46	339.8	132.57	127.46	339.8	132.57	BHTP	18.6	52.75	52.75	18.6	52.75	52.75	18.6	52.75	52.75

Figure 5.3 – Results of the sensitivity analysis using MFrac for Hydraulic Fracture (HF) length stimulation modeling; Abbreviations: SR=Slurry Rate,  $K_{Ic}$ =fracture toughness,  $\nabla S_{hmin}$ = Minimum horizontal stress gradient, L=HF length, H=HF Height, w=HF width,  $P_{inf}$ =Internal fracture pressure,  $P_{surf}$ =Surface pressure, BHFP=Bottom Hole Fluid Pressure, BHTP=Bottom Hole Treatment Pressure - This figure is available in a larger format in Supplementary material

To answer the question of the extent to which the different variables influence the HF propagation, we can safely state that the total injected volume has the largest influence on the HF dimensions, and that the  $SR$  impacts mainly the fracture lateral propagation. Contrary to the  $SR$ , the  $\nabla S_{hmin}$  when increasing, reduces lateral propagation favoring an up-ward propagation.

Therefore, concerning the second question, answered in the next study (section 5.4), which focuses on the actual model of Acoculco geothermal EAC1 well, we recommend to use a Slurry rate of  $6\text{ m}^3/\text{min}$  favoring a lateral propagation. As seen in fig. 5.3, in this case, a volume of  $100\text{ m}^3$  would induce a fracture of about 50 m long, and a volume of  $600\text{ m}^3$  would create a fracture of about 70 m.

### 5.4. EAC1 HF PREDICTIVE STIMULATION, LABORATORY DATA MODEL

Based on the previous analysis, we know which variables influence the HF stimulation. We can now analyze the real case of Acoculco geothermal field and more specifically, EAC1 well using values presented in Section 5.2.3. EAC1 well is currently open-hole from 800 m to Total Depth (TD), which might not be ideal for a stimulation work. therefore, we compare the following scenarios:

- open-hole well from 800 to 1900m MD, as it is today;
- cased hole with perforations: 1500 to 1600 m MD (Marble rock properties);
- cased hole with perforations: 1700 to 1800 m MD (Skarn rock properties);
- cased hole with perforations: 1800 to 1900 m MD (Granodiorite rock properties).

and for each scenario we are testing the influence of injected volume on the HF dimensions, by increasing the total injected volume from 500 m<sup>3</sup>, to 1000 m<sup>3</sup> and 2500 m<sup>3</sup>.

5

#### 5.4.1. STIMULATING THE WELL, WITH AN OPEN-HOLE, FROM 800 TO 1900M MD

Here we calculate the influence of varying the total injected volume from 500 m<sup>3</sup>, to 1000 m<sup>3</sup> and then 2500 m<sup>3</sup>. These would induce a fracture of about 24 m, 29 m, and 37 m long, respectively.

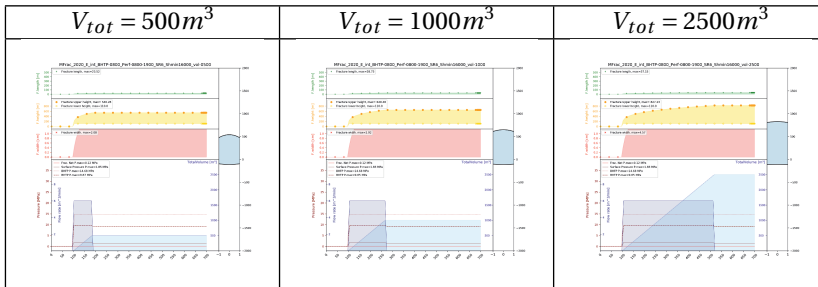


Table 5.10 – Stimulation job lab-model: Open-hole @ Depth 800 to 1900 m MD

#### 5.4.2. STIMULATING THE WELL, WITH A CASED-HOLE, PERFORATED FROM 1500 TO 1600M MD

Here we calculate the influence of varying the total injected volume from 500 m<sup>3</sup>, to 1000 m<sup>3</sup> and then 2500 m<sup>3</sup>. These would induce a fracture of about 75 m, 85 m, and 98 m long, respectively.

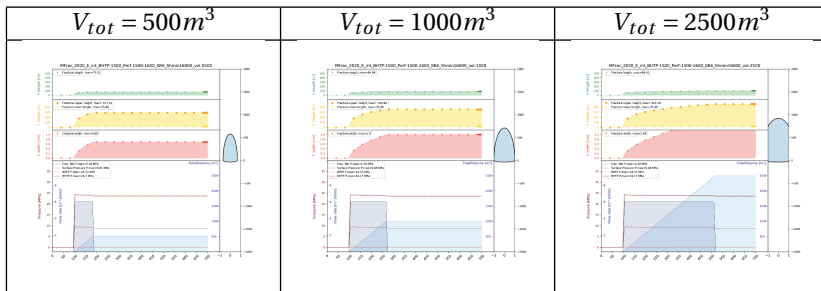


Table 5.11 – Stimulation job lab-model: Perfos @ Depth 1500 to 1600 m MD

### 5.4.3. STIMULATING THE SKARN, WITH A CASED HOLE, PERFORATED FROM 1700 TO 1800M MD

Here we calculate the influence of varying the total injected volume from 500 m<sup>3</sup>, to 1000 m<sup>3</sup> and then 2500 m<sup>3</sup>. These would induce a fracture of about 72 m, 83 m, and 100 m long, respectively.

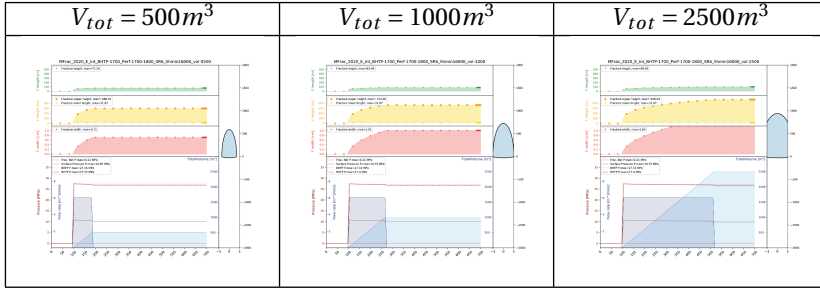


Table 5.12 – Stimulation job lab-model: Perfos @ Depth 1700 to 1800 m MD

5

### 5.4.4. STIMULATING THE GRANODIORITE, WITH A CASED HOLE, PERFORATED FROM 1800 TO 1900M MD

Here we calculate the influence of varying the total injected volume from 500 m<sup>3</sup>, to 1000 m<sup>3</sup> and then 2500 m<sup>3</sup>. These would induce a fracture of about 70 m, 82 m, and 100 m long, respectively.

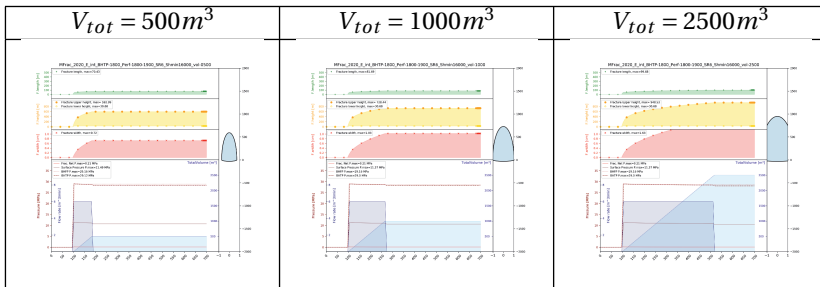


Table 5.13 – Stimulation job lab-model: Perfos @ Depth 1800 to 1900 m MD

### 5.5. EAC1 HF PREDICTIVE STIMULATION, HOEK-BROWN GSI MODEL

In this part, we are running the same simulation scenarios as before, but we change the mechanical properties of the rock. According to Hoek et al. (2002); Marinos and Hoek (2018) the rock mass stiffness (elastic parameters) is function of natural fracture (NF) distribution. The larger the amount of NF in the formation, the lower the stiffness of the rock. Table 5.14 presents the results of testing the influence of varying the Young’s Modulus  $E$  from 30 GPa, to 40 GPa, and 50 GPa. The results show a clear correlation between the rock stiffness and the HF dimensions. The higher the stiffness, the larger the HF dimension. This suggests that we need to correct the intact rock stiffness measured in

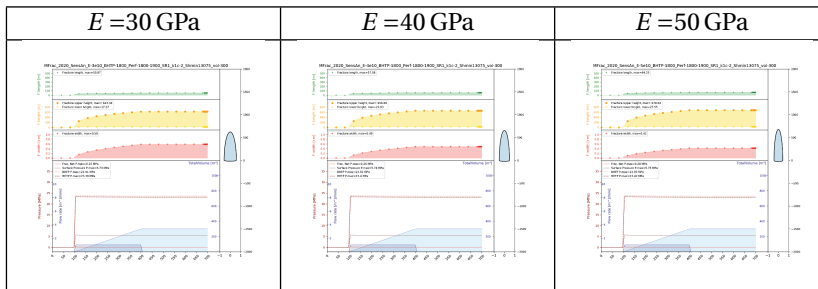


Table 5.14 – Sensitivity analysis of the Young’s modulus: Perfos @ Depth 1800 to 1900 m MD

the rock physics laboratory by applying the Geological Strength Index (GSI) correction. With Acoculco input values, using the Hoek and Brown  $GSI = 70$ , this would lead to the following correction:

- Marble:  $E_{int} = 49.1GPa \rightarrow E_{rm} = 36GPa$
- Skarn:  $E_{int} = 49GPa \rightarrow E_{rm} = 35.9GPa$
- Granodiorite:  $E_{int} = 42.8GPa \rightarrow E_{rm} = 31.4GPa$

Where  $E_{int}$  stands for “Young’s modulus in intact rock”, and  $E_{rm}$  stands for “Young’s modulus of the rock mass (i.e. including the NF)” Table 5.15 summarizes the corrected values in MFrac input table:



## 5

Zone (lithology)	TVD Bot. ( <i>m</i> )	$\nabla$ Stress ( <i>Pa/m</i> )	Stress ( <i>Pa</i> )	<i>E</i> ( <i>Pa</i> )	$\nu$	$K_{Ic}$ ( <i>MPa.m<sup>1/2</sup></i> )
Volcanic cover	830	16000	1.33e+07	3.00e+10	0.3	1.648
Marble	1650	16000	2.64e+07	3.60e+10	0.27	1.87
Skarn	1800	16000	2.88e+07	3.59e+10	0.13	2.31
Granodiorite	1900	16000	3.04e+07	3.14e+10	0.35	2.36

Table 5.15 – Rock properties input data following MFrac description, for EAC1 well-bore using Hoek and Brown GSI correction; - As the well is vertical with no deviation, True Vertical Depth (TVD) and Measured Depth (MD) are identical

**5.5.1. STIMULATING THE OPEN-HOLE WELL, FROM 800 TO 1900M MD**

Here we calculate the influence of varying the total injected volume from  $500\text{ m}^3$ , to  $1000\text{ m}^3$  and then  $2500\text{ m}^3$ . These would induce a fracture of about 23 m, 28 m, and 37 m long, respectively.

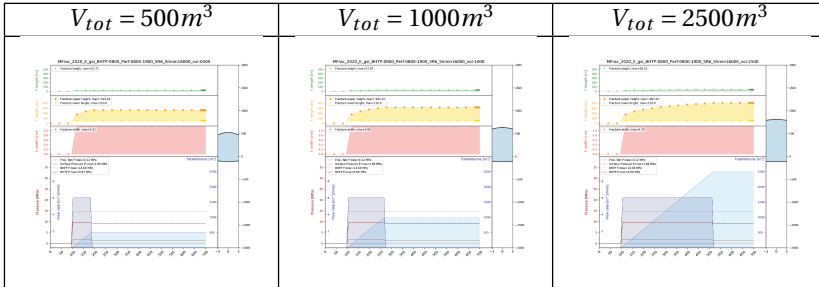


Table 5.16 – Stimulation job GSI-model: Open-hole @ Depth 800 to 1900 m MD

**5.5.2. STIMULATING THE MARBLE, CASED HOLE PERFORATED FROM 1500 TO 1600M MD**

Here we calculate the influence of varying the total injected volume from  $500\text{ m}^3$ , to  $1000\text{ m}^3$  and then  $2500\text{ m}^3$ . These would induce a fracture of about 65 m, 75 m, and 90 m long, respectively.

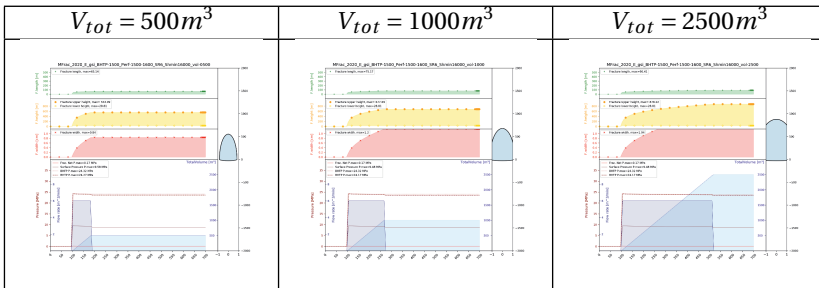


Table 5.17 – Stimulation job GSI-model: Perfos @ Depth 1500 to 1600 m MD

### 5.5.3. STIMULATING THE SKARN, WITH A CASED HOLE, PERFORATED FROM 1700 TO 1800M MD

Here we calculate the influence of varying the total injected volume from 500 m<sup>3</sup>, to 1000 m<sup>3</sup> and then 2500 m<sup>3</sup>. These would induce a fracture of about 62 m, 73 m, and 90 m long, respectively.

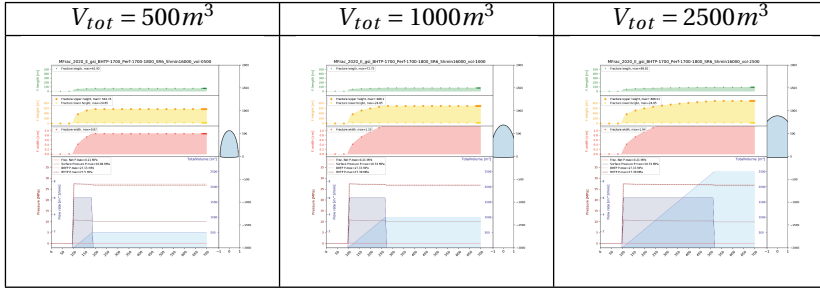


Table 5.18 – Stimulation job GSI-model: Perfos @ Depth 1700 to 1800 m MD

5

### 5.5.4. STIMULATING THE GRANODIORITE, WITH A CASED HOLE, PERFORATED FROM 1800 TO 1900M MD

Here we calculate the influence of varying the total injected volume from 500 m<sup>3</sup>, to 1000 m<sup>3</sup> and then 2500 m<sup>3</sup>. These would induce a fracture of about 60 m, 71 m, and 88 m long, respectively.

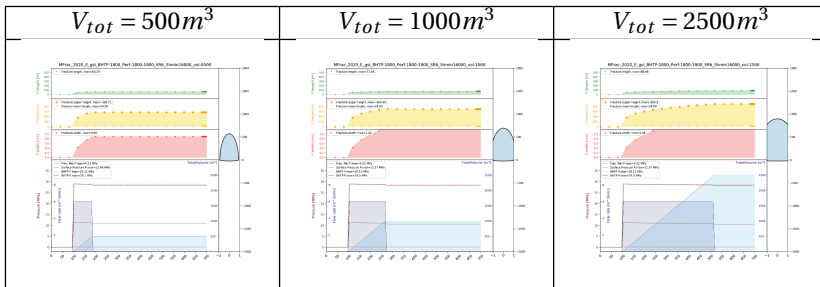


Table 5.19 – Stimulation job GSI-model: Perfos @ Depth 1800 to 1900 m MD

## 5.6. CONCLUSION

The first conclusion is about casing the well. Setting down a completion is expensive. However, this study clearly shows that: Firstly, stimulating an open hole well is very difficult, and that most likely, the stimulation ends at stimulating the casing shoe. Secondly, without a cased hole, stimulating a fracture requires a much larger volume of fluid. Using selective production packers could be an alternative solution. The question is then to know the applicability of using such packers in this well, in regards of: i) the high temperature; ii) the shape of the well which was drilled in 1995 and not maintained. Because of the tectonical stress regime, one could expect an eventual deformation of the well-bore shape. Hence, to case the well implies costs in the short term, but this would significantly reduce the needs on surface wellhead pressure and volume of fluids to be pumped in, and because of that, it will reduce the well operation costs in the long term.

The second conclusion concerns the depth to target for stimulation. Following the results of this study, which is highly controlled by the rock mechanical properties, it seems really clear that stimulating in the Marble (perfos @ 1500-1600 m MD) would be much easier than in the Skarn (perfos @ 1700-1800 m MD), or in the Granodiorite (perfos @ 1800-1900 m MD). Also, it is important to keep in mind that the lithological log used in this study is a model. Occurrence of Skarns is difficult to predict, and for instance Skarns could be found at a shallower depth.

The Hoek-Brown GSI correction helps evaluating the range of uncertainty in fracture dimensions. In this case, the GSI gives a correction on the rock stiffness (and more specifically the Young's Modulus  $E$ ) from NF distribution in the whole rock mass formation. As seen in fig. 5.4, this correction would decrease the fracture height and length by 5% to 10%.

In terms of costs and efficiency, according to this analysis, it would seem wise to stimulate the Marble at a reasonable depth (as per example from 1500 to 1600 m MD). This depth range would keep the stimulation job safe from the high strength ( $K_{Ic}$ ) rocks (Skarn or Granodiorite). EAC1 & EAC2 wells showed temperatures above 200 °C deeper than 1500m MD, which is certainly a high enough temperature to produce an efficient geothermal system. In this case, injecting only 1000 m<sup>3</sup> of water would already create a fracture of about 100 m. In this scenario, of stimulation from 1500 to 1600 m MD, it is important to note, that according to the model, injecting a total volume of 2500 m<sup>3</sup> would create a fracture propagating vertically until breaking through the volcanic deposits, which covers the marbles. This might connect the stimulated reservoir to more permeable shallow layers, breaking the seal.

This model is an estimation for the stimulation of HF dimensions assuming a bi-wing, planar tensile fracture. This assumption does not consider the rock mass heterogeneities as per example how could NF influence the HF pathway when propagating?

		$V_{tot} = 500 \text{ m}^3$	$V_{tot} = 500 \text{ m}^3$	$V_{tot} = 1000 \text{ m}^3$	$V_{tot} = 1000 \text{ m}^3$	$V_{tot} = 2500 \text{ m}^3$	$V_{tot} = 2500 \text{ m}^3$
		$E_{int}$	$E_{rm}$	$E_{int}$	$E_{rm}$	$E_{int}$	$E_{rm}$
Perfos 800-1900	L	23.52	22.71	28.73	27.87	37.15	36.22
	H	650.28	633.26	759.48	741.32	937.23	917.63
	w	2.08	2.21	2.92	3.08	4.57	4.79
	P_inF	0.12	0.12	0.12	0.12	0.12	0.12
	P_surf	1.85	1.85	1.83	1.84	1.83	1.84
	BHFP	14.68	14.68	14.68	14.68	14.68	14.68
	BHTP	9.67	9.67	9.65	9.66	9.65	9.66
Perfos 1500-1600	L	75.51	65.14	84.98	75.17	98.41	90.41
	H	612.58	581.9	745.45	705.9	957.02	907.03
	w	0.69	0.84	1	1.2	1.69	1.94
	P_inF	0.18	0.17	0.18	0.17	0.18	0.17
	P_surf	9.61	9.58	9.48	9.48	9.48	9.48
	BHFP	24.33	24.32	24.33	24.32	24.33	24.32
	BHTP	24.3	24.27	24.17	24.17	24.17	24.17
Perfos 1700-1800	L	72.24	61.92	83.49	72.72	99.83	89.81
	H	620.12	589.61	755.05	712.95	970.28	913.36
	w	0.71	0.87	1.01	1.23	1.64	1.94
	P_inF	0.21	0.21	0.21	0.21	0.21	0.21
	P_surf	10.87	10.84	10.75	10.74	10.75	10.74
	BHFP	27.56	27.55	27.56	27.55	27.56	27.55
	BHTP	27.52	27.5	27.4	27.39	27.4	27.39
Perfos 1800-1900	L	70.43	60.29	81.69	71.06	99.68	88.48
	H	623.67	592.8	759.12	716.78	979.21	918.99
	w	0.72	0.89	1.03	1.25	1.63	1.96
	P_inF	0.21	0.21	0.21	0.21	0.21	0.21
	P_surf	11.49	11.46	11.37	11.37	11.37	11.37
	BHFP	29.16	29.15	29.16	29.15	29.16	29.15
	BHTP	29.12	29.1	29	29	29	29

Figure 5.4 – Results of Stimulation job models, comparing stimulation depths and impact of Hoek and Brown's GSI correction, using MFrac

## 5.7. ABBREVIATIONS & SYMBOLS

Table 5.20 – List of abbreviations

Abbreviations	Descriptions
Bot.	Bottom
Cst.	Constant
D	Depth
HF	Hydraulic fracture
MD	Meter drilled
Sec.	Section
SR	Slurry rate
TD	Total Depth
TVD	True Vertical Depth
$H$	Fracture height
$L$	Fracture length
$w$	Fracture width
GDK	Fracture Kristianovich-Geertsma-De Klerk
PKN	Fracture Perkins-Kern-Nordgren
3D	Fracture 3-dimensional
$BHTP$	Bottom Hole Treatment Pressure
$BHFP$	Bottom Hole Fluid Pressure
$c_t$	Total compressibility
$E$	Young's modulus
$k$	Permeability
$K_{IC}$	Fracture toughness
$\mu$	Fluid viscosity
$\mu_{Res}$	Reservoir fluid viscosity
$\mu_{filt}$	Filtrate fluid viscosity
$\nabla P_{res}$	Reservoir pressure Gradient
$\nu$	Poisson's ratio
$\Phi$	Porosity
$P_{InF}$	Internal Fracture pressure ( Fracture net pressure)
$P_{Surf}$	Surface (Well head) pressure
$P_{res}$	Reservoir pressure
$S_V$	Vertical Stress
$S_{Hmax}$	Maximum Horizontal Stress
$S_{hmin}$	Minimum Horizontal Stress
$T_{Vol}$	Total Injected Volume



# 6

## HYDRAULIC FRACTURE STIMULATION MODEL, IN 2D FRACTURED RESERVOIR

*In every tight formation reservoir, natural fractures play an important role for mass and energy transport and stress distribution. Enhanced Geothermal Systems (EGS) make no exception and stimulation aims at increasing the reservoir permeability to enhance fluid circulation and heat transport. EGS development relies upon the complex task of predicting accurate hydraulic fracture propagation pathway by taking into account reservoir heterogeneities and natural or pre-existing fractures. In this contribution, we employ the variational phase-field method which handles hydraulic fracture initiation, propagation and interaction with natural fractures and is tested under varying conditions of rock mechanical properties and natural fractures distributions. We run bi-dimensional finite element simulations employing the open-source software OpenGeoSys and apply the model to simulate realistic stimulation scenarios, each one built from field data and considering complex natural fracture geometries in the order of a thousand of fractures. Key mechanical properties are derived from laboratory measurements on samples obtained in the field. Simulations results confirm the fundamental role played by natural fractures in stimulation's predictions, which is essential for developing successful EGS projects.*



## 6.1. INTRODUCTION

Interest in predicting Hydraulic Fracture propagation is picking up since the Enhanced Geothermal System (EGS) concept could become a competitive solution as a sustainable and essentially carbon-free energy resource. In EGS, the reservoir is stimulated by injecting pressurized fluids in reservoir rock formations with the aim of enhancing permeability. Early application of permeability enhancement were performed in oil and gas reservoirs (Economides and Nolte, 1989) while nowadays the principles of hydraulic fracture mechanics are applied to a broad range of problems, such as nuclear waste disposal (Zoback et al., 2003), carbon-capture and storage (Fu et al., 2017), glacier dynamics (Tsai and Rice, 2010), earthquake nucleation (Garagash and Germanovich, 2012) and geothermal systems (Legarth and Saadat, 2005; McClure and Horne, 2014; Fox et al., 2013). Hydraulic fracture propagation is intrinsically a multi-scale problem (Garagash et al., 2011), with a wide range of scales of time and length controlling the fluid-driven crack propagation (Detournay, 2016). Under simplified assumptions of problem geometry and physical behavior, analytical solutions (Garagash and Detournay, 2000; Adachi and Detournay, 2002; Savitski and Detournay, 2002; Detournay, 2016) give good predictions of multi-scale asymptotic behavior which has been confirmed by laboratory experiments in highly controlled environments (Bunger and Detournay, 2008). Numerical methods are more computationally costly but can also overcome the simplifications typical of analytical solutions (Lecampion et al., 2018), such as planar cracks and homogeneous material properties (Bunger et al., 2013). Most numerical methods are based on Linear Elastic Fracture Mechanics (LEFM) (Adachi et al., 2007) and the problem of hydraulic fracture propagation has been addressed either by i) assuming planar and single mode crack propagation or ii) accounting for non-planar propagating cracks that interact with pre-existing natural fractures (Weng, 2014).

The first approach assumes the crack as a planar object splitting the material in two parts with a displacement discontinuity that evolves over time: the dimensions of the hydraulic fracture (such as its length, height and aperture) change as the fluid is injected. Models of three-dimensional (3D) bi-wing planar fractures rely upon the known fracture models from Perkins, Kern and Nordgren (PKN) (Perkins and Kern, 1961), Geertsma and de Klerk (GDK) (Geertsma and De Klerk, 1969) and more generalized three-dimensional models (Nordgren, 1972). The crack propagation criterion is based on the energy-release rate (Griffith, 1921) and propagation occurs if the stress intensity factor reaches the critical value (Adachi et al., 2007). Viscous dissipation of fluid is an additional source of energy dissipation in hydraulic fracturing where the LEFM solution is coupled with Poiseuille's flow in the fracture and Carter's equation for leak-off from the fracture to the formation (Detournay and Cheng, 1993). The crack propagates along trajectories in a parametric space whose asymptotic regimes are characterized by a prevailing mechanism among leak-off, toughness, storage and viscosity (Detournay, 2016). Rock's stiffness, strength and permeability, fluid's viscosity and injection rate control the trajectories of the parametric space. Although single mode-I planar crack models give good estimates of the fracture dimensions whenever the basic assumptions hold valid, they fall short whenever heterogeneities cannot be neglected—a typical occurrence in geothermal reservoirs.

Models of fracture interaction (Warpinski and Teufel, 1987; Jeffrey et al., 1994, 2009; Renshaw and Pollard, 1995; Weng, 2014; McClure et al., 2015) have to account for hy-

draulic fracture arrest, cross or branch at the intersection with a natural fracture (Figure 6.1). Although Yew and Weng (2015) report the Unconventional Fracture Model (UFM) by Weng et al. (2011) as one of the first models of hydraulic fracture propagation that accounts for fluid flow and complex network of natural fractures, several problems regarding the computational mechanics of hydraulic fracture remain unsolved. Two main approaches have so far emerged: i) the first one employs the Displacement Discontinuity Method (DDM), such as the Unconventional Fracture Model (UFM) or Crack Tip Open Displacement (CTOD) and ii) the second one uses Finite Elements or Finite Volumes Methods (FEM or FVM), where natural fractures are either smeared using an implicit approach (Non-local Damage or Phase-Field) or embedded into Cohesive Zone Models. The DDM is computationally inexpensive, as it requires discretization of the boundaries only, but cannot handle reservoir heterogeneities. The FEM with explicit embedded discontinuities faces two main drawbacks: i) it requires fine crack-tip discretization to preserve accuracy, hampering its applicability to real-case scenarios where the hydraulic fracture is expected to propagate for several hundreds of meters, and ii) it suffers from element-distortion issues that generate inaccuracies in crack opening calculations and induce numerical instabilities. The eXtended Finite Element Method (Belytschko and Black, 1999; Belytschko et al., 2001; Moës et al., 1999; Yazid et al., 2009; Gupta and Duarte, 2016; Wang, 2019) overcomes the classical finite elements limitations of resolving field discontinuities by use of enriched shape-function, although it is computationally expensive, can hardly handle *hydraulic fracture - natural fractures* interaction and can on occasions be numerically unstable.

The phase-field method of fracture is a valid and promising alternative. Given its success in modeling propagation of brittle fracture, its development has been extended to ductile (Ambati et al., 2015; Miehe et al., 2015a; Kuhn et al., 2016; Alessi et al., 2017), fatigue (Alessi et al., 2018; Seiler et al., 2018; Carrara et al., 2019), and dynamic fractures (Bourdin et al., 2011; Borden et al., 2012; Hofacker and Miehe, 2012; Schlüter et al., 2014; Li et al., 2016; Fischer and Marigo, 2019). The variational phase-field (V-pf) is a generalized Griffith criterion (Francfort and Marigo, 1998) numerically implemented using a phase-field variable, which smears the sharp interface fracture with a smooth transition function (Bourdin et al., 2000). The phase-field variable describes the transition from intact to fully damaged state of the material over a specific length scale. Seminal works of the application of the V-pf approach to hydraulic fracture include Bourdin et al. (2012); Chukwudozie et al. (2013) while following studies addressed problems related to poroelasticity (Wheeler et al., 2014; Mikelić et al., 2015; Miehe et al., 2015b; Wilson and Landis, 2016; Santillán et al., 2017), fracture width computation (Xia et al., 2017; Lee et al., 2017), coupling with the theory of porous media (Ehlers and Luo, 2017; Heider and Markert, 2017), pressure dependent failure mechanisms (Choo and Sun, 2018), mass conservation (Chukwudozie et al., 2019), in-situ stresses (Shiozawa et al., 2019). The smeared representation can handle complex fracture topology where natural fractures can be represented within non-conforming discretizations, without a-priori assumptions on their geometry or restriction on hydraulic fracture growth trajectories (Yoshioka and Bourdin, 2016).

In this study, we solve the toughness dominated hydraulic fracturing problem where the pressure drop within the fracture is negligible with a V-pf approach formulated with

the constitutive model known as no-tension or masonry model (Freddi and Royer-Carfagni, 2011; Del Piero, 1989). The main goal is to study the hydraulic fracture interaction with reservoir heterogeneities in the form of pre-existing natural fractures with efficient computational V-pf models. We apply the V-pf method to a real case study of a potential EGS system, i.e., the Aocolco geothermal field located in Puebla, Mexico. Two exploration wells were drilled within the geothermal field and, through log data analysis, a high temperature ( $T \sim 300^\circ\text{C}$ ) and low permeable ( $k = 1 \times 10^{-18} \text{ m}^2$ ) reservoir was identified at  $\sim 2 \text{ km}$  depth. Natural fractures are modeled as complex Discrete Fracture Networks (DFN) calculated from outcrop field measurements and mechanical rock properties are derived from laboratory testing on samples collected in the field.

This article is structured as follows: in section 6.2, we introduce the governing equations of the V-pf model, their implementation in the open-source software OpenGeoSys (Kolditz et al., 2012), the experimental program and the stochastic method to build DFNs. In Section 6.3 we introduce applications of simple computational scenarios and geothermal reservoir stimulation. Section 6.4 presents the results of the simulations and contains a wider discussion of our results as well as broader implications of our main findings. Finally, we draw general conclusions of the study in section 6.6.

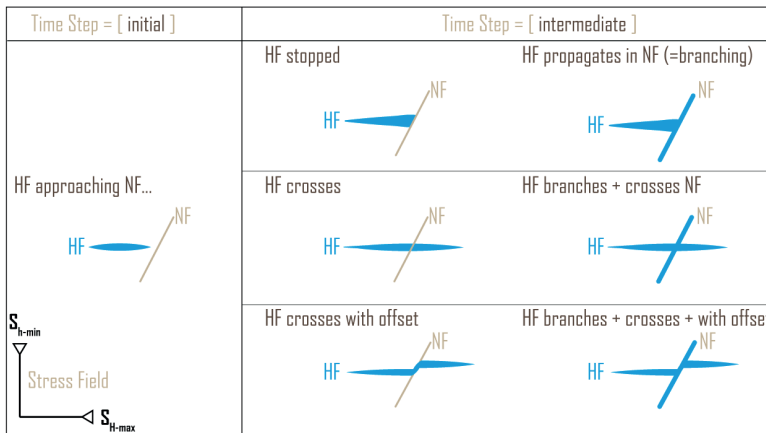


Figure 6.1 – Possible interaction process of hydraulic fracture and natural fractures: i) Hydraulic fracture encounters a natural fracture can either arrests, cross or be deviated by the natural fracture; ii) hydraulic fracture encounters a natural fracture and propagates along its direction, which can generate branching.

## 6.2. VARIATIONAL PHASE-FIELD MODEL

### 6.2.1. VARIATIONAL APPROACH TO FRACTURE

LEFM is based on Griffith's observation that the energy dissipation by a propagating crack equals the mechanical energy decay (Griffith, 1921). Thus the criterion for fracture propagation is given as

$$G_c = G, \quad (6.1)$$

where  $G_c$  is the critical surface energy release rate and  $G$  is the mechanical energy restitution rate. The energy restitution rate is defined as the derivative of the elastic energy  $\mathcal{P}$  with respect to a crack increment length  $a$ , which is often derived using the concept of stress intensity factor Irwin (1957). Griffith criterion reads then as

$$\frac{\partial \mathcal{P}}{\partial a} = G_c, \quad (6.2)$$

which was revisited by Francfort and Marigo (1998) noticing that it can be described in terms of critical values of the following total energy along a prescribed path as

$$\mathcal{P} + G_c a. \quad (6.3)$$

The Griffith's criterion was generalized in the variational framework by considering a total energy with any crack set  $\Gamma$  as opposed to a prescribed path  $a$  as

$$\underbrace{\mathcal{F}}_{\text{Total energy}} = \underbrace{\mathcal{P}}_{\text{Mechanical energy}} + \underbrace{\int_{\Gamma} G_c dS}_{\text{Surface energy}}, \quad (6.4)$$

such that the fracture propagation criterion is obtained by solving for the set of mechanical energy  $\mathcal{P}$  and the crack geometry  $\Gamma$  that minimizes Equation (6.4). For a prescribed crack path (e.g.,  $a$ ), the approach converges to Griffith's criterion which can be viewed as a local energy minimum problem.

### 6.2.2. GOVERNING EQUATIONS

The linear elastic constitutive equation of a brittle-elastic porous medium occupying a domain  $\Omega$  can be expressed as (Biot, 1941)

$$\boldsymbol{\sigma} = \mathbf{C} : \boldsymbol{\varepsilon}(\mathbf{u}) + \alpha p_p \mathbf{I}, \quad (6.5)$$

where  $\mathbf{C}$  is the fourth order linear elastic tangent operator,  $\alpha$  is the Biot's coefficient,  $p_p$  is the pore-pressure,  $\mathbf{I}$  is the identity matrix, and  $\boldsymbol{\varepsilon}$  is the linearized strain tensor defined as the symmetric part of the displacement gradient  $\nabla \mathbf{u}$

$$\boldsymbol{\varepsilon}(\mathbf{u}) := \frac{\nabla \mathbf{u} + \nabla \mathbf{u}^t}{2}. \quad (6.6)$$

Also, consider crack set  $\Gamma$  filled with a fluid at pressure  $p_f$  and let  $\partial\Omega_N$  be a portion of its boundary and  $\partial\Omega_D := \partial\Omega \setminus \partial\Omega_N$  the remaining part, static equilibrium and continuity of stress at the interfaces mandates that

$$\begin{cases} \nabla \cdot \boldsymbol{\sigma}(\mathbf{u}) = \mathbf{0} & \text{in } \Omega \setminus \Gamma, \\ \boldsymbol{\sigma} \cdot \mathbf{n} = \boldsymbol{\tau} & \text{on } \partial\Omega_N, \\ \mathbf{u} = \mathbf{u}_0 & \text{on } \partial\Omega_D, \\ \boldsymbol{\sigma}^\pm \cdot \mathbf{n}_{\Gamma^\pm} = p_f \mathbf{n}_{\Gamma^\pm} & \text{on } \Gamma^\pm. \end{cases} \quad (6.7)$$

where  $\mathbf{f}$  denotes an external body force and  $\boldsymbol{\tau}$  is a traction force. Multiplying (6.7) by a test function  $\delta \mathbf{u} \in H^1(\Omega \setminus \Gamma)$  that vanishes on  $\partial\Omega_D$  and using Green's theorem, we obtain

$$\int_{\Omega \setminus \Gamma} \mathbf{C} \left( \boldsymbol{\varepsilon}(\mathbf{u}) - \frac{\alpha}{N\kappa} p_p \mathbf{I} \right) \cdot \boldsymbol{\varepsilon}(\delta \mathbf{u}) \, dV = \int_{\partial\Omega_N^m} \boldsymbol{\tau} \cdot \delta \mathbf{u} \, dS + \int_{\Gamma} p_f [\delta \mathbf{u} \cdot \mathbf{n}_{\Gamma}] \, dS + \int_{\Omega \setminus \Gamma} \mathbf{f} \cdot \delta \mathbf{u} \, dV, \quad (6.8)$$

where  $N = 2$  and  $N = 3$  for 2D and 3D respectively and  $\kappa$  denotes the material's bulk modulus. We recall that given  $p_p$ ,  $p_f$ , and  $\Gamma$ , Equation (6.9) is the unique solution of the minimization among all kinematically admissible displacement of

$$\mathcal{P} = \int_{\Omega \setminus \Gamma} W(\boldsymbol{\varepsilon}(\mathbf{u}), p_p) \, dV - \int_{\partial\Omega_N^m} \boldsymbol{\tau} \cdot \mathbf{u} \, dS - \int_{\Gamma} p_f [\mathbf{u} \cdot \mathbf{n}_{\Gamma}] \, dS - \int_{\Omega \setminus \Gamma} \mathbf{f} \cdot \mathbf{u} \, dV, \quad (6.9)$$

where

$$W(\boldsymbol{\varepsilon}(\mathbf{u}), p) := \frac{1}{2} \mathbf{C} \left( \boldsymbol{\varepsilon}(\mathbf{u}) - \frac{\alpha}{N\kappa} p_p \mathbf{I} \right) \cdot \left( \boldsymbol{\varepsilon}(\mathbf{u}) - \frac{\alpha}{N\kappa} p_p \mathbf{I} \right), \quad (6.10)$$

is the poro-elastic strain energy density (Yoshioka and Bourdin, 2016).

## 6

### 6.2.3. PHASE-FIELD APPROXIMATION

The numerical implementation of the minimization of Equation (6.4) involves discontinuous deformation across unknown discontinuity surfaces (the cracks),  $\Gamma$ , which pose significant challenges in terms of numerical implementation. Instead, Equation (6.4) is regularized using the phase-field approach (Bourdin et al., 2000, 2008).

Introducing a scalar phase-field variable,  $v : \Omega \mapsto [0, 1]$ , which represents a state of the material from intact material ( $v = 1.0$ ) to fully broken ( $v = 0.0$ ) with a continuous function and a regularization parameter with the dimension of a length,  $\ell_s > 0$ , which controls the transition length of the phase-field variable, Equation (6.4) can be approximated as (Bourdin et al., 2012)

$$\mathcal{F}_{\ell_f} = \int_{\Omega} v^2 W \, dV - \int_{\partial\Omega_N^m} \boldsymbol{\tau} \cdot \mathbf{u} \, dS - \int_{\Omega} \mathbf{f} \cdot \mathbf{u} \, dV + \int_{\Omega} p_f \mathbf{u} \cdot \nabla v \, dV + \frac{1}{4c_n} \int_{\Omega} G_c \left( \frac{(1-v)^n}{\ell_s} + \ell_s |\nabla v|^2 \right) \, dV, \quad (6.11)$$

where  $c_n$  is a normalization parameter defined as  $c_n := \int_0^1 (1-s)^{n/2} \, ds$ . Case  $n = 1$  is often referred as  $AT_1$  ( $c_n = 3/2$ ) and case  $n = 2$  as  $AT_2$  ( $c_n = 1/2$ ) (Tanné et al., 2018). It can then be shown (Ambrosio and Tortorelli, 1990, 1992; Braides, 1998) that as  $\ell_s$  approaches 0, the minimizers of Equation (6.11) converge to that of Equation (6.4) in the sense that the phase-field function  $v$  takes value 1 far from the crack  $\Gamma$  and transitions to 0 in a region of thickness of order  $\ell_s$  along each crack faces of  $\Gamma$ .

We can observe that in Equation (6.11), the evolution of the phase-field ( $v$ ) is driven by the strain energy ( $W$ ) regardless of the deformation direction, which leads to equal strength in tension and compression – a wrong approximation for granular material such as rock. To overcome the limitation, the strain energy can be decomposed into the positive (extension) and negative (shortening) parts

$$W = W^+ + W^-. \quad (6.12)$$

Among the several approaches for the strain decomposition (Amor et al., 2009; Miehe et al., 2010; Freddi and Royer-Carfagni, 2011), we employ the so-called masonry model (Freddi and Royer-Carfagni, 2011), in which the material will not withstand tensile stresses.

Open natural fractures can be represented by assigning either the phase-field variable  $\nu = 0.0$  (Yoshioka and Bourdin, 2016; Ni et al., 2020) or the fracture toughness  $G_c^{\text{int}} = 0.0$  ( $\nu = 0.0$  is achieved where  $G_c^{\text{int}}$  is assigned with 0.0 at the first iteration). In this study we represent discontinuous interfaces by a diffused variable of the phase-field type ( $\tilde{G}_c^{\text{int}}$ ) whose fracture toughness or cohesive strength ( $G_c$ ) is different from the surrounding (Fig. 6.2). Altering  $G_c$  gives us a greater flexibility as it can represent from open ( $G_c^{\text{int}} = 0.0$ ), partially cemented/weakly bonded ( $G_c^{\text{int}} < G_c^{\text{bulk}}$ ), to cemented with a stiffer material ( $G_c^{\text{int}} > G_c^{\text{bulk}}$ ) while  $\nu$  represents a diffused state of fracture not the strength. To compensate the fracture toughness in the smeared interface  $x < b$ , we solve the surface energy functional in Equation (6.11) for the effective fracture toughness,  $\tilde{G}_c^{\text{int}}$  (Hansen-Dörr et al., 2019). The surface energy equality can be imposed as

$$\tilde{G}_c^{\text{int}} \int_{\Omega} S dV = G_c^{\text{int}} \int_{\xi=0}^{\xi=b} S dV + G_c^{\text{bulk}} \int_{\xi=b}^{\infty} S dV, \quad (6.13)$$

where

$$S = \frac{1}{4c_n} \left( \frac{(1-\nu)^n}{\ell_s} + \ell_s |\nabla \nu|^2 \right), \quad (6.14)$$

and  $\xi$  is the distance from the crack ( $\nu = 0$ ). We built the FEM model containing natural fractures by assigning the equivalent fracture toughness computed in Equation (6.13) to the region within distance  $b$  from the fractures.

#### 6.2.4. NUMERICAL IMPLEMENTATION

We neglect leak-off to the rock mass because the permeability of the rock mass is sufficiently low. The pore-pressure  $p_p$  can be considered invariant and set as  $p_p = 0$ , and  $p'_f = p_f - p_p$  in the governing equations. We adopt the notation  $p'_f = p$ . Considering hydraulic fracturing in the toughness dominated regime (Detournay, 2016), the pressure loss within the crack is negligible and  $p$  is spatially constant. Equation (6.11) is solved by the alternate minimization with respect to the displacement  $\mathbf{u}$  and the phase-field  $\nu$  with a constraint of prescribed time-evolving fluid volume which must be equal to the crack volume, i.e.,  $V_{\text{inj}} = V_{\text{crack}} = \int_{\Omega} \mathbf{u} \cdot \nabla d d\Omega$  (Yoshioka et al., 2019). The minimization problem can be stated as

$$(\mathbf{u}, \nu, p)^* = \arg \min \mathcal{F}_{\ell_f}(\mathbf{u}, d, p), \quad (6.15)$$

$$\begin{cases} \mathbf{u} \in H^1 \\ \nu \in H^1, \nu^t \subset \nu^{t+\Delta t} \end{cases}$$

with the constrain

$$V_{\text{inj}} = \int_{\Omega} \mathbf{u} \cdot \nabla v \, d\Omega. \quad (6.16)$$

The first variation of the energy functional with respect to  $\mathbf{u}$  is

$$\begin{aligned} \delta \mathcal{F}_{\ell_f}(\mathbf{u}, v, p; \delta \mathbf{u}) &= \frac{1}{2} \int_{\Omega} \boldsymbol{\varepsilon}(\delta \mathbf{u}) : (v^2 \mathbf{C}^+ + \mathbf{C}^-) : \boldsymbol{\varepsilon}(\mathbf{u}) \, d\Omega \\ &\quad - \int_{\partial_N \Omega} \boldsymbol{\tau} \cdot \delta \mathbf{u} \, d\Gamma - \int_{\Omega} \mathbf{f} \cdot \delta \tilde{\mathbf{u}} \, d\Omega + \int_{\Omega} p \delta \mathbf{u} \cdot \nabla v \, d\Omega, \end{aligned} \quad (6.17)$$

where  $\mathbf{C}^{\pm}$  is the tangent stiffness tensor

$$\mathbf{C}^{\pm} = \frac{\partial}{\partial \boldsymbol{\varepsilon}} \left( \frac{\partial W^{\pm}}{\partial \boldsymbol{\varepsilon}} \right). \quad (6.18)$$

The first variation of the energy functional with respect to  $v$  for AT<sub>1</sub> is

$$\delta \mathcal{F}_{\ell_s}(\mathbf{u}, v, p; \delta v) = \int_{\Omega} v \delta v \mathbf{C}^+ \boldsymbol{\varepsilon}(\mathbf{u}) \cdot \boldsymbol{\varepsilon}(\mathbf{u}) \, dV + \frac{3}{8} \int_{\Omega} G_c \left( -\frac{\delta v}{\ell_s} + 2\ell_s \nabla v \cdot \nabla \delta v \right) \, dV - \int_{\Omega} p \mathbf{u} \cdot \nabla \delta v \, dV, \quad (6.19)$$

and for AT<sub>2</sub> is

$$\delta \mathcal{F}_{\ell_s}(\mathbf{u}, v, p; \delta v) = \int_{\Omega} v \delta v \mathbf{C}^+ \boldsymbol{\varepsilon}(\mathbf{u}) \cdot \boldsymbol{\varepsilon}(\mathbf{u}) \, dV + \int_{\Omega} G_c \left( \frac{v-1}{\ell_s} \delta v + \ell_s \nabla v \cdot \nabla \delta v \right) \, dV - \int_{\Omega} p \mathbf{u} \cdot \nabla \delta v \, dV. \quad (6.20)$$

Equation (6.7) is linear to  $p$  and if we let the displacement solution with  $p = 1.0$  be equal to  $\mathbf{u}_1$ , the displacement solution  $p = p$  is obtained as  $\mathbf{u} = p \mathbf{u}_1$  and the crack volume is

$$\int_{\Omega} \mathbf{u} \cdot \nabla v \, d\Omega = p \int_{\Omega} \mathbf{u}_1 \cdot \nabla v \, d\Omega. \quad (6.21)$$

At a given time step, a volume  $V_{\text{inj}}$  is injected and equation (6.16) yields the mass balance in the porous medium such that the corresponding  $p$  is

$$p = \frac{V_{\text{inj}}}{V_p}, \quad (6.22)$$

where

$$V_p = \int_{\Omega} \mathbf{u}_1 \cdot \nabla v \, d\Omega, \quad (6.23)$$

and the whole solution procedure is described in Algorithm 1.

Parallel simulations were run on the high-performance computing system JUWELS, maintained at the Jülich Supercomputing Centre. The total number of degree of freedom for the Aocolulco case scenarios is 513 108 with 170 996 linear quadrilateral elements with a few triangular elements in the mesh resolution transition zone. Domain-decomposition was done using METIS (Karypis and Kumar, 1998) and both linear and non-linear solvers

from PETSc Balay et al. (2019) were used. More specifically, the Newton–Raphson solver for the deformation problem and a Newton based variational inequality solver for the phase-field, since the phase-field solution is bounded in  $[0, 1]$  domain and constrained by the irreversibility. The simulations were distributed into 384 cores over 8 nodes (Dual Intel Xeon Platinum 8168) with  $2 \times 24$  cores. While the computation time differs depending on the non-linearity of each problem, all the simulations shown in the subsequent section were completed within  $\sim 20$  h.

---

**Algorithm 1** Incorporation of the volume constraint in the phase-field model.
 

---

- 1: **repeat**
  - 2:   Update the injected volume,  $V_{\text{inj}}(t_n + \Delta t)$
  - 3:   **repeat**
  - 4:     Solve for  $\mathbf{u}_1^i$ , given  $v^{i-1}$  and  $p = 1.0$
  - 5:     Solve for  $v^i$ , given  $\mathbf{u}^i$  and  $p = p^{i-1}$
  - 6:     Calculate  $V_p^i$  from  $\int_{\Omega} \mathbf{u}^i \cdot \nabla v^i \, d\Omega$
  - 7:     Update pressure,  $p^i = V_{\text{inj}} / V_p^i$
  - 8:   **until**  $\|v^i - v^{i-1}\| < 10^{-4}$
  - 9: **until**  $V < V_{\text{final}}$
- 

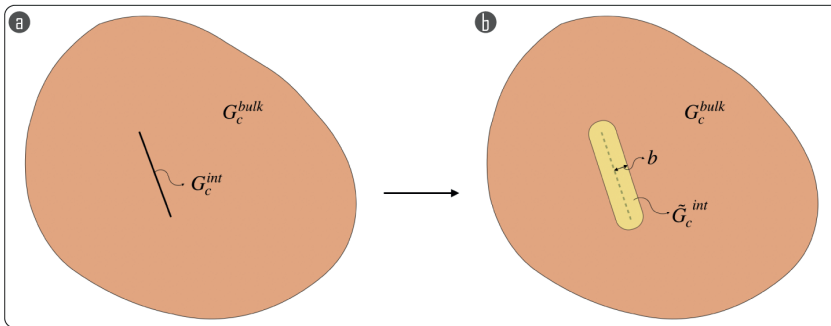


Figure 6.2 – Diffused representation of a discontinuous interface

## 6.3. APPLICATIONS

### 6.3.1. SENSITIVITY ANALYZES

We perform a sensitivity analysis to highlight the complex interactions between fluid-driven propagating fractures and existing ones. We analyze simplified models assuming a perfectly homogeneous brittle linear elastic material containing one or two pre-existing natural fractures. We evaluate the impact on fracture initiation and propagation given by stiffness (elastic parameters) and strength (fracture toughness) of the bulk rock, existing fractures, state of stress and orientation angle of the natural fractures. The base case parameters of the sensitivity analysis are in the range of the studied rocks of the Aconcuelco reservoir, i.e.,  $G_c = 100$  Pam,  $E = 25$  GPa and  $\nu = 0.2$ .



As implemented in the V-pf, the interaction with the pre-existing natural fractures is partly controlled by the critical energy release rate of the natural fracture  $\tilde{G}_c^{\text{int}}$ . We compare results for  $G_c = 1$  with different values of  $\tilde{G}_c^{\text{int}}$  spanning four orders of magnitude, i.e.,  $\tilde{G}_c^{\text{int}} = 0.01, 0.05, 0.1, 10$ . We analyze the impact of the far-field deviatoric stress by increasing the  $S_{Hmax}$  from 21 MPa to 60 MPa with a fixed  $S_{hmin} = 20$  MPa. All case scenarios are presented in Table 6.1. We finally analyze the influence of a natural fracture oriented  $45^\circ$  from the direction of hydraulic fracture propagation to study the effect of the incidence angle between the direction of propagation and the orientation of a natural fracture.

Table 6.1 – Case scenarios of the sensitivity analysis with different stress fields applied. Stress values are expressed in MPa.

Case	$S_{Hmax}$	$S_{hmin}$
A	21	20
B	30	20
C	40	20
D	60	20

### 6.3.2. THE ACOCULCO GEOTHERMAL RESERVOIR

In this manuscript, we analyze the potential permeability enhancement in a fractured reservoir by modeling the fracture growth from a well-bore injection. We apply the developed numerical methodology described in section 6.2 on the Acoculco case scenario, considering the local geological features and the rock properties gathered from field campaigns and laboratory measurements. Here we report a brief synthesis of the experimental program, field campaign, DFN construction algorithm and results, while further details can be found in the original works (Lepillier et al., 2020a, 2019).

The Acoculco geothermal field, located in Mexico, hosts two vertical exploration wells (named EAC1 and EAC2) drilled at  $\sim 500$  m apart horizontally, both reaching a total depth of  $\sim 2$  km (López-Hernández et al., 2009; Canet et al., 2015a; Weydt et al., 2018). On the one hand, Acoculco is considered a tight reservoir because the rock formations are little permeable ( $10^{-18}$  m<sup>2</sup>) and the fractures are scarcely connected (Lepillier et al., 2020a); on the other hand, it is a suitable candidate for EGS development because of its high geothermal energy potential given that the geothermal gradient is above average ( $\sim 150^\circ\text{C km}^{-1}$ ). The stratigraphy encountered during drilling is simplified into three lithological units: Limestones, Marbles, Skarns. Stiffness ( $E$  and  $\nu$ ), strength and critical energy release rate ( $G_c$ ) of the three lithologies were measured in the rock physics laboratory. Young's modulus and Poisson's ratio were determined by Unconfined Compression Strength (UCS) tests (UCS - 20 experiments). Brazilian disc (BD - 80 experiments) and Chevron Bend tests (CB - 12 experiments) were employed to determine the fracture toughness  $K_{Ic}$  of the rock formations, which was later employed to derive the critical energy release rate ( $G_c$ ). Fracture toughness was determined from the two sets of experiments: i) from BD tests, it was done following the method proposed by Guo et al. (1993) and ii) for CB tests, following the method suggested by Franklin et al. (1988). All material parameters employed in the model are summarized in Table 6.2.

Table 6.2 – Rock mechanical properties from rock physics laboratory measurements. This table summarizes the main results of the laboratory measurements for the concerned lithologies: Limestones, Marbles and Skarns. For each of them the table gives: the Young's modulus ( $E$ ), the Poisson's ratio ( $\nu$ ), the fracture toughness ( $K_{Ic}$ ), and Griffith's critical energy release rate ( $G_c$ ). A single final value for specific lithology was selected as the average between different locations outcrops.

Lithology	$E$ GPa	$\nu$ -	$K_{Ic}$ MPam <sup>1/2</sup>	$G_c$ Pam
Limestone Late Cretaceous	37.8	0.31	2.76	201
Limestone Early Cretaceous	37.9	0.23	2.49	164
<b>Limestone</b>	<b>37.9</b>	<b>0.27</b>	<b>2.63</b>	<b>182</b>
Marble from Pueblo Nuevo	46.8	0.25	1.90	77.3
Marble from Tatatila	51.6	0.29	1.85	66.2
<b>Marble</b>	<b>49.2</b>	<b>0.27</b>	<b>1.87</b>	<b>71.4</b>
Exo-skarn from Eldorado	56.9	0.11	2.70	127
Endo-skarn from Boquillas	41.1	0.13	1.92	89.3
<b>Skarn</b>	<b>49.0</b>	<b>0.13</b>	<b>2.31</b>	<b>108</b>

The general DFN is derived from scanline measurements from multiple outcrops analogues of the Acoculco geothermal system (Lepillier et al., 2020a) that are later extrapolated using the multiple point statistic method (Bruna et al., 2019). The method yields three separate DFNs, i.e., one per lithology. Each one of the three DFNs is a bi-dimensional geo-referenced section of  $600 \times 600 \text{ m}^2$  (fig. 6.3). Some further processing is necessary to build the FEM models. In the first step, we extracted from each DFN a smaller sub-domain of  $100 \times 100 \text{ m}^2$  (Figure 6.3). Each extraction has a specific fracture distribution: to analyze the impact of stimulating one or another specific section of the domain. In the second step we extracted an additional three sub-domain from each of the DFNs. The three sub-DFNs, one for each DFN, are then rotated in the third step to align the maximum horizontal stress  $S_{Hmax}$  with the  $x$ -axis and further down-scaled in the fourth step to fit the a-dimensional V-pf formulation.

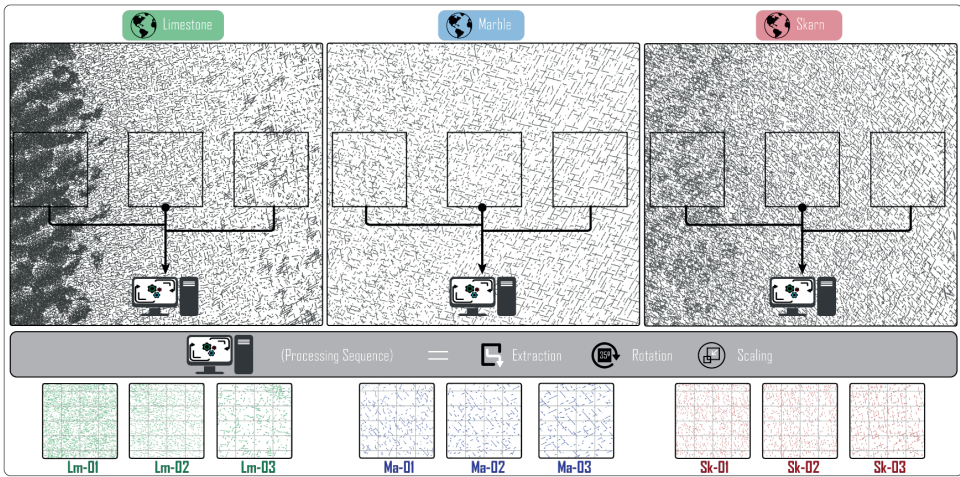


Figure 6.3 – This figure presents the pre-processing sequence: from original reservoir scale DFN, to extracted, rotated and scaled models to fit the numerical analyzes requirements. From left to right, the DFN for the Limestone formation, the DFN for the Marble formation and the DFN for the Skarn formation. Symbols Lm/Ma/Sk-01,-02,-03 are referred to the sub-DFN extracted from initial DFN.

## 6

The in-situ stress state is believed to be of the normal faulting type and the orientation of the stress tensor is taken from the World Stress Map (Lepillier et al., 2019; Heibach et al., 2016). Based on this assumption, having  $S_v > S_{Hmax} > S_{hmin}$ , we defined certain values for  $S_{Hmax}$  and  $S_{hmin}$ . In normal-faulting regime, the hydraulic fracture propagates along the vertical plane oriented perpendicular to  $S_{hmin}$ . Because of this, we assume 2-dimensional plane-strain conditions were we assign only  $S_{Hmax}$  and  $S_{hmin}$ .

## 6.4. RESULTS

### 6.4.1. SENSITIVITY ANALYSIS

Figure 6.4 shows the influence of strength ( $G_c$ ) and stiffness ( $E$  and  $\nu$ ) on the internal fracture over-pressure and length evolution during hydraulic fracture propagation at constant fluid injection-rate. The critical energy release rate  $G_c$  is the dominant parameter controlling the hydraulic fracture response (fig. 6.4a):  $G_c$  represents the resistance to fracture propagation, hence is proportional to the maximum overpressure reached and inversely proportional to the rate of crack length growth during injection. The stiffness parameters play a smaller role on the problem evolution, and, whilst the influence of Poisson's ratio seems to be negligible over the selected range (Figure 6.4c), an increase in Young's modulus entails an increase in fracture propagation resistance (fig. 6.4b). Maximum over-pressure is proportional to Young's modulus and inversely proportional to the injected volume at propagation onset.

The delay in crack propagation onset is a consequence of lower stiffness: the more the rock is compliant, the larger the volume of fluid needs to be injected before the crack internal pressure reaches the propagation condition and the energy release rate equals its critical value. Globally, it can be interpreted as a higher system compressibility, where

more compliant systems require higher volume of injected fluids.

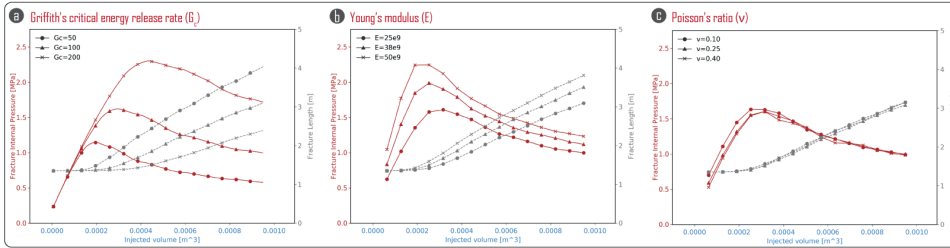


Figure 6.4 – Sensitivity analysis of mechanical material properties. The plots report the evolution of fracture internal over-pressure (reds) and fracture length (greys) against the injected volume: in (a) for different values of the critical energy release rate of the bulk solid  $G_c = 50, 100, 200 \text{ Pa}\cdot\text{m}^{-1}$ ; in (b) for different elastic parameters of Young's modulus with  $E = 25, 38, 50 \text{ GPa}$ ; and (c) different Poisson's ratio  $\nu = 0.10, 0.25, 0.40$ .

Figure 6.5 shows results of the sensitivity analysis of the interaction between a fluid-driven fracture (the phase-field) and two natural fractures at equivalent time steps.

When the natural fracture strength is considerably weaker, the fracture turns at and propagates along the vertical natural fractures ( $\tilde{G}_c^{\text{int}} = 0.01$  and  $\tilde{G}_c^{\text{int}} = 0.05$ ). These cases exhibit asymmetrical growth when the tips hit the natural fractures by extending only one of the tips rather than the both. Energetically, propagation of one of the tips is as easy as that of the other while propagating the both simultaneously is more expensive. In other words, the energy required to propagate the right tip equals the energy required for the left tip propagation. As a consequence of the energy minimization in such a situation, propagation of one of the tips (not the both) will be eventually chosen as “minimum” energy state since numerically one of the energies is always smaller than the other by some truncation. However, once either one is chosen, this side will be always the easier direction (will require less energy) in the subsequent propagation. For  $\tilde{G}_c^{\text{int}} = 0.1$ , the natural fractures do not have low enough strength and are crossed by the hydraulic fracture without branching (fig. 6.5). For  $\tilde{G}_c^{\text{int}} > G_c$ , the natural fractures act as a barrier to the hydraulic fracture. After the crack hits the natural fracture, it propagates in a path avoiding the natural fracture. In this case, the natural fracture acts as a barrier, shielding the hydraulic fracture propagation. Note that branching in general is energetically more expensive (less favored) as it is avoided in the  $\tilde{G}_c^{\text{int}} = 10$  case, but does happen when the surface energy of the natural fractures are so low that crack propagation along them becomes more attractive.

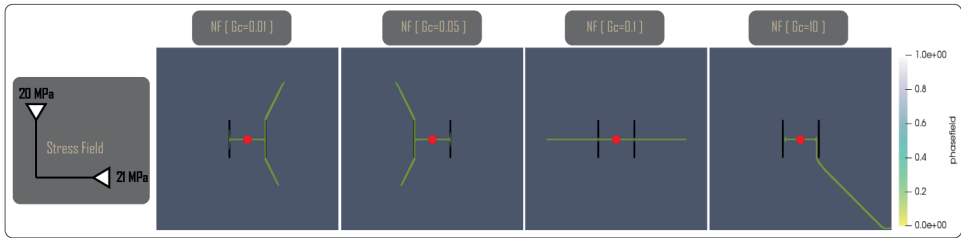


Figure 6.5 – Sensitivity analysis of the influence of two vertical natural fractures. The results show the phase-field distribution contour map in the domain at the same time step for a constant stress field and different critical energy release rate of the natural fracture  $\tilde{G}_c^{\text{int}}$ . The stress field is oriented such that  $S_{Hmax}$  is aligned along the horizontal direction. The red dots represents the well-bore and initial fracture position (and initial phase-field implementation)

At increasing values of differential stress (fig. 6.6), and for fixed  $\tilde{G}_c^{\text{int}} = 0.01$ , the branching observed at low deviatoric stress disappears for  $S_{Hmax} \geq 30$  MPa. The critical stress intensity factor at the tip of the natural fracture is proportional to the horizontal stress and propagating a fracture parallel to  $S_{Hmax}$  through the bulk rock requires less energy than propagating it through the vertical natural fracture. Therefore, with higher deviatoric stress, considering a natural fracture oriented  $90^\circ$  will not change the propagation direction as the stress dictates the propagation direction.

6

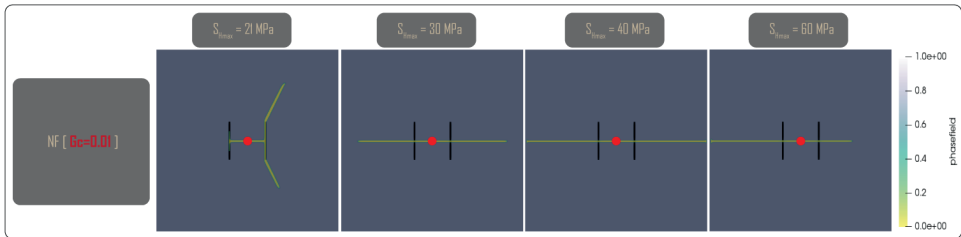


Figure 6.6 – Sensitivity analysis of the influence of two vertical natural fractures. The results show the phase-field distribution contour map in the domain at the same time step for a constant critical energy release rate of the natural fracture  $\tilde{G}_c^{\text{int}}$  and different stress field values  $\tilde{G}_c^{\text{int}} = 0.01$ . The stress field is oriented such that  $S_{Hmax}$  is aligned along the horizontal direction. The red dots represents the well-bore and initial fracture position (and initial phase-field implementation)

A  $45^\circ$ -oriented fracture has an orientation which is closer to the critical one for the given state of stress, hence it influences the propagation and interaction regime differently than vertical natural fracture (fig. 6.7). With only one natural fracture present, the problem is intrinsically asymmetric. At  $\tilde{G}_c^{\text{int}} = 0.01$ , the hydraulic fracture first interacts with the natural fracture and later propagates in the direction of  $S_{Hmax}$  (fig. 6.7a) and at  $\tilde{G}_c^{\text{int}} = 0.1$ , the hydraulic fracture propagation is still attracted by the inclined natural fracture but not as much as the case with  $\tilde{G}_c^{\text{int}} = 0.1$ . For high values of the natural fractures' critical energy release rate, i.e., for  $\tilde{G}_c^{\text{int}} = 10$ , even though the natural fracture is more favorably oriented, it becomes once again a barrier to fracture propagation (fig. 6.7a). For  $\tilde{G}_c^{\text{int}} = 0.01$  with varying horizontal stresses  $S_{Hmax}$ , the hydraulic fracture

propagation along the natural fracture is progressively hindered with increasing  $S_{Hmax}$  (fig. 6.7b). At  $S_{Hmax} = 40$  MPa, the hydraulic fracture shows a small offset at the natural fracture's crossing point while the hydraulic fracture becomes agnostic to the natural fracture with  $S_{Hmax} = 60$  MPa.

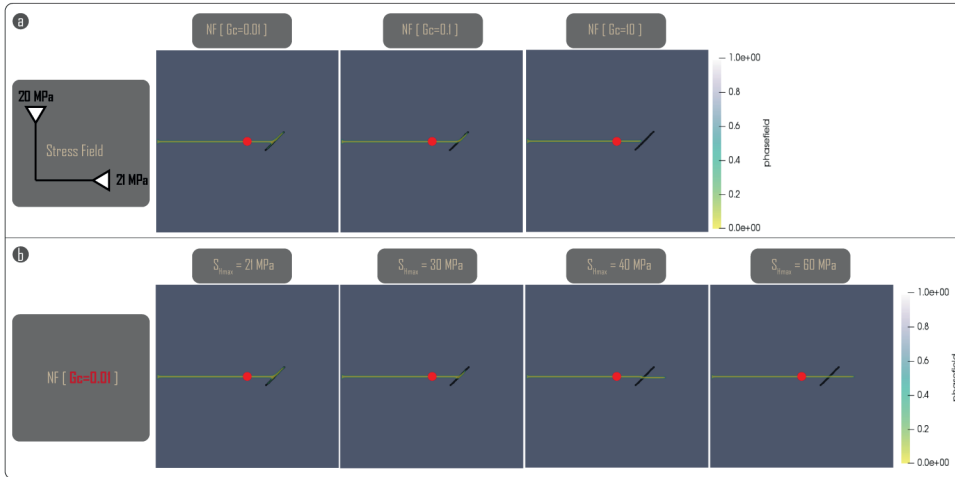


Figure 6.7 – Sensitivity analysis of the influence of one natural fracture inclined at  $45^\circ$  from the horizontal axis. The results show: (a) the phase-field distribution contour map in the domain at the same time step for a constant stress field and different critical energy release rate of the natural fracture  $G_c^{int}$ ; and in (b) for different values of the stress field and a constant critical energy release rate of the natural fracture  $G_c^{int} = 0.01$  (b). The stress field is oriented such that  $S_{Hmax}$  is aligned along the horizontal direction. The red dots represents the well-bore and initial fracture position (and initial phase-field implementation)

#### 6.4.2. STIMULATION OF THE ACOCULCO GEOTHERMAL RESERVOIR

The natural fractures of the Acoculco reservoir are assumed to be cemented and hydraulically closed prior to stimulation. Following our sensitivity studies, we assume the fracture toughness of the natural fracture is 10% of the surrounding ( $G_c^{int} = 0.1 G_c^{bulk}$ ). The simulated domain is discretized using a fixed mesh where the element size is 25 cm.

Figures 6.8, 6.9 and 6.10 show the results of the stimulation scenarios in the Acoculco geothermal reservoir for the different lithologies and for different DFNs. On the left of all figures is plotted the fracture pressure and length with injected volume, while on the right is shown the contour map of the phase-field along with the distribution of natural fractures. For all the cases, the propagation pressure decreases with injected volume as the crack length increases. The pressures started declining rapidly from the onset of the injection/stimulation. This is because the simulations were initiated with a borehole without setting a priori (initial) fracture lengths, as often done in practice, which led to the high breakdown pressures. Such high pressure responses may not be observed in fields because: 1) the borehole intersects with pre-existing fractures or defects or 2) the borehole is completed with perforations or well production packers. However, if fracture is initiated in a intact rock, this level of high pressure should be expected. The fracture length increment with time shows a burst-like behavior: whenever the hydraulic fracture

interacts with a natural fracture, the pressure drops as a consequence of the increase in available fluid storage capacity given by the crack sudden propagation over a finite distance within the natural fracture.

Considering all lithologies, the final fracture length ranges between  $\sim 75$  m to  $\sim 95$  m and the lowest propagation pressure is observed for the Marble stimulation cases (fig. 6.9), whilst the highest propagation pressure is observed for the stimulation into the Limestone formation (fig. 6.8)—a result in agreement with the sensitivity analysis.

## 6

Figure 6.11 shows a polar representation of the hydraulic fracture deviation from the  $x$  direction during propagation. The Limestone simulations show the larger range of fracture lengths spanning from  $\sim 75$  m to  $\sim 95$  m while the Marble's one have the smallest range, spanning from  $\sim 78$  m to  $\sim 79$  m. The angular deviation ranges in an interval of  $20^\circ$  above and below the reference axis given by  $S_{Hmax}$  direction. Maximum deviations are observed in Marble and Skarn simulations, reaching  $30^\circ$  in both simulations, while the deviation angle for the Limestone simulations is contained in a  $20^\circ$  interval.

The asymmetrical propagation of hydraulic fracture from the borehole is a consequence of the intersection angle between natural fracture and the approaching hydraulic fracture. Assuming  $\theta$  as the angle between a natural fracture and the  $S_{Hmax}$  axis, we observed that: *i)* low- $\theta$  natural fracture act as pathways for the hydraulic fracture, which propagates faster along natural fractures; *ii)* high- $\theta$  natural fracture ( $\sim 90^\circ$ ) are by-passed by the hydraulic fracture and no interaction takes place. Intermediate values of  $\theta$  offer a pathway for hydraulic fracture to propagate along a certain distance, until the pressure build-up is sufficiently high to allow further propagation within in the matrix.

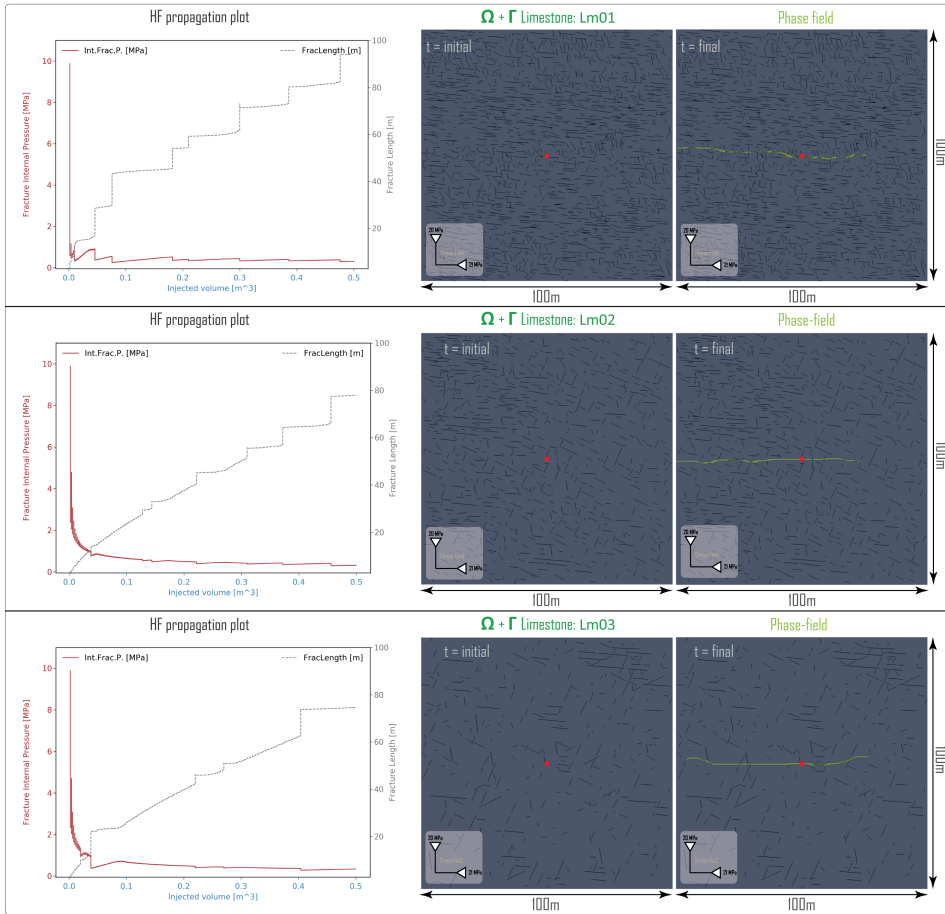


Figure 6.8 – Hydraulic fracture models using V-pf with the sub-DFN of the Limestone reservoir. The matrix material domain  $\Omega$  is represented in grey, the natural fracture  $\Gamma$  are discretized in black. Lm01 is composed with 1483 natural fractures, Lm02 is composed with 709 natural fractures, Lm03 is composed with 327 natural fractures. The stress field is oriented such that  $S_{Hmax}$  is aligned along the horizontal direction. The red dots represent the well-bore and initial fracture position (and initial phase-field implementation)



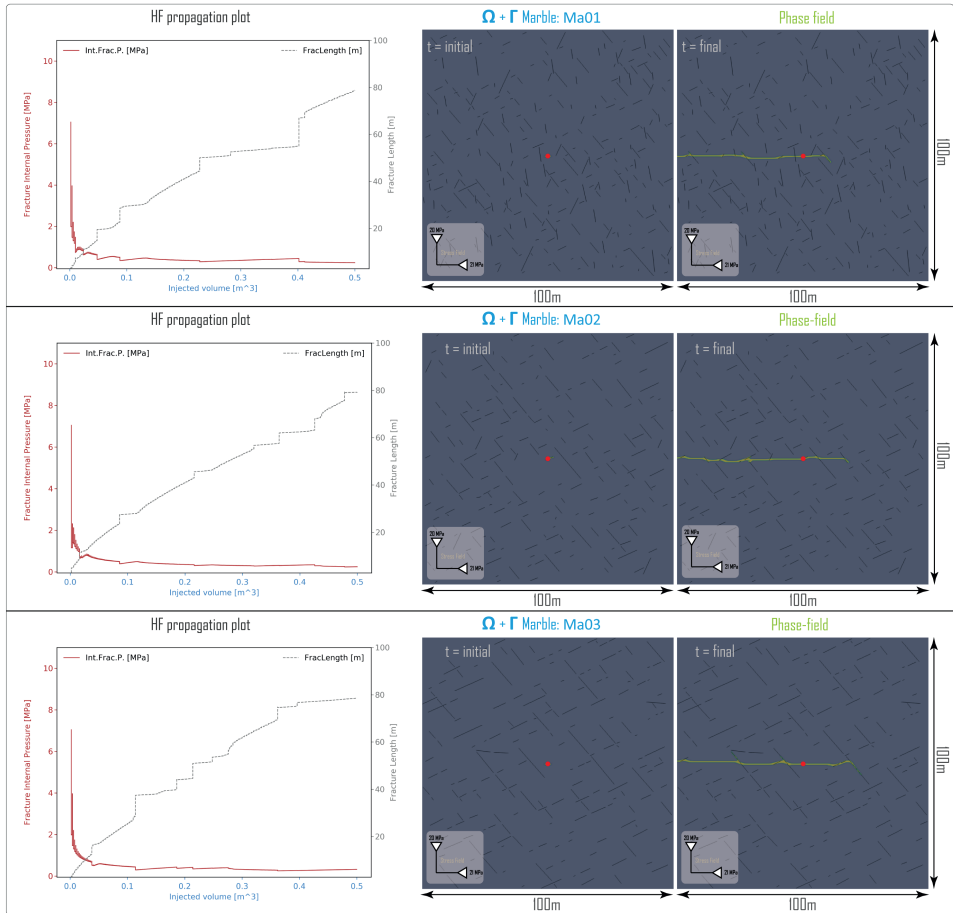


Figure 6.9 – Hydraulic fracture models using V-pf with the sub-DFN of the Marble reservoir. The matrix material domain  $\Omega$  is represented in grey, the natural fractures  $\Gamma$  are discretized in black. Ma01 is composed with 295 natural fractures, Ma02 is composed with 215 natural fractures, Ma03 is composed with 198 natural fractures. The stress field is oriented such that  $S_{Hmax}$  is aligned along the horizontal direction. The red dots represent the well-bore and initial fracture position (and initial phase-field implementation)

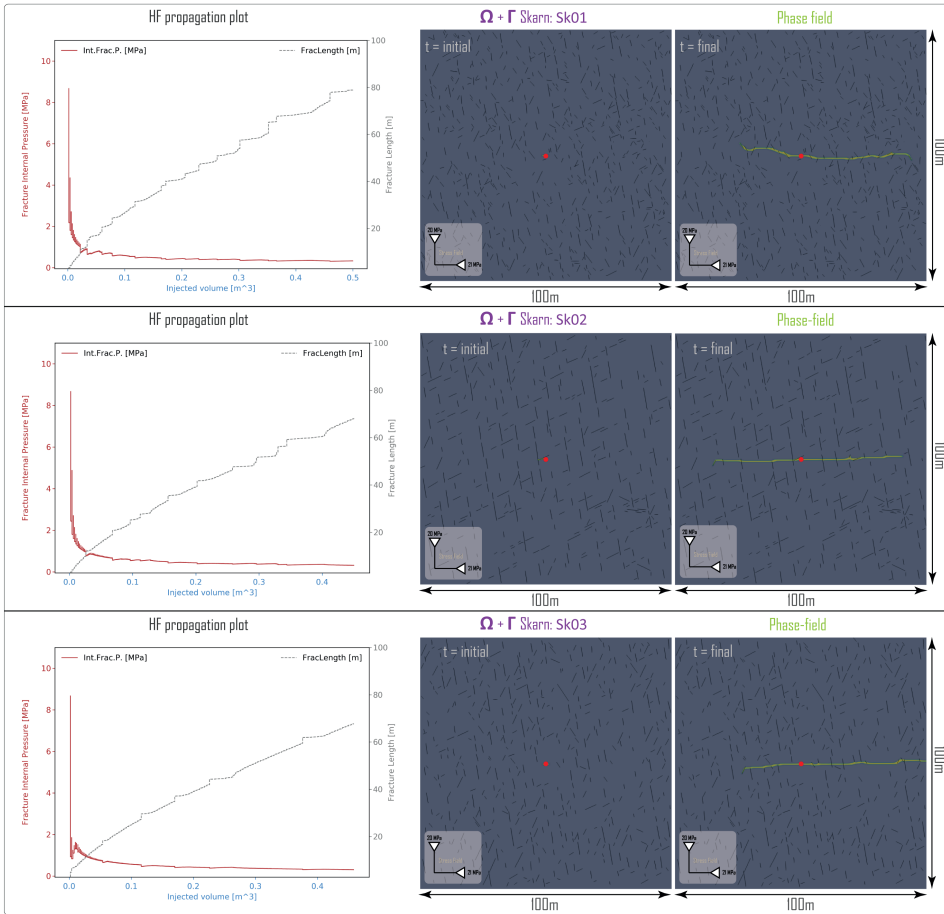


Figure 6.10 – Hydraulic fracture models using V-pf with the sub-DFN of the Skarn reservoir. The martix material domain  $\Omega$  is represented in grey, the natural fractures  $\Gamma$  are discretized in black. Sk01 is composed with 706 natural fractures, Sk02 is composed with 495 natural fractures, Sk03 is composed with 375 natural fractures. The stress field is oriented such that  $S_{Hmax}$  is aligned along the horizontal direction. The red dots represent the well-bore and initial fracture position (and initial phase-field implementation)

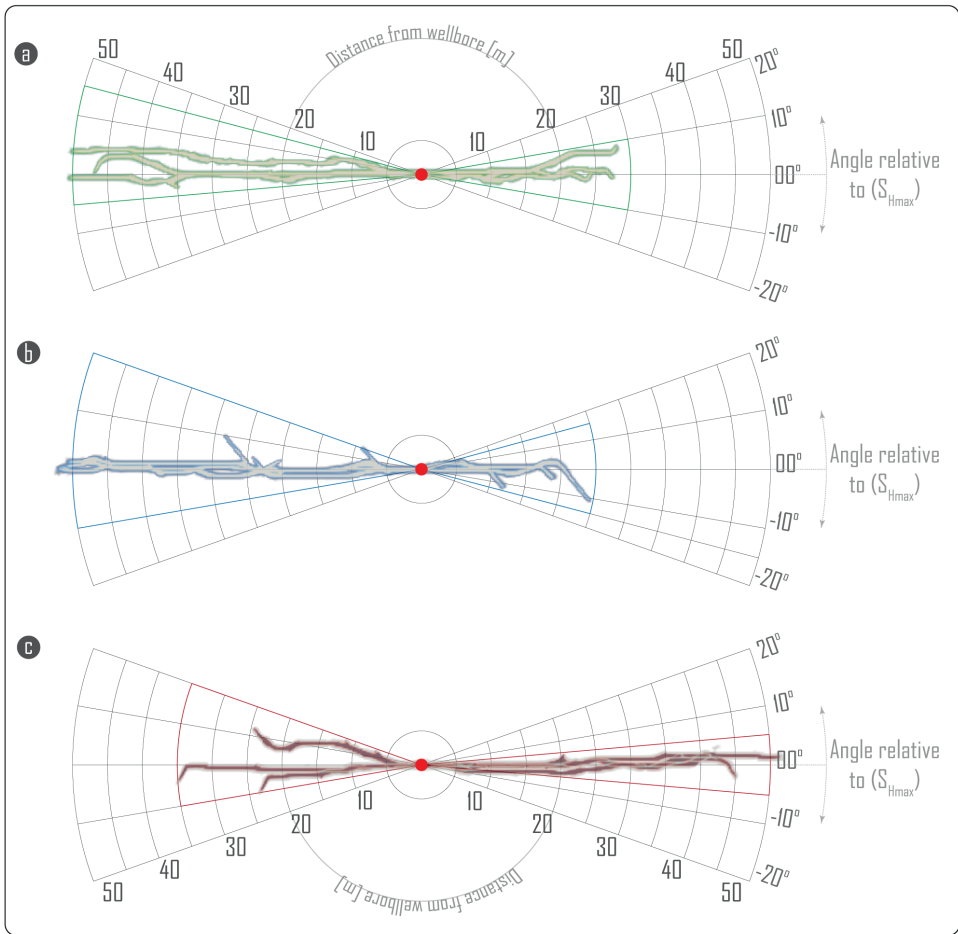


Figure 6.11 – A comparison of hydraulic fracture simulation V-pf models for : a) the Limestones (green color); b) the Marbles (blue color); c) the Skarns (red color); hydraulic fracture lengths are given by the concentric dividers, and hydraulic fracture angles compared to  $S_{Hmax}$ 's orientation is given by the radial dividers.

## 6.5. DISCUSSION

The V-pf method presented here is an implicit smeared approach which represents the fracture with a smoothly transitioning function that spans from intact to fully damaged state of the material. Natural fractures are represented in a non-conforming mesh with the reduced fracture toughness by enforcing energetic equivalence, which is one of the advantages of the method since it allows exploring multiple DFNs scenarios with a single discretization. As presented in this study, the ability of the V-pf is to handle complex fracture topologies with a unified criteria – energy minimization – that seeks for an admissible displacement and a set of fracture geometry that minimizes the total energy without a need for ad-hoc criteria for branching or turning. The model exhibits asymmetric crack growth under some circumstances: the phenomenon is intrinsic to the vari-

ational approach, where the energy minimization leads to the occurrence of asymmetric solutions whenever the total energy of the system is smaller than its symmetric counterpart Tanne (2017). This instability has been theoretically pointed out by Gao and Rice (1987) and it is observed in experiments for a penny-shape crack propagation in toughness dominated regime Bunger et al. (2008, 2013).

The interaction behavior between hydraulic fracture and natural fractures depends: i) on the combination of the critically energy release rate ratio between natural fractures and bulk rock ( $\bar{G}_c^{\text{int}}/G_c$ ); ii) on the natural fractures orientation relative to the stress field; and iii) on the magnitude of principal stress components. Natural fractures can either favor or hamper the propagation of a hydro-fracture according to specific combinations of the input parameters. Natural fractures attract hydraulic fractures for relatively low values of critical energy release rate ratio, when they have orientations close to the critical ones and for relatively isotropic stress states. Natural fractures can be an obstacle to hydraulic fracture growth whenever the fracture resistance becomes higher than the one of the intact rock. Although counter-intuitive, the presence of higher strength discontinuities is a relatively frequent occurrence in deep geothermal systems: the environmental conditions could enhance geochemical reactions of dissolution and precipitation (Singurindy and Berkowitz, 2005; Watanabe et al., 2020), such as silica precipitation (Scott and Driesner, 2018; Lu et al., 2018), and the existence of active volcanism could favor the presence of magmatic intrusions even at shallow depth (Elders et al., 2014) which, if old and cold enough, could represent higher strength and stiffness bodies.

In our analyzes, we have assumed a low permeability that is typical of poorly fractured crystalline rock, an hypothesis that entails no leak-off between the fracture and the porous rock. Such an assumption is equivalent to an undrained response where the change in effective stress within the porous rock is null during injection. Although the fracture toughness (critical energy release rate) is more predominant in controlling propagation conditions when compared to stiffness, Young's modulus of the rock also plays a role. In particular, a more compliant rock requires higher injected volumes, but overall generates lower over-pressure. On the contrary, stiff rocks generate higher over-pressure for a lower injected volume. Because of the high fracture strength, high stiffness and low permeability of basement crystalline rocks, during stimulation of a deep geothermal reservoir high over-pressure can be achieved with relatively low values of injected volume (Ellsworth et al., 2019).

The V-pf simulations of the Acoculco reservoir highlighted a fluctuation in the pressure and crack-length response in time, with intermittent crack advancement and burst-like behavior—a phenomenon observed during several hydraulic stimulations (Milanese et al., 2016). The V-pf implementation adopted is numerically stable and provides continuous pressure-volume response in absence of viscous flow dissipation. The intermittent advancements are a direct consequence of the interaction between existing fractures with lower crack resistance and the fluid driven crack: whenever the hydraulic fracture encounters a natural fracture, if the latter is favorably oriented, the hydraulic fracture encounters almost no resistance and propagates rapidly over a finite length. The pressure drop is associated with a stress release in the rock, which in combination with the crack length increment, can be associated with micro-earthquakes. Micro-seismicity has been widely observed during hydraulic fracturing (Davies et al., 2013; Schultz et al.,

2015; Lopez-Comino et al., 2017) and our results suggest that, in crystalline reservoirs, the phenomenon is associated with hydraulic fractures propagating along pre-existing natural fractures.

Results show that the Marble formation in the Acoculco reservoir is the optimal one for a potential stimulation because the lowest values of propagation over-pressure. The orientation of the natural fractures controls the propagation extent and direction independently of the lithology and the fracture topology dominates the hydraulic fracture response in all cases analyzed. In the present case study we have analyzed homogeneous rock matrix properties, although a more realistic approach should be based on representing fluctuation of the material properties within the rock matrix. Three-dimensional analyzes would be an additional improvement of the current scenarios. Nonetheless, the additional complexity of a three-dimensional reservoir model should be justified by a sufficient knowledge of the reservoir's structure and its property—a current shortcoming for the Acoculco reservoir. Although a normal fault regime is likely at Acoculco reservoir and hydraulic fractures are expected to propagate mainly vertically, there are indications that a strike-slip faulting system could also be active (Liotta et al., 2020), making the full three-dimensional propagation topology rather complex and difficult to estimate a-priori.

There is current uncertainty about the in-situ state of stress at the Acoculco geothermal reservoir and different values of the stress components could yield a different output in terms of hydraulic fracture propagation. Although the DFNs that are built from outcrop extrapolations are also a source of additional uncertainty, the small prominence of fractures in the DFNs seems to be in good agreement with the very low permeability that was observed during well logging: small and poorly connected fractures hamper fluid flow in the tight reservoir.

Stimulating a highly fractured zone of the Acoculco geothermal reservoir requires a lower stimulation pressure, therefore reducing the drilling costs. Additionally, according to the well temperature measurements, the Marble and Skarn formations are more likely to be targeted for stimulation because they are present at a higher depth and therefore, they are at a higher temperature. The formation breakdown pressure is lower for the Marble, which also has a lower density of natural fractures. Nonetheless, the natural fractures in the Marble are longer and better connected when compared to the ones in the Skarn, which are shorter but more frequent. A trade-off arises between the objective of stimulating the hotter formations of the reservoir on the one hand, and stimulating the formations that would yield a longer propagation of the hydraulic fracture on the other hand. The optimal solution would depend on the ultimate goals of the EGS development and a detailed cost-balance analysis is necessary to optimize the stimulation depth.

## 6.6. CONCLUSION

We have presented a method for modeling hydraulic fracture propagation and interaction with a network of natural fractures in a geothermal reservoir. The fracture simulations are based on a variational phase-field approach that proved high numerical stability. We have highlighted the main factors controlling the hydraulic fracture propagation and its interaction with natural fractures through sensitivity analyzes on simplified models. We have applied the method to model a realistic EGS stimulation scenario of

the geothermal reservoir of Acoculco, Mexico. The numerical model is built from field data and model parameters are derived from laboratory experiments.

Building a realistic DFN is an essential piece of the puzzle for numerical analyses of stimulation of complex reservoirs, which can lead to counter-intuitive findings of the propagation mechanisms as opposed to simplified models of single-oriented crack families. Pressure fluctuations and burst-like crack propagation are intrinsically connected to the presence of the complex network of natural fractures.

The numerical model is implemented in the open-source software OpenGeoSys ([www.opengeosys.org](http://www.opengeosys.org)), which can be freely downloaded at <https://github.com/ufz/ogs>. We provide a working methodology for the study of EGS systems and the feasibility analyses of hydraulic stimulation of geothermal reservoirs.

## 6.7. ACKNOWLEDGMENTS

This work is part of the GEMex consortium, a European-Mexican collaboration, which aims at investigating non-conventional geothermal systems: i) an enhanced geothermal system, as studied in the case of Acoculco site; ii) and a supercritical system, as studied in the geothermal field of Los Humeros. We would like to thank all the GEMex team, and especially our Mexican partners who guided us in the field. GEMex has received funding from the European Union's Horizon 2020 research and innovation programme under grant agreement No. 727550 and the Mexican Energy Sustainability Fund CONACYT-SENER, project 2015-04-268074. More information is available on: [www.gemex-h2020.eu](http://www.gemex-h2020.eu).

K.Y. gratefully acknowledges the funding provided by the German Federal Ministry of Education and Research (BMBF) for the GeomInt project, Grant Number 03G0866A, within the BMBF Geoscientific Research Program "Geo:N Geosciences for Sustainability". The contribution of E.P. and K.Y. was funded by the Deutsche Forschungsgemeinschaft (DFG, German Research Foundation) – project number PA 3451/1-1.

Laboratory works who not have been possible without help and support from the laboratory staff. B.L., R.B. and D.B. give thanks to the Delft University of Technology GSE laboratory staff.

The authors gratefully acknowledge the Earth System Modeling Project (ESM) for funding this work by providing computing time on the ESM partition of the supercomputer JUWELS at the Jülich Supercomputing Centre (JSC)

The datasets generated during and analyzed during the current study are available in the repository:

<https://doi.org/10.6084/m9.figshare.12033624.v2>



# 7

## RESULTS, A FULLY INTEGRATED EGS EVALUATION WORKFLOW

*In this study, we develop a workflow to assess the feasibility of applying the EGS approach to the Acoolco geothermal field. The approach aims at generating a realistic predictive mechanical model for hydraulic fracture stimulation from the well borehole. The strength of the method stands in the combination of reliable data obtained from field work and experimental measurements on mechanical properties of the target rocks, used together to populate a numerical model. The workflow starts with the identification and description of the surface discontinuities using the scanline survey method. These surveys are interpolated and extrapolated using the multiple point statistics method to generate geological discrete fracture networks. These discrete fracture networks, together with the mechanical properties measured in the rock physics laboratory are then used to analyze the fracture propagation and its interaction with the pre-existing natural fractures. The results of the hydraulic fracture propagation simulations are then used in a finite element method program to evaluate the heat and fluid flow transfer, comparing reservoir properties before and after treatment. The method offers a physically sound prediction of the reservoir flow characteristics as well as an accurate mechanical model of the fracture propagation and the pressure distribution for well borehole stimulation. Because the workflow is based on easily accessible data and thanks to its simplicity, this approach could be applied in most EGS case studies.*



## 7.1. INTRODUCTION

### 7.1.1. BACKGROUND

In geothermal resource exploration and production, it is essential to understand the role of the Natural Fractures (NF) in subsurface reservoirs (Economides and Nolte, 1989). This is even more true when evaluating the feasibility of an Enhanced Geothermal System (EGS). The concept of the EGS relies upon enhancing the reservoir permeability by stimulating the opening of existing fractures and creation of new ones. The stimulation can be mechanical, chemical, thermal or a combination of all aforementioned. Two main streams could be considered for mechanical stimulations: i) the first one consists of creating or reactivating one large fracture or fault; ii) the second one consists of stimulating a network of NF (Tester et al., 2006; Gallup, 2009). The strong influence of NF on the reservoir's hydraulic flow is well known (Zoback, 2007). It is also known that a propagating fracture is sensitive to rock material heterogeneities (Warpinski and Teufel, 1987; Weng, 2014). NF represent a major part of the reservoir heterogeneities, hence the necessity to evaluate the extent of NF influence on the reservoir stimulation treatment and the field production. The main scientific questions are: i) How to predict a field scale fracture model from outcrop measurements? ii) How to predict a hydraulic fracture (HF) stimulation in a highly fractured reservoir? And iii) how to quantify the effect of NF and stimulated fractures in a geothermal reservoir system?

As this research is part of the GEMex project, an international collaboration between two consortia, from Europe and from Mexico; our workflow has been applied to the Acoculco geothermal field, foreseen as a potential EGS. In this manuscript, we propose a fully integrated workflow: firstly, in section section 7.2.1, we present a method that starts in the field with measuring the NF at an outcrop to build discrete fracture networks (DFN). Secondly, in section section 7.2.2, we introduce a method for modeling HF stimulation in a complex NF reservoir, using the Variational phase-field (V-pf) approach (Alessi et al., 2017; Chukwudozie et al., 2019; Yoshioka et al., 2019) implemented in the open-source OpenGeoSys FEM software (Kolditz et al., 2012). Thirdly, in section section 7.2.3, we evaluate the reservoir enhancement via modeling the heat and fluid mass transfer in the fractured media, comparing performances before and after the stimulation treatment.

### 7.1.2. STUDY CONTEXT

Acoculco is a village located in Puebla at about one hundred kilometers North-East of Mexico City. The field is part of a caldera system, which is part of the country-wide Trans-Mexican Volcanic Belt system. The geological system is made of recent volcanic deposits, covering a large carbonate sequence made of marbles and skarns resulting from a granodioritic intrusion. Two geothermal exploration wells, EAC1 & EAC2, were drilled, in 1995 and 2008 respectively, about 500 m apart from each other. Both wells reached a total drilled depth of about 2 km, and both of them measured a thermal gradient around  $150^{\circ}\text{Ckm}^{-1}$  and very low permeability (Viggiano-Guerra et al., 2011; López-Hernández et al., 2009; Flores-Armenta et al., 2014). According to the geological model, three different lithological formations could be considered as a potential reservoir: the marble formation, the skarn formation or the granodiorite formation (Viggiano-Guerra et al., 2011;

López-Hernández et al., 2009; Flores-Armenta et al., 2014; Lorenzo Pulido et al., 2010; Canet et al., 2015b). Based on recent research (Weydt et al., 2018; Lepillier et al., 2019, 2020a) this manuscript focuses on modelling the stimulation of the marble formation.

### 7.1.3. INNOVATION

As the workflow starts in the field, from sampling rock and measuring fractures, the whole dataset used in this work represents the natural complexity of a subsurface reservoir (fig. 7.1). The resulting discrete fracture networks are very complex and made of thousands of fractures. The rock material properties are derived from rock physics laboratory tests results. Each step of this workflow involves recently developed techniques: i) the DFN are created using a combination of a new processing tool called SkaPy, with the Multiple Point Statistic (MPS) method (Bruna et al., 2019; Lepillier et al., 2020a); ii) HF simulation is modeled by the variational phase-field method (Bourdin et al., 2012; Yoshioka et al., 2019); and iii) the heat and fluid transfer model simulates flow through a highly fractured medium to which the calculated HF is added, which enables to evaluate the impact of the stimulation on the reservoir production performance (Lepillier et al., 2019).

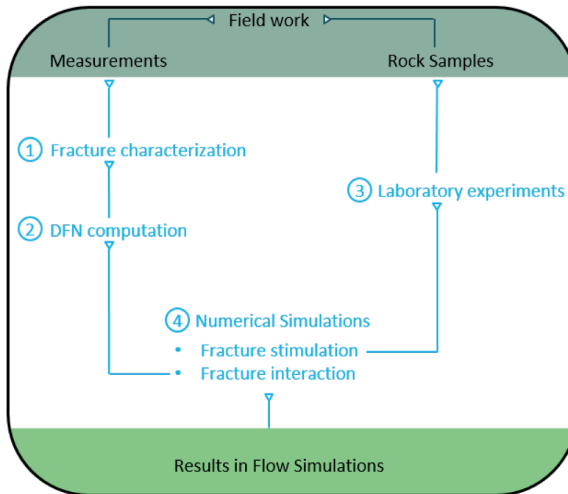


Figure 7.1 – Workflow for developing an Enhanced Geothermal System predictive model. Starting in the field with fracture measurements and rock sampling: Step 1) Fracture characterization; Step 2) DFN computation; Step 3) Rock laboratory testing; Step 4) Numerical simulations: for fracture stimulation and fracture interaction; Results: simulations of thermal and fluid flow through naturally fractured and enhanced fractured media

## 7.2. METHOD & RESULTS

### 7.2.1. FROM SCANLINE TO DFN

NF in reservoir result from phenomena of different origins, sizes, and forces, all of which directly affect the fracture response of the material. As a consequence, NF are organized in space and usually present regular arrangements: the fracture networks. Dif-

ferent methods exist to measure and characterize these networks, such as well log data combined with a high resolution seismic dataset. Unfortunately, accessing the subsurface is expensive and not often available. A common way to analyze the NF organization in space is by using surface analogue outcrops. Recent methods are based on high resolution aerial imagery analysis (using helicopters, airplane, unmanned aerial vehicle or drone), scanning large areas of rock cropping out at the surface. Nevertheless, aerial methods are not always applicable, as in the Acoculco case and its analogue of Las Minas. In Las Minas, the vegetation often covers part of the outcrops, hence automating the imagery processing is tedious. Therefore, we used the linear scanline survey method. The scanline survey method consists of reporting every discontinuity crossing a reference line, by describing the properties of these discontinuities (such as the orientation: strike and dip, length, connectivity, roughness, aperture, filling material, etc.) (e.g. ISRM, 1978; Lamarche et al., 2012; Lavenu et al., 2014).

Scanline surveys result in very detailed datasets. The problem arising then is to find a method to extrapolate from the outcrop scale to the geothermal field scale, while honoring the field characteristics. We apply here an innovative processing procedure that was recently proposed in (Lepillier et al., 2020a). As illustrated in Figure 7.2, the scanline dataset is analyzed and processed using a Python™ script SkaPy. The script screens all fractures and associated measurements, classifies the fractures into sets and extracts the statistical distributions of their properties (such as fracture heights, lengths, apertures, etc). Then SkaPy plots the scanline survey and data in a geo-referenced system allowing its extrapolation. This extrapolation is done manually so that the linear data are converted into a 2 dimensional dataset. This 2D image is here called a Training Image (TI). The created TIs are then analyzed with the MPS method as described in Bruna et al. (2019). The algorithm uses the TIs as pixel-based datasets expressing their discontinuity patterns. These patterns are preserved and used to populate a larger domain computing large field scale DFNs. This method allows to extrapolate outcrop scanlines into, in our case, (600 x 600)m<sup>2</sup> sized DFN models.

### 7.2.2. HYDRAULIC FRACTURE MODELING WITH THE VARIATIONAL PHASE-FIELD (V-PF)

Conventionally, HF modeling is solved by considering that the HF is a planar object opening over time following the principles of Linear Elastic Fracture Mechanics (LEFM) (Adachi et al., 2007). HF models account for different complexity and accuracy, which rely on founding theories of HF modeling (Griffith, 1921; Perkins and Kern, 1961; Geertsma and De Klerk, 1969; Nordgren, 1972), to more recent approaches integrating fluid flow equations and fracture leak-off models (Detournay and Cheng, 1993; Detournay, 2016). These models are acceptable as long as the hypothesis of a disc-shaped HF holds valid. To overcome the disc-shaped hypothesis HF should integrates reservoir heterogeneities and their influence on the HF geometry, including its tortuosity (Weng, 2014). The question then is to what extent NF could influence the HF propagation (Warpinski and Teufel, 1987; Renshaw and Pollard, 1995; Weng, 2014). To address this issue, several numerical approaches were developed, a non-comprehensive list includes the Crack Tip Open Displacement (CTOD) implemented with the Displacement Discontinuity Method (DDM), the Non-Local-Damage (NLD) and Cohesive Zone Model (CZM) implemented with the

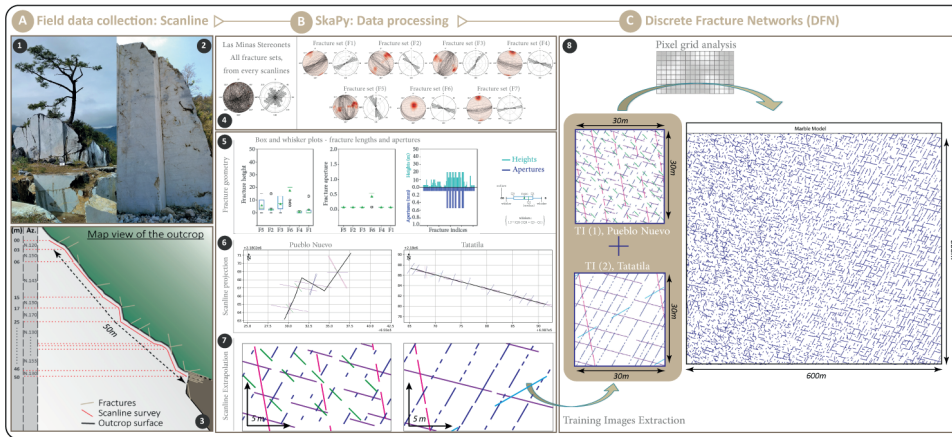


Figure 7.2 – Workflow proposed to create DFNs from surface outcrop scanline surveys, using the SkaPy script and Multiple Point Statistics (MPS) method: A) 1-picture of Pueblo-Nuevo marble outcrop; 2-picture of one of the Tatatila marble quarry walls; 3-sketch describing the scanline reporting method from a map view; B) Example of some SkaPy output: 4-classified fractures into stereonet plots; 5-fracture geometry distributions (here: heights and apertures); 6-plotted scanline survey (black line) and reported fractures (colored lineaments) in a georeferenced system; 7-manually extrapolated model of the fracture distribution used to compute the Training Images (TIs) of the MPS; C) 8- application of the MPS algorithm to the TIs and the resulting DFN model for the marble formation.

Finite Element or Finite Volume Methods (FEM, FVM). More recently the eXtended / Generalized Finite Element Method (XFEM/GFEM), and the variational phase-field (V-pf) approach (e.g. Francfort and Marigo, 1998; Bourdin et al., 2000). The latter is employed in this study using the open-source FEM software OpenGeoSys (Kolditz et al., 2012). The V-pf is a smeared representation of the damage, thus the HF and its propagation over time are represented using a smooth transition function instead of a sharp interface implemented with a non-conforming discretization, which enables handling of HF with complex geometry.

In the Aocolulco case study, as described in Section 7.2.1, we computed a  $(600 \times 600)\text{m}^2$  DFN model of the marble formation. Due to the large uncertainty of the geological context we focused our analysis on a 2D model. From the original DFN, we extract two sub-DFN models of  $(100 \times 100)\text{m}^2$  each. The matter here is to optimize the model between accuracy of the solutions and the computation load. The sub-DFNs, Marble-simulation 1 and Marble-simulation 2, are then populated ( $\Gamma$ ), together with the rock material properties ( $\Omega$ ) obtained from rock laboratory experiments. As very low permeability was measured in the formation downhole as well as on the rock samples in the laboratory, the domain is considered as impermeable, and the fracture leak-off is therefore not considered. Assuming a constant fluid injection rate, the V-pf model for HF propagation is mainly driven by the rock strength ( $G_c$ ), stiffness ( $E$  and  $\nu$ ) and the far field initial state of stress. An illustrative sketch of the model for HF initiation is given in Figure 7.3-A, and for HF interaction in Figure 7.3-B. Figure 7.3-C shows the results of the simulations for Marble simulation 1 and Marble simulation 2. Although the orientation of the HF propagation is mainly controlled by the stress field, the orientation of NF can significantly

change the original trajectory.

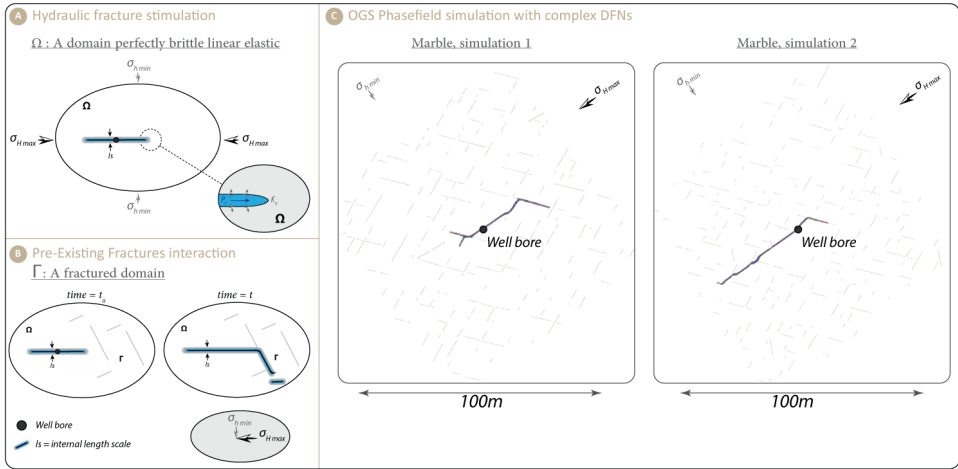


Figure 7.3 – Hydraulic Fracture modeling implementation and results: A) illustration of the HF stimulation initiation controlled by the rock strength ( $G_c$ ), stiffness ( $E$ ,  $\nu$ ), and stress state conditions (stress field); B) Illustration of the HF propagation and interaction with NF over time; C) Results of the HF modeling with the variational phase-field (V-pf) implementation in OpenGeoSys FEM software (left: Marble simulation 1, right: Marble simulation 2)

### 7.2.3. THERMAL & FLUID FLOW MODEL

Once we estimate the NF patterns in the marble formation and simulate the HF propagation in this formation using the extracted sub-DFNs Marble simulation 1 and Marble simulation 2, the reservoir performances, before and after the (simulated) HF treatment, are compared.

The 2D horizontal domain is composed of two sub-domains:  $\Omega$ , representing the porous media, populated with the marble formation properties; and  $\Gamma$ , a second sub-domain discretizing the NF, populated with the geometrical properties (i.e. the fracture aperture) measured at the outcrop during the scanline survey. 1) Firstly, in a steady state analysis, we calculate a mechanical correction of the fracture apertures by applying the stress field conditions to the domain; 2) Secondly, in a transient analysis, we model the heat and fluid flow transfer between two wells, one injector and one producer. The flow rate is set to  $100 \text{ ls}^{-1}$ , the reservoir temperature is at  $300^\circ \text{C}$  and injected fluid is considered pure water at  $50^\circ \text{C}$ . The solid mechanics and the subsurface fluid flow in porous media and the heat transfer are solved by using COMSOL Multiphysics®FEM. Injection and production of fluid from the well bores are idealized as points and placed on a fracture for calculation simplicity. The fully detailed analysis can be found in Lepillier et al. (2019).

Figure 7.4-A illustrates the implementation of the model with the two sub-domains  $\Omega$  and  $\Gamma$ . The permeability of the marble is very low,  $k < 10^{-17} \text{ m}^2$ . Thus, in this model the fluid transports essentially via the NF. The fracture permeability is controlled by the fracture aperture. Figure 7.4-B illustrates the first (steady-state) analysis, where the frac-

ture apertures are corrected by applying the in-situ stresses to the model. Note that we assign a theoretical value of the permeability ( $k = 10^{-14} \text{ m}^2$ ) to the stimulated fracture. This value is deliberately over-estimated to emphasize the results of the simulation. Finally, Figure 7.4-C shows the results of the heat and fluid flow simulations. Here the production performance is evaluated as the estimated fluid flow between the injection and the production wells. As the in-flow and out-flow at the wells, are constrained by the boundary conditions of the model, we look at the lowest  $\Delta P$  as a representation of the best flow. In Figure 7.4-C, the upper left plot represents the  $\Delta P$  over time between the two wells. In red is the simulation before and in green is after the stimulation treatment. The results are really clear, as in the post-stimulation treatment scenario the wells are almost directly communicating. This is also visible in the upper right plot which represents the evolution of temperature over time. The simulation before treatment shows that the flow rate between the wells is really low as the production temperature at the production well (continuous red curve) never declines. The enhanced simulated model shows a cold front (thermal breakthrough) reaching the production well (continuous green curve) after a little more than 30 years.

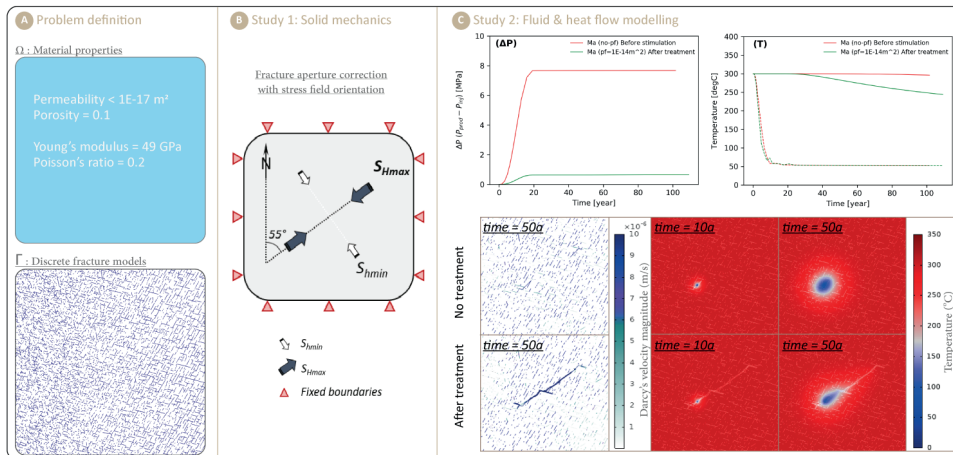


Figure 7.4 – A) Problem definition for heat and fluid flow simulation; B) 1st analysis: steady state, assigning stresses; C) Results of the heat and fluid flow model – upper left: Differential pressure between injection-production wells over time; - upper right: temperature plot at the injection wells (dashed lines) and production wells (continuous line) over time; - lower left: Graphic representation of Darcy's velocity magnitude (left) and temperatures (right) before and after HF treatment.

### 7.3. DISCUSSION

This workflow has been developed to analyze the potential and feasibility of developing an EGS in the Aocolco geothermal field. To obtain a realistic estimation, we need to work with field data. But as the geological model is still relatively uncertain, we focus on 2-Dimensional analyses for solving the essential questions that are related to the NF: how to characterize NF at the field reservoir scale? What is the role of the NF in this reservoir and how do these NF control the current fluid flow? To what extent could the

NF influence the HF propagation? In the process of fracture characterization and DFN generation Section 7.2.1, when the DFN is created, no data from the subsurface are integrated, simply because we had no access to such subsurface data, nor did we include data from the geological map, because the aim is essentially to evaluate the variability of the fracture distributions in space, from one outcrop to the next. Nevertheless, integrating additional geological constrains could generate even more realistic DFNs. Regarding the implementation of the V-pf for HF propagation and interaction with NF: the model was tested under several complex NF scenarios and with different mechanical properties. According to our results, the V-pf model is a robust method that leads to unexpected results that are worth of more refined analyses. The production simulation models in this study are implemented with a very high fracture permeability in the created HF. This is of course not realistic and would therefore benefit from a more accurate estimate. For instance, the HF could be implemented in the steady state analysis to be also corrected with the field stress. This is however not relevant yet as we do not have any constrains on the type of fracture filling material, and thus and their mechanical properties. Here the wells have been positioned such that the HF simulated would overlap and hence make sure that the permeability and production enhancement is observed. Now that the model is verified it would be interesting to estimate a more realistic well spacing. A final point could be raised regarding the way we look at the natural fractures. It is interesting to see that the best NF orientation for fluid flow production might differs from the one for HF stimulation.

## 7.4. CONCLUSION

When investigating the feasibility of an Enhanced Geothermal System, it is fundamental to quantify the role of the natural fracture system. In this study we propose a workflow to predict natural fracture distribution at a field scale from outcrop data. Obtained DFNs results go well beyond a single statistical representation of the fracture networks observed at the surface. By preserving the real fracture distribution as well as measured fracture characteristics such as apertures, lengths and orientations, the DFNs computed can be used to predict reservoir properties, such as bulk permeability. The second part of this article presents the preliminary results of the HF modeling using the variational phase-field method. The results seem to confirm the fundamental role of NF in the HF propagation prediction. By combining the fracture characterization Section 7.2.1, the HF stimulation Section 7.2.2, and the fracture reservoir thermal and fluid flow model Section 7.2.3, we show that even though the targeted formations are highly fractured, the fractures connectivity is the limiting factor for fluid flow circulation through the reservoir but also for predicting HF propagation route. A robust description and quantification of NF could significantly narrow-down the risks and uncertainties in EGS feasibility analyses. The comprehensive analysis of the NF is therefore fundamental when assessing field development strategies, and would thus be a major improvement in the development of the EGS technology.

# 8

## CONCLUSION



Our society works hard to solve the Energy-Climate problem. In this quest, significant research and hope are deployed towards geothermal resources. Among the different ways of using geothermal systems, Enhanced Geothermal Systems (EGS), could make a considerable change by offering a sustainable energy resource.

To date, not many cases proved successful because the technique used for enhancing a reservoir permeability is still very challenging. As seen in this thesis, where only the geological aspect of the EGS technique is treated, identifying the natural fracture distribution in the subsurface reservoirs is very complex; discretizing and modeling the fluid flow in the fractures in addition to the porous media is very complex; predicting the shape and pathway of a stimulated hydraulic fracture is also very complex. Beyond these geological challenges it would be easy to extend to other domains spanning from the well drilling industry, who develops techniques to cope with very high temperatures and pressures, to the social sciences where scientists investigate the reasons of social acceptance through communication and awareness. All these domains are improving, progressively.

In this thesis, I introduced a workflow which covers a large spectrum of the geological domain.

First, I proposed a method to quantify the distribution of natural pre-existing fractures in the subsurface. This integrated workflow is based on easily accessible data, such as for instance scanline survey datasets, and smartly processed using the open-source SkaPy Python<sup>TM</sup> script, and extrapolated with the Multiple Point Statistics method. This workflow has been built with the will of being easily replicable to any datasets. Using the Multiple Point Statistic method in the workflow results in geologically sound models. Producing such realistic models of the subsurface based on surface data is a major step for EGS exploration (chapter 4).

Once the natural fracture distribution in the geothermal reservoir is quantified, the second problem is to evaluate their contribution to mass and heat transfer in a geothermal reservoir. Therefore, I discretized the complex fracture networks and implemented them in a finite element model. Knowing that the fracture distributions within the reservoir formations are not homogeneous, the model compares multi-production scenarios. The different geological formations of Aocolulco geothermal field are investigated using a multi-reservoir analysis. Hence, the models offer comparative production predictions for multiple reservoirs and multiple wellbore positioning scenarios. This is a major step in the process of EGS potential evaluation and risk assessment.

However, there would be no reliable EGS evaluation without a thorough hydraulic fracture prediction model. The third challenge investigated in this thesis is the hydraulic fracture prediction. I covered it using two different methods. The first method focuses on the operational aspect, using a perfectly planar 3-dimensional fracture model. I identified the most influencing parameter involved in the hydraulic fracturing process. Then, using the Aocolulco specific geothermal system, I calculated the relation between the total injected volume and the hydraulic fracture dimensions. The model integrates all the well design and reservoir properties necessary to predict the pressure and stresses induced by the fluid injection. Through the sensitivity analysis and the multiple scenarios analyzed in this study, the model significantly reduces the risks related to reservoir uncertainties. Because the propagating hydraulic fracture could be influenced by

the reservoir heterogeneities, such as natural pre-existing fractures, I studied a second method. Building on the classical hydraulic fracture model, I integrated the reservoir heterogeneities related to natural fractures into the problem. The model uses the variational phase-field, a smeared representation of the damage, thus the hydraulic fracturing process and its propagation over time are represented using a smooth transition function instead of a sharp interface. This difference from a sharp interface to a smooth function is a game changer in the problem of hydraulic fracture numerical modeling: the smooth function considerably increases the calculation stability. The discretization is implemented using a non-conforming mesh, which enables to solve complex geometries. Hence, the hydraulic fracture propagation process is predicted accounting for its potential interaction with natural pre-existing fractures. The results of these simulations confirm the fundamental role played by natural pre-existing fractures in hydraulic fracture predictions, which is essential for developing successful EGS projects.

In conclusion, the exercise of characterizing the fracture distribution in the subsurface would probably always be better solved with accessing subsurface data. However, obtaining such realistic models from surface data is a major step. It makes subsurface reservoir characterization much more accessible to everyone. Solving the fluid flow for both porous media and fractured media is still very complex. In this thesis, we proved that a wise simplification of the problem together with a smart implementation can result in fast computing and accurate results. Finally, we did not only prove the significant role of the natural fractures to predict the hydraulic fracture propagation but also, we implemented it in a very novel approach: the variational phase-field. This fully integrated workflow gives a well constrained analysis for EGS feasibility evaluation. The workflow provides a good estimation of the initial conditions of the reservoir characteristics, including the natural pre-existing fracture influence, before stimulation. Then, this estimation is completed with adding the rock mechanical properties, giving the right inputs to calculate and predict the reservoir stimulation. Finally, the numerical simulations provide a precise estimation of the potential reservoir enhancement. The workflow is illustrated using the Acoculco geothermal field, studied within GEMex.

The Acoculco geothermal field was explored with two geothermal wells and can be well characterized by several analogue outcrops nearby in the Las Minas area, which makes the Acoculco field good site to study an EGS feasibility. However, the workflow presented in this thesis is not restricted to the Acoculco geothermal field but applicable to any field and any location where a fracture dataset and reservoir mechanical data can be acquired. In other words, this integrated workflow could be replicated to any field where an EGS potential needs to be evaluated.



**A**

**APPENDIX**

Code name	Date name	Sampled	GEI Mix. Name	Location Name	Sample Description	Rock Type	Lat (Dec. Deg.)	Long (Dec. Deg.)	Analysis (I)	Status	Analysis (Z)	StatusZ
04-AC-EC	04-AC-EC	Jan-17	04-17-AC-EC	San Miguel Tenango	Early Cretaceous	Limestone	19.89472222	-97.91027222	-97.91027222			
02-AC-EC	02-AC-EC	Jan-17	02-17-AC-EC	San Miguel Tenango	Early Cretaceous	Limestone	19.89555556	19.89555556	-97.91083333			
03-AC-EC	03-AC-EC	Jan-17	03-17-AC-EC	San Miguel Tenango	Early Cretaceous	Limestone	19.89555556	19.89555556	-97.91083333			
04-AC-EC	04-AC-EC	Jan-17	04-17-AC-EC-003	San Miguel Tenango	Early Cretaceous	Limestone	19.89555556	19.89555556	-97.91027778	Indirect Tensile Strength (Brazilian Test)	Porosity	
04-AC-EC	04-AC-EC	Jan-17	04-17-AC-EC-004	San Miguel Tenango	Early Cretaceous	Limestone	19.89555556	19.89555556	-97.91027778	Indirect Tensile Strength (Brazilian Test)	Porosity	
04-AC-EC	04-AC-EC	Jan-17	04-17-AC-EC-005	San Miguel Tenango	Early Cretaceous	Limestone	19.89555556	19.89555556	-97.91027778	Indirect Tensile Strength (Brazilian Test)	Porosity	
04-AC-EC	04-AC-EC	Jan-17	04-17-AC-EC-006	San Miguel Tenango	Early Cretaceous	Limestone	19.89555556	19.89555556	-97.91027778	Indirect Tensile Strength (Brazilian Test)		
04-AC-EC	04-AC-EC	Jan-17	04-17-AC-EC-007	San Miguel Tenango	Early Cretaceous	Limestone	19.89555556	19.89555556	-97.91027778	Indirect Tensile Strength (Brazilian Test)		
04-AC-EC	04-AC-EC	Jan-17	04-17-AC-EC-008	San Miguel Tenango	Early Cretaceous	Limestone	19.89555556	19.89555556	-97.91027778	Indirect Tensile Strength (Brazilian Test)		
04-AC-EC	04-AC-EC	Jan-17	04-17-AC-EC-009	San Miguel Tenango	Early Cretaceous	Limestone	19.89555556	19.89555556	-97.91027778	Indirect Tensile Strength (Brazilian Test)		
04-AC-EC	04-AC-EC	Jan-17	04-17-AC-EC-010	San Miguel Tenango	Early Cretaceous	Limestone	19.89555556	19.89555556	-97.91027778	Indirect Tensile Strength (Brazilian Test)		
04-AC-EC	04-AC-EC	Jan-17	04-17-AC-EC-011	San Miguel Tenango	Early Cretaceous	Limestone	19.89555556	19.89555556	-97.91027778	Indirect Tensile Strength (Brazilian Test)		
04-AC-EC	04-AC-EC	Jan-17	04-17-AC-EC-012	San Miguel Tenango	Early Cretaceous	Limestone	19.89555556	19.89555556	-97.91027778	Indirect Tensile Strength (Brazilian Test)		
04-AC-EC	04-AC-EC	Jan-17	04-17-AC-EC-013	San Miguel Tenango	Early Cretaceous	Limestone	19.89555556	19.89555556	-97.91027778	Indirect Tensile Strength (Brazilian Test)		
04-AC-EC	04-AC-EC	Jan-17	04-17-AC-EC-014	San Miguel Tenango	Early Cretaceous	Limestone	19.89555556	19.89555556	-97.91027778	UCS		
04-AC-EC	04-AC-EC	Jan-17	04-17-AC-EC-015	San Miguel Tenango	Early Cretaceous	Limestone	19.89555556	19.89555556	-97.91027778	UCS		
06-AC-EC	06-AC-EC	Jan-17	06-17-AC-EC	San Miguel Tenango	Early Cretaceous	Marl	19.89888889	19.89888889	-97.93361111			
07-AC-EC	07-AC-EC	Jan-17	07-17-AC-EC	San Miguel Tenango	Late Cretaceous	Limestone	19.89166667	19.89166667	-97.93361111			
08-AC-EC	08-AC-EC	Jan-17	08-17-AC-EC	San Miguel Tenango	Late Cretaceous	Limestone	19.89166667	19.89166667	-97.93361111			
09-AC-EC	09-AC-EC	Jan-17	09-17-AC-EC	San Miguel Tenango	Late Cretaceous	Limestone	19.89166667	19.89166667	-97.93361111			
10-AC-EC	10-AC-EC	Jan-17	10-17-AC-EC	San Miguel Tenango	Late Cretaceous	Limestone	19.89166667	19.89166667	-97.93361111			
11-AC-PB	11-AC-PB	Jan-17	11-17-AC-PB	Eagle Rock (San Miguel)	Pyroclastic Breccia	Pyroclastic Breccia	19.91138889	19.91138889	-97.93361111			
12-AC-PC	12-AC-PC	Jan-17	12-17-AC-PC	San Miguel Tenango	Pyroclastite	Pyroclastite	19.90305556	19.90305556	-97.93361111			
13-AC-PC	13-AC-PC	Jan-17	13-17-AC-PC	San Miguel Tenango	Pyroclastite	Pyroclastite	19.90305556	19.90305556	-97.93361111			
14-AC-EC	14-AC-EC	Jan-17	14-17-AC-EC-005	San Miguel Tenango	Late Cretaceous	Limestone	19.92555556	19.92555556	-97.92222222	Indirect Tensile Strength (Brazilian Test)	Porosity	
14-AC-EC	14-AC-EC	Jan-17	14-17-AC-EC-006	San Miguel Tenango	Late Cretaceous	Limestone	19.92555556	19.92555556	-97.92222222	Indirect Tensile Strength (Brazilian Test)	Porosity	
14-AC-EC	14-AC-EC	Jan-17	14-17-AC-EC-007	San Miguel Tenango	Late Cretaceous	Limestone	19.92555556	19.92555556	-97.92222222	Indirect Tensile Strength (Brazilian Test)	Porosity	
14-AC-EC	14-AC-EC	Jan-17	14-17-AC-EC-008	San Miguel Tenango	Late Cretaceous	Limestone	19.92555556	19.92555556	-97.92222222	Indirect Tensile Strength (Brazilian Test)	Porosity	
14-AC-EC	14-AC-EC	Jan-17	14-17-AC-EC-009	San Miguel Tenango	Late Cretaceous	Limestone	19.92555556	19.92555556	-97.92222222	Indirect Tensile Strength (Brazilian Test)	Porosity	
14-AC-EC	14-AC-EC	Jan-17	14-17-AC-EC-010	San Miguel Tenango	Late Cretaceous	Limestone	19.92555556	19.92555556	-97.92222222	Indirect Tensile Strength (Brazilian Test)	Porosity	
14-AC-EC	14-AC-EC	Jan-17	14-17-AC-EC-011	San Miguel Tenango	Late Cretaceous	Limestone	19.92555556	19.92555556	-97.92222222	Indirect Tensile Strength (Brazilian Test)	Porosity	
14-AC-EC	14-AC-EC	Jan-17	14-17-AC-EC-012	San Miguel Tenango	Late Cretaceous	Limestone	19.92555556	19.92555556	-97.92222222	Indirect Tensile Strength (Brazilian Test)	Porosity	
14-AC-EC	14-AC-EC	Jan-17	14-17-AC-EC-013	San Miguel Tenango	Late Cretaceous	Limestone	19.92555556	19.92555556	-97.92222222	Indirect Tensile Strength (Brazilian Test)	Porosity	
14-AC-EC	14-AC-EC	Jan-17	14-17-AC-EC-014	San Miguel Tenango	Late Cretaceous	Limestone	19.92555556	19.92555556	-97.92222222	Indirect Tensile Strength (Brazilian Test)	Porosity	
14-AC-EC	14-AC-EC	Jan-17	14-17-AC-EC-015	San Miguel Tenango	Late Cretaceous	Limestone	19.92555556	19.92555556	-97.92222222	Indirect Tensile Strength (Brazilian Test)	Porosity	
14-AC-EC	14-AC-EC	Jan-17	14-17-AC-EC-016	San Miguel Tenango	Late Cretaceous	Limestone	19.92555556	19.92555556	-97.92222222	Indirect Tensile Strength (Brazilian Test)	Porosity	
14-AC-EC	14-AC-EC	Jan-17	14-17-AC-EC-017	San Miguel Tenango	Late Cretaceous	Limestone	19.92555556	19.92555556	-97.92222222	Indirect Tensile Strength (Brazilian Test)	Porosity	
15-AC-EC	15-AC-EC	Jan-17	15-17-AC-EC	Las Minas - river	Argillite	Argillite	19.93972222	19.93972222	-97.88883333			
16-AC-GD	16-AC-GD	Jan-17	16-17-AC-GD	Las Minas - Boquillas	GD	Gnomoilite	19.69722222	19.69722222	-97.145			
17-AC-GD/SK	17-AC-GD/SK	Jan-17	17-17-AC-GD/SK	Las Minas - Boquillas	GD/SK	Gnomoilite/Skarn	19.69277778	19.69277778	-97.145			
18-AC-GD	18-AC-GD	Jan-17	18-17-AC-GD	Las Minas - Boquillas	GD	Gnomoilite	19.69277778	19.69277778	-97.145			
19-AC-SK	19-AC-SK	Jan-17	19-17-AC-SK	Las Minas - Boquillas	SK	Skarn	19.69277778	19.69277778	-97.145			
20-AC-WA	20-AC-WA	Jan-17	20-17-AC-WA	Las Minas - Eldorado	MA	Marble	19.68861111	19.68861111	-97.14527778			
21-AC-SK	21-AC-SK	Jan-17	21-17-AC-SK	Las Minas - Eldorado	SK	Skarn	19.68861111	19.68861111	-97.14527778			
22-AC-HE	22-AC-HE	Jan-17	22-17-AC-HE	Las Minas - Monte fall	HE	Skarn-Hematite	19.685	19.685	-97.14533333			
23-AC-SK	23-AC-SK	Jan-17	23-17-AC-SK	Las Minas - Monte fall	SK	Skarn	19.685	19.685	-97.14533333			
24-AC-RH	24-AC-RH	Jan-17	24-17-AC-RH	Acoculco Quarry	RH	Rhyolite	19.93277778	19.93277778	-98.20333333			

Figure A.1 – Sample list (description and location fo field work January 2017).



A (Norte)	Columna1	Jun-18	A.1 Rinco/JB-AC-MA	Rinconada	Rinco	Material	19.668151	97.16112	Resalt	Columna2	Permeability	Columna3
GDPA-C01	G1 (Paromita)	May-17	GDPA_G1-M1B-LH-GD-C01	Las Minas River	Boulder from the river	Granodiorite	19.697838	-97.14224	Cleoron bend test			
GDPA-C02	G1 (Paromita)	May-17	GDPA_G1-M1B-LH-GD-C02	Las Minas River	Boulder from the river	Granodiorite	19.697838	-97.14224	Cleoron bend test			
GDPA-C03	G1 (Paromita)	May-17	GDPA_G1-M1B-LH-GD-C03	Las Minas River	Boulder from the river	Granodiorite	19.697838	-97.14224	Cleoron bend test			
GDPA-C04	G2 (Paromita)	May-17	GDPA_G2-M1B-LH-GD-C04	Las Minas River	Boulder from the river	Granodiorite	19.697838	-97.14224	Cleoron bend test			
GDPA-C05	G2 (Paromita)	May-17	GDPA_G2-M1B-LH-GD-C05	Las Minas River	Boulder from the river	Granodiorite	19.697838	-97.14224	Cleoron bend test			
GDPA-C06	G3 (Paromita)	May-17	GDPA_G3-M1B-LH-GD-C06	Las Minas River	Boulder from the river	Granodiorite	19.697838	-97.14224	Cleoron bend test			
GDPA-C07	G3 (Paromita)	May-17	GDPA_G3-M1B-LH-GD-C07	Las Minas River	Boulder from the river	Granodiorite	19.697838	-97.14224	Cleoron bend test			
GDPA-C08	G4 (Paromita)	May-17	GDPA_G4-M1B-LH-GD-C08	Las Minas River	Boulder from the river	Granodiorite	19.697838	-97.14224	Cleoron bend test			
GDPA-C09	G4 (Paromita)	May-17	GDPA_G4-M1B-LH-GD-C09	Las Minas River	Boulder from the river	Granodiorite	19.697838	-97.14224	Cleoron bend test			
GDPA-C10	G5 (Paromita)	May-17	GDPA_G5-M1B-LH-GD-C10	Las Minas River	Boulder from the river	Granodiorite	19.697838	-97.14224	Cleoron bend test			
GDPA-C11	G5 (Paromita)	May-17	GDPA_G5-M1B-LH-GD-C11	Las Minas River	Boulder from the river	Granodiorite	19.697838	-97.14224	Cleoron bend test			
GDPA-C12	G6 (Paromita)	May-17	GDPA_G6-M1B-LH-GD-C12	Las Minas River	Boulder from the river	Granodiorite	19.697838	-97.14224	Cleoron bend test			
GDPA-C13	G6 (Paromita)	May-17	GDPA_G6-M1B-LH-GD-C13	Las Minas River	Boulder from the river	Granodiorite	19.697838	-97.14224	Cleoron bend test			
MAPA-C01	S1 (Paromita)	May-17	MAPA_S1-M1B-LH-MA-C01	Pueblo Nuevo	Pueblo Nuevo Oy	Marble	19.708517	-97.158128	Cleoron bend test			Porosity
MAPA-C02	S1 (Paromita)	May-17	MAPA_S1-M1B-LH-MA-C02	Pueblo Nuevo	Pueblo Nuevo Oy	Marble	19.708517	-97.158128	Cleoron bend test			Porosity
MAPA-C03	S1 (Paromita)	May-17	MAPA_S1-M1B-LH-MA-C03	Pueblo Nuevo	Pueblo Nuevo Oy	Marble	19.708517	-97.158128	Cleoron bend test			Porosity
MAPA-C04	S2 (Paromita)	May-17	MAPA_S2-M1B-LH-MA-C04	Pueblo Nuevo	Pueblo Nuevo Oy	Marble	19.708517	-97.158128	Cleoron bend test			
MAPA-C05	S2 (Paromita)	May-17	MAPA_S2-M1B-LH-MA-C05	Pueblo Nuevo	Pueblo Nuevo Oy	Marble	19.708517	-97.158128	Cleoron bend test			
MAPA-C06	S2 (Paromita)	May-17	MAPA_S2-M1B-LH-MA-C06	Pueblo Nuevo	Pueblo Nuevo Oy	Marble	19.708517	-97.158128	Cleoron bend test			
MAPA-C07	S3 (Paromita)	May-17	MAPA_S3-M1B-LH-MA-C07	Pueblo Nuevo	Pueblo Nuevo Oy	Marble	19.708517	-97.158128	Cleoron bend test			
MAPA-C08	S3 (Paromita)	May-17	MAPA_S3-M1B-LH-MA-C08	Pueblo Nuevo	Pueblo Nuevo Oy	Marble	19.708517	-97.158128	Cleoron bend test			
MAPA-C09	S3 (Paromita)	May-17	MAPA_S3-M1B-LH-MA-C09	Pueblo Nuevo	Pueblo Nuevo Oy	Marble	19.708517	-97.158128	Cleoron bend test			
MAPA-C10	S4 (Paromita)	May-17	MAPA_S4-M1B-LH-MA-C10	Pueblo Nuevo	Pueblo Nuevo Oy	Marble	19.708517	-97.158128	Cleoron bend test			
MAPA-C11	S4 (Paromita)	May-17	MAPA_S4-M1B-LH-MA-C11	Pueblo Nuevo	Pueblo Nuevo Oy	Marble	19.708517	-97.158128	Cleoron bend test			
MAPA-C12	S5 (Paromita)	May-17	MAPA_S5-M1B-LH-MA-C12	Pueblo Nuevo	Pueblo Nuevo Oy	Marble	19.708517	-97.158128	Cleoron bend test			
MAPA-C13	S5 (Paromita)	May-17	MAPA_S5-M1B-LH-MA-C13	Pueblo Nuevo	Pueblo Nuevo Oy	Marble	19.708517	-97.158128	Cleoron bend test			

Figure A.2 – Sample list (description and location for field work May 2017).





	Perfos 800-1900				Perfos 800-900				Perfos 1800-1900				Perfos 800-900				Perfos 1800-1900				Perfos 800-900				Perfos 1800-1900				
SR=1	L	260.13	305.85*2	303.46	304.55*2	303.46	304.55*2	303.46	304.55*2	260.13	305.85*2	303.46	304.55*2	303.46	304.55*2	260.13	305.85*2	303.46	304.55*2	260.13	305.85*2	303.46	304.55*2	303.46	304.55*2	260.13	305.85*2	303.46	304.55*2
	H	0.12	0.17	0.11	0.11	0.11	0.11	0.11	0.11	0.12	0.17	0.11	0.11	0.11	0.11	0.12	0.17	0.11	0.11	0.12	0.17	0.11	0.11	0.11	0.11	0.12	0.17	0.11	0.11
	w	0.33	0.33	0.33	0.33	0.33	0.33	0.33	0.33	0.33	0.33	0.33	0.33	0.33	0.33	0.33	0.33	0.33	0.33	0.33	0.33	0.33	0.33	0.33	0.33	0.33	0.33	0.33	0.33
	P <sub>inf</sub>	11.77	16.81	6.99	6.99	6.99	6.99	6.99	6.99	11.77	16.81	6.99	6.99	6.99	6.99	11.77	16.81	6.99	6.99	11.77	16.81	6.99	6.99	6.99	6.99	11.77	16.81	6.99	6.99
SR=4	L	260.13	305.85*2	303.46	304.55*2	303.46	304.55*2	303.46	304.55*2	260.13	305.85*2	303.46	304.55*2	303.46	304.55*2	260.13	305.85*2	303.46	304.55*2	260.13	305.85*2	303.46	304.55*2	303.46	304.55*2	260.13	305.85*2	303.46	304.55*2
	H	0.12	0.17	0.11	0.11	0.11	0.11	0.11	0.11	0.12	0.17	0.11	0.11	0.11	0.11	0.12	0.17	0.11	0.11	0.12	0.17	0.11	0.11	0.11	0.11	0.12	0.17	0.11	0.11
	w	0.33	0.33	0.33	0.33	0.33	0.33	0.33	0.33	0.33	0.33	0.33	0.33	0.33	0.33	0.33	0.33	0.33	0.33	0.33	0.33	0.33	0.33	0.33	0.33	0.33	0.33	0.33	0.33
	P <sub>inf</sub>	11.77	16.81	6.99	6.99	6.99	6.99	6.99	6.99	11.77	16.81	6.99	6.99	6.99	6.99	11.77	16.81	6.99	6.99	11.77	16.81	6.99	6.99	6.99	6.99	11.77	16.81	6.99	6.99
SR=6	L	261.37	306.97	306.97	307.45*2	306.97	307.45*2	306.97	307.45*2	261.37	306.97	306.97	307.45*2	306.97	307.45*2	261.37	306.97	306.97	307.45*2	261.37	306.97	306.97	307.45*2	306.97	307.45*2	261.37	306.97	306.97	307.45*2
	H	0.14	0.18	0.12	0.12	0.12	0.12	0.12	0.12	0.14	0.18	0.12	0.12	0.12	0.12	0.14	0.18	0.12	0.12	0.14	0.18	0.12	0.12	0.12	0.12	0.14	0.18	0.12	0.12
	w	0.38	0.29	0.29	0.29	0.29	0.29	0.29	0.29	0.38	0.29	0.29	0.29	0.29	0.29	0.38	0.29	0.29	0.29	0.38	0.29	0.29	0.29	0.29	0.29	0.38	0.29	0.29	0.29
	P <sub>inf</sub>	12.18	17.17	7.35	7.35	7.35	7.35	7.35	7.35	12.18	17.17	7.35	7.35	7.35	7.35	12.18	17.17	7.35	7.35	12.18	17.17	7.35	7.35	7.35	7.35	12.18	17.17	7.35	7.35
SR=10	L	262.25	307.74*2	309.18	309.18	309.18	309.18	309.18	309.18	262.25	307.74*2	309.18	309.18	309.18	309.18	262.25	307.74*2	309.18	309.18	262.25	307.74*2	309.18	309.18	309.18	309.18	262.25	307.74*2	309.18	309.18
	H	0.15	0.15	0.13	0.13	0.13	0.13	0.13	0.13	0.15	0.15	0.13	0.13	0.13	0.13	0.15	0.15	0.13	0.13	0.15	0.15	0.13	0.13	0.13	0.13	0.15	0.15	0.13	0.13
	w	0.19	0.29	0.29	0.29	0.29	0.29	0.29	0.29	0.19	0.29	0.29	0.29	0.29	0.29	0.19	0.29	0.29	0.29	0.19	0.29	0.29	0.29	0.29	0.29	0.19	0.29	0.29	0.29
	P <sub>inf</sub>	12.9	17.88	8.07	8.07	8.07	8.07	8.07	8.07	12.9	17.88	8.07	8.07	8.07	8.07	12.9	17.88	8.07	8.07	12.9	17.88	8.07	8.07	8.07	8.07	12.9	17.88	8.07	8.07

Figure A.4 – Results of the sensitivity analysis using MFrac for Hydraulic Fracture (HF) length stimulation modeling; Abbreviations: SR=Slurry Rate, K1c=fracture toughness,  $\nabla S_{hmin}$ = Minimum horizontal stress gradient, L=HF length, H=HF Height, w=HF width,  $P_{inf}$ =Internal fracture pressure,  $P_{surf}$ =Surface pressure, BHFP=Bottom Hole Fluid Pressure, BHTP=Bottom Hole Treatment Pressure





# B

## ABBREVIATIONS

Table B.1 – List of abbreviations

Abbreviations	Descriptions
EGS	Enhanced Geothermal System
GEMex	Geothermal Mexico ( <a href="http://www.gemex-h2020.eu/">http://www.gemex-h2020.eu/</a> )
TMVB	Trans-Mexican Volcanic Belt
HF	Hydraulic Fracture
NF	Natural (pre-existing) Fracture
FEM	Finite Elements Method
FVM	Finite Volume Method
XFEM	Extended Finite Elements Method
V-pf	Variational Phase-Field
DFM	Discrete Fracture Model
DFN	Discrete Fracture Network
RVE	Representative Volume Element
TH	Thermo-hydraulic (modeling)
THM	Thermo-hydraulic-Mechanical (modeling)
LEFM	Linear Elastic Fracture Mechanics
GDK	Fracture Kristianovich-Geertsma-De Klerk
PKN	Fracture Perkins-Kern-Nordgren
3D	Fracture 3-dimensional
CTOD	Crack Tip Open Displacement
NLD	Non-Local Damage
CZM	Cohesive Zone Model
UCS	Unconfined Compressive Strength
UTS	Unconfined Tensile Strength
LVDT	Linear Variable Differential Transformer
BHTP	Bottom Hole Treatment Pressure
BHFP	Bottom Hole Fluid Pressure
Bot.	Bottom
Cst.	Constant
D	Depth
DAF	Deformed Aperture of the Fracture
GSI	Geological Strength Index (Hoek-Brown)
MD	Meter drilled
Sec.	Section
SR	Slurry rate
TD	Total Depth
TVD	True Vertical Depth

Table B.2 – List of variables

Variables	Descriptions
<b>D</b>	Whole simulated Domain
$\Omega$	Matrix domain
$\Gamma$	Fractures domain
A	the cross-sectional area of the sample
L	sample length for rock physics laboratory tests
Q	flow rate for rock physics laboratory tests
H	Fracture height
L	Fracture length
w	Fracture width
$d_f$	fracture aperture
DAF	Deformed Aperture of the Fracture
E	Young's modulus
$\nu$	Poisson's ratio
$K_{IC}$	Fracture toughness
$f_s$	force/unit area
u	displacement
K	stiffness matrix
$k_n$	spring constant, stiffness in the normal direction
k	Permeability
$k_f$	Fracture permeability
$k_m$	Matrix permeability
$\Phi$	Porosity
$\mu$	Fluid viscosity
$c_t$	Total compressibility
$\mu_{Res}$	Reservoir fluid viscosity
$\mu_{filt}$	Filtrate fluid viscosity
$\nabla P_{res}$	Reservoir pressure Gradient
$P_{res}$	Reservoir pressure
$\Delta p$	Fracture net pressure
$P_{InF}$	Internal Fracture pressure
$P_{surf}$	Surface pressure
S	Far field stress tensor
$S_V$	Vertical Stress
$S_{Hmax}$	Maximum Horizontal Stress
$S_{hmin}$	Minimum Horizontal Stress



# C

## BIBLIOGRAPHY



# REFERENCES

- J. Adachi, E. Siebrits, A. Peirce, and J. Desroches. Computer simulation of hydraulic fractures. *International Journal of Rock Mechanics and Mining Sciences*, 44(5):739–757, 2007. ISSN 13651609. doi: 10.1016/j.ijrmms.2006.11.006.
- J I Adachi and E Detournay. Self-similar solution of a plane-strain fracture driven by a power-law fluid. *International Journal for Numerical and Analytical Methods in Geomechanics*, 26(6):579–604, 2002.
- R Alessi, J J. Marigo, C Maurini, and S Vidoli. Coupling damage and plasticity for a phase-field regularisation of brittle, cohesive and ductile fracture: One-dimensional examples. *International Journal of Mechanical Sciences*, pages 1–18, 2017. ISSN 00207403. doi: 10.1016/j.ijmecsci.2017.05.047. URL <http://dx.doi.org/10.1016/j.ijmecsci.2017.05.047>.
- R Alessi, S Vidoli, and L De Lorenzis. A phenomenological approach to fatigue with a variational phase-field model: The one-dimensional case. *Engineering Fracture Mechanics*, 190:53–73, 2018. ISSN 00137944. doi: 10.1016/j.engfracmech.2017.11.036. URL <https://doi.org/10.1016/j.engfracmech.2017.11.036>.
- M Ambati, T Gerasimov, and L De Lorenzis. Phase-field modeling of ductile fracture. *Computational Mechanics*, 55(5):1017–1040, 2015. ISSN 01787675. doi: 10.1007/s00466-015-1151-4. URL <http://dx.doi.org/10.1007/s00466-015-1151-4>.
- L Ambrosio and V M Tortorelli. Approximation of functional depending on jumps by elliptic functional via  $\Gamma$  convergence. *Communications on Pure and Applied Mathematics*, 43(8):999–1036, 1990.
- L Ambrosio and V M Tortorelli. On the approximation of free discontinuity problems. *Boll. Un. Mat. Ital. B (7)*, 6(1):105–123, 1992.
- Hanen Amor, Jean-jacques Marigo, and Corrado Maurini. Regularized formulation of the variational brittle fracture with unilateral contact: numerical experiments. *Journal of Mechanics and Physics of Solids*, 57(8):1209–1229, 2009. ISSN 2173-5808. doi: 10.1016/j.cardiores.2006.11.005.
- S Balay, S Abhyankar, M. F. Adams, J Brown, P Brune, K Buschelman, L Dalcin, A Dener, V Eijkhout, W. D. Gropp, D Karpayev, D Kaushik, M. G. Knepley, D. A. May, L. C. McInnes, R. T. Mills, T Munson, K Rupp, P Sanan, B. F. Smith, S Zampini, H Zhang, and H Zhang. {PETS}c Users Manual. Technical Report ANL-95/11 - Revision 3.11, Argonne National Laboratory, 2019.



- Mickael Barbier, Youri Hamon, Jean Paul Callot, Marc Floquet, and Jean Marc Daniel. Sedimentary and diagenetic controls on the multiscale fracturing pattern of a carbonate reservoir: The Madison Formation (Sheep Mountain, Wyoming, USA). *Marine and Petroleum Geology*, 29(1):50–67, 2012. ISSN 02648172. doi: 10.1016/j.marpetgeo.2011.08.009. URL <http://dx.doi.org/10.1016/j.marpetgeo.2011.08.009>.
- N. Barton and V. Choubey. The Shear Strength of Rock Joints in Theory and Practice. *Rock Mechanics*, 10(1-2):1–54, 1977. ISSN 1434-453X. doi: <https://doi.org/10.1007/BF01261801>.
- T. Belytschko and T. Black. Elastic crack growth in finite elements with minimal remeshing. *International Journal for Numerical Methods in Engineering*, 45(5):601–620, 1999. ISSN 00295981. doi: 10.1002/(SICI)1097-0207(19990620)45:5<601::AID-NME598>3.0.CO;2-S.
- T. Belytschko, N. Moës, S. Usui, and C. Parimi. Arbitrary discontinuities in finite elements. *International Journal for Numerical Methods in Engineering*, 50(4):993–1013, 2001. ISSN 00295981. doi: 10.1002/1097-0207(20010210)50:4<993::AID-NME164>3.0.CO;2-M.
- M A Biot. General Theory of Three-Dimensional Consolidation. *Journal of Applied Physics*, 12(2):155–164, 1941.
- M J Borden, C V Verhoosel, M A Scott, T J R Hughes, and C M Landis. A phase-field description of dynamic brittle fracture. *Computer Methods in Applied Mechanics and Engineering*, 217-220:77–95, 2012. ISSN 00457825. doi: 10.1016/j.cma.2012.01.008. URL <http://dx.doi.org/10.1016/j.cma.2012.01.008>.
- B Bourdin, G A Francfort, and J.-J. Marigo. Numerical experiments in revisited brittle fracture. *J. Mech. and Phys. of Solids*, 48(4):797–826, 2000.
- B Bourdin, G A Francfort, and J.-J. Marigo. The variational approach to fracture. *Journal of Elasticity*, 91(1-3):5–148, 2008.
- B Bourdin, C J Larsen, and C L Richardson. A time-discrete model for dynamic fracture based on crack regularization. *International Journal of Fracture*, 168(2):133–143, 2011. ISSN 03769429. doi: 10.1007/s10704-010-9562-x.
- Blaise Bourdin, Chukwudi Chukwudozie, and Keita Yoshioka. A variational approach to the numerical simulation of hydraulic fracturing. *Proceedings - SPE Annual Technical Conference and Exhibition*, 2:1442–1452, 2012. doi: 10.2118/159154-ms.
- A Braides. *Approximation of Free-Discontinuity Problems*. Number 1694 in Lecture Notes in Mathematics. Springer, 1998. URL <http://www.springerlink.com/content/978-3-540-64771-3/>.
- Pierre-Olivier Bruna, Rahul Prabhakaran, Giovanni Bertotti, Andrea Succo, Andrea Bistacchi, and Fabrizio Storti. Multiscale 3D prediction of fracture network geometry and fluid flow efficiency in folded carbonate reservoir analogues ; Case study of the

- Island of Pag ( Croatia ). *Third EAGE Workshop on Naturally Fractures Reservoirs*, 2018 (February):1, 2018.
- Pierre Olivier Bruna, Julien Straubhaar, Rahul Prabhakaran, Giovanni Bertotti, Kevin Bisdorn, Gregoire Mariethoz, and Marco Meda. A new methodology to train fracture network simulation using multiple-point statistics. *Solid Earth*, 10(2):537–559, 2019. ISSN 18699529. doi: 10.5194/se-10-537-2019.
- Simon J Buckley, Kari Ringdal, Nicole Naumann, Benjamin Dolva, Tobias H Kurz, John A Howell, and Thomas J B Dewez. LIME : Software for 3-D visualization , interpretation , and communication of virtual geoscience models. *Geosphere*, 15(1):1–14, 2019. ISSN 1553-040X. doi: 10.1130/GES02002.1/4610849/ges02002.pdf.
- Andrew P Bunger and Emmanuel Detournay. Experimental validation of the tip asymptotics for a fluid-driven crack. *Journal of the Mechanics and Physics of Solids*, 56(11): 3101–3115, 2008.
- Andrew P Bunger, Robert G Jeffrey, and Emmanuel Detournay. Evolution and morphology of saucer-shaped sills in analogue experiments. In *Structure and Emplacement of High-Level Magmatic Systems*, pages 109–120. Geological Society, London, 2008.
- Andrew P Bunger, Elizaveta Gordeliy, and Emmanuel Detournay. Comparison between laboratory experiments and coupled simulations of saucer-shaped hydraulic fractures in homogeneous brittle-elastic solids. *Journal of the Mechanics and Physics of Solids*, 61(7):1636–1654, 2013.
- José Oscar Campos-Enriquez and Victor Hugo Garduño-Monroy. The shallow structure of Los Humeros and Las Derrumbadas geothermal fields, Mexico. *Geothermics*, 16 (5-6):539–554, 1987. ISSN 03756505. doi: 10.1016/0375-6505(87)90038-1.
- Carles Canet, Berenice Hernández-Cruz, Abigail Jiménez-Franco, Teresa Pi, Berenice Peláez, Ruth E. Villanueva-Estrada, Pura Alfonso, Eduardo González-Partida, and Sergio Salinas. Combining ammonium mapping and short-wave infrared (SWIR) reflectance spectroscopy to constrain a model of hydrothermal alteration for the Acoculco geothermal zone, Eastern Mexico. *Geothermics*, 53(July):154–165, 2015a. ISSN 03756505. doi: 10.1016/j.geothermics.2014.05.012.
- Carles Canet, Frederic Trillaud, Rosa María Prol-Ledesma, Galia González-Hernández, Berenice Peláez, Berenice Hernández-Cruz, and María M. Sánchez-Córdova. Thermal history of the Acoculco geothermal system, eastern Mexico: Insights from numerical modeling and radiocarbon dating. *Journal of Volcanology and Geothermal Research*, 305:56–62, 2015b. ISSN 03770273. doi: 10.1016/j.jvolgeores.2015.09.019. URL <http://dx.doi.org/10.1016/j.jvolgeores.2015.09.019>.
- P Carrara, M Ambati, R Alessi, and L De Lorenzis. A framework to model the fatigue behavior of brittle materials based on a variational phase-field approach. *Computer Methods in Applied Mechanics and Engineering*, page 112731, 2019. ISSN 0045-7825. doi: <https://doi.org/10.1016/j.cma.2019.112731>. URL <http://www.sciencedirect.com/science/article/pii/S0045782519306218>.

- Gerardo Carrasco Núñez, Javier Hernández, Lorena De León, Pablo Dávila, Gianluca Norini, Juan Pablo Bernal, Brian Jicha, Mario Navarro, Penélope López-Quiroz, and Terra Digitalis. Geologic Map of Los Humeros volcanic complex and geothermal field, eastern Trans-Mexican Volcanic Belt Mapa geológico del complejo volcánico Los Humeros y campo geotérmico, sector oriental del Cinturón Volcánico Trans-Mexicano. *Terra Digitalis*, 1(2):1–11, 2017. doi: 10.22201/igg.terradigitalis.2017.2.24.78.
- R. Chesnaux, D. M. Allen, and S. Jenni. Regional fracture network permeability using outcrop scale measurements. *Engineering Geology*, 108(3-4):259–271, 2009. ISSN 00137952. doi: 10.1016/j.enggeo.2009.06.024. URL <http://dx.doi.org/10.1016/j.enggeo.2009.06.024>.
- Jinhyun Choo and Wai Ching Sun. Cracking and damage from crystallization in pores: Coupled chemo-hydro-mechanics and phase-field modeling. *Computer Methods in Applied Mechanics and Engineering*, 335(March):347–379, 2018. ISSN 00457825. doi: 10.1016/j.cma.2018.01.044.
- T. Chugunova, V. Corpel, and J. P. Gomez. Explicit Fracture Network Modelling: From Multiple Point Statistics to Dynamic Simulation. *Mathematical Geosciences*, 49(4): 541–553, 2017. ISSN 18748953. doi: 10.1007/s11004-017-9687-9.
- C. Chukwudozie, B. Bourdin, K. Yoshioka, T. Buchmann, and P. Connolly. A new modeling approach to natural fracturing process. *47th US Rock Mechanics / Geomechanics Symposium 2013*, 4:2663–2672, 2013.
- Chukwudi Chukwudozie, Blaise Bourdin, and Keita Yoshioka. A variational phase-field model for hydraulic fracturing in porous media. *Computer Methods in Applied Mechanics and Engineering*, 347:957–982, 2019. ISSN 00457825. doi: 10.1016/j.cma.2018.12.037. URL <https://doi.org/10.1016/j.cma.2018.12.037>.
- CloudCompare. CloudCompare, 2019. URL <http://www.cloudcompare.org/>.
- B. Cotterell and J.R. Rice. Slightly curved or kinked cracks. *International Journal of Fracture*, 16(2):155–169, 1980. doi: <https://doi.org/10.1007/BF00012619>.
- Richard Davies, Gillian Foulger, Annette Bindley, and Peter Styles. Induced seismicity and hydraulic fracturing for the recovery of hydrocarbons. *Marine and petroleum geology*, 45:171–185, 2013.
- Ali Naghi Dehghan, Kamran Goshtasbi, and Kaveh Ahangari. European Journal of Environmental and Civil Engineering Mechanism of fracture initiation and propagation using a tri-axial hydraulic fracturing test system in naturally fractured reservoirs. *European Journal of Environmental and Civil Engineering*, 2015. doi: 10.1080/19648189.2015.1056384. URL <http://dx.doi.org/10.1080/19648189.2015.1056384>PLEASE.
- Gianpietro Del Piero. Constitutive equation and compatibility of the external loads for linear elastic masonry-like materials. *Meccanica*, 24(3):150–162, 1989. ISSN 00256455. doi: 10.1007/BF01559418.

- W S Dershowitz, P R La Pointe, and T W Doe. Advances in discrete fracture network modeling. *Proceedings of the US EPA/NGWA Fractured Rock Conference*, 2004:882–894, 2004.
- E. Detournay and A. H.D. D Cheng. Fundamentals of poroelasticity. *Comprehensive rock engineering*. Vol. 2, II:113–171, 1993. ISSN 01489062. doi: 10.1017/cbo9781139051132.003.
- Emmanuel Detournay. Mechanics of Hydraulic Fractures. *Annual Review of Fluid Mechanics*, 48(1):311–339, 2016. ISSN 0066-4189. doi: 10.1146/annurev-fluid-010814-014736.
- T. J.B. Dewez, D. Girardeau-Montaut, C. Allanic, and J. Rohmer. Facets : A cloudcompare plugin to extract geological planes from unstructured 3d point clouds. *International Archives of the Photogrammetry, Remote Sensing and Spatial Information Sciences - ISPRS Archives*, 41(June):799–804, 2016. ISSN 16821750. doi: 10.5194/isprsarchives-XLI-B5-799-2016.
- Michael J. Economides and Kenneth G Nolte. *Reservoir Stimulation*. Number Third Edition. Wiley, 1989. ISBN 9789004310087. doi: 10.15713/ins.mmj.3.
- W Ehlers and C Luo. A phase-field approach embedded in the Theory of Porous Media for the description of dynamic hydraulic fracturing. *Comput. Methods Appl. Mech. Engrg.*, 315:348–368, 2017. ISSN 00457825. doi: 10.1016/j.cma.2016.10.045. URL <http://dx.doi.org/10.1016/j.cma.2016.10.045>.
- W A Elders, G Ó Fridhlefsson, and A Albertsson. Drilling into magma and the implications of the Iceland Deep Drilling Project (IDDP) for high-temperature geothermal systems worldwide. *Geothermics*, 49:111–118, 2014.
- William L Ellsworth, Domenico Giardini, John Townend, Shemin Ge, and Toshihiko Shimamoto. Triggering of the Pohang, Korea, Earthquake (M w 5.5) by Enhanced Geothermal System Stimulation. *Seismological Research Letters*, 90(5):1844–1858, 2019.
- Luca Ferrari, Teresa Orozco-Esquivel, Vlad Manea, and Marina Manea. The dynamic history of the Trans-Mexican Volcanic Belt and the Mexico subduction zone. *Tectonophysics*, 522-523:122–149, 2012. ISSN 00401951. doi: 10.1016/j.tecto.2011.09.018. URL <http://dx.doi.org/10.1016/j.tecto.2011.09.018>.
- A G Fischer and J.-J. Marigo. Gradient damage models applied to dynamic fragmentation of brittle materials. *International Journal of Fracture*, 2019. ISSN 1573-2673. doi: 10.1007/s10704-019-00356-y. URL <https://doi.org/10.1007/s10704-019-00356-y>.
- Bernd Flemisch, Inga Berre, Wietse Boon, Alessio Fumagalli, Nicolas Schwenck, Anna Scotti, Ivar Stefansson, and Alexandru Tatomir. Benchmarks for single-phase flow in fractured porous media. *Advances in Water Resources*, 111:239–258, 2018. ISSN 03091708. doi: 10.1016/j.advwatres.2017.10.036.

- Magaly Flores-Armenta, Miguel Ramírez-Montes, and Lilibeth Morales-Alcalá. GEOTHERMAL ACTIVITY AND DEVELOPMENT IN MEXICO – Keeping the production going. “Short Course VI on Utilization of Low- and Medium-Enthalpy Geothermal Resources and Financial Aspects of Utilization, pages 1–12, 2014.
- Haakon Fossen. *Structural Geology*. Cambridge University Press, 2013. ISBN 978-0-511-77282-5. URL <http://www.cambridge.org/9780521516648>.
- Don B. Fox, Daniel Sutter, Koenraad F. Beckers, Maciej Z. Lukawski, Donald L. Koch, Brian J. Anderson, and Jefferson W. Tester. Sustainable heat farming: Modeling extraction and recovery in discretely fractured geothermal reservoirs. *Geothermics*, 46: 42–54, 2013. ISSN 03756505. doi: 10.1016/j.geothermics.2012.09.001. URL <http://dx.doi.org/10.1016/j.geothermics.2012.09.001>.
- Don Bruce Fox, Donald Lyle Koch, and Jefferson William Tester. The effect of spatial aperture variations on the thermal performance of discretely fractured geothermal reservoirs. *Geothermal Energy*, 3(1):1–29, 2015. ISSN 21959706. doi: 10.1186/s40517-015-0039-z.
- G A Francfort and J.-J Marigo. Revisiting brittle fracture as an energy minimization problem. *J. Mech. and Phys. of Solids*, 46(8):1319–1342, 1998.
- J.A. Franklin, Sun Zongqi, B.K. Atkinson, P.G. Meredith, F. Rummel, W. Muller, Y. Nishimatsu, H. Takahashi, L.S. Costin, A.R. Ingraffea, and G.F. Bobrov. ISRM SUGGESTED METHODS FOR DETERMINING THE FRACTURE TOUGHNESS OF ROCK. *International Journal of Rock Mechanics and Mining Sciences & Geomechanics Abstracts*, 25 (2):71–96, 1988. ISSN 01489062. doi: 10.1016/S0148-9062(96)00015-0. URL <http://linkinghub.elsevier.com/retrieve/pii/S0148906296000150>.
- Francesco Freddi and Gianni Royer-Carfagni. Variational fracture mechanics to model compressive splitting of masonry-like materials. *Annals of Solid and Structural Mechanics*, 2(2-4):57–67, 2011. ISSN 18676936. doi: 10.1007/s12356-011-0018-4.
- Pengcheng Fu, Randolph R. Settgast, Yue Hao, Joseph P. Morris, and Frederick J. Ryerson. The Influence of Hydraulic Fracturing on Carbon Storage Performance. *Journal of Geophysical Research: Solid Earth*, 122(12):9931–9949, 2017. ISSN 21699356. doi: 10.1002/2017JB014942.
- Darrell L. Gallup. Production engineering in geothermal technology: A review. *Geothermics*, 38(3):326–334, 2009. ISSN 03756505. doi: 10.1016/j.geothermics.2009.03.001.
- H Gao and J R Rice. Somewhat circular tensile cracks. *International Journal of Fracture*, pages 155–174, 1987.
- D Garagash and E Detournay. The tip region of a fluid-driven fracture in an elastic medium. *J. Appl. Mech.*, 67(1):183–192, 2000.
- Dmitry I Garagash and Leonid N Germanovich. Nucleation and arrest of dynamic slip on a pressurized fault. *Journal of Geophysical Research: Solid Earth*, 117(B10), 2012.

- Dmitry I Garagash, Emmanuel Detournay, and Jose I Adachi. Multiscale tip asymptotics in hydraulic fracture with leak-off. *Journal of Fluid Mechanics*, 669:260–297, 2011.
- T. T. Garipov, M. Karimi-Fard, and H. A. Tchelepi. Discrete fracture model for coupled flow and geomechanics. *Computational Geosciences*, 20(1):149–160, 2016. ISSN 15731499. doi: 10.1007/s10596-015-9554-z.
- J Geertsma and F De Klerk. Rapid Method of Predicting Width and Extent of Hydraulically Induced Fractures. *J Petroleum Technology*, 21(12):1571–1581, 1969. ISSN 0149-2136. doi: 10.2118/2458-pa.
- Sebastian Geiger and Stephan Matthäi. What can we learn from high-resolution numerical simulations of single- and multi-phase fluid flow in fractured outcrop analogues? *Geological Society, London, Special Publications*, 374(1):125–144, 2012. ISSN 0305-8719. doi: 10.1144/sp374.8.
- P.A. Gillespie, C.B. Howard, J.J. Walsh, and J. Watterson. Measurement and characterisation of spatial distributions of fractures. *Tectonophysics*, 226(1-4):113–141, 1993. ISSN 15206904. doi: 10.1016/0040-1951(93)90114-Y. URL [https://doi.org/10.1016/0040-1951\(93\)90114-Y](https://doi.org/10.1016/0040-1951(93)90114-Y).
- Golder Associates. FracMan®7.7. Copyright © 2018 Golder Associates. All rights reserved., (1), 2019. URL <http://www.golder.com>.
- A. A. Griffith. The Phenomena of Rupture and Flow in Solids. *Philosophical transactions of the royal society of london. Series A, containing papers of a mathematical or physical character*, 221(1921):163–198, 1921. URL <https://www.jstor.org/stable/91192>.
- H. Guo, N. I. Aziz, and L. C. Schmidt. Rock fracture-toughness determination by the Brazilian test. *Engineering Geology*, 33(3):177–188, 1993. ISSN 00137952. doi: 10.1016/0013-7952(93)90056-I.
- P Gupta and C A Duarte. Coupled formulation and algorithms for the simulation of non-planar three-dimensional hydraulic fractures using the generalized finite element method. *International Journal for Numerical and Analytical Methods in Geomechanics*, 40(10):1402–1437, 2016. ISSN 10969853. doi: 10.1002/nag.2485.
- Arne Claus Hansen-Dörr, René de Borst, Paul Hennig, and Markus Kästner. Phase-field modelling of interface failure in brittle materials. *Computer Methods in Applied Mechanics and Engineering*, 346:25–42, 2019. ISSN 0045-7825. doi: <https://doi.org/10.1016/j.cma.2018.11.020>. URL <http://www.sciencedirect.com/science/article/pii/S0045782518305772>.
- David Healy, Thomas G. Blenkinsop, Nicholas E. Timms, Philip G. Meredith, Thomas M. Mitchell, and Michele L. Cooke. Polymodal faulting: Time for a new angle on shear failure. *Journal of Structural Geology*, 80:57–71, 2015. ISSN 01918141. doi: 10.1016/j.jsg.2015.08.013. URL <http://dx.doi.org/10.1016/j.jsg.2015.08.013>.

- David Healy, Roberto E. Rizzo, David G. Cornwell, Natalie J.C. Farrell, Hannah Watkins, Nick E. Timms, Enrique Gomez-Rivas, and Michael Smith. FracPaQ: A MATLAB™ toolbox for the quantification of fracture patterns. *Journal of Structural Geology*, 95: 1–16, 2017. ISSN 01918141. doi: 10.1016/j.jsg.2016.12.003.
- Oliver Heidbach, Mojtaba Rajabi, Karsten Reiter, Moritz Ziegler, and Team WSM. World Stress Map Database Release 2016. *GFZ Data Services*, 2016. URL <http://doi.org/10.5880/WSM.2016.001>.
- Y Heider and B Markert. A phase-field modeling approach of hydraulic fracture in saturated porous media. *Mechanics Research Communications*, 80:38–46, 2017. ISSN 00936413. doi: 10.1016/j.mechrescom.2016.07.002. URL <http://dx.doi.org/10.1016/j.mechrescom.2016.07.002>.
- Evert Hoek, Carlos Carranza-Torres, and Brent Corkum. Estimating the Strength of Rock Materials. *Journal of The South African Institute of Mining and Metallurgy*, 74(8):312–320, 2002. doi: 10.1016/0148-9062(74)91782-3.
- M Hofacker and C Miehe. Continuum phase field modeling of dynamic fracture: Variational principles and staggered FE implementation. *International Journal of Fracture*, 178(1-2):113–129, 2012. ISSN 03769429. doi: 10.1007/s10704-012-9753-8.
- International Energy Agency (IEA). World Energy Outlook 2019. *Flagship report*, (November), 2019. URL <https://www.iea.org/reports/world-energy-outlook-2019>.
- G R Irwin. Analysis of Stresses and Strains Near the End of a Crack Traversing a Plate. *Journal of Applied Mechanics*, 24:361–364, 1957.
- ISRM. Suggested methods for the quantitative description of discontinuities in rock masses. *International Journal of Rock Mechanics and Mining Sciences & Geomechanics Abstracts*, 16(2):22, 1978. ISSN 01489062. doi: 10.1016/0148-9062(79)91476-1. URL <http://linkinghub.elsevier.com/retrieve/pii/0148906279914761>.
- J.C. Jaeger, N.G.M. Cook, and R.W. Zimmerman. *Fundamentals of rock mechanics*, volume 38. Blackwell Publishing, 4th edition, 2007. ISBN 1444308912. doi: 10.1016/0040-1951(77)90223-2. URL <http://linkinghub.elsevier.com/retrieve/pii/0040195177902232>.
- Pierre Jeanne, Yves Guglielmi, Jonny Rutqvist, Christophe Nussbaum, and Jens Birkholzer. Field characterization of elastic properties across a fault zone reactivated by fluid injection. *Journal of Geophysical Research: Solid Earth*, 122(8):6583–6598, 2017. ISSN 21699356. doi: 10.1002/2017JB014384.
- R. G. Jeffrey, C. R. Weber, William Vlahovic, and J. R. Enever. Hydraulic fracturing experiments in the great northern coal seam. *SPE - Asia Pacific Oil & Gas Conference*, pages 361–371, 1994. doi: 10.2523/28779-ms.

- R. G. Jeffrey, A. P. Bungler, B. Lecampion, X. Zhang, Z. R. Chen, A. Van As, D. P. Allison, W. De Beer, J. W. Dudley, E. Siebrits, M. Thiercelin, and M. Mainguy. Measuring hydraulic fracture growth in naturally fractured rock. *Proceedings - SPE Annual Technical Conference and Exhibition*, 6(January):3750–3768, 2009. doi: 10.2118/124919-ms.
- Anna Jentsch, Egbert Jolie, David G. Jones, Helen Taylor-Curran, Loïc Peiffer, Martin Zimmer, and Bob Lister. Magmatic volatiles to assess permeable volcano-tectonic structures in the Los Humeros geothermal field, Mexico. *Journal of Volcanology and Geothermal Research*, 394, 2020. ISSN 03770273. doi: 10.1016/j.jvolgeores.2020.106820. URL <https://doi.org/10.1016/j.jvolgeores.2020.106820>.
- Egbert Jolie, David Bruhn, Aída López Hernández, Domenico Liotta, Hugo Garduño-Monroy, Matteo Lelli, Gylfi Páll Hersir, Claudia Arango-Galván, Damien Bonté, Philippe Calcagno, Paromita Deb, Christoph Clauser, Elisabeth Peters, Abel F Hernández Ochoa, Ernst Huenges, Zayre Ivonne González Acevedo, Katrin Kieling, Eugenio Trumpy, Julio Vargas, Luis Carlos Gutiérrez-Negrín, Alfonso Aragón-Aguilar, Saeunn Halldórsdóttir, Eduardo González Partida, Jan-Diederik Van Wees, Miguel Angel, Ramírez Montes, Heber Didier, Diez León, and Gemex Team. GEMex – A Mexican-European Research Cooperation on Development of Superhot and Engineered Geothermal Systems. *PROCEEDINGS Geothermal Reservoir Engineering Stanford University*, pages 1–10, 2018.
- Reinhard Jung. EGS - Goodbye or Back to the Future. *Effective and Sustainable Hydraulic Fracturing*, 2013. ISSN 9789533070865. doi: 10.5772/52807. URL [dx.doi.org/10.5772/56458](http://dx.doi.org/10.5772/56458).
- George Karypis and Vipin Kumar. A fast and high quality multilevel scheme for partitioning irregular graphs. *SIAM Journal of Scientific Computing*, 20(1):359–392, 1998. ISSN 10648275. doi: 10.1137/S1064827595287997.
- J. Duncan Keppie. Terranes of Mexico Revisited: A 1.3 Billion year Odyssey. *International Geology Review*, 46(9):765–794, 2004. ISSN 0020-6814. doi: 10.2747/0020-6814.46.9.765. URL <http://www.tandfonline.com/doi/abs/10.2747/0020-6814.46.9.765>.
- L.J. Klinkenberg. The Permeability of Porous Media To Liquids and Gases. *Drilling Production Practice*, pages 200–213, 1941.
- O. Kolditz, S. Bauer, L. Bilke, N. Böttcher, J. O. Delfs, T. Fischer, U. J. Görke, T. Kalbacher, G. Kosakowski, C. I. McDermott, C. H. Park, F. Radu, K. Rink, H. B. Shao, H. B. Shao, F. Sun, Y. Y. Sun, A. K. Singh, J. Taron, M. Walther, W. Wang, N. Watanabe, Y. Wu, M. Xie, W. Xu, and B. Zehner. OpenGeoSys: An open-source initiative for numerical simulation of thermo-hydro-mechanical/chemical (THM/C) processes in porous media. *Environmental Earth Sciences*, 67(2):589–599, 2012. ISSN 18666280. doi: 10.1007/s12665-012-1546-x.
- Michał Kruszewski. Predictions of in-situ stresses based on field data from the Acoculco geothermal field. *GEMex Report pre-Deliverables, WP8*, 2019.



- C Kuhn, T Noll, and R Müller. On phase field modeling of ductile fracture. *GAMM Mitteilungen*, 39(1):35–54, 2016. ISSN 09367195. doi: 10.1002/gamm.201610003.
- Grzegorz Kwiatek, Tero Saarno, Thomas Ader, Felix Bluemle, Marco Bohnhoff, Michael Chendorain, Georg Dresen, Pekka Heikkinen, Ilmo Kukkonen, Peter Leary, Maria Leonhardt, Peter Malin, Patricia Martínez-Garzón, Kevin Passmore, Paul Passmore, Sergio Valenzuela, and Christopher Wollin. Controlling fluid-induced seismicity during a 6.1-km-deep geothermal stimulation in Finland. *Science Advances*, 5(5):1–12, 2019. ISSN 23752548. doi: 10.1126/sciadv.aav7224.
- Juliette Lamarche, Arthur P.C. Lavenu, Bertrand D.M. Gauthier, Yves Guglielmi, and Océane Jayet. Relationships between fracture patterns, geodynamics and mechanical stratigraphy in Carbonates (South-East Basin, France). *Tectonophysics*, 581:231–245, 2012. ISSN 00401951. doi: 10.1016/j.tecto.2012.06.042. URL <http://dx.doi.org/10.1016/j.tecto.2012.06.042>.
- Arthur P.C. Lavenu, Juliette Lamarche, Roland Salardon, Arnaud Gallois, Lionel Marié, and Bertrand D.M. Gauthier. Relating background fractures to diagenesis and rock physical properties in a platform-slope transect. Example of the Maiella Mountain (central Italy). *Marine and Petroleum Geology*, 51:2–19, 2014. ISSN 02648172. doi: 10.1016/j.marpetgeo.2013.11.012. URL <http://dx.doi.org/10.1016/j.marpetgeo.2013.11.012>.
- Brice Lecampion, Andrew Bunger, and Xi Zhang. Numerical methods for hydraulic fracture propagation: a review of recent trends. *Journal of natural gas science and engineering*, 49:66–83, 2018.
- S Lee, M F Wheeler, and T Wick. Iterative coupling of flow, geomechanics and adaptive phase-field fracture including level-set crack width approaches. *Journal of Computational and Applied Mathematics*, 314:40–60, 2017. ISSN 03770427. doi: 10.1016/j.cam.2016.10.022. URL <http://dx.doi.org/10.1016/j.cam.2016.10.022>.
- Bjoern A Legarth and Ali Saadat. Energy Consumption for Geothermal Wells. *Database*, (April):24–29, 2005.
- F. Lehner and Mark Kachanov. On modelling of “winged” cracks forming under compression. *International Journal of Fracture*, 77:R69–R75, 1996.
- Qinghua Lei, John Paul Latham, and Chin Fu Tsang. The use of discrete fracture networks for modelling coupled geomechanical and hydrological behaviour of fractured rocks. *Computers and Geotechnics*, 85:151–176, 2017. ISSN 18737633. doi: 10.1016/j.compgeo.2016.12.024. URL <http://dx.doi.org/10.1016/j.compgeo.2016.12.024>.
- Baptiste Lepillier, Alexandros Daniilidis, Nima Gholizadeh, Pierre-olivier Bruna, Kummerow Juliane, and David Bruhn. A fracture flow permeability and stress dependency simulation applied to multi-reservoirs , multi-production scenarios analysis. *Geothermal Energy*, 2019. doi: <https://doi.org/10.1186/s40517-019-0141-8>. URL <https://rdcu.be/bPyIc>.

- Baptiste Lepillier, Pierre-Olivier Bruna, David Bruhn, Eivind Bastesen, Alexandros Daniilidis, Óscar Garcia, Anita Torabi, and Walter Wheeler. From outcrop scanlines to discrete fracture networks, an integrative workflow. *Journal of Structural Geology*, 133(January):103992, 2020a. ISSN 0191-8141. doi: <https://doi.org/10.1016/j.jsg.2020.103992>. URL <http://www.sciencedirect.com/science/article/pii/S0191814119303050>.
- Baptiste Lepillier, Alexandros Daniilidis, Francesco Parisio, Keita Yoshioka, Pierre-olivier Bruna, and David Bruhn. A fully integrated EGS evaluation workflow. *PROCEEDINGS, 45th Workshop on Geothermal Reservoir Engineering Stanford*, (February 10-12, 2020): 1–7, 2020b.
- Baptiste Lepillier, Keita Yoshioka, Francesco Parisio, Richard Bakker, and David Bruhn. Variational Phase-field modeling of hydraulic fracture interaction with natural fractures and application to Enhanced Geothermal Systems. *Journal of Geophysical Research: Solid Earth*, 2020c.
- J. Z. Li, S. E. Laubach, J. F.W. Gale, and R. A. Marrett. Quantifying opening-mode fracture spatial organization in horizontal wellbore image logs, core and outcrop: Application to Upper Cretaceous Frontier Formation tight gas sandstones, USA. *Journal of Structural Geology*, 108:137–156, 2018. ISSN 01918141. doi: 10.1016/j.jsg.2017.07.005.
- T Li, J.-J. Marigo, D Guilbaud, and S Potapov. Gradient damage modeling of brittle fracture in an explicit dynamic context. *International Journal for Numerical Methods in Engineering*, 00(March):1–25, 2016. ISSN 0743-1619. doi: 10.1002/nme.
- Wei Li, Keith Yost, and Rita Sousa. Heat Transfer between Fluid Flow and Fractured Rocks. *GRC 2013 Annual Meeting*, 37:165–171, 2013. ISSN 01935933.
- Yanrong Li and Yongbo Zhang. Quantitative estimation of joint roughness coefficient using statistical parameters. *International Journal of Rock Mechanics and Mining Sciences*, 77:27–35, 2015. ISSN 13651609. doi: 10.1016/j.ijrmmms.2015.03.016. URL <http://dx.doi.org/10.1016/j.ijrmmms.2015.03.016>.
- Domenico Liotta, Eivind Bastesen, Caterina Bianco, Andrea Brogi, Alfredo Caggianelli, Victor-Hugo Garduño-Monroy, Edoardo Gonzalez-Partida, Adrian Jimenez-Haro, Wiesła Kozdrój, Alicja Lacinska, Baptiste Lepillier, Guia Morelli, Jerzy Nawrocki, Emmanuel Olvera-Garcia, Magdalena Pańczyk-Nawrocka, Christopher Rochelle, Giovanni Ruggieri, Anita Torabi, Gennaro Ventruti, Walter Wheeler, Krystian Wójcik, Małgorzata Ziółkowska- Kozdrój, and Martina Zucchi. Analogue Geothermal Systems In Mexico : Insights Into The Deep Part Of Los Humeros Geothermal Field From The Las Minas Mining Area ( Eastern Mexico ). *Proceedings World Geothermal Congress 2020*, pages 1–9, 2020.
- Xiaohuan Liu, Sanjay Srinivasan, and Dale Wong. Geological Characterization Of Naturally Fractured Reservoirs Using Multiple Point Geostatistics. *SPE/DOE Improved Oil Recovery Symposium*, page 12, 2002. doi: 10.2118/75246-MS. URL <https://doi.org/10.2118/75246-MS>.

- Jose Angel Lopez-Comino, Simone Cesca, Marius Kriegerowski, Sebastian Heimann, Torsten Dahm, Janusz Mirek, and Stanislaw Lasocki. Monitoring performance using synthetic data for induced microseismicity by hydrofracking at the Wysin site (Poland). *Geophysical Journal International*, pages 42–55, 2017.
- Aída López-Hernández, Gerardo García-Estrada, Gerardo Aguirre-Díaz, Eduardo González-Partida, Hugo Palma-Guzmán, and José L. Quijano-León. Hydrothermal activity in the Tulancingo-Acocolco Caldera Complex, central Mexico: Exploratory studies. *Geothermics*, 38(3):279–293, 2009. ISSN 03756505. doi: 10.1016/j.geothermics.2009.05.001.
- Cecilia Lorenzo Pulido, Magaly Flores Armenta, and Gérman Ramírez Silva. Characterization of the Acocolco Geothermal Zone as a HDR System. *Grc Transactions*, 34: 369–372, 2010. ISSN 01935933.
- Renchao Lu, Thomas Nagel, Hua Shao, Olaf Kolditz, and Haibing Shao. Modeling of Dissolution-Induced Permeability Evolution of a Granite Fracture Under Crustal Conditions. *Journal of Geophysical Research: Solid Earth*, 123(7):5609–5627, 2018.
- John W Lund. 100 Years of Geothermal Power Product. *PROCEEDINGS Thirtieth Workshop on Geothermal Reservoir Engineering Stanford University*, pages 1–10, 2005.
- Ernest L. Majer, Roy Baria, Mitch Stark, Stephen Oates, Julian Bommer, Bill Smith, and Hiroshi Asanuma. Induced seismicity associated with Enhanced Geothermal Systems. *Geothermics*, 36(3):185–222, 2007. ISSN 03756505. doi: 10.1016/j.geothermics.2007.03.003.
- V. C. Manea, M. Manea, and L. Ferrari. A geodynamical perspective on the subduction of Cocos and Rivera plates beneath Mexico and Central America. *Tectonophysics*, 609 (January):56–81, 2013. ISSN 00401951. doi: 10.1016/j.tecto.2012.12.039.
- Paul Marinos and Evert Hoek. GSI: A geologically friendly tool for rock mass strength estimation. *ISRM International Symposium 2000, IS 2000*, 2018.
- M. Markovaara-Koivisto and E. Laine. MATLAB script for analyzing and visualizing scan-line data. *Computers and Geosciences*, 40:185–193, 2012. ISSN 00983004. doi: 10.1016/j.cageo.2011.07.010. URL <http://dx.doi.org/10.1016/j.cageo.2011.07.010>.
- M. Mauldon. Estimating mean fracture trace length and density from observations in convex windows. *Rock Mechanics and Rock Engineering*, 31(4):201–216, 1998. ISSN 07232632. doi: 10.1007/s006030050021.
- M. Mauldon, W. M. Dunne, and M. B. Rohrbaugh. Circular scanlines and circular windows: New tools for characterizing the geometry of fracture traces. *Journal of Structural Geology*, 23(2-3):247–258, 2001. ISSN 01918141. doi: 10.1016/S0191-8141(00)00094-8.
- Mark McClure, Mohsen Babazadeh, Sogo Shiozawa, and Jian Huang. Fully Coupled Hydromechanical Simulation of Hydraulic Fracturing in Three-Dimensional Discrete

- Fracture Networks. *SPE Hydraulic Fracturing Technology Conference, Texas, USA*, 2015. doi: 10.2118/173354-MS. URL <http://www.onepetro.org/doi/10.2118/173354-MS>.
- Mark W. McClure and Roland N. Horne. Investigation of injection-induced seismicity using a coupled fluid flow and rate/state friction model. *Geophysics*, 76(6), 2011. ISSN 00168033. doi: 10.1190/geo2011-0064.1.
- Mark W. McClure and Roland N. Horne. An investigation of stimulation mechanisms in Enhanced Geothermal Systems. *International Journal of Rock Mechanics and Mining Sciences*, 72(November):242–260, 2014. ISSN 13651609. doi: 10.1016/j.ijrmms.2014.07.011. URL <http://dx.doi.org/10.1016/j.ijrmms.2014.07.011>.
- Midland Valley. Move. ©Midland Valley Exploration Ltd 2019, (1), 2019. URL <https://www.mve.com/software>.
- C Miehe, F Welschinger, and M Hofacker. Thermodynamically consistent phase-field models of fracture: Variational principles and multi-field FE implementations. *International Journal for Numerical Methods in Engineering*, 83(10):1273–1311, 2010. ISSN 1097-0207. doi: 10.1002/nme.2861. URL <http://dx.doi.org/10.1002/nme.2861>.
- C Miehe, M Hofacker, L M Schänzel, and F Aldakheel. Phase field modeling of fracture in multi-physics problems. Part II. Coupled brittle-to-ductile failure criteria and crack propagation in thermo-elastic-plastic solids. *Computer Methods in Applied Mechanics and Engineering*, 294:486–522, 2015a. ISSN 00457825. doi: 10.1016/j.cma.2014.11.017.
- Christian Miehe, Steffen Mauthe, and Stephan Teichtmeister. Minimization principles for the coupled problem of Darcy-Biot-type fluid transport in porous media linked to phase field modeling of fracture. *Journal of the Mechanics and Physics of Solids*, 82: 186–217, 2015b. ISSN 00225096. doi: 10.1016/j.jmps.2015.04.006. URL <http://dx.doi.org/10.1016/j.jmps.2015.04.006>.
- A Mikelić, M F Wheeler, and T Wick. A Phase-Field method for propagating fluid-filled fractures coupled to a surrounding porous medium. *Multiscale Modeling & Simulation*, 48(1):162–186, 2015.
- E Milanese, P Rizzato, F Pesavento, S Secchi, and B A Schrefler. An explanation for the intermittent crack tip advancement and pressure fluctuations in hydraulic fracturing. *Hydraul Fract J*, 3(2):30–43, 2016.
- Nicolas Moës, John Dolbow, and Ted Belytschko. A finite element method for crack growth without remeshing. *International Journal for Numerical Methods in Engineering*, 46(1):131–150, 1999. ISSN 00295981. doi: 10.1002/(SICI)1097-0207(19990910)46:1<131::AID-NME726>3.0.CO;2-J.
- Lin Ni, Xue Zhang, Liangchao Zou, and Jinsong Huang. Phase-field modeling of hydraulic fracture network propagation in poroelastic rocks. *Computational Geosciences*, 2020.

- R.P. Nordgren. Propagation of a Vertical Hydraulic Fracture. *Society of Petroleum Engineers Journal*, 12(04):306–314, 1972. ISSN 0197-7520. doi: 10.2118/3009-pa.
- G. Norini, G. Groppelli, R. Sulpizio, G. Carrasco-Núñez, P. Dávila-Harris, C. Pellicioli, F. Zucca, and R. De Franco. Structural analysis and thermal remote sensing of the Los Humeros Volcanic Complex: Implications for volcano structure and geothermal exploration. *Journal of Volcanology and Geothermal Research*, 301:221–237, 2015. ISSN 03770273. doi: 10.1016/j.jvolgeores.2015.05.014. URL <http://dx.doi.org/10.1016/j.jvolgeores.2015.05.014>.
- P. Olasolo, M. C. Juárez, M. P. Morales, Sebastiano Damico, and I. A. Liarte. Enhanced geothermal systems (EGS): A review. *Renewable and Sustainable Energy Reviews*, 56: 133–144, 2016. ISSN 18790690. doi: 10.1016/j.rser.2015.11.031. URL <http://dx.doi.org/10.1016/j.rser.2015.11.031>.
- Emmanuel Olvera-garcía, Caterina Bianco, Víctor Hugo Garduño-monroy, Andrea Brogi, Walter Wheeler, Fidel Gómez-alvarez, Sergio Najera-blas, Adrián Jiménez-haro, Alejandro Guevara-alday, Eivind Bastesen, Baptiste Lepillier, Martina Zucchi, and Alfredo Caggianelli. Geological Map of Las Minas (Veracruz, Mexico). *Journal of Maps*, 2020.
- Ricardo J Padilla. GIS project of the Tectonic Map of Mexico. *AAPG Datapages*, (1), 2013. URL <http://www.datapages.com/gis-map-publishing-program/gis-open-files/geographic/tectonic-map-of-mexico-2013>.
- D. C.P. Peacock, C. W. Nixon, A. Rotevatn, D. J. Sanderson, and L. F. Zuluaga. Glossary of fault and other fracture networks. *Journal of Structural Geology*, 92(September):12–29, 2016. ISSN 01918141. doi: 10.1016/j.jsg.2016.09.008.
- T.K. K Perkins and L.R. R Kern. Widths of Hydraulic Fractures. *Journal of Petroleum Technology*, 13(09):937–949, 1961. ISSN 0149-2136. doi: 10.2118/89-pa.
- S. D. Priest and J. A. Hudson. Estimation of discontinuity spacing and trace length using scanline surveys. *International Journal of Rock Mechanics and Mining Sciences and*, 18(3):183–197, 1981. ISSN 01489062. doi: 10.1016/0148-9062(81)90973-6.
- Python Software Foundation. Python. *Copyright ©2001-2018. Python Software Foundation*, (1), 2019. URL <https://www.python.org/>.
- C. E. Renshaw and D. D. Pollard. An experimentally verified criterion for propagation across unbounded frictional interfaces in brittle, linear elastic materials. *International Journal of Rock Mechanics and Mining Sciences and*, 32(3):237–249, 1995. ISSN 01489062. doi: 10.1016/0148-9062(94)00037-4.
- Jonny Rutqvist, Jahan Noorishad, Chin-fu Tsang, and Ove Stephansson. Determination of fracture storativity in hard rocks using high-pressure injection testing. *Water Resources Research*, 34(10):2551–2560, 1998.
- D Santillán, R Juanes, and L Cueto-Felgueroso. Phase field model of fluid-driven fracture in elastic media: Immersed-fracture formulation and validation with analytical solutions. *J Geophys. Res.-Sol Ea.*, 2017. ISSN 21699356. doi: 10.1002/2016JB013572.

- A A Savitski and E Detournay. Propagation of a penny-shaped fluid-driven fracture in an impermeable rock: asymptotic solutions. *International journal of solids and structures*, 39(26):6311–6337, 2002.
- A.E Scheidegger. The Physics of Flow Through Porous Media. *Univ. of Toronto Press*, (3), 1974.
- Schlumberger Limited. Petrel. © 2018 Schlumberger Limited. All rights reserved., (1), 2019. URL <https://www.software.slb.com/products/petrel/petrel-2018>.
- A Schlüter, A Willenbücher, C Kuhn, and R Müller. Phase field approximation of dynamic brittle fracture. *Computational Mechanics*, 54(5):1141–1161, 2014. ISSN 01787675. doi: 10.1007/s00466-014-1045-x.
- Jean Schmittbuhl, Olivier Lengliné, François Cornet, Nicolas Cuenot, and Albert Genter. Induced seismicity in EGS reservoir: the creep route. *Geothermal Energy*, 2(1):1–13, 2014. ISSN 21959706. doi: 10.1186/s40517-014-0014-0.
- Ryan Schultz, Virginia Stern, Mark Novakovic, Gail Atkinson, and Yu Jeffrey Gu. Hydraulic fracturing and the Crooked Lake Sequences: Insights gleaned from regional seismic networks. *Geophysical Research Letters*, 42(8):2750–2758, 2015.
- Samuel W Scott and Thomas Driesner. Permeability changes resulting from quartz precipitation and dissolution around upper crustal intrusions. *Geofluids*, 2018, 2018.
- M Seiler, P Hantschke, A Brosius, and M Kästner. A numerically efficient phase-field model for fatigue fracture - 1D analysis. *Pamm*, 18(1):e201800207, 2018. doi: 10.1002/pamm.201800207.
- Servicio Geológico Mexicano. Carta Geológico-Minera Zacatlán E14-B14, Puebla, Esc. 1:50,000 Edition: 1. *Servicio Geológico Mexicano*, E14-B14(Figure 1), 1997. URL <http://www.gob.mx/sgm>.
- Servicio Geológico Mexicano. Carta Geológico-Minera Huauchinango F14-D83, Hidalgo y Puebla, Esc. 1:50,000 Edition: 1. *Servicio Geológico Mexicano*, F14-D83(1), 2002. URL <http://www.gob.mx/sgm>.
- S Shiozawa, S Lee, and M F Wheeler. The effect of stress boundary conditions on fluid-driven fracture propagation in porous media using a phase-field modeling approach. *International Journal for Numerical and Analytical Methods in Geomechanics*, (February 2018):1–25, 2019. ISSN 10969853. doi: 10.1002/nag.2899.
- B.B.S. Singhal and R.P. Gupta. *Applied Hydrogeology of Fractured Rocks*. Number february 2010. Springer Dordrecht Heidelberg London New York, 2010. ISBN 9789048187980. doi: 10.1007/978-90-481-8799-7.
- Olga Singurindy and Brian Berkowitz. The role of fractures on coupled dissolution and precipitation patterns in carbonate rocks. *Advances in water resources*, 28(5):507–521, 2005.

- David Snow. Anisotropic Permeability of Fractured Media. *Water Resources Research*, 5(6):1273–1289, 1969. doi: WR005i006p01273. URL <https://doi.org/10.1029/WR005i006p01273>.
- Ingrid Stober and Kurt Bucher. *Geothermal Energy - From Theoretical Models to Exploration and Development*. Springer, 2016. ISBN 9783642133510. doi: 10.1007/978-3-642-13352-7.
- Julien Straubhaar, Philippe Renard, Grégoire Mariethoz, Roland Froidevaux, and Olivier Besson. An improved parallel multiple-point algorithm using a list approach. *Mathematical Geosciences*, 43(3):305–328, 2011. ISSN 18748961. doi: 10.1007/s11004-011-9328-7.
- Megan J. Surette. *Quantifying heterogeneity in variably fractured rock using a hydrostructural domain approach*. [M.Sc. thesis]: British Columbia, Burnaby, Simon Fraser University, 2006.
- Pejman Tahmasebi. *Handbook of Mathematical Geosciences*. Number June. Springer International Publishing, 2018. ISBN 9783319789996. doi: [https://doi.org/10.1007/978-3-319-78999-6\\_30](https://doi.org/10.1007/978-3-319-78999-6_30). URL [http://dx.doi.org/10.1007/978-3-319-78999-6\\_{ }30](http://dx.doi.org/10.1007/978-3-319-78999-6_{ }30).
- Wataru Tanikawa and Toshihiko Shimamoto. Frictional and transport properties of the Chelungpu fault from shallow borehole data and their correlation with seismic behavior during the 1999 Chi-Chi earthquake. *Journal of Geophysical Research: Solid Earth*, 114(1):1–15, 2009. ISSN 21699356. doi: 10.1029/2008JB005750.
- E Tanné, T Li, B Bourdin, J-J. Marigo, and C Maurini. Crack nucleation in variational phase-field models of brittle fracture. *J. Mech. Phys. Solids*, 110:80–99, 2018. doi: 10.1016/j.jmps.2017.09.006.
- Erwan Tanne. *Variational phase-field models from brittle to ductile fracture : nucleation and propagation*. Theses, Université Paris-Saclay, dec 2017. URL <https://pastel.archives-ouvertes.fr/tel-01758354>.
- Ruth D. Terzaghi. Sources of Error in Joint Surveys. *Géotechnique*, 15(3):287–304, 1965. ISSN 0016-8505. doi: 10.1680/geot.1965.15.3.287.
- Jefferson W. Tester, Brian J. Anderson, Anthony S. Batchelor, David D. Blackwell, and Ronald DiPippo. *The Future of Geothermal Energy. Impact of Enhanced Geothermal Systems (EGS) on the United States in the 21st Century*. Massachusetts Institute of Technology, 2006. ISBN 0615134386.
- The MathWorks Inc. MATLAB. © 1994-2019 The MathWorks, Inc., 2019. URL <https://it.mathworks.com/>.
- The Organisation for Economic Co-operation and Development (OECD). *Environment at a Glance 2020*. Paris, 2020. ISBN 9789264498556. doi: 10.1787/ac4b8b89-en. URL <https://doi.org/10.1787/4ea7d35f-en.{ }0AISBN>.

- Victor C Tsai and James R Rice. A model for turbulent hydraulic fracture and application to crack propagation at glacier beds. *Journal of Geophysical Research: Earth Surface*, 115(F3), 2010.
- R. Tse and D. M. Cruden. Estimating joint roughness coefficients. *International Journal of Rock Mechanics and Mining Sciences and*, 16(5):303–307, 1979. ISSN 01489062. doi: 10.1016/0148-9062(79)90241-9.
- Julio Cesar Viggiano-Guerra, Magaly Flores Armenta, and German R Ramirez Silva. Evolucion del sistema geotérmico de Acoculco, Pue., México: Un estudio con base en estudios petrograficos del pozo EAC-2 y en otras consideraciones. *Geotermia*, 24(1):14–24, 2011. ISSN 01865897.
- Han Yi Wang. Hydraulic fracture propagation in naturally fractured reservoirs: Complex fracture or fracture networks. *Journal of Natural Gas Science and Engineering*, 68(June):102911, 2019. ISSN 18755100. doi: 10.1016/j.jngse.2019.102911. URL <https://doi.org/10.1016/j.jngse.2019.102911>.
- N.R. R Warpinski and L.W. W Teufel. Influence of Geologic Discontinuities on Hydraulic Fracture Propagation (includes associated papers 17011 and 17074). *Journal of Petroleum Technology*, 39(02):209–220, 1987. ISSN 0149-2136. doi: 10.2118/13224-pa.
- Noriaki Watanabe, Kohei Saito, Atsushi Okamoto, Kengo Nakamura, Takuya Ishibashi, Hanae Saishu, Takeshi Komai, and Noriyoshi Tsuchiya. Stabilizing and enhancing permeability for sustainable and profitable energy extraction from superhot geothermal environments. *Applied Energy*, 260:114306, 2020.
- Hannah Watkins, Clare E. Bond, Dave Healy, and Robert W.H. Butler. Appraisal of fracture sampling methods and a new workflow to characterise heterogeneous fracture networks at outcrop. *Journal of Structural Geology*, 72:67–82, 2015. ISSN 01918141. doi: 10.1016/j.jsg.2015.02.001. URL <http://dx.doi.org/10.1016/j.jsg.2015.02.001>.
- X. Weng, O. Kresse, C. Cohen, R. Wu, and H. Gu. Modeling of hydraulic fracture network propagation in a naturally fractured formation. *Society of Petroleum Engineers - SPE Hydraulic Fracturing Technology Conference 2011*, i:298–315, 2011. doi: 10.2118/140253-ms.
- Xiaowei Weng. Modeling of complex hydraulic fractures in naturally fractured formation. *Journal of Unconventional Oil and Gas Resources*, 9:114–135, 2014. ISSN 22133976. doi: 10.1016/j.juogr.2014.07.001. URL <http://dx.doi.org/10.1016/j.juogr.2014.07.001>.
- Leandra Weydt, Kristian Bär, Ingo Sas, Chiara Colombero, Cesare Comina, Paromita Deb, Baptiste Lepillier, Giuseppe Mandrone, Harald Milsch, Christopher Rochelle, Federico Vagnon, and Ingo Sass. Outcrop analogue study to determine reservoir properties of the Los Humeros and Acoculco geothermal fields, Mexico. *Geophysical Research Abstracts EGU General Assembly*, 20(727550):2018–7228, 2018. ISSN 16807359. doi: 10.5194/adgeo-45-281-2018.



- M F Wheeler, T Wick, and W Wollner. An augmented-Lagrangian method for the phase-field approach for pressurized fractures. *Computer Methods in Applied Mechanics and Engineering*, 271:69–85, 2014. ISSN 00457825. doi: 10.1016/j.cma.2013.12.005. URL <http://dx.doi.org/10.1016/j.cma.2013.12.005>.
- Z. A. Wilson and C. M. Landis. Phase-field modeling of hydraulic fracture. *J. Mech. Phys. Solids*, 96:264–290, 2016. ISSN 00225096. doi: 10.1016/j.jmps.2016.07.019. URL <http://dx.doi.org/10.1016/j.jmps.2016.07.019>.
- L Xia, J Yvonnet, and S Ghabezloo. Phase field modeling of hydraulic fracturing with interfacial damage in highly heterogeneous fluid-saturated porous media. *Engineering Fracture Mechanics*, 186(October):158–180, 2017. ISSN 00137944. doi: 10.1016/j.engfracmech.2017.10.005.
- Abdelaziz Yazid, Nabbou Abdelkader, and Hamouine Abdelmadjid. A state-of-the-art review of the X-FEM for computational fracture mechanics. *Applied Mathematical Modelling*, 33(12):4269–4282, 2009. ISSN 0307904X. doi: 10.1016/j.apm.2009.02.010.
- Ching H. Yew and Xiaowei Weng. Fracture propagation in a naturally fractured formation. *Mechanics of Hydraulic Fracturing*, 1:133–175, 2015. doi: 10.1016/b978-0-12-420003-6.00007-0.
- Keita Yoshioka and Blaise Bourdin. A variational hydraulic fracturing model coupled to a reservoir simulator. *International Journal of Rock Mechanics and Mining Sciences*, 88:137–150, 2016. ISSN 13651609. doi: 10.1016/j.ijrmms.2016.07.020. URL <http://dx.doi.org/10.1016/j.ijrmms.2016.07.020>.
- Keita Yoshioka, Francesco Parisio, Dmitri Naumov, Renchao Lu, Olaf Kolditz, and Thomas Nagel. Comparative verification of discrete and smeared numerical approaches for the simulation of hydraulic fracturing. *GEM - International Journal on Geomathematics*, 10(1):1–35, 2019. ISSN 18692680. doi: 10.1007/s13137-019-0126-6. URL <https://doi.org/10.1007/s13137-019-0126-6>.
- Conny Zeeb, Enrique Gomez-Rivas, Paul D. Bons, Simon Virgo, and Philipp Blum. Fracture network evaluation program (FraNEP): A software for analyzing 2D fracture trace-line maps. *Computers and Geosciences*, 60:11–22, 2013. ISSN 00983004. doi: 10.1016/j.cageo.2013.04.027. URL <http://dx.doi.org/10.1016/j.cageo.2013.04.027>.
- J. Zhang, W. B. Standifird, J. C. Roegiers, and Y. Zhang. Stress-dependent fluid flow and permeability in fractured media: From lab experiments to engineering applications. *Rock Mechanics and Rock Engineering*, 40(1):3–21, 2007. ISSN 07232632. doi: 10.1007/s00603-006-0103-x.
- Lei Zhang, Qinjun Kang, Li Chen, and Jun Yao. Simulation of Flow in Multi-Scale Porous Media Using the Lattice Boltzmann Method on Quadtree Grids. *Communications in Computational Physics*, 19(04):998–1014, 2016. ISSN 1815-2406. doi: 10.4208/cicp.110315.190815a.

- M. D. Zoback, C. A. Barton, M. Brudy, D. A. Castillo, T. Finkbeiner, B. R. Grollimund, D. B. Moos, P. Peska, C. D. Ward, and D. J. Wiprut. Determination of stress orientation and magnitude in deep wells. *International Journal of Rock Mechanics and Mining Sciences*, 40(7-8):1049–1076, 2003. ISSN 13651609. doi: 10.1016/j.ijrmms.2003.07.001.
- Mark D. Zoback. *Reservoir Geomechanics*. Cambridge University Press, 2007. ISBN 9780521770699.



# ACKNOWLEDGEMENTS

---

If there should be only one person to be named in this section, then this person would be DavidGathe. David, for offering me chance of doing this PhD, Agathe for pushing me just considering this offer.

Lieber David, Du war auf der Suche nach einem unabhängigen Studenten und ich brauchte meine Autonomie. Ich bin Dir sehr dankbar, dass du mich von Anfang an vertraut hast. Du hast immer alles getan, um mich auf dem persönlichen wie auf dem professionellen Ebene zu helfen. Ohne Dich und ohne deine Hilfe wäre das Ganze nicht möglich geworden. Ein Riesendank und Gratulierung für das Empathiebeispiel, das du auf einer täglichen Basis vermittelst.

GEMex is a large project, that some would call a big family. I enjoyed a lot being part of this nice family, we shared a lot of adventures from Mexico to Iceland, from the Dutch borrels to the never ending Italian dinners, from the field to the bar.

Dentro de la gran familia GEMex, especialmente a los que tuvieron la suerte de participar a las excursiones de campo, las vibras mexicanas son prominentes. Ninguno de estos proyectos hubieran sido posibles sin la ayuda de mis colegas mexicanos, incluyendo todos los estudiantes como Adrián, Emmanuel, Fidel y Oscar y para no olvidar a nadie la mejor banda Mexicana: *Los Piroxenos*. Por supuesto me gustaría expresar mi cariño y condolencias a Víctor Hugo Garduño Monroy. Quien es un ejemplo de generosidad y alegría. Fue un gran profesor y seguramente ninguno de estos proyectos hubiera sido posible sin el.

Domenico, Caterina, Andrea, Martina, grazie anche a voi! Grazie per il vostro entusiasmo nell'insegnamento della geologia, è stato un grande piacere lavorare con voi nel campo in Messico e all'Elba.

Til Anita, Eivind og Walter, jeg satt veldig stor pris på å dele med dere det Meksikansk felt arbeid og jeg var så glad å besøke dere i Bergen. Jeg er skuffet at vårt arbeid på Lime ikke bli en suksess men jeg er glad for vårt samarbeid. Tusen takk for alle våre diskusjoner om alt fra "deformation bands" til plastic avfall og "Chili-baguets"!

GEMex war von unterschiedlichen Elementen und von vielen Leuten abhängig. Auch wenn niemand auf der Erde unersetzbar ist, hat jede Regel eine Ausnahme : ohne Katrin hätte GEMex nie Erfolg gehabt! Gratulierung und Riesendank!

Natuurlijk wil ik al mijn collega's van de TU Delft bedanken. Startend met de secretarissen, altijd vriendelijk en geduldig en stonden altijd klaar om mij met van alles en nog

wat te helpen. Dank ook aan The Graduate School, bovenal Ilse & Wilma, die fantastisch werk leverden. Daarnaast wil ik mijn tweede Promotor Giovanni bedanken voor al onze discussies en zijn beschikbaarheid. Ik had het genoegen om samen te mogen werken met Anne, Sanaz, Maren en in algemene zin het voltallig geothermal team. In het bijzonder wil ik Richard bedanken, diegene die mij alles heeft geleerd in het experimenteel werk, voor zijn sturing. Dankjewel Lab technici, voor de waardevolle hulp zowel binnen als buiten het lab voor de niet zo werk gerelateerde activiteiten, zoals het repareren van fietsen, lassen en boren... hartelijk dank aan Marc, Jens, Wim, Karel en Ellen.

Αλεξ, Απόλαυσα ειλικρινά τη συνεργασία μαζί σας. Έμαθα πολλά από εσάς. Σας ευχαριστώ που ανοίξατε σε εμένα τον κόσμο του ' Δατα-Σεισιενζε ', ελπίζω ότι κάποια μέρα θα μπορέσουμε να ανοίξουμε το κέντρο επιστήμη-δεδομένων. Σας ευχαριστώ φίλε μου.

PoB, soyons clair, sans toi pas de MPS, pas de MPS, pas de fractures, pas de fractures, pas de DFN, pas de DFN, pas de modele. Pas de modele... Pas de modele. 22 fois, Merci.

Remi, Merci à toi. Tu m'as apporté bien plus que tu ne pourrais le croire, et là je parle aussi de la science!

Yann D., merci pour toutes nos discussions, tout au long de cette these, pour tes visites improvisées!

Francesco, mi hai accolto in UFZ, mi hai aperto la strada a OGS e condiviso con me, pazientemente, le tue conoscenze tecniche e personali e la tua esperienza. Grazie per questo, grazie per la tua generosità nel condividere le tue conoscenze, lo apprezzo molto e lo ritengo molto prezioso.

ケイタ、あなたはFrancescoと一緒にgeomechanicsとphase-fieldを私に教えてくれるのに多くの時間を費やしてくれました。そして、私たちの素晴らしい結果を得るために常に多くのモデルの計算を行うことで最大限助けてくれ、誰もできなかったくらい努めてくれました。これまでのすべての協力に感謝します。私はそれを非常に楽しみました。またあなたと協力する機会があれば、と思います。

Thanks to my PhD fellows, from TU Delft (special thanks to Cees for the Surf sessions, Reuben as my Python Master, Lisanne for the Zoback MOOC team work, Martha for the Tanzanian adventures and to Yang... my Bro!), PhD fellows in GFZ (especially Anna, Tania, Christian, Martin and Marton) and in GEMex (Emmanuel, Lenadra, Paromita... Paromita you are a PhD, right?) and co.

Merci à l'Univeristé GéoSciences Réunion, à Geneviève qui m'a laissé entrer dans le labo, à Camille qui m'a accueilli, à Laurent de m'avoir offert un bureau et au reste de l'équipe (Alicia, Anthony D., Anthony E, Bhavani, Fabrice, Rachel et Vincent), à tous un grand merci pour votre accueil spontané et généreux.

Many thanks to all the Houtrust squash team and especially my team-mates : Houtrust-H8!!! Clear Mind Full heart!

Succint mais sincère, Merci à ma famille, à mes amis. Merci encore et surtout à mon Lutin, pour tout et bien plus.

To end this, I am grateful to all the persons who helped me translating, many thanks to Atsushi, Alexis à qui j'ajoute un remerciement special aussi à Montse pour m'avoir hébergé et fait faire le tour des meilleurs restaurants de Mexico city, à Gene (et Alain qui a surement bien aidé à cette traduction), à notre confinée Jujulius, à Michel & Nina, to Jos & Suus, Marcel & Yvonne, and Sarah & Alberto.



# CURRICULUM VITÆ

## **Baptiste Patrick LEPILLIER**

13-05-1985      Born in Le Havre, France.

### **EDUCATION**

2005–2009      Master of Science in Geology  
Institut Polytechnique LaSalle-Beauvais  
Beauvais, France

2016–2020      PhD Candidate  
*Thesis :*          Characterization of Fracture-controlled EGS system  
*Promotor :*      Prof. dr. D. Bruhn

### **PROFESSIONAL EXPERIENCES**

2009–2010      Sedimentologist Cartographer  
SHOM (Service Hydrographique Oceanographique de la Marine)

2010–2012      Field development Geophysicist  
Total E&P Qatar

2012–2015      Exploration Geologist  
Engie





# LIST OF PUBLICATIONS

## C.1. PUBLICATIONS

13. **B. Lepillier**, K. Yoshioka, F. Parisio, R. Bakker, D. Bruhn, *Variational Phase-field modeling of hydraulic fracture interaction with natural fractures and application to Enhanced Geothermal Systems*, Journal of Geophysical Research, (2020).
12. **B. Lepillier**, A. Daniilidis, F. Parisio, K. Yoshioka, P.-o. Bruna, D. Bruhn, *A fully integrated EGS evaluation workflow*, Proceedings, 45th Workshop on Geothermal Reservoir Engineering Stanford, (2020).
11. **B. Lepillier** and D. Bruhn, *Predictive Mechanical Model for Fracture Stimulation in an EGS Context*, Proceedings, World Geothermal Congress, (2020).
10. **B. Lepillier**, P.-O. Bruna, D. Bruhn, E. Bastesen, A. Daniilidis, Ó. Garcia, A. Torabi, W. Wheeler, *From outcrop scanlines to discrete fracture networks, an integrative workflow*, Journal of Structural Geology 133, 103992, (2020).
9. **B. Lepillier**, A. Daniilidis, N. Gholizadeh, P.-o. Bruna, J. Kummerow, D. Bruhn, *A fracture flow permeability and stress dependency simulation applied to multi-reservoirs, multi-production scenarios analysis*, Geothermal Energy, (2019).
8. L. M. Weydt, Á. A. Ramírez-Guzmán, A. Pola-Villaseñor, **B. Lepillier**, J. Kummerow, G. Mandrone, C. Comina, P. Deb, G. Norini, E. Gonzalez-Partida, D. R. Avellán-López, J. L. Macias-Vázquez, K. Bär, I. Sass, *Petrophysical and mechanical rock property database of the Los Humeros and Aocolulco geothermal fields (Mexico)*, Earth System Science Data, (2020).
7. E. Olvera-garcía, C. Bianco, V.H. Garduño-monroy, A. Brogi, W. Wheeler, F. Gómez-alvarez, S. Najera-blas, A. Jiménez-haro, A. Guevara-alday, E. Bastesen, **B. Lepillier**, M. Zucchi, A. Caggianelli, *Geological Map of Las Minas (Veracruz, Mexico)* Journal of Maps, (2020)
6. K. Yoshioka, F. Parisio, **B. Lepillier**, D. Bruhn, O. Kolditz, T. Li, *A Variational phasefield model for toughness dominated hydraulic fracturing with no-tension constitutive model*, (2020).
5. D. Liotta, E. Bastesen, C. Bianco, A. Brogi, A. Caggianelli, V.-H. Garduño-Monroy, E. Gonzalez-Partida, A. Jimenez-Haro, W. Kozdrój, A. Lacinska, **B. Lepillier**, G. Morelli, J. Nawrocki, E. Olvera-Garcia, M. Pańczyk-Nawrocka, C. Rochelle, G. Ruggieri, A. Torabi, G. Ventruti, W. Wheeler, K. Wójcik, M. Ziółkowska-Kozdrój, and M. Zucchi, *Analogue Geothermal Systems In Mexico : Insights Into The Deep Part Of Los Humeros Geothermal Field From The Las Minas Mining Area (Eastern Mexico)*, Proceedings World Geothermal Congress, (2020).
4. H. Hofmann, E. Peters, A. Filipe Hernández Ochoa, F. Parisio, **B. Lepillier**, *Hydraulic stimulation scenarios for a potential Enhanced Geothermal System (EGS) in Aocolulco, Mexico*, Proceedings World Geothermal Congress, (2020).

3. F. Parisio, K. Yoshioka, **B. Lepillier**, J. Kummerow, O. Kolditz, *Hydro-fracturing Scenarios for a High-Temperature Geothermal System*, Proceedings World Geothermal Congress, (2020).
2. L. Weydt, K. Bär, C. Colombero, C. Comina, P. Deb, **B. Lepillier**, G. Mandrone, H. Milsch, C. Rochelle, F. Vagnon, I. Sass, *Outcrop analogue study to determine reservoir properties of the Los Humeros and Aocolulco geothermal fields, Mexico*, Geophysical Research Abstracts EGU General Assembly 20, (2018).
1. A. Cattaneo, N. Babonneau, G. Dan, J. Deverchere, A. Domzig, V. Gaullier, **B. Lepillier**, B.-M. de Lepinay, A. Nougues, P. Strzerzynski, N. Sultan, K. Yelles, *Submarine landslides along the Algerian margin : a review of their occurrence and potential link with tectonic structures*, Submarine Mass Movements and Their Consequences - 4th International Symposium, p515-525, (2010).

## C.2. CONFERENCES

10. GEMex Final Conference, (*Potsdam DE, 2020*)
9. Stanford Geothermal Workshop, SGW (*Palo Alto, California USA, 2020*)
8. European Geothermal Congres, EGC (*Den Haag NL, 2019*)
7. European Geothermal PhD Days, EGPD (*Potsdam DE, 2019*)
6. European Geothermal Workshop, EGW (*Karlsruhe DE, 2019*)
5. European Geothermal Workshop, EGW (*Strasbourg FR, 2018*)
4. European Geothermal PhD Days, EGPD (*Zurich CH, 2018*)
3. European Geoscience Union, EGU (*Vienna AT, 2018*)
2. Geothermal Resources Council, GRC (*Reno, Nevada USA, 2018*)
1. European Geothermal PhD Days, EGPD (*Bochum DE, 2017*)



